Collisions of ultracold dipolar molecules controlled by electric and electromagnetic fields

Lucas Lassabliere

université PARIS-SACLAY

Collisions of ultracold dipolar molecules controlled by electric and electromagnetic fields

Collisions de molécules dipolaires ultra-froides contrôlées par champs électrique et électromagnétique

Thèse de doctorat de l'université Paris-Saclay

École doctorale n° 572, Ondes et Matière (EDOM)
Spécialité de doctorat : Physique
Graduate School : Physique, Référent : Faculté des sciences d'Orsay

Thèse préparée dans la unité de recherche **Laboratoire Aimé Cotton** (Université Paris-Saclay, CNRS), sous la direction de **Goulven QUÉMÉNER**, Chargé de recherche

Thèse soutenue à Paris-Saclay, le 09 décembre 2021, par

Lucas LASSABLIÈRE

Composition du jury

Fabien GATTI Directeur de recherche, Institut des Sciences Moléculaires d'Orsay, CNRS, Université Paris-Saclay	Président
Guido PUPILLO Professeur des universités, Institut de Science et d'Ingénierie Supramoléculaires, Université de Strasbourg	Rapporteur & Examinateur
Andrea SIMONI Maître de conférences, Institut de Physique de Rennes, Université de Rennes 1	Rapporteur & Examinateur
Astrid BERGEAT Maître de conférences, Institut des Sciences Moléculaires, Université de Bordeaux	Examinatrice
François LIQUE Professeur des universités, Institut de Physique de Rennes, Université de Rennes 1	Examinateur
Goulven QUÉMÉNER Chargé de recherche, Laboratoire Aimé Cotton, CNRS, Université Paris-Saclay	Directeur de thèse

THESE DE DOCTORAT
NNT : 2021UPASP132

Remerciements

Mon aventure au laboratoire Aimé Cotton a commencé il y a un peu plus de trois ans lorsque j'ai rencontré Goulven Quéméner en cours de M2 et qui a accepté que je réalise mon stage puis ma thèse à ses côtés. Je tiens à lui exprimer ma profonde gratitude car il a su prendre le temps pour m'initier au domaine des molécules ultra-froides, au formalisme collisionnel et plus généralement au monde profesionnel de la recherche. Grâce à lui, j'ai acquis des qualités qui me serviront toute ma vie telle que la rigueur, l'autonomie et la persévérance.

Je remercie tous les membres de l'équipe THEOMOL : Nadia Bouloufa-Mafaa, Djamel Benredjem, Olivier Dulieu, Laurent Wiesenfeld, Maurice Raoult, Goulven Quéméner, Romain Véxiau, Fréderic Carlier, Eliane Luc, Charbel Karam, Xiaodong Xing, Ting Xie, Adrien Devolder et Humberto Da Silva avec qui j'ai passé de merveilleux moments. Merci pour avoir pris le temps de répondre à toutes mes questions lorsque je venais vous voir dans vos bureaux ou lors des réunions d'équipe. Merci également pour toutes les discussions intéressantes lors des pauses café.

Je remercie Brian Kendrick qui a pris le temps de répondre à toutes mes questions sur les coordonnées hypersphériques et sur le formalisme dont je me suis fortement inspiré pendant mes trois années de thèse.

Je tiens à remercier tous les membres de l'équipe MFC avec qui j'ai eu de nombreuses discussions scientifiques ou sur la vie en général. Je vous remercie également pour les parties d'échecs qui pouvaient durer plusieurs semaines et qui animaient parfois des journées entières.

Je remercie également tous les doctorants et plus particulièrement Thibault et Ky-Luc qui sont devenus de véritables amis. En espérant recroiser Thibault vers Toulouse et courage à Ky-Luc pour sortir ton premier 8A (attention j'arrive).

Je souhaite remercier Olivier Dulieu qui a succédé à Djamel Benredjem en tant que directeur du laboratoire Aimé Cotton il y a maintenant deux ans. Je pense sincèrement que le LAC peut être fier d'avoir un directeur aussi investi que toi. Merci pour ta réactivité et ta bienveillance lorsque je rencontrais des embuches sur mon chemin. Je te remercie également pour m'avoir fait confiance en acceptant que j'encadre un stagiaire et en me donnant des responsabilités lors des conseils de laboratoire.

Je remercie Christine Goncalves, pour avoir su gérer toute l'administration du LAC d'une main de maître. Je te remercie pour ton professionnalisme et également ta réactivité car tout était résolu en un claquement doigt, y compris lorsqu'il s'agissait de faire le plein de petits écoliers quand nous mourrions de faim.

Je remercie tous les membres du LAC Tech' avec qui je n'ai malheureusement pas eu

l'occasion de collaboré scientifiquement mais avec qui j'ai toujours eu de bonnes relations. Je repense aux discussions avec Christophe Siour et aux anecdotes de Bruno Vivans qui mettait toujours de bonne humeur.

Je souhaite remercier Guido Pupillo et Andrea Simoni qui ont accepté d'être rapporteur ainsi que Astrid Bergeat, Fabien Gatti et François Lique d'avoir accepté d'être examinateur lors de ma soutenance de thèse. Je vous remercie pour les discussions intéressantes que nous avons eues avant, pendant et après la soutenance de thèse.

Une thèse c'est avant de tout la recherche mais également de l'enseignement. Je remercie Hanna Enriquez et Khuon-Viet Pham pour m'avoir fait confiance en acceptant que je donne des TDs et TPs dans vos UEs. J'ai beaucoup appris à vos cotés et vous m'avez réconforté dans l'idée que l'enseignement est une véritable passion. Je remercie également tous les élèves Jérémy, Tanguy, Paul, Camélia, Metkham, Adé, Juju... avec qui j'ai passé d'agréablement moments.

Je remercie tous mes amis qui étaient dans les parages pendant ces trois années Joffrey, Ky-Luc, Ky-Vinh, Floriane, Louis, Eli, Peter, Meumeu, Emile, Soso, Louise, Mic, Victor, Robin... avec qui j'ai passé des moments inoubliables en soirée ou à Arkose.

Je remercie également tous mes amis qui étaient loin pendant ces cinq années dans la région parisienne mais avec qui nous avons gardé une réelle complicité : Terry, Marine, Elo, Marcelline, Thibs, Thalie, Mylie, Dylan, Clem.

Je remercie toute ma famille qui m'a toujours poussé à me dépasser et qui m'a toujours soutenu malgré les jours où je n'étais pas très présent. Une pensée à mon papi qui s'en est allé pendant ma thèse.

Tout mon amour à Metkham, merci pour le soutien que tu as su me donner au quotidien au cours de cette dernière année malgré les nuits blanches passées à travailler.

Je remercie Pasqal pour avoir accepté que je continue à leurs côtés avant même que je termine ma thèse. J'espère que la route avec vous sera belle.

Merci à toi lecteur de l'ombre, j'espère que ma thèse répondra aux questions que tu te poses.

Contents

List of Figures

Chapter 1

Synthèse en français

Il y a une vingtaine d'années, la physique atomique et moléculaire a été révolutionnée par des avancées conceptuelles et technologiques majeures. Le développement de méthodes de refroidissement et de piégeage telles que le refroidissement Doppler ou les mélasses optiques a permis de refroidir des atomes à des températures sans précédent, de l'ordre du millikelvin. Récompensées par le prix Nobel de physique en 1997, les recherches de Claude Cohen-Tannoudji, William Daniel Phillips et Steven Chu ont propulsé sur le devant de la scène internationale le domaine de la physique atomique froide et ultrafroide. Quelques années plus tard, des températures encore plus basses de quelques centaines de nanokelvins ont été atteintes grâce au développement de nouvelles techniques de refroidissement telles que le refroidissement par évaporation.

Les premiers gaz de molécules dipolaires ultra-froides préparées dans leur état fondamental rovibronique ont été formés dans les années 2000. Au travers des expériences, les physiciens ont constaté que quelque soit le caractère réactif ou non des molécules, des processus à courte portée conduisent à la perte des molécules. Des solutions doivent être trouvées pour réduire ces processus de perte afin de pouvoir atteindre expérimentalement les densités requises à la formation de gaz quantiques dégénérés. Les solutions développées sont regroupées sous le terme général d'écrantage. Elles sont basées sur le contrôle des collisions par l'application de champs externes. Actuellement, il existe quatre méthodes principales pour réduire ces pertes à courte portée. La première méthode utilise des réseaux optiques de différentes dimensions pour confiner les molécules loin les unes des autres. La seconde méthode est l'écrantage par champ électrique statique. En appliquant une valeur de champ électrique statique bien définie, on peut créer une barrière de potentiel à longue portée dans la voie incidente en profitant des propriétés de l'interaction dipôle-dipôle à longue portée. Les molécules sont alors maintenues éloignées les unes des autres et protégées des pertes à courte portée. La troisième méthode est l'écrantage par champ micro-onde. L'idée est également de contrôler les interactions dipôle-dipôle à longue portée en appliquant un champ micro-onde polarisé circulairement. La dernière méthode est l'écrantage optique, où le champ micro-onde est remplacé par un champ optique. Le mécanisme repose alors sur le couplage d'états électroniques plutôt que sur des états rotationnels.

L'un des objectifs de cette thèse est de développer une méthode pour écranter des molécules initialement préparées dans leur état rotationnel fondamental. Pour ce faire, je vais suivre la méthode d'écrantage optique initialement développée pour des atomes et l'adapter aux molécules. Un des défis est d'implémenter le champ électromagnétique dans un formalisme indépendant du temps et de trouver les paramètres du champ (fréquence et intensité) pour lesquels l'écrantage est efficace. Un deuxième objectif est de trouver des solutions pour réduire les pertes à trois corps tout en maintenant un écrantage efficace à deux corps. Avant de passer à l'étude des trois corps, je dois réduire autant que possible la complexité du problème à deux corps, car le nombre d'états augmente considérablement lorsqu'on passe à trois corps. Ensuite, je dois comprendre comment fonctionnent les collisions à trois corps et comment les étudier. Il existe différentes coordonnées hypersphériques, mais chacune présente des avantages et des inconvénients. Les coordonnées les plus appropriées sont les coordonnées APH, car elles traitent toutes les configurations atome-diatome de manière égale. En contrepartie, des termes divergents, également appelés singularités d'Eckart, apparaissent dans l'hamiltonien total. Ces termes divergents sont très importants car s'ils ne sont pas traités correctement, des erreurs importantes peuvent apparaître dans les résultats. Mon défi est de développer un code de collision à trois corps utilisant ces coordonnées APH tout en traitant correctement tous les termes singuliers. Ensuite, je dois l'adapter et l'appliquer au cas de l'écrantage à trois corps.

Ce manuscrit sera séparé en deux parties. La première partie traite des techniques d'écrantage appliquées aux collisions à deux corps. Le chapitre 3 passe en revue les bases théoriques de l'étude des collisions ultra-froides entre deux molécules. J'explique comment prendre en compte les pertes à courte portée et comment extraire les observables dont j'ai besoin en utilisant la théorie de la matrice de diffusion S. Dans le chapitre 4, j'applique ce formalisme pour décrire la méthode d'écrantage par champ micro-onde. Je montre que le taux de perte peut être largement réduit en faveur du taux de collision élastique pour un grand nombre de molécules dipolaires. Je présente également dans ce chapitre une méthode permettant de contrôler la longueur de diffusion molécule-molécule en ajustant l'intensité et la fréquence du champ micro-onde. Dans le chapitre 5, je montre comment simplifier grandement l'étude de l'écrantage via le développement d'un modèle simplifié. Je démontre que l'on peut obtenir des résultats similaires au calcul quantique complet sous certaines conditions qui sont explicitement présentées.

La deuxième partie traite des collisions à trois corps. Le chapitre 6 présente le formalisme pour traiter les collisions en coordonnées hypersphériques. Je démontre comment relier les différents types de coordonnées (Jacobi, Delves, Hypersphérique) et comment traiter avec précision les singularités d'Eckart. Dans le chapitre 7, j'adapte ce formalisme pour étudier la supression des pertes à trois corps. Dans le chapitre 8, je me concentre sur les collisions $Li+Li_2$ et utilise les résultats d'articles récents pour vérifier mon code à trois corps. Enfin, je conclurai et donnerai quelques perspectives dans le chapitre 9.

Chapter 2

Introduction

About twenty years ago, atomic and molecular physics was revolutionized by major conceptual and technological advances [1, 2, 3]. The development of cooling and trapping methods such as Doppler cooling or optical molasses [4, 5] allowed to cool atoms to unprecedented temperatures in the millikelvin range. Rewarded by the Nobel Prize in Physics in 1997, the research of Claude Cohen-Tannoudji, William Daniel Phillips and Steven Chu [4, 5, 6] has brought the field of cold and ultracold atomic physics to the forefront of science. A few years later, even lower temperatures of a few hundred nanokelvins were reached through the development of new cooling techniques such as evaporative cooling [7].

When the velocity of a particle decreases, its wave function expands in space. Its so-called de Broglie length, which provides an estimate of its spatial expansion, becomes larger. When its value exceeds the mean distance between the particles in a gas, the wave functions of the particles overlap and interfere. In this case, a classical description of the system is no longer possible. Therefore, ultracold particles are ideal candidates for testing quantum mechanics and validating phenomena that have been predicted for many years. It is in this context that the first Bose-Einstein condensate [8, 9] and the first degenerate Fermi gas [10] of atoms were produced. Nowadays, research has been extended to the study of Rydberg atoms [11, 12, 13, 14, 15, 16, 17, 18], Rydberg molecules [19, 20, 21, 22, 23, 24], ions [25, 26, 27, 28, 29, 30, 31, 32, 33, 34, 35] and molecules [36, 37, 38, 39, 40, 41, 42, 43, 44, 45, 46]. In this thesis, I will mainly focus on diatomic molecules.

How to cool down atoms?

Laser cooling techniques applied to atomic ions and neutral atoms have been developed and improved over the past 40 years. Atoms can be cooled down to ultracold temperatures by taking advantage of radiative optical forces. To illustrate this, consider an atom moving toward a light source that is in resonance with a closed atomic transition. When the atom absorbs a photon, it receives a momentum kick in the direction of propagation of the incident wave and is slowed down. The atom then de-excites by spontaneous emission and is kicked back again, but this time in a random direction. After a large number of absorption and emission cycles, the average recoil generated by the

spontaneous emission is zero and does not affect the speed of the atom. However, as the recoil due to the repeated absorption is always induced in the same direction, the atom is slowed down. By adding three pairs of counter-propagating laser beams, one can cool the molecules in all directions. These so-called *optical molasses* can be supplemented by deeper cooling methods if necessary.

How to form ultracold molecules?

The previous cooling method is particularly complicated to transpose to molecules because it is not easy to identify an appropriate level scheme to achieve a closed cycle of absorption and emission. Indeed, once the molecules are excited, they desexcite in a large number of vibrational states following the Franck-Condon principle [47]. A solution would be to use a number of pumping lasers equivalent to the number of levels accessible by spontaneous emission, but this is not experimentally reasonable. For most molecules, new cooling methods have to be developed. Some direct methods [48] are based on the production of supersonic beams obtained either by adiabatic expansion or cryogenic processes and do not require any laser. Such beams can then be cooled by means of Stark or Zeeman decelerators [49, 50, 51, 52]. However, these techniques only allow to reach temperatures too far above the desired ultracold regime. In response to this problem, the idea of producing molecules from initially ultracold atoms has emerged. Nowadays, two subsequent methods are used to form ultracold molecules in a given internal state:

- The first is magneto-association [53, 54, 55] and is illustrated in Fig. 2.1 (Left). Two atoms prepared in their ground state collide with a relative kinetic energy E_k (blue). Consider a second potential energy curve (red) with a bound state (green) that is energetically closed. By applying a magnetic field, one can bring the incident state into resonance with the molecular bound state. If a coupling exists between the two states, one can efficiently transfer the pair of atoms into the desired molecular bound state by what is called a *Fano-Feshbach* resonance.

- The second method is called Stimulated Raman Adiabatic Passage (STIRAP) [36, 38, 39] which is illustrated in Fig. 2.1 (Right). Let us consider a system with three levels: the first one $|1\rangle$ represents the initial continuum state, the second one $|2\rangle$ is an intermediate state and the final one $|3\rangle$ represents in general the ground rovibronic state. A first pumping laser couples the states $|1\rangle$ and $|2\rangle$, while a second Stokes laser couples the states $|2\rangle$ and $|3\rangle$. With this method, one can completely transfer the population from state $|1\rangle$ to $|3\rangle$ without ever populating state $|2\rangle$ by precisely controlling the delay and the duration of the two lasers. In this way, all the problems associated with spontaneous emission are avoided.

Note that historically, photo-association [56, 57, 58, 59] has been widely used in experiments. However, the control of the final populated vibrational and rotational states due to spontaneous emission is hard and not quite usable for most applications. Other methods such as Sisyphus cooling [60, 61, 62], optoelectrical cooling [63, 64], direct laser cooling [65, 66, 67] can work for some specific molecules but will not be discussed here.

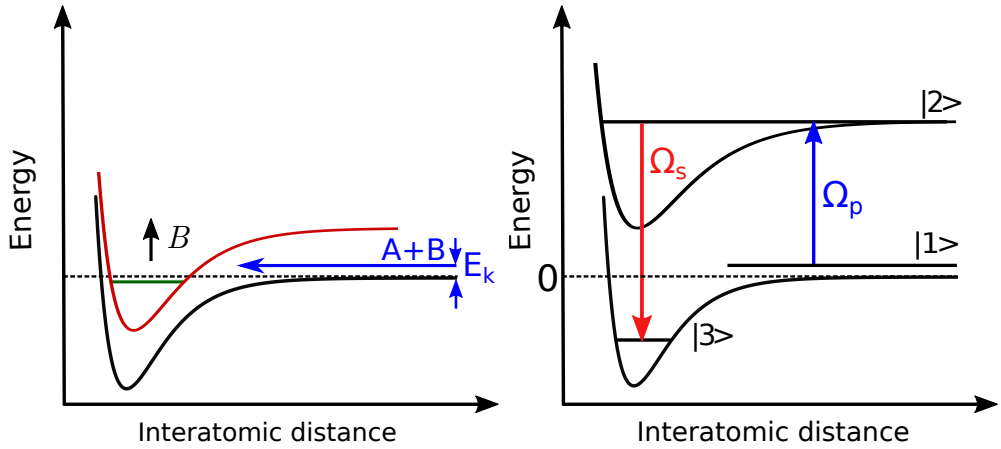

Figure 2.1: Left: Schematic view of the magneto-association method where E_{k} is the relative kinetic energy, B is a magnetic field and A and B are two initially separated atoms. Right: Schematic view of the STIRAP method where Ω_p and Ω_s are the Rabi frequencies of the pump and Stokes laser. The states $|1\rangle$, $|2\rangle$ and $|3\rangle$ correspond respectively to the initial continuum state, an intermediate state and the final state.

How to trap ultracold molecules?

As molecules have similar light shifts to atomic ones, they can also be trapped with optical dipole traps. That means we can benefit from the many years of experience and improvement acquired during their development for atoms. If one apply a non-resonant field on atoms, we induce a light shift on the atomic energy levels proportional to the light intensity. Consequently, a force proportional to the light intensity gradient appears. For a red detuned laser, the induced force attracts the atoms towards the maximum intensity of the laser. If the beam is highly focused, the atom remains confined at the focal point of the laser beam: this is the principle of optical tweezers [68, 69]. When two continuous counter-propagating beams are used, a standing wave is formed. The atoms immersed in this wave form a one-dimensional lattice [70]. If a second pair of lasers is added along a second axis, the trapped atoms can only move along the unrestricted axis: a two-dimensional pancake-shaped optical lattice is then created [71]. Finally, if a third pair of lasers is added in the third spatial axis, the trapped atoms are completely confined in a three-dimensional optical lattice [72]. It should be noted that laser frequencies must be tuned far from any allowed transitions to avoid heating the atoms by recoil kicks.

There are many other types of traps, such as magnetic [73], electric [74] or magneto-optical traps [75] which can trap molecules for several seconds. I will not go into details but more sophisticated models [76, 77] have also been developed recently and allow much longer trapping times, of the order of 60 seconds.

Short-range losses: a common issue for reactive and non-reactive molecules

The first gas of ultracold dipolar molecules prepared in their rovibronic ground state

was realized by Ni et al. [36] at JILA in 2008. Through their experiments [36, 78, 38], they showed that a large number of particles were lost due to the short-range exothermic chemical reaction KRb + KRb → K_2 + Rb_2 [79, 80, 81]. They confirmed that barrierless reactive collisions occur when two reactants are sufficiently close to each other. In other words, the loss rate coefficients are universal, i.e. they do not depend on the short-range part of the potential (where molecules are lost with unit probability), but rather on the long-range part. To illustrate this process, they placed the molecules in a three-dimensional optical lattice with a distance between two sites large enough that molecules could not chemically react. They showed that the lifetime of the gas was greatly improved because short-range losses were strongly suppressed [82].

Nowadays, one of the main challenge is to reach the quantum degeneracy regime which requires much higher densities than those existing in optical lattices. Non-reactive molecules seem to be ideal candidates to obtain long-lived gases, since losses due to reactive collisions no longer exist. This is why, many experiments have been initiated to produce ultracold non-reactive dipolar molecules such as $^{87}Rb^{133}Cs$ [40, 43], $^{23}Na^{40}K$ [41, 83, 44, 45], $^{23}Na^{87}Rb$ [42, 84], $^{6}Li^{23}Na$ [85]. Unfortunately, short-range losses with loss rate coefficients similar to those obtained with chemically reactive molecules were observed. Some theoretical calculations [86, 87] later predicted, for non-reactive molecules with a large density of Fano-Feshbach resonances around their collision threshold, that the molecules could stick together and form a tetramer complex at short-range. The exact way that tetramer complexes are lost remains an open question. A first hypothesis is that the tetramer lifetime is long enough to lead to two-body collisions (between a diatom and a tetramer) to occur and lead to losses. A second hypothesis suggested by recent experiments [88, 89] and theoretical calculations [90, 91] proposed that the complexes are lost due to trapping-laser-induced losses.

A solution to reduce short-range losses: the shielding

Whether the molecules are chemically reactive or not, solutions must be found to reduce these loss processes: the proposed solutions are grouped hereafter under the general term of shielding. They are based on the control of collisions through the application of external fields. The objective is to suppress the quenching (inelastic + loss) rate coefficients in favor of the elastic ones. At present, there are four main methods to reduce short-range losses:

- The first uses optical lattices of different dimensions to confine the molecules far from each other [92, 93, 94, 95, 82]. This method has already proved its efficiency experimentally but is not suitable to obtain degenerate quantum gases as explained before.

- The second is the static electric field shielding [96, 97, 98]. By applying a magic static electric field, one can create a long-range potential barrier in the incident channel by taking advantage of the long-range dipole-dipole interaction properties. The molecules are then kept far from each other and protected from short-range losses. It has recently been proven that this technique works experimentally in a two-dimensional gas [99] or not [100].

- The third is the microwave shielding [101, 102, 103, 104, 105, 106]. The idea is also to control the long-range dipole-dipole interactions by applying a circularly polarized microwave field. A first experiment observed this phenomenon recently on CaF molecules [107]. I have demonstrated that the control of the molecule-molecule scattering length is also possible for a large range of molecules [103]. The control of this quantity is very important because it defines the stability and lifetime of a degenerate quantum gas. Unlike atoms whose scattering length could be controlled via Fano-Feshbach resonances, no method of scattering length control existed before my investigations for molecules.

- The fourth is the optical shielding method [108] based on similar grounds, except that the microwave field is replaced by an optical field and the mechanism relies on excited electronic states rather than excited rotational states.

Now that shielding techniques have proven to be experimentally successful, the race to create the first condensate has begun. In 2019, the JILA group produced the first degenerate Fermi gas of dipolar molecules [109], paving the way of many-body studies in the years to come.

Applications with ultracold molecules

Molecules have degrees of freedom (rotation, vibration) that do not exist in atoms. These unique properties provide new interesting tools to control both their interactions and their dynamics. These qualities make them ideal candidates for a wide range of applications.

Once placed in optical lattices, the position of the molecules and thus the control of their interactions can be finely tuned. The field of quantum simulations takes advantage of this set-up for simulating complex N-body systems that are currently insoluble by numerical simulations. With these studies, we can understand more deeply phenomena of condensed matter physics, quantum magnetism or many-body physics [110, 111, 112, 113, 101, 114, 115, 116]. Moreover, the possibility to induce dipole moments via the application of electric fields and therefore to control some long-range interactions opens the way to the creation of different quantum gate schemes, notably used in quantum computing [117, 118, 119, 120, 121, 122].

Thanks to major experimental advances such as the production of molecules in well-defined states (with well defined collision energies, orientation, alignment, internal states) and to major theoretical advances (the computation of accurate potential energy surfaces...), we can understand and follow every step of a chemical reaction. This is the objective of cold and ultracold chemistry to accurately determine the initial reactants, the intermediates states and the final products by calculating and measuring relevant quantities such as cross sections and elastic/inelastic collision rate coefficients [123, 124, 125, 126, 127, 128, 37, 129, 130, 131]. Recently, the formation of a single molecule from only two atoms trapped by optical tweezers has been observed [132].

Finally, ultracold molecules are excellent candidates for fundamental tests. The cooling methods increase both the interrogation and coherence time of the molecules. They also reduce the number of levels that can be thermally populated and thus increase

the number of molecules in the state of interest. This allows one to realize very precise measurements with reduced uncertainties compared to hot molecules. This is why ultracold molecules are used for testing temporal variations of fundamental constants such as the fine structure constant or the mass ratio between the proton and the electron [133, 134]. Molecules, by their adjacent rotational states possessing opposite parities, are well adapted for testing the violations of the P symmetry via the extraction of anapolar magnetic moment contributions [135]. Measurements on CP symmetry violations are also carried out via the search for a permanent electric dipole moment of the electron [136, 137, 138, 139].

Objectives and structure of the thesis

One of my objectives is to develop an alternative method to shield molecules that are initially prepared in their ground rotational state. To do this, I will follow the optical shielding method initially developed for atoms [140, 141, 58, 142] and adapt it to molecules. One of the challenge is to implement the electromagnetic field in a time-independent formalism and to find the parameters of the field (frequency and intensity) for which the shielding is effective.

A second objective is to find solutions to reduce three-body losses while maintaining an effective two-body shielding. Before moving to the three-body study, I need to reduce the complexity of the two-body problem as much as possible because the number of states increases dramatically when moving to three bodies. Then, I need to understand how three-body collisions work and how to study them. Different hyperspherical coordinates exist [143, 144, 145, 146, 147, 148, 149, 150, 151] but each has advantages and disadvantages. The most suitable coordinates are the APH coordinates [148, 149, 150] because they treat all atom-diatom configurations equally. In return, divergent terms, also called Eckart singularities, appear in the total Hamiltonian. These divergent terms are very important because if they are not treated correctly, significant errors can appear in the results [152]. My challenge is to develop a three-body collisional code using these APH coordinates while treating accurately all the singular terms. Then, I must adapt and apply it to the case of the three-body shielding.

This manuscript will be separated in two parts. The first one deals with the shielding techniques applied to two-body collisions. The chapter 3 reviews the theoretical basis for the study of ultracold collisions between two molecules [153]. I explain how to consider short-range losses and how to extract the observable I need using the S-matrix theory. In chapter 4, I apply this formalism to describe the microwave shielding method. I show that the loss rate coefficient can be largely reduced in favor of the elastic one for a large range of dipolar molecules. I also present in this chapter a method to control the molecule-molecule scattering length by adjusting the intensity and frequency of the microwave field. This chapter is largely inspired by my paper [103]. Chapter 5 starts from the results in [96, 97, 98] on the static electric field shielding. I show how to greatly simplify the study of shielding via the development of a simplified model. I demonstrate that one can obtain results similar to the complete quantum calculation under certain conditions which are explicitly presented. Our results have been verified experimentally

with the JILA team with which I have contributed in a joint paper [100].

The second part deals with three-body collisions. Chapter 6 presents the formalism for treating collisions in hyperspherical coordinates [150, 151, 152]. I demonstrate how to relate the different types of coordinates (Jacobi, Delves, Hyperspherical) and how to accurately treat Eckart singularities [152]. In chapter 7, I adapt this formalism to study the shielding of three-body losses. In chapter 8, I focus on Li+Li_2 collisions and use the results from [154] to check my three-body code. Finally, I will conclude and give some perspectives in chapter 9.

Part I

Two-body collisions

Chapter 3

General formalism

This chapter lays the foundations of the time-independent formalism used to describe two-body collisions of diatomic molecules. Unlike atoms, molecules have a rich internal structure (rotation, vibration) which provide additional tools to control both their interactions and collisions. We will focus on dipolar molecules which are excellent candidates for a wide range of application because long-range interactions (dipole-dipole, quadrupole-dipole etc...) can be controlled using external fields. The formalism presented here is based on the partial waves expansion of the wave functions and is specially suited for ultralow collision energies because only few partial waves are required to perform the collisional study of the system. We start in section 3.1 with a description of the different kinds of collisions and present the different loss processes we must consider. We continue with a brief reminder about the Schrödinger equation for one (section 3.2) and two molecules (section 3.3). Then, section 3.4 describes the general collision formalism starting from the description of the asymptotic wave function and ending with the derivation of a system of coupled equations. These equations describe the behaviour of the wave function in the region where the molecules highly interact. This is also where we expand the scattered wave function in terms of partial waves. In section 3.5, we present the numerical method of propagation of the logarithmic derivative matrix of the wavefunction. We show how to obtain the reactance, scattering, and transition matrices and how to extract the observables we need. Finally, we give the general laws describing their behavior in the ultracold regime. For more details, refer to the book chapter [153].

3.1 Types of collisions and loss processes

During a collision, the total energy is conserved. Such as a harmonic oscillator where the potential energy can be converted into kinetic energy, the internal energy of the molecules can be converted into kinetic and potential energy. Internal states whose energies are lower than the total energy are accessible during the collision and are called open states. On the other hand, states whose energies are greater than the total energy are inaccessible and are called closed states.

In Fig. 3.1, we represented the schematic representation of elastic and inelastic pro-

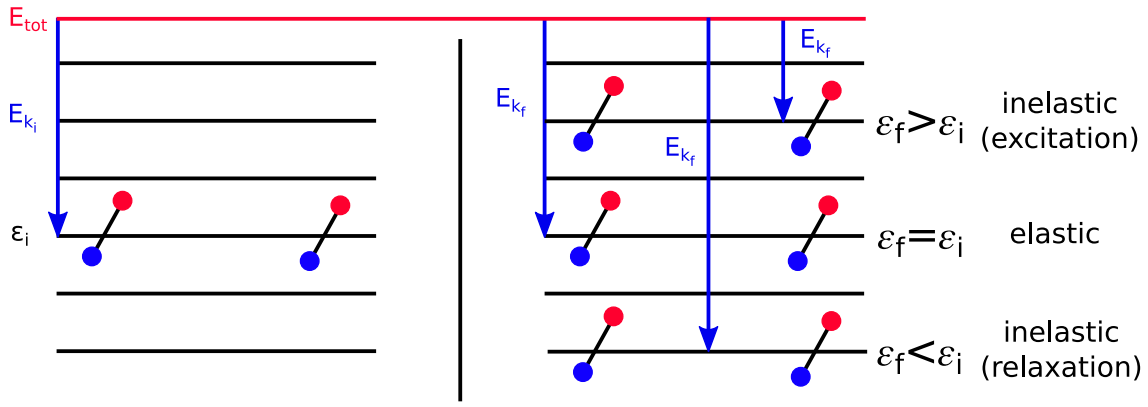

Figure 3.1: Schematic representation of elastic and inelastic processes. The total energy E_{tot} is conserved during collisions. The initial internal energy and relative kinetic energy are given by ε_i and E_{k_i}. The final internal energy and relative kinetic energy are given by ε_f and E_{k_f}. If the molecules remain in the same internal state after collision then the kinetic energy is conserved: these are called elastic collisions. If the molecules change their internal states then the kinetic energy is modified: these are called inelastic collisions.

cesses where ε_i and ε_f are the initial and final internal energies and where E_{k_i} and E_{k_f} are the initial and final relative kinetic energies. Since E_{tot} is conserved during a collision, we have:

$$E_{\text{tot}} = E_{\text{k}_i} + \varepsilon_i = E_{\text{k}_f} + \varepsilon_f. \tag{3.1.1}$$

Therefore, among the open states we can distinguish two types of collisions:

- Elastic collisions where the internal state is conserved (i.e. $E_{\text{k}_i} = E_{\text{k}_f}$). This type of collision has no influence on the lifetime of ultracold molecular gases as there is no modification of the internal structure of the molecules. Indeed, if we set $E_{\text{k}_i} = E_{\text{k}_f}$ in Eq. 3.1.1, the internal energies before and after the collisions are unchanged $\varepsilon_i = \varepsilon_f$.

- Inelastic collisions where the kinetic energy is no longer conserved (i.e. $E_{\text{k}_i} \neq E_{\text{k}_f}$). If $\varepsilon_f > \varepsilon_i$ then a part of the kinetic energy has been used to excite the molecules: this is called excitation. If $\varepsilon_f < \varepsilon_i$ then the lost internal energy has been transformed into kinetic energy: this is called relaxation. These kinds of collisions are harmful because we usually want to keep the molecules in their initial state.

In some cases, interatomic bonds can be broken and/or formed during collisions: these are called reactive collisions. As explained in chapter 2, these collisions lead to the loss of the molecules in the short-range region. If the reactive process is exothermic, the reactive collisions can occur even without initial collision energies. For example, in an ultracold KRb gas, molecules can be lost via the transformation [155, 156]:

$$\text{KRb} + \text{KRb} \rightarrow \text{K}_2 + \text{Rb}_2$$

where the bonds between the K and Rb atoms have been broken to form two homonuclear molecules K_2 and Rb_2. If the reactive process is endothermic, the reactive collisions can

occur only if a sufficient amounts of collision energy is available. At ultralow energies, these reactions generally can't occur, but it has been demonstrated that non-reaction molecules are still lost via another process: the *long-lived sticky collisions* [87, 86, 157, 158, 159]. This mechanism is not yet fully understood but some theoretical investigations predict that the molecules can form long-lived tetramer complexes at short-range. For example, collisions of ^{23}Na^{87}Rb molecules in their absolute ground state are endothermic at ultralow energies such that reactive collisions like:

$$^{23}\mathrm{Na}^{87}\mathrm{Rb} + {}^{23}\mathrm{Na}^{87}\mathrm{Rb} \not\to {}^{23}\mathrm{Na}_2 + {}^{87}\mathrm{Rb}_2$$

cannot occur. However, it has been observed that these molecules are still lost with collision rate coefficients whose behaviors are similar to that of reactive collisions [42].

In the following, we will group under the term of quenching all the processes leading to the loss of molecules or to the change of their internal states (i.e. short-range losses and inelastic collisions). This term contains all the harmful processes for the creation of degenerate quantum gases which requires high densities of molecules remaining in the same internal state to be formed. The objective of the following sections is to introduce the quantum formalism to include all these processes in the case of two-body collisions.

3.2 Schrödinger equation for a particle

When a particle of mass m is placed in a potential characterized by the operator $\hat{V} = V(\vec{r}, t)$, the time evolution of its wave function $\Psi(\vec{r}, t) \equiv \langle \vec{r} | \Psi(t) \rangle$ is governed by the Schrödinger equation:

$$i\hbar \frac{\partial}{\partial t} |\Psi(\vec{r}, t)\rangle = \left[\hat{T} + \hat{V}\right] |\Psi(\vec{r}, t)\rangle \tag{3.2.1}$$

with $\hat{T} \equiv -\frac{\hbar^2}{2m}\nabla^2_{\vec{r}}$ the kinetic energy operator. If the potential energy operator is time-independent $\hat{V}(\vec{r}, t) = V(\vec{r})$, the solutions $|\Psi(\vec{r}, t)\rangle$ are separable into a product of a spatial and temporal part:

$$|\Psi_{E_{\mathrm{tot}}}(\vec{r}, t)\rangle = e^{-i\frac{E_{\mathrm{tot}}t}{\hbar}} |\psi_{E_{\mathrm{tot}}}(\vec{r})\rangle \tag{3.2.2}$$

and are called stationary states. The spatial parts $|\psi_{E_{\mathrm{tot}}}(\vec{r})\rangle$ are solution of the time-independent Schrödinger equation:

$$\hat{H} |\psi_{E_{\mathrm{tot}}}(\vec{r})\rangle = \left[-\frac{\hbar^2}{2m}\nabla^2_{\vec{r}} + V(\vec{r})\right] |\psi_{E_{\mathrm{tot}}}(\vec{r})\rangle = E_{\mathrm{tot}} |\psi_{E_{\mathrm{tot}}}(\vec{r})\rangle \tag{3.2.3}$$

and have for eigenvalues E_{tot}. This time-independent formalism is usually used for collisions study and it still applies when static external fields are used.

3.3 Schrödinger equation for two particles

In this section, we will present the Jacobi coordinates and derive the Schrödinger equation for a system composed of two molecules.

3.3.1 Jacobi coordinates

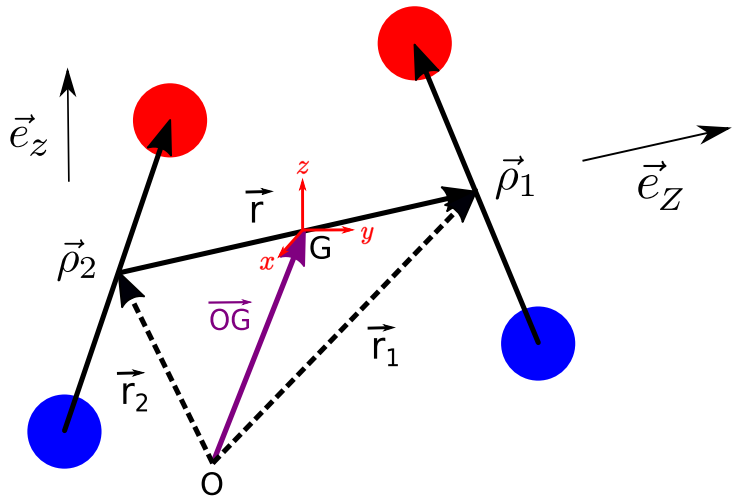

Figure 3.2: Sets of coordinates required to describe a system composed of two diatomic molecules. The vectors $\vec{\rho}_1$ and $\vec{\rho}_2$ describe the motion of the two atoms composing respectively the first and the second molecule. The vectors $\vec{r}_1$ and $\vec{r}_2$ give the position of the center of mass of each molecule relative to an arbitrary point O. The vector $\vec{r}$ describes the relative motion between the two molecules for which G is the total center of mass. The axis of quantization is chosen along $\vec{e}_Z$ for the body-fixed frame and along $\vec{e}_z$ for the space-fixed frame.

Consider two diatomic molecules $\tau = 1, 2$ defined by their mass m_1 and m_2. Let $\vec{r}_1$ and $\vec{r}_2$ be the position vectors of their center of mass with respect to an arbitrary point O and let $\vec{\rho}_1$ and $\vec{\rho}_2$ be the position vectors describing the relative position of the two atoms composing them. We can define the center of mass $\overrightarrow{OG}$ and the total mass M:

$$\overrightarrow{OG} = \frac{m_1\vec{r}_1 + m_2\vec{r}_2}{M} \qquad M = m_1 + m_2 \tag{3.3.1}$$

as well as the relative position of the two molecules $\vec{r}$ and the reduced mass μ:

$$\vec{r} = \vec{r}_1 - \vec{r}_2 \qquad \mu = \frac{m_1 m_2}{m_1 + m_2}. \tag{3.3.2}$$

As shown in Fig 3.2, it is possible to define two different frames:

- The body-fixed frame $(\vec{e}_X, \vec{e}_Y, \vec{e}_Z)$ whose origin coincides with the centre of mass G with $\vec{e}_Z$ oriented along the vector $\vec{r}$.
- The space-fixed frame $(\vec{e}_x, \vec{e}_y, \vec{e}_z)$ whose origin is a point O randomly chosen in space with $\vec{e}_z$ arbitrarily placed in space.

As we will study molecules in presence of external fields which are polarized along a fixed direction in the laboratory (along $\vec{e}_z$ by convention), we will only consider the space-fixed

frame. Consequently, the Oz axis is chosen as the quantization axis.

From an angular point of view, we will use spherical coordinates to describe the vectors $(\vec{r}, \vec{\rho}_1, \vec{\rho}_2)$. Let us note:

$$\hat{r}^{SF} = (\theta_r^{SF}, \phi_r^{SF}) \qquad \hat{\rho}_1^{SF} = (\theta_{\rho_1}^{SF}, \phi_{\rho_1}^{SF}) \qquad \hat{\rho}_2^{SF} = (\theta_{\rho_2}^{SF}, \phi_{\rho_2}^{SF}) \quad (3.3.3)$$

their angular components in the space-fixed frame. For better visibility, we will omit the label SF hereafter. The momentum operators associated with these three vectors are:

$$\hat{\vec{p}} = -i\hbar\nabla_{\vec{r}} \qquad \hat{\vec{P}}_1 = -i\hbar\nabla_{\vec{\rho}_1} \qquad \hat{\vec{P}}_2 = -i\hbar\nabla_{\vec{\rho}_2} \quad (3.3.4)$$

and the momentum angular operators are given by:

$$\hat{\vec{l}} = \hat{\vec{r}} \times \hat{\vec{p}} \qquad \hat{\vec{j}}_1 = \hat{\vec{\rho}}_1 \times \hat{\vec{P}}_1. \qquad \hat{\vec{j}}_2 = \hat{\vec{\rho}}_2 \times \hat{\vec{P}}_2. \quad (3.3.5)$$

We note $\hat{l}_z$, $\hat{j}_{1_z}$ and $\hat{j}_{2_z}$ their projection on the Oz axis and m_l, m_{j_1} and m_{j_2} their associated quantum numbers. The total angular momentum $\hat{\vec{J}}$ and the quantum number M_J related to its projection on the Oz axis are given by:

$$\hat{\vec{J}} = \hat{\vec{l}} + \hat{\vec{j}}_1 + \hat{\vec{j}}_2 \qquad M_J = m_l + m_{j_1} + m_{j_2}. \quad (3.3.6)$$

Usually, both of these quantities are conserved during collisions. However, in the presence of a static electric field or an electromagnetic field, only M_J is conserved.

3.3.2 Schrödinger equation

The two-body Hamiltonian which fully describes the system is given by:

$$\hat{H} = -\frac{\hbar^2}{2m_1}\nabla^2_{\vec{r}_1} - \frac{\hbar^2}{2m_1}\nabla^2_{\vec{\rho}_1} - \frac{\hbar^2}{2m_2}\nabla^2_{\vec{r}_2} - \frac{\hbar^2}{2m_2}\nabla^2_{\vec{\rho}_2} + V(\vec{\rho}_1, \vec{\rho}_2, \vec{r}_1, \vec{r}_2). \quad (3.3.7)$$

The first four terms correspond respectively to the external and internal kinetic energies of the individual molecules and V is the total potential energy. At long distance, the two molecules do not interact with each other. Then, the asymptotic potential energy is composed of the internal potential energy of each molecule $\hat{v}_\tau^{int}(\vec{\rho}_\tau)$ plus their individual interactions with possible external fields $\hat{v}_\tau^{ext}(\vec{\rho}_\tau)$. When the molecules approach to each other, they start to interact via many interactions (van der Waals, dipole-dipole, etc...) that we group without distinction in a total potential energy operator $U_{\text{int}}(\vec{\rho}_1, \vec{\rho}_2, \vec{r})$ called *potential energy surface* (PES). Note that U_{int} does not depend on the absolute position of the molecules but only on their relative position. This term is generally determined by *ab initio* calculations under the Born–Oppenheimer approximation [160]. This amount to separating the electronic dynamics from the nuclear one because nuclei are much heavier than electrons ($m_n/m_e \gg 1$). Hence, the total potential energy can be decomposed as:

$$V(\vec{\rho}_1, \vec{\rho}_2, \vec{r}_1, \vec{r}_2) = U_{\text{int}}(\vec{\rho}_1, \vec{\rho}_2, \vec{r}) + \hat{v}_1^{int}(\vec{\rho}_1) + \hat{v}_2^{int}(\vec{\rho}_2) + \hat{v}_1^{ext}(\vec{\rho}_1) + \hat{v}_2^{ext}(\vec{\rho}_2) \quad (3.3.8)$$

where the two-body interaction term vanishes at long-range because the molecules are too far from each other to interact:

$$U_{\text{int}}(\vec{\rho}_1, \vec{\rho}_2, \vec{r}) \underset{r\to\infty}{\to} 0. \tag{3.3.9}$$

We can introduce the internal eigenvalue equation for the molecule τ:

$$\hat{h}_\tau \left|\phi_{\alpha_\tau}\right\rangle = \left[-\frac{\hbar^2}{2m_\tau}\nabla^2_{\vec{\rho}_\tau} + \hat{v}^{int}_\tau(\vec{\rho}_\tau) + \hat{v}^{ext}_\tau(\vec{\rho}_\tau)\right]\left|\phi_{\alpha_\tau}\right\rangle = \varepsilon_{\alpha_\tau}\left|\phi_{\alpha_\tau}\right\rangle \tag{3.3.10}$$

where $\left|\phi_{\alpha_\tau}\right\rangle$ and $\varepsilon_{\alpha_\tau}$ represent respectively the eigenstates and the internal energies of the molecule τ in presence of an external field. In the following, we consider the distance between the two atoms composing the molecules as fixed and we neglect any coupling between rotations and vibrations. Under this so-called *rigid rotor approximation*, the rotational energies (without external fields) are given by:

$$\hat{h}^{\text{rot}}_\tau \left|j_\tau, m_{j_\tau}\right\rangle = \left[-\frac{\hbar^2}{2m_\tau}\nabla^2_{\vec{\rho}_\tau}\right]\left|j_\tau, m_{j_\tau}\right\rangle = B\, j_\tau(j_\tau+1)\left|j_\tau, m_{j_\tau}\right\rangle \tag{3.3.11}$$

with B the rotational constant of the molecule. The states $\left|j_\tau, m_{j_\tau}\right\rangle$ are the usual spherical harmonics $\mathcal{Y}^{m_{j_\tau}}_{j_\tau}(\theta^{SF}_{\rho_\tau}, \phi^{SF}_{\rho_\tau})$ in the $\left\langle\theta^{SF}_{\rho_\tau}, \phi^{SF}_{\rho_\tau}\right|$ representation.

If we consider a system composed of two molecules, the state describing the internal states of the two molecules can be written in the tensorial form $\left|\phi_\alpha\right\rangle = \left|\phi_{\alpha_1}\right\rangle\left|\phi_{\alpha_2}\right\rangle$. To simplify the notations, we will note $\varepsilon_\alpha = \varepsilon_{\alpha_1} + \varepsilon_{\alpha_2}$, the total asymptotic energies associated to the state $\left|\phi_\alpha\right\rangle$.

As the potential depends only on the relative position of the particles and as the internal motion of the molecules is described by the internal Hamiltonian given in Eq. 3.3.10, it is more convenient to rewrite the two-body Schrödinger equation (Cf. Eq. 3.3.7) in terms of relative coordinates:

$$\left[-\frac{\hbar^2}{2\mu}\nabla^2_{\vec{r}} + U_{\text{int}}(\vec{\rho}_1, \vec{\rho}_2, \vec{r}) + \hat{h}_1(\vec{\rho}_1) + \hat{h}_2(\vec{\rho}_2)\right]\left|\psi(\vec{\rho}_1, \vec{\rho}_2, \vec{r})\right\rangle = E_{\text{tot}}\left|\psi(\vec{\rho}_1, \vec{\rho}_2, \vec{r})\right\rangle \tag{3.3.12}$$

where $E_{\text{tot}} = \varepsilon_\alpha + E_{\text{k}}$ is expressed in term of the relative motion E_{k} which will be called *collision energy* in the following. The term $\nabla^2_{\vec{r}}$ can be express in terms of radial derivatives and angular momentum:

$$\nabla^2_{\vec{r}} = \frac{1}{r}\left(\frac{\partial^2}{\partial r}r + \frac{1}{r^2}\hat{l}^2\right) \tag{3.3.13}$$

with:

$$\hat{l}^2 = -\frac{\hbar^2}{\sin\theta_r}\frac{\partial}{\partial\theta_r}\sin\theta_r\frac{\partial}{\partial\theta_r} + \frac{\hat{l}^2_z}{\sin^2\theta_r} \qquad \hat{l}^2_z = -\hbar^2\frac{\partial^2}{\partial\phi^2_r}. \tag{3.3.14}$$

In the next section, we will present the primitive basis in which we will express the matrix elements of the Hamiltonian.

3.4 Collision formalism of two molecules

By studying the asymptotic form of the total wave function (where molecules are considered free), we will show that the total wave function can be developed in terms of partial waves. Using even at short distances these partial waves as primitive basis, we will show that the collisional study can be reduced to the resolution of a set of coupled equations.

3.4.1 Asymptotic study

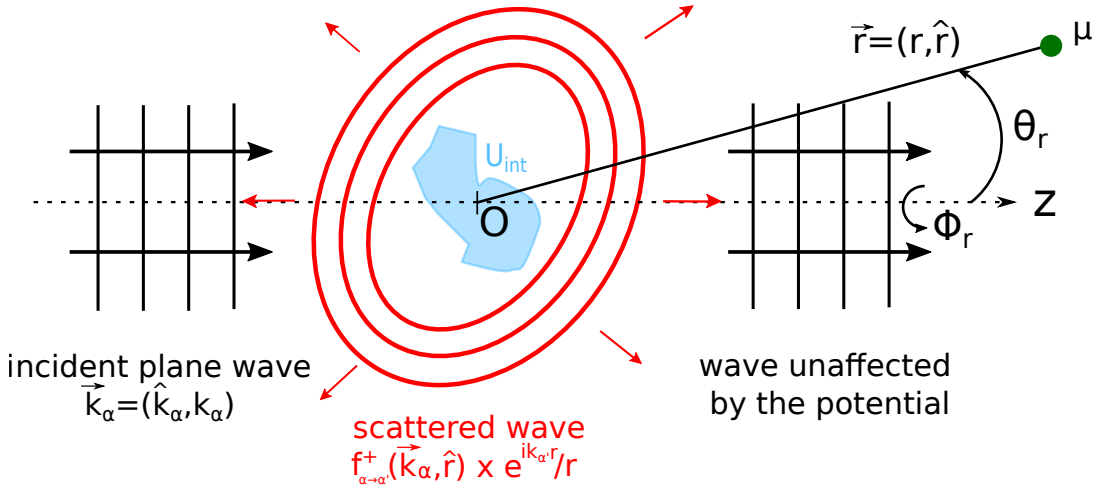

Figure 3.3: Effect of the potential on the radial wave function. The vector $\vec{k}_\alpha$ corresponds to the wave vector of the initial state and $\vec{k}_{\alpha'}$ corresponds to the one for the final state. The vector $\vec{r}$ corresponds to the relative distance between the two molecules and μ is the reduced mass.

Let's consider the scattering on any central potential of a fictitious particle of reduced mass μ and initially prepared in the state ϕ_α. If the particle has not yet interacted with the potential, it can be considered as a free particle. Therefore, its wave function is given by:

$$\psi_{\text{inc}}(\vec{\rho}_1, \vec{\rho}_2, \vec{r}) \propto e^{i\vec{k}_\alpha . \vec{r}} \phi_\alpha(\vec{\rho}_1, \vec{\rho}_2) \tag{3.4.1}$$

with $k_\alpha = \sqrt{\frac{2\mu E_{\text{k}}}{\hbar^2}}$. As shown in Fig. 3.3, after scattering and quite far from the effect of the potential, we can imagine two scenarios:

- The wave has not been affected by the potential and remains a plane wave.
- The wave has been affected by the potential. Since the scattering process is generally anisotropic, the isotropic part of the wave $\frac{e^{ik_{\alpha'}r}}{r}$ is multiplied by the amplitude $f^+_{\alpha\to\alpha'}(\vec{k}_\alpha, \hat{r})$ which depends on the direction we consider. Due to inelastic collisions, the internal state α can change during the collision, hence $\alpha \to \alpha'$ in the scattered amplitude.

In short, the asymptotic wave function can be defined as:

$$\begin{aligned}\psi_{\text{rel}}(\vec{\rho}_1,\vec{\rho}_2,\vec{r}) &\underset{r\to\infty}{=} \mathcal{N}\left[e^{i\vec{k}_\alpha\cdot\vec{r}}\phi_\alpha(\vec{\rho}_1,\vec{\rho}_2)+\sum_{\alpha'} f^+_{\alpha\to\alpha'}(\vec{k}_\alpha,\hat{r})\frac{e^{ik_{\alpha'}r}}{r}\phi_{\alpha'}(\vec{\rho}_1,\vec{\rho}_2)\right] \\ &= \psi_{\text{inc}}+\psi_{\text{diff}}\end{aligned} \tag{3.4.2}$$

where $\mathcal{N}$ is a normalization factor. Let's note that the wave function is a linear combination of all accessible internal states $\phi_{\alpha'}$.

3.4.2 A partial wave expansion

Now that we have explained how the radial wave function can be described asymptotically, we will discuss how to describe it when the molecules start to interact and collide. We have shown in Eq. 3.3.12 that the angular part of the kinetic energy operator is entirely included into the two operators $\{\hat{\vec{l}}^2,\hat{\vec{l}_z}\}$. The spherical harmonics are the eigenfunctions of these two operators and satisfy:

$$\hat{\vec{l}}^2\,\mathcal{Y}_l^{m_l} = l(l+1)\,\mathcal{Y}_l^{m_l} \qquad\qquad \hat{\vec{l}_z}\,\mathcal{Y}_l^{m_l} = m_l\,\mathcal{Y}_l^{m_l}. \tag{3.4.3}$$

Therefore, using the spherical harmonic addition theorem, we can expand the incident plane wave (given in Eq. 3.4.2) in terms of spherical harmonics:

$$\begin{aligned}\psi_{\text{inc}} &= \mathcal{N}\,\mathrm{e}^{i\vec{k}_\alpha\cdot\vec{r}}\phi_\alpha\left(\vec{\rho}_1,\vec{\rho}_2\right) \\ &= \mathcal{N}\,4\pi\sum_{l=0}^{\infty}\sum_{m_l=-l}^{l} i^l j_l\left(k_\alpha r\right)\left[Y_l^{m_l}\left(\hat{k}_\alpha\right)\right]^* Y_l^{m_l}(\hat{r})\phi_\alpha\left(\vec{\rho}_1,\vec{\rho}_2\right)\end{aligned} \tag{3.4.4}$$

where j_l are the regular spherical Bessel functions. We can demonstrate that the asymptotic behavior of ψ_{inc} is given by:

$$\psi_{\text{inc}} \underset{r\to\infty}{\to} \sum_{l=0}^{\infty}\sum_{m=-l}^{+l} N^{\text{inc}}_{\alpha l m_l}(\vec{k}_\alpha)\psi^{\text{inc}}_{\alpha l m_l}(\vec{\rho}_1,\vec{\rho}_2,\vec{r}) \tag{3.4.5}$$

where $N^{\text{inc}}_{\alpha l m_l}(\vec{k}_\alpha)$ is a normalization factor independent of $\vec{r}$ and where the functions $\psi^{\text{inc}}_{\alpha l m_l}$:

$$\psi^{\text{inc}}_{\alpha l m_l}(\vec{\rho}_1,\vec{\rho}_2,\vec{r}) \equiv \frac{f^{\text{inc}}(r)}{r}\mathcal{Y}_l^{m_l}(\hat{r})\phi_\alpha(\vec{\rho}_1,\vec{\rho}_2) \tag{3.4.6}$$

are called the *partial waves*. The incident radial wave function is given by

$$f^{\text{inc}}(r) = (e^{-i(k_\alpha r - l\pi/2)} - e^{i(k_\alpha r - l\pi/2)})/k_\alpha^{1/2} \tag{3.4.7}$$

and schematically described an incoming spherical wave which converges to $r = 0$ and which is distorted and reflected by the potential giving rise to an outgoing spherical wave out of phase by $l\pi$. The total wave function is then described as a linear combination of spherical waves for which the phase shifts are different as they depend on the value of l.

This expansion over the quantum numbers l and m_l is called the partial wave expansion and illustrates how molecules collide in terms of orbital angular momentum. For example, for the case $l = 0$, the spherical harmonics are isotropic which means that no angular direction is favored during collisions while for the case $l = 1$ and $m_l = 0$, the spherical harmonics are mainly oriented along the z-axis.

Finally, we can extend this partial wave expansion to any r for the total wave function:

$$\psi^{E_{\text{tot}}}_{\alpha,\vec{k}_\alpha}(\vec{\rho}_1,\vec{\rho}_2,\vec{r}) = \sum_{l=0}^{\infty}\sum_{m=-l}^{+l} N_{\alpha l m_l}(\vec{k}_\alpha)\psi^{E_{\text{tot}}}_{\alpha l m_l}(\vec{\rho}_1,\vec{\rho}_2,\vec{r}) \tag{3.4.8}$$

where $\psi^{E_{\text{tot}}}_{\alpha l m_l}(\vec{\rho}_1,\vec{\rho}_2,\vec{r})$ is a linear combination of all accessible states:

$$\psi^{E_{\text{tot}}}_{\alpha l m_l}(\vec{\rho}_1,\vec{\rho}_2,\vec{r}) = \sum_{\alpha'}\sum_{l'=0}^{\infty}\sum_{m'=-l'}^{+l'} \frac{f_{\alpha' l' m'_l,\alpha l m_l}(r)}{r}\mathcal{Y}^{m'_l}_{l'}(\hat{r})\phi_{\alpha'}(\vec{\rho}_1,\vec{\rho}_2). \tag{3.4.9}$$

The radial wave function $f_{\alpha' l' m'_l,\alpha l m_l}(r)$ contains the phase shift δ_l accumulated during the passage of the wave through the potential. It depends both on the partial wave studied l but also on the total energy. Subsequently, the set formed by the quantum numbers $i = (\alpha, l, m_l)$ will be called *channel*.

3.4.3 Coupled equations

If we insert Eq. 3.4.9 into Eq. 3.3.12, multiply on the left-side by $\left[Y^{m''_l}_{l''}(\hat{r})\phi_{\alpha''}(\vec{\rho}_1,\vec{\rho}_2)\right]^*$ and integrate over the angular part, we obtain the usual system of coupled equations:

$$\begin{aligned}\sum_{\alpha'}\sum_{l'=0}^{\infty}\sum_{m'=-l'}^{+l'}\Bigg[\left\{-\frac{\hbar^2}{2\mu}\frac{d^2}{dr^2}+\frac{\hbar^2 l'(l'+1)}{2\mu r^2}+\varepsilon_{\alpha'}-E_{\text{tot}}\right\}\delta_{\alpha',\alpha''}\delta_{l',l''}\delta_{m'_l,m''_l}\\ +\mathcal{U}^{\text{int}}_{\alpha'' l'' m''_l,\alpha' l' m'_l}(r)\Bigg] f^{E_{\text{tot}}}_{\alpha' l' m'_l,\alpha l m_l}(r) = 0\end{aligned} \tag{3.4.10}$$

which describe the radial evolution of the wave function. Roughly speaking, when r is small the molecules are colliding and interacting and when r is large the collision is finished. The coupling matrix elements $\mathcal{U}^{\text{int}}_{\alpha'' l'' m''_l,\alpha' l' m'_l}(r)$ are given by:

$$\begin{aligned}\mathcal{U}^{\text{int}}_{\alpha'' l'' m''_l,\alpha' l' m'_l}(r) = \int \mathrm{d}\vec{\rho}_1\mathrm{d}\vec{\rho}_2\mathrm{d}\hat{r}\left[\mathcal{Y}^{m''_l}_{l''}(\hat{r})\right]^*\phi^*_{\alpha''}(\vec{\rho}_1,\vec{\rho}_2)\,U_{\text{int}}(\vec{\rho}_1,\vec{\rho}_1,\vec{r})\\ \mathcal{Y}^{m'_l}_{l'}(\hat{r})\,\phi_{\alpha'}(\vec{\rho}_1,\vec{\rho}_2)\end{aligned} \tag{3.4.11}$$

and describe the couplings between the individual channels. This matrix is symmetric, real and generally non-diagonal. Let's note

$$\mathcal{U}^{\text{cent}}_{i'',i'}(r) = \frac{\hbar^2 l'(l'+1)}{2\mu r^2}\,\delta_{\alpha',\alpha''}\,\delta_{l',l''}\,\delta_{m'_l,m''_l} \tag{3.4.12}$$

the diagonal centrifugal matrix elements. Finally, it is possible to rewrite the actual potential as:

$$\mathcal{U}^{\text{eff}}_{i'',i'}(r) = \mathcal{U}^{\text{cent}}_{i'',i'}(r) + \mathcal{U}^{\text{int}}_{i'',i'}(r) + \varepsilon_{\alpha'}\delta_{i',i''}. \tag{3.4.13}$$

If only the diagonal elements are plotted, the so-called *diabatic curves* are obtained. On the other hand, if we diagonalize the matrix for each value of r then we obtain the so-called *adiabatic curves*. The angular eigenfunctions $\Phi_t(\theta_r^{SF}, \phi_r^{SF}; r)$ obtained are called *surface functions*. The subscript t is used to identify the surface functions because they can no longer be identified to a particular initial channel but in a linear combination of them. The comparison of the two curves gives us a good idea of the effect of the coupling induced by the potential, especially in the vicinity of avoided crossings. Asymptotically, the diabatic and adiabatic curves tend to the total internal energies $\varepsilon_{\alpha'}$ (calculated from Eq. 3.3.10) as the molecules no longer interact.

In the following chapters, we want to control the long-range part of the interactions to prevent the molecules to come at short-distances where loss processes occur. A series expansion of the potential, called multipolar expansion, gives the asymptotic behaviour of the potential surface [161]:

$$\begin{aligned} U_{\text{mult}} =& \frac{1}{4\pi\varepsilon_0} \sum_{\lambda_1\lambda_2\lambda} \sum_{\omega_{\lambda_1}\omega_{\lambda_2}} (-1)^{\lambda_1} \left(\frac{(2\lambda_1 + 2\lambda_2 + 1)!}{(2\lambda_1)!(2\lambda_2)!} \right)^{1/2} \frac{Q_{\lambda_1\omega_{\lambda_1}} Q_{\lambda_2\omega_{\lambda_2}}}{r^{\lambda+1}} \\ & \times \delta_{\lambda,\lambda_1+\lambda_2} \sum_{m_{\lambda_1} m_{\lambda_2} m_\lambda} \mathcal{A}(\hat{\rho}_1, \hat{\rho}_2, \hat{r}) \end{aligned} \tag{3.4.14}$$

with $\lambda = \lambda_1 + \lambda_2$. The angular part is given by:

$$\mathcal{A}(\hat{\rho}_1, \hat{\rho}_2, \hat{r}) = \begin{pmatrix} \lambda_1 & \lambda_2 & \lambda \\ m_{\lambda_1} & m_{\lambda_2} & -m_\lambda \end{pmatrix} \times [D^{\lambda_1}_{m_{\lambda_1}\omega_{\lambda_1}}]^* [D^{\lambda_2}_{m_{\lambda_2}\omega_{\lambda_2}}]^* [D^{\lambda}_{-m_\lambda 0}]^*. \tag{3.4.15}$$

The symbol (: :) corresponds to a $3j$ symbol and is non-zero only if $m_\lambda = m_{\lambda_1} + m_{\lambda_2}$. We note $Q_{\lambda_\tau\omega_{\lambda_\tau}}$ the generalized multipole of the molecule τ. λ_τ is an angular momentum and refers to the order of the multipole (monopole, dipole...). We call $m_{\lambda_\tau} = [-\lambda_\tau, +\lambda_\tau]$ the projection of λ_τ on the space-fixed axis and $\omega_{\lambda_\tau} = [-\lambda_\tau, +\lambda_\tau]$ the projection of λ_τ on the intermolecular axis. The potential energy surface can also be noted:

$$U_{\text{mult}} = \sum_i \frac{C_i}{R^i} \tag{3.4.16}$$

which clearly separates the contribution of the different multipoles according to their scope of interaction:

- the terms $\propto R^{-1}$ describe the interactions between two total charges,
- the terms $\propto R^{-2}$ describe the interactions between a total charge and a dipole moment,

- the terms $\propto R^{-3}$ describe the interactions between two dipoles or between a charge and a quadrupole,
- etc.

This interaction term U_{mult} will then be included in the matrix elements $\mathcal{U}^{\text{int}}_{\alpha'' l'' m_l'', \alpha' l' m_l'}(r)$ from Eq. 3.4.10 to describe the interactions between molecules at large distances.

3.5 Propagation and Observables

In the previous section, we derived a set of coupled equations describing the dynamics of the radial wave function. To obtain the different observables we need (cross sections, rate coefficients, ...), we need to solve this set of coupled equations for any value of r. In this section, we will describe how to numerically perform the propagation of the radial wave function over the intermolecular distance while including the short-range loss processes. Finally, we will show that by matching the propagated radial wave function with its asymptotic part, we can extract the observables we want.

3.5.1 Numerical propagation

Let's rewrite the system of coupled differential equations (given in Eq. 3.4.10) in the matrix form:

$$\left\{ \mathbf{I} \frac{\mathrm{d}^2}{\mathrm{d}r^2} - \frac{2\mu}{\hbar^2} \left[\boldsymbol{\mathcal{U}}^{\mathbf{eff}}(r) - \mathbf{I}\, E_{\text{tot}} \right] \right\} \mathbf{F}(r) = \left\{ \mathbf{D}^2(r) + \mathbf{W}(r) \right\} \mathbf{F}(r) = 0 \tag{3.5.1}$$

with $\mathbf{I}$ the identity matrix and:

$$\mathbf{D}^2(r) = \mathbf{I} \frac{d^2}{dr^2} \qquad \mathbf{W}(r) = -\frac{2\mu}{\hbar^2} \left[\boldsymbol{\mathcal{U}}^{\mathbf{eff}}(r) - \mathbf{I}\, E_{\text{tot}} \right] \qquad \mathbf{F}(r) = f^{E_{\text{tot}}}_{i',i}(r). \tag{3.5.2}$$

Several methods exist to solve this type of system of coupled differential equations. There are two main approaches:

- The system of coupled equations is solved numerically, in its differential or integral form, in this case we talk about an *approximate-solution approach* [162, 163, 164, 165].
- The potential matrix is approximated in a sufficiently acceptable way and the system of coupled equations is solved exactly, in this case we talk about an *approximate-potential approach* [166, 167, 168].

In both cases, either the wave function or the logarithmic derivative of the wave function or its inverse (R-matrix) is propagated (i.e. the functions are followed step by step from the inner region to the asymptotic region). In all our calculations, we will use the approximate-solution approach described by Johnson [162] defining and propagating over r the logarithmic derivative matrix:

$$\mathbf{Z}(r) = \mathbf{F'}(r)\mathbf{F}^{-1}(r). \tag{3.5.3}$$

This method is convenient because it imposes only one condition at $r_{\min}$, it removes any factor of normalization and it avoids numerical instabilities of the radial wave functions when reaching a classically forbidden region. Depending on the imposed conditions at $r_{\min}$, this matrix can be either real or complex. To propagate this function, we apply a diabatic-by-sector technique (see Fig. 3.4). We perform a numerical separation by partitioning the intermolecular distance r into n_s sectors. Let's consider the sector ξ defined between $[r_\xi^l, r_\xi^r]$ and centered on r_ξ^m. The superscripts l, r, m identify respectively the left, right and middle part of the sector. We solve the angular part of the problem at the center of each sector by obtaining the surface functions $\Phi_t(\theta_r^{SF}, \phi_r^{SF}; r_\xi^m)$. By initially knowing $\mathbf{Z}(r_\xi^l; r_\xi^m)$ (which means $\mathbf{Z}(r_\xi^l)$ expressed in the basis centered on r_ξ^m), the Z-matrix is obtained at r_ξ^r using the following recurrence relations:

$$\mathbf{Z}(r_\xi^m; r_\xi^m) = \hat{\mathcal{Y}}_4(r_\xi^l, r_\xi^m) - \hat{\mathcal{Y}}_3(r_\xi^l, r_\xi^m) - \left[\mathbf{Z}(r_\xi^l; r_\xi^m) + \hat{\mathcal{Y}}_1(r_\xi^l, r_\xi^m)\right]^{-1} \hat{\mathcal{Y}}_2(r_\xi^l, r_\xi^m) \tag{3.5.4}$$

$$\mathbf{Z}(r_\xi^r; r_\xi^m) = \hat{\mathcal{Y}}_4(r_\xi^m, r_\xi^r) - \hat{\mathcal{Y}}_3(r_\xi^m, r_\xi^r) - \left[\mathbf{Z}(r_\xi^m; r_\xi^m) + \hat{\mathcal{Y}}_1(r_\xi^m, r_\xi^r)\right]^{-1} \hat{\mathcal{Y}}_2(r_\xi^m, r_\xi^r) \tag{3.5.5}$$

with $\hat{\mathcal{Y}}_1$, $\hat{\mathcal{Y}}_2$, $\hat{\mathcal{Y}}_3$ and $\hat{\mathcal{Y}}_4$ given by Johnson [162]. They depend on the width of the sector and on $\mathbf{W}(r; r_\xi^m)$. Since the relation $\hat{\mathcal{Y}}_2 = \hat{\mathcal{Y}}_3$ is true all along the propagation, then $\mathbf{Z}(r)$ stays symmetric. As the adiabatic bases change from one sector to another, we must transform $\mathbf{Z}(r_\xi^r; r_\xi^m)$ into the following sector $\mathbf{Z}(r_{\xi+1}^l; r_{\xi+1}^m)$ using the unitary transformation:

$$\mathbf{Z}(r_{\xi+1}^l; r_{\xi+1}^m) = \mathbf{O}\mathbf{Z}(r_\xi^r; r_\xi^m)\mathbf{O}^{-1} \tag{3.5.6}$$

with the overlap matrix elements given by:

$$O_{t,t'} = \left\langle \Phi_t(\theta_r^{SF}, \phi_r^{SF}; r_\xi^m) \middle| \Phi_{t'}(\theta_r^{SF}, \phi_r^{SF}; r_{\xi+1}^m) \right\rangle . \tag{3.5.7}$$

This matrix is not symmetric but must be close to the unit matrix. If the sectors are chosen too large, then a lot of information is lost in the avoided crossing zones (or when the adiabatic energy curves strongly vary) and the overlap matrix deviates from the unit matrix.

3.5.2 Initial condition on the Z-matrix at $r_{\min}$

Nowadays, constructing potential energy surfaces describing molecule-molecule collisions of alkali metal dimers is a major challenge [169]. For heavy alkali metal dimers, it is not yet possible to obtain these short-range potential energy surfaces. Therefore, a model has been developed to simplify what happens in the short-range domain [97]. In this section, we demonstrate how this model has been obtained and how it imposes an initial condition on the Z-matrix at $r_{\min}$.

Let's replace the real potential energy by a square well potential (Fig. 3.5). We can split the potential into two parts. The first one (I) contains the short-range potential ($r \in [0, r_{\min}]$) and the second one (II) contains the long-range part ($r > r_{\min}$). Solving the Schrödinger equation in the part I gives:

$$\Psi_{\mathrm{I}} = \mathcal{N}[e^{-ik_1 r} - e^{+ik_1 r}] \tag{3.5.8}$$

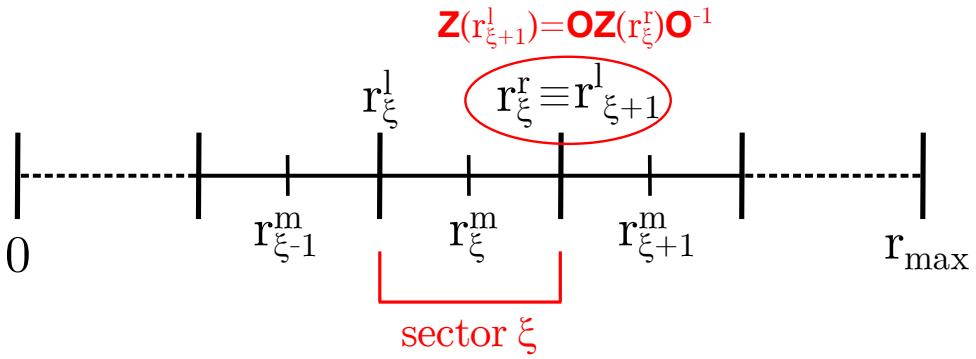

Figure 3.4: Representation of the diabatic-by-sector technique. The total distance of propagation $[r_{\min}, r_{\max}]$ is split into sectors. The left, middle and right part of a given sector (ξ) are represented respectively by r_ξ^l, r_ξ^m and r_ξ^r. To switch from the sector (ξ) to the next one $(\xi+1)$, the Z-matrix is transformed at $r_\xi^r \equiv r_{\xi+1}^l$ using Eq. 3.5.6.

with $k_1 = \frac{2\mu}{\hbar^2}(E - V(r_{\min}))$ and $\mathcal{N}$ a normalization term. Now, let's assume that the short-range potential is not well known for $r < r_{\min}$ and has two major effects:

- The wave function has a probability P_{SR} to be absorbed and to be lost. In other words, it corresponds to the probability of losing the molecules via reactive or sticky collisions.
- The potential modify the phase of the wave function. We note δ_{SR} the accumulated phase.

By properly choosing P_{SR} and δ_{SR}, we can reproduce the effect of any real potential on the wave function. Once out of the interaction area, the reflected wave function can be described by:

$$e^{+ik_1 r} \longrightarrow \sqrt{1 - P_{SR}}\, e^{2i\delta_{SR}}\, e^{+ik_1 r}. \tag{3.5.9}$$

The term $\sqrt{1-P_{SR}}$ corresponds to the part of the wave function that comes out of the potential without being lost and $e^{2i\delta_{SR}}$ is the phase accumulated during the round trip of the wave function in the potential. If we compute the log-derivative function at $r_{\min}$, we get:

$$\begin{aligned} Z(r = r_{\min}) = & \frac{4k_1 sc\sqrt{1-P_{SR}}}{c^2(\sqrt{1-P_{SR}}-1)^2 + s^2(\sqrt{1-P_{SR}}+1)^2} \\ & -i\frac{k_1 P_{SR}}{c^2(\sqrt{1-P_{SR}}-1)^2 + s^2(\sqrt{1-P_{SR}}+1)^2} \end{aligned} \tag{3.5.10}$$

with $c = \cos(k_1 r + \delta_{SR})$ and $s = \sin(k_1 r + \delta_{SR})$.

Let us now imagine the following extreme case: any probability flux penetrating the potential at a given distance $r_{\min}$ is totally lost ($P_{SR} = 1$). This idea comes from the fact that short-range losses are unitary either the molecules are chemically reactive or not. This translates into a diagonal and purely imaginary log-derivative at $r_{\min}$ [97]:

$$Z_{i,i}(r_{\min}) = -ik_1. \tag{3.5.11}$$

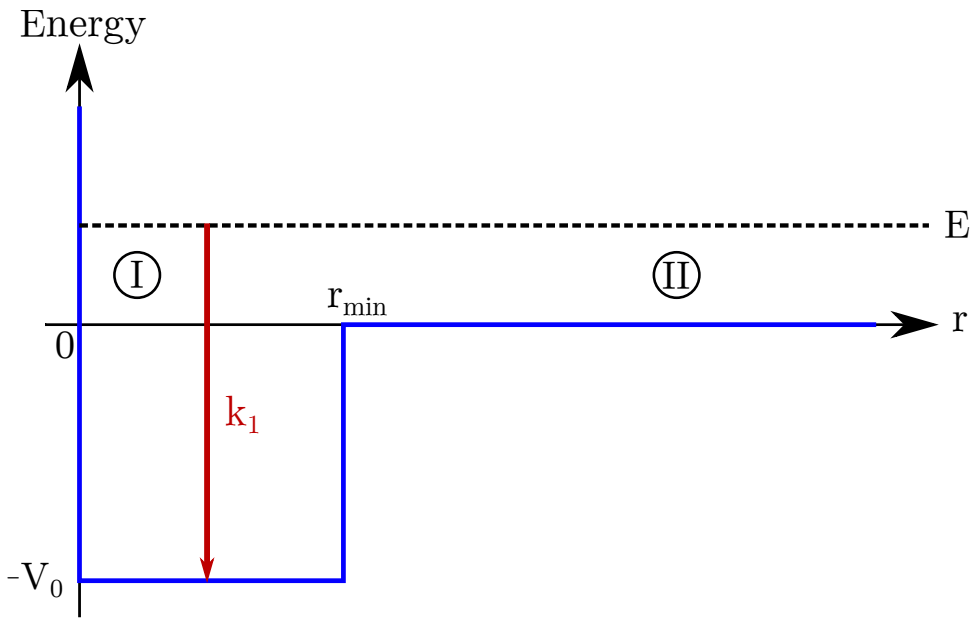

Figure 3.5: The potential well model used to described short-range losses. The potential is characterized by a well of depth $-V_0$ between $[0, r_{\text{min}}]$ (region I). The wave vector is described by k_1 in this region. For $r > r_{\text{min}}$ (region II), the potential is considered as zero.

Under these conditions, collision rate coefficients and cross sections become independent of the accumulated phase. This is expected because if the molecules are lost with a unit probability, then when they come too close to each other, no reflected wave comes back from the short-range part. Consequently, the accumulated phase is no longer meaningful.

In conclusion, short-range effects are included in the initial condition of the log-derivative matrix $\mathbf{Z}(r_{\text{min}})$. As a result, we don't need the potential energy surface of the tetramer (i.e. for $r < r_{\text{min}}$). We only need the potential at long-range (i.e. for $r > r_{\text{min}}$) which is given by the multipolar expansion defined in the previous part. Some results have shown that this model reproduces well experimental data [155, 99, 100].

3.5.3 Asymptotic matching and observables

At the matching point r_{max}, we obtain the Z-matrix at a sufficient large distance where the potential reaches its asymptotic behavior. We can connect the short-range part to the external part solving the asymptotic part of Eq. 3.4.10 given by:

$$\left[-\frac{\hbar^2}{2\mu}\frac{d^2}{dr^2} + \frac{\hbar^2 l(l+1)}{2\mu r^2} + \varepsilon_\alpha - E_{\text{tot}}\right] f^{E_{\text{tot}}}_{\alpha l m_l, \alpha l m_l}(r) = 0. \tag{3.5.12}$$

Let's note $\mathbf{F}^{(1)}$ and $\mathbf{F}^{(2)}$ the general solutions:

$$\mathbf{F}(r) = \mathbf{F}^{(1)}\mathbf{A} + \mathbf{F}^{(2)}\mathbf{B}\big|_{r=r_{\text{max}}} \tag{3.5.13}$$

where:

$$f_{i,i'}^{(1)\,E_{\rm tot}}(r) = r\sqrt{k_\alpha}\, j_l(k_\alpha r)\delta_{i,i'} \qquad f_{i,i'}^{(2)\,E_{\rm tot}}(r) = r\sqrt{k_\alpha}\, n_l(k_\alpha r)\delta_{i,i'} \tag{3.5.14}$$

are expressed in function of the well known Ricatti-Bessel (j_l) and Ricatti-Neumann functions (n_l) [170]. We can notice that these terms are diagonal because asymptotically the molecules do not interact anymore and the channels are thus uncoupled. The non-radial prefactors in Eq. 3.5.14 are chosen so that the Wronskian matrix:

$$\mathbf{W} = \mathbf{F}^{(1)}\mathbf{F}'^{(2)} - \mathbf{F}^{(2)}\mathbf{F}'^{(1)} \tag{3.5.15}$$

equal to the identity matrix (i.e. the solutions are independent). We can also write Eq. 3.5.13 as:

$$\mathbf{F}(r) = \mathbf{F}^K(r)\mathbf{N}^K\big|_{r=r_{\rm max}} \tag{3.5.16}$$

with

$$\mathbf{F}^K(r) = \left\{\mathbf{F}^{(1)} - \mathbf{F}^{(2)}\mathbf{K}\right\}. \tag{3.5.17}$$

$\mathbf{N}^K \equiv \mathbf{A}$ is a real normalisation matrix and $\mathbf{K} \equiv -\mathbf{B}\mathbf{A}^{-1}$ is the reactance matrix (K-matrix). Using matrix algebra, we can relate the K-matrix to the Z-matrix via:

$$\mathbf{K} = \left\{\mathbf{Z}\mathbf{F}^{(2)} - \mathbf{F}'^{(2)}\right\}^{-1}\left\{\mathbf{Z}\mathbf{F}^{(1)} - \mathbf{F}'^{(1)}\right\}\Big|_{r=r_{\rm max}}. \tag{3.5.18}$$

By construction, this matrix is symmetric and if $\mathbf{Z}$ is real (complex) then $\mathbf{K}$ is also real (complex). Its off-diagonal matrix elements give an indication of the character of the other final channels (due to the couplings from the interaction potential energy) in the wave function of a given incident initial colliding channel. The usual scattering matrix (S-matrix) is obtained from the K-matrix using:

$$\mathbf{S} = \frac{\mathbf{I} + i\mathbf{K}}{\mathbf{I} - i\mathbf{K}}. \tag{3.5.19}$$

This matrix, strong in physical meaning, is symmetric and complex. Indeed, the element $|S_{i',i}|^2$ corresponds to the transition probability of going from an incident channel i to a final channel i' (i.e. inelastic collisions). The diagonal term $|S_{i,i}|^2$ corresponds to the probability of staying in the same channel i (i.e. elastic collisions). With the imposed short-range loss condition, the S-matrix is no longer unitary and:

$$1 - \sum_i |S_{i,i'}|^2 \equiv P_{\rm loss} \neq 0 \tag{3.5.20}$$

gives the probability of the incident radial wave function to be lost at short-range.

Finally, the transition matrix $\mathbf{T} = \mathbf{S} - \mathbf{I}$ gives all the observables we need. For example, we can extract the total accumulated phase shift δ_l or go back to more general observables such as cross sections:

$$\sigma_{\alpha\to\alpha'}(E_{\rm k}) = \kappa \times \frac{\pi}{k_\alpha^2}\sum_l\sum_{m_l}\sum_{l'}\sum_{m_l'}|T_{\alpha' l' m_l', \alpha l m_l}(k_\alpha)|^2 \tag{3.5.21}$$

where κ is a coefficient appearing when applying the permutation operator to the wave function. If the two particles are indistinguishable $\kappa = 2$, on the other hand if the

particles are distinguishable $\kappa = 1$ [171]. Subsequently, we will mostly use collision rate coefficients:

$$\beta_{\alpha\to\alpha'}(E_\mathrm{k}) = \sigma_{\alpha\to\alpha'}(E_\mathrm{k}) \times v \tag{3.5.22}$$

where $v = \sqrt{\frac{2E_\mathrm{k}}{\mu}}$ is the relative velocity of the particles. In the following, rate coefficients are expressed in $\mathrm{cm}^3.\mathrm{s}^{-1}$.

3.5.4 Behavior at very low energy

When the collision energy $E_\mathrm{k} \to 0$, the system of coupled Schrödinger equations (Eq. 3.4.10) becomes independent of the collision energy. Therefore, the radial function and the log-derivative are also no longer collision energy dependent. In this section, we will show that under these conditions, the observables can all be expressed from a single quantity full of physical meaning: the scattering length. To simplify the discussion, let's consider the case of structure-less particles (i.e. we drop the α index).

Using the fact that $K_l = \tan(\delta_l)$, we obtain, after some mathematical manipulations, an expression connecting collision energy and the phase accumulated by the wave function in contact of the potential:

$$\tan(\delta_l) \underset{k\to 0}{=} -\mathcal{L}k^{2l+1}. \tag{3.5.23}$$

In the framework of our study, we will be interested in collisions of bosonic molecules where only the $l = 0$ wave is relevant at ultralow energy. Hense, the constant $\mathcal{L}$ has the dimension of a length. We define the scattering length:

$$a = \lim_{k\to 0} -\frac{\tan\delta_0(k)}{k} \tag{3.5.24}$$

the relevant quantity which describes the distance from which a fictitious particle is affected by the potential. The larger this quantity, the more the potential is considered to affect the wave function at long range. Cross sections can be expressed from this using:

$$\sigma_{l=0}(k) = \frac{4\pi}{k^2}\sin^2\delta_0(k) \underset{k\to 0}{\to} 4\pi a^2. \tag{3.5.25}$$

We can see that cross sections are described by a sphere of radius a. We can assimilate this isotropic potential to the model of hard sphere: the potential is equal to 0 outside of this sphere ($r > a$) and infinite inside ($r \leq a$). The scattering length is therefore, at very low energy, the physical quantity describing completely ultracold collisions.

The Bethe–Wigner laws [172, 173] summarize the behaviour of cross sections and collision rate coefficients at very low energy. The elastic cross sections σ_l^el and the elastic collision rate coefficients β_l^el are expressed as:

$$\sigma_l^\mathrm{el} \underset{k\to 0}{\propto} k^{4l} \underset{k\to 0}{\propto} E_\mathrm{k}^{2l} \qquad\qquad \beta_l^\mathrm{el} \underset{k\to 0}{\propto} k^{4l+1} \underset{k\to 0}{\propto} E_\mathrm{k}^{2l+1/2} \tag{3.5.26}$$

while inelastic and reactive cross sections $\sigma_l^\mathrm{in/re}$ and inelastic and reactive collision rate coefficient $\beta_l^\mathrm{in/re}$ are given by:

$$\sigma_l^\mathrm{in/re} \underset{k\to 0}{\propto} k^{2l-1} \underset{k\to 0}{\propto} E_\mathrm{k}^{l-1/2} \qquad\qquad \beta_l^\mathrm{in/re} \underset{k\to 0}{\propto} k^{2l} \underset{k\to 0}{\propto} E_\mathrm{k}^{l}. \tag{3.5.27}$$

In the case $l = 0$, we can extract the real part $a_{\rm re}$ and the imaginary part $a_{\rm im}$ from the scattering length such that $a = a_{\rm re} - i a_{\rm im}$ ($a_{\rm im} > 0$). Cross sections and collision rate coefficients can be expressed exclusively as a function of the scattering length:

$$\sigma_{\rm el} = 4\pi |a|^2 \kappa \qquad \sigma_{\rm in/re} = \frac{4\pi a_{\rm im}}{k}\kappa \tag{3.5.28}$$

$$\beta_{\rm el} = \frac{4\pi\hbar k |a|^2}{\mu}\kappa \qquad \beta_{\rm in/re} = \frac{4\pi\hbar a_{\rm im}}{\mu}\kappa \tag{3.5.29}$$

with $\kappa = 2$ if the two particles are indistinguishable and $\kappa = 1$ if the particles are distinguishable. Note that only $a_{\rm im}$ is related to inelastic collisions and loss processes.

The scattering length also appears in the Gross-Pitaevskii equation [174, 175]:

$$i\hbar\frac{\partial\Psi(r,t)}{\partial t} = \left(-\frac{\hbar^2}{2m}\nabla^2_{\vec{r}} + V(r) + \frac{4\pi\hbar^2 a}{m}|\Psi(r,t)|^2\right)\Psi(r,t) \tag{3.5.30}$$

which describes the dynamics of a gas of bosons. If $a < 0$, the average effect of the interactions of the N-1 other bodies is an attractive interaction: the condensate collapses and disappears. If $a > 0$, the interaction is repulsive: the gas is stable. As a consequence, both the real and the imaginary part play a central role in the creation of degenerate gases. We will present in chapter 4, a method to control the scattering length using a microwave electromagnetic field.

3.6 Permutation symmetry

In the next two chapters, we will only study collisions of identical molecules. Therefore, the total wave function must be symmetrize with respect to the permutation of the two molecules. If we apply the permutation operator $\hat{P}_{12}$ on the total wave function, we have:

$$\hat{P}_{12}\,\psi^{E_{tot}} = \epsilon_P\,\psi^{E_{\rm tot}} \tag{3.6.1}$$

with $\epsilon_P = +1$ if the molecules are identical bosons and $\epsilon_P = -1$ if the molecules are identical fermions. To find the definition of ϵ_P, we must study the effect of the permutation operator on the internal wave functions and on the spherical harmonics respectively. Let's note that the permutation of the two particles is equivalent to the transformation $(\vec{\rho}_1, \vec{\rho}_2, \vec{r}) \rightarrow (\vec{\rho}_2, \vec{\rho}_1, -\vec{r})$. Since the internal wave functions depend only on the coordinates $(\vec{\rho}_1, \vec{\rho}_2)$, we have:

$$\hat{P}_{12}\,\phi_\alpha\left(\vec{\rho}_1, \vec{\rho}_2\right) = \hat{P}_{12}\,\phi_{\alpha_1}\left(\vec{\rho}_1\right)\phi_{\alpha_2}\left(\vec{\rho}_2\right) = \phi_{\alpha_2}\left(\vec{\rho}_1\right)\phi_{\alpha_1}\left(\vec{\rho}_2\right). \tag{3.6.2}$$

We can then form a properly symmetrized internal wave function:

$$\phi_{\alpha,\eta}\left(\vec{\rho}_1, \vec{\rho}_2\right) = \frac{1}{\sqrt{2\left(1+\delta_{\alpha_1,\alpha_2}\right)}}\left\{\phi_{\alpha_1}\left(\vec{\rho}_1\right)\phi_{\alpha_2}\left(\vec{\rho}_2\right) + \eta\phi_{\alpha_2}\left(\vec{\rho}_1\right)\phi_{\alpha_1}\left(\vec{\rho}_2\right)\right\} \tag{3.6.3}$$

where $\eta = \pm 1$ gives respectively a symmetric and anti-symmetric internal wave function. Since $\vec{r} \to -\vec{r}$ is equivalent to $(r, \theta_r, \varphi_r) \to (r, \pi - \theta_r, \varphi_r + \pi)$, we have for the spherical harmonics:

$$\hat{P}_{12}\, Y_l^{m_l}(\vec{r}) = Y_l^{m_l}(-\hat{r}) = (-1)^l Y_l^{m_l}(\hat{r}) \tag{3.6.4}$$

and Eq. 3.6.1 becomes:

$$\hat{P}_{12}\, \psi^{E_{tot}} = \varepsilon_P\, \psi^{E_{\rm tot}} = \eta(-1)^l\, \psi^{E_{\rm tot}}. \tag{3.6.5}$$

Therefore, we have $\varepsilon_P = \eta(-1)^l$. In the following, we will only study collisions of indistinguishable molecules. Therefore only $\eta = +1$ exists otherwise the symmetrized internal wave function cancels. The sign of ϵ_P depends only if the quantum number l is even or odd:

- In the case of identical bosons $\epsilon_P = +1$, only even partial waves $l = 0, 2, 4 \ldots$ are required.
- In the case of identical fermions $\epsilon_P = -1$, only odd partial waves $l = 1, 3, 5 \ldots$ are required.

The lowest partial wave for bosons is then the s-wave ($l = 0$) for which the centrifugal term is zero while for fermions it corresponds to a p-wave ($l = 1$).

Chapter 4

Microwave shielding

Over the last decade, several methods for controlling molecular collisions have been developed. Some methods, based on the confinement of molecules [92, 93, 94, 95, 82], are particularly effective for shielding molecules against short-range losses. They force the molecules to collide in configurations where the dipole-dipole interaction is most repulsive to keep the molecules apart. Another method, described in chapter 5, uses a static electric field to reduce short-range losses and, by definition, the imaginary part of the molecule-molecule scattering length [97, 98, 99, 100]. The other methods usually used for atoms cannot be applied to molecules because of a very high density of tetramer bound states in the vicinity of the collisional threshold.

In this chapter, we present a method, using a circularly polarized microwave field, to control both the real and the imaginary part of the molecule-molecule scattering length for molecules initially prepared in the ground rovibronic state. First, we present in section 4.1 the physical principle of the microwave shielding method. The general formalism presented in the previous chapter (reactive collisions, internal Schrödinger equation, coupled equations) is extended for collisions in presence of an electromagnetic field. In section 4.3, we show the effect of the microwave field polarization on the adiabatic energy curves. Then, we show that we can engineer a long-range potential barrier which shields the molecules from short-range losses. The consequences on the rate coefficients are presented in section 4.3. We also explain how we can precisely control both the real and imaginary part of the molecule-molecule scattering length [103]. In section 4.4, we present an adimensional formalism to illustrate the effects of the microwave field on collisions of fictitious molecules. By changing the parameters describing the fictitious molecules, we can study every alkali metal dimers collisions and select the good candidates for the microwave shielding. Moreover, we show that for a lot of molecules, we can tune the molecule-molecule scattering length which will certainly open a new regime of strongly interacting and correlated physics with ultracold dipolar molecules.

4.1 Physical principle

Let's imagine two molecules prepared in their fundamental rotational state $j = 0$. They approach to each other with a relative kinetic energy E_k following their molecular

potential energy curve. An electromagnetic field couples the fundamental molecular rotational state ($j = 0 + j = 0$) with the first repulsive rotational state ($j = 0 + j = 1$) as illustrated in Fig. 4.1. In the Fock representation, this translates by dressing the fundamental state by the energy of one photon. If the laser frequency is blue-detuned ($\hbar\omega > 2B$), the fundamental state becomes above the excited state. When the microwave field is turned off, the molecules follow the black attractive diabatic energy curve and are lost at short-range. However, when the microwave field is turned on, the molecules follow the red adiabatic potential energy curves. As a two level system, the stronger the coupling, the more repulsive will be the upper state. This is through this mechanism that appears a barrier at long-range in the incident channel. If the barrier is higher than E_{k}, the major part of the radial wave function will be reflected. Therefore, the barrier shields the molecules and protects them from short-range losses.

The basis of this method comes from the idea of atomic optical shielding [140, 141, 142, 58] which uses the transition between an s to a p electronic state of an atom. This has also been recently adapted for molecular optical shielding [108].

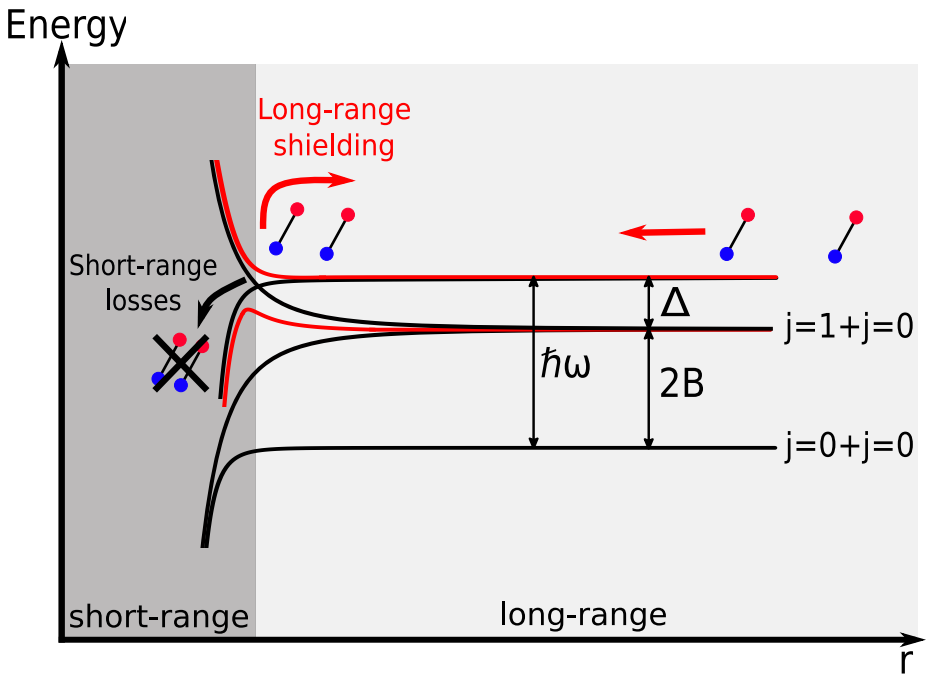

Figure 4.1: Schematic process of a collisional shielding of ground state rotational molecules $j = 0$, using a blue-detuned, circularly polarized microwave field. $\Delta > 0$ is the detuning between the energy of the microwave field $\hbar\omega$ and $2B$, the energy level of the first excited rotational state $j = 1$ of a molecule. The dipole-dipole interaction creates an effective repulsive adiabatic curve in the $j = 0 + j = 0$ corresponding curve, preventing the molecules to approach at short-range.

4.2 Time-independent formalism

In this chapter, the electromagnetic field is quantified according to the principle of second quantization [142, 176, 177]. It will thus be described by a quantum state describing the number of photon contained in the mode of the electromagnetic wave. The formalism used is equivalent to the Flocket formalism [178, 179, 180] describing the periodic time dependence of the electric field of an electromagnetic wave.

4.2.1 Quantization of the electromagnetic field

Let's consider a single-mode electromagnetic field characterized by an angular frequency ω and an energy $E_{phot} = \hbar\omega$. The quantized field can be represented by the state [181]:

$$|\bar{n} + n\rangle \tag{4.2.1}$$

where $\bar{n} \in \mathbb{N}$ is a constant corresponding to the average number of photons in the cavity and $n \in \mathbb{Z}$ corresponds to the number of photons lost or gained by the mode (via absorption or emission of photons by the molecules). In the semi-classical limit, this mode is populated by a large number of photon (i.e. $\bar{n} \gg n$). In the following, we will only deal with the deviations n around $\bar{n}$:

$$|\bar{n} + n\rangle \longrightarrow |n\rangle\,. \tag{4.2.2}$$

The Hamiltonian of the field is the same as the one of a harmonic oscillator of natural frequency ω:

$$h_f = \hbar\omega\,(\hat{a}^\dagger\hat{a} + \frac{1}{2}) \tag{4.2.3}$$

where $\hat{a}^\dagger$ and $\hat{a}$ correspond respectively to the creation and annihilation operators. Physically, the operator a describes the absorption of a photon by a molecule, while the operator $a^\dagger$ describes the emission of a photon by a molecule. Mathematically, this translates into:

$$\hat{a}^\dagger\,|n\rangle = \sqrt{n+1}\,|n+1\rangle \tag{4.2.4}$$

$$\hat{a}\,|n\rangle = \sqrt{n}\,|n-1\rangle\,. \tag{4.2.5}$$

The associated energies are given by:

$$h_f\,|n\rangle = \varepsilon_n\,|n\rangle = \hbar\omega(n + \frac{1}{2})\,|n\rangle\,. \tag{4.2.6}$$

Let's remark that if the mean value of photons $\bar{n}$ was kept, an additional constant energy term $\hbar\omega(\bar{n} + \frac{1}{2})$ would have appeared. We ignored this term because this is a constant that can be set to 0. Finally, we add this new quantum state $|n\rangle$ to the basis set functions. Thanks to this, we remain in a time-independent formalism.

4.2.2 Interaction of a molecule with the electromagnetic field

An other term to consider is the interaction $\hat{h}_{\mathrm{m}_\tau.\mathrm{f}}$ [177] of a dipolar molecule τ with the electric field E of the electromagnetic wave. For linear polarization ($p = 0$), this is given by:

$$\hat{h}_{\mathrm{m}_\tau.\mathrm{f}} = -\frac{\hbar\Omega}{2\sqrt{\bar{n}}}(\hat{a} + \hat{a}^\dagger)\cos\theta_{\rho_\tau}^{SF} \tag{4.2.7}$$

where $\theta_{\rho_\tau}^{SF}$ is the angle between the electric dipole moment and the polarization axis of the electric field. Therefore, the propagation of the electromagnetic wave is perpendicular to the quantization axis. We note:

$$\Omega = \frac{dE}{\hbar} \tag{4.2.8}$$

the Rabi frequency expressed in function of the permanent electric dipole moment d of the molecule and the electric field E of the electromagnetic wave. In the basis $|j_\tau, m_{j_\tau}\rangle\,|n\rangle$, the matrix elements of the Hamiltonian are:

$$\langle j_\tau, m_{j_\tau}, n|\, H_{\mathrm{m}_\tau.\mathrm{f}}^{p=0}\,\big|j_\tau{}', m'_{j_\tau}, n'\big\rangle = -\frac{\hbar\Omega}{2}(\delta_{n,n'-1} + \delta_{n,n'+1})b^p_{j_\tau\, m_{j_\tau}, j_\tau{}'\, m'_{j_\tau}}\,\delta_{m_{j_\tau}, m'_{j_\tau}} \tag{4.2.9}$$

with the elements $b^p_{j_\tau\, m_{j_\tau}, j_\tau{}'\, m'_{j_\tau}}$ determined by the Wigner-Eckart theorem [182]:

$$b^k_{j_\tau\, m_{j_\tau}, j_\tau{}'\, m'_{j_\tau}} = (-1)^{m_{j_\tau}}\sqrt{(2j_\tau+1)(2j'_\tau+1)}\begin{pmatrix} j_\tau & 1 & j_\tau{}' \\ 0 & 0 & 0 \end{pmatrix}\begin{pmatrix} j_\tau & 1 & j'_\tau \\ -m_{j_\tau} & k & m'_{j_\tau} \end{pmatrix}. \tag{4.2.10}$$

It can be noted that $\delta_{n,n'-1}$ represents the absorption of a photon by the molecule and $\delta_{n,n'+1}$ represents the emission of a photon by the molecule. According to the $3j$ symbol, if $p = 0$, then $\Delta m_{j_\tau} = m'_{j_\tau} - m_{j_\tau} = 0$. As the photon does carry a zero polarization, rotational quantum numbers with same projections are coupled. Consequently, m_{j_τ} is a good quantum number for the individual molecule.

For circular polarization $p = \pm 1$, the Hamiltonian is given by:

$$\hat{h}_{\mathrm{m}_\tau.\mathrm{f}}^{p=\pm1} = -\frac{\hbar\Omega}{2\sqrt{\bar{n}}}\left(\frac{4\pi}{3}\right)^{\frac{1}{2}}[\mp\hat{a}\mathcal{Y}_1^p(\hat{\rho}_\tau^{SF}) \pm \hat{a}^\dagger\mathcal{Y}_1^{-p}(\hat{\rho}_\tau^{SF})]. \tag{4.2.11}$$

For this case, the axis of quantization is chosen to be the axis perpendicular to the plane in which the electric field circularly rotates. The propagation of the electromagnetic wave is now parallel to the quantization axis. Its matrix elements in the basis $|j_\tau, m_{j_\tau}\rangle\,|n\rangle$ are:

$$\begin{aligned}\langle j_\tau, m_{j_\tau}, n|\, h_{\mathrm{m}_\tau.\mathrm{f}}^{p=\pm1}\,\big|j_\tau{}', m'_{j_\tau}, n'\big\rangle = -\frac{\hbar\Omega}{2}(\mp\delta_{n,n'-1}b^p_{j_\tau\, m_{j_\tau}, j_\tau{}'\, m'_{j_\tau}} \\ \pm\delta_{n,n'+1}b^{-p}_{j_\tau\, m_{j_\tau}, j_\tau{}'\, m'_{j_\tau}}).\end{aligned} \tag{4.2.12}$$

In this case, we have $\Delta m_{j_\tau} = \pm 1$ for both $p = +1$ and $p = -1$. Then, m_{j_τ} is not a good quantum number anymore. The total angular momentum of the system {molecule + field} is given by:

$$m_{\mathrm{tot}} = m_{j_\tau} + n \times p. \tag{4.2.13}$$

To conserve the total angular momentum of the system, the condition $\Delta m_{\rm tot} = 0$ must be fulfilled which implies that $\Delta n \times p = -\Delta m_{j_\tau}$. If $\Delta n = n' - n = +1$, the molecule absorbs a photon and wins the projection $p = \pm 1$ of the photon while the quantum number m'_{j_τ} loses the value of p.

Regardless of the polarisation used, the symbols $3j$ couples angular moments of rotation $\Delta j = \pm 1$.

4.2.3 Schrödinger equation for one molecule in the presence of an electromagnetic field

The internal Schrödinger Eq. 3.3.10 in the uncoupled basis $|j_\tau, m_{j_\tau}\rangle |n\rangle$ is given by:

$$\hat{h}_\tau |j_\tau, m_{j_\tau}\rangle |n\rangle = [\hat{h}_{\rm rot_\tau} + \hat{h}_f + \hat{h}_{\rm m_\tau.f}] |j_\tau, m_{j_\tau}\rangle |n\rangle \tag{4.2.14}$$

where $\hat{h}_{\rm rot_\tau}$ (given in Eq. 3.3.11) is diagonal in n. Due to the non-diagonal elements of $\hat{h}_{\rm m_\tau.f}$, the eigenvectors obtained after diagonalization are a linear combination of the bare states $|j_\tau, m_{j_\tau}\rangle |n\rangle$. In the case $p = 0$, the electromagnetic field lifts a partial degeneracy of the rotational levels into $(j_\tau + 1)$ levels because m_{j_τ} remains a good quantum number. The eigenvectors noted $\left|\tilde{j}_\tau, m_{j_\tau}\right\rangle |\tilde{n}\rangle$ are given by:

$$\left|\tilde{j}_\tau, m_{j_\tau}\right\rangle |\tilde{n}\rangle = \sum_{j_\tau} \sum_{n} C_{j_\tau, m_{j_\tau}, n} |j_\tau, m_{j_\tau}\rangle |n\rangle \,. \tag{4.2.15}$$

In the case $p = \pm 1$, the electromagnetic field mixes a bigger number of states because m_{j_τ} is no longer a good quantum number. The eigenstates, noted $\left|\tilde{j}_\tau, \tilde{m}_{j_\tau}\right\rangle |\tilde{n}\rangle$, are given by:

$$\left|\tilde{j}_\tau, \tilde{m}_{j_\tau}\right\rangle |\tilde{n}\rangle = \sum_{j_\tau} \sum_{m_{j_\tau}} \sum_{n} C_{j_\tau, m_{j_\tau}, n} |j_\tau, m_{j_\tau}\rangle |n\rangle \,. \tag{4.2.16}$$

For both cases, $C_{j_\tau, m_{j_\tau}, n}$ depends on the value of the electric field of the electromagnetic wave. Hereafter, we will note the dressed states and their associated energies respectively $|\tilde{\alpha}\rangle \equiv \{|j_\tau, m_{j_\tau}\rangle |n\rangle\}$ and $\epsilon_{\tilde{\alpha}}$ regardless of the polarization studied. If the electric field is turned off ($E = 0\,\mathrm{kV\,cm^{-1}}$), the eigenstates naturally tend to the $(2j + 1)$ degenerate states:

$$\{|j_\tau, m_{j_\tau}\rangle |n\rangle\} \underset{E=0}{\rightarrow} |j_\tau, m_{j_\tau}\rangle |n\rangle \tag{4.2.17}$$

with their corresponding eigenenergies:

$$\epsilon_{\tilde{\alpha}} \underset{E=0}{\rightarrow} \epsilon_\alpha = [B\, j_\tau(j_\tau + 1) + \varepsilon_n]. \tag{4.2.18}$$

where ε_n is the energy given in Eq. 4.2.6 which describes the energy of the field for a given number of photon n and B is the rotational constant of the molecule.

We show in Fig. 4.2 the effect of the electric field E on the energy levels of a bosonic ^{23}Na^{87}Rb molecule in the case $p = 0$ (top panel) and $p = +1$ (bottom panel). The energy of a photon is $E_{phot} = 204\,\mathrm{mK}$, that is almost in resonance with the $j_\tau = 0 \leftrightarrow j_\tau = 1$

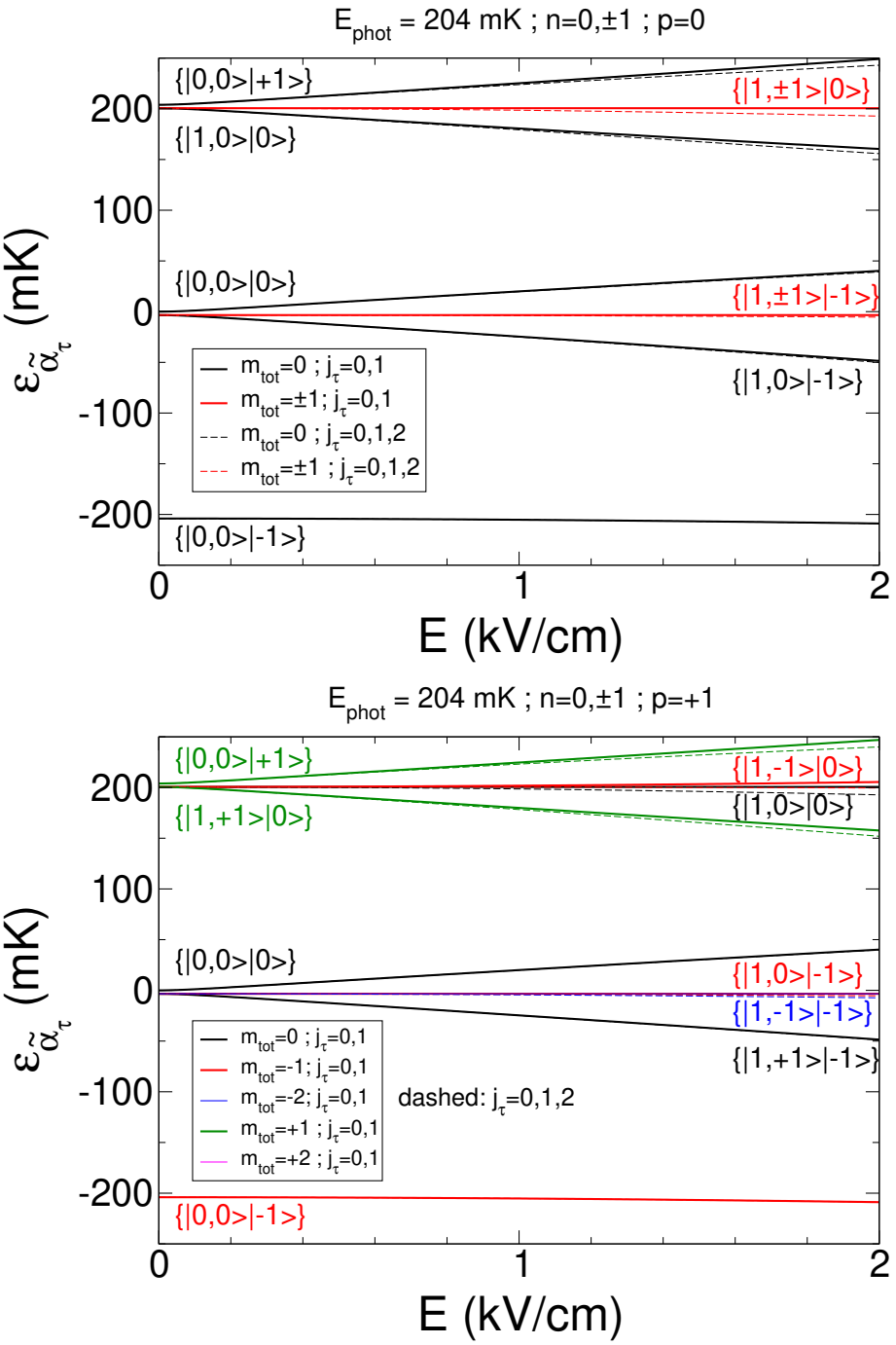

Figure 4.2: Energy of a bosonic ^{23}Na^{87}Rb molecule as a function of the electric field E of an electromagnetic wave for $E_{phot} = 204\,\mathrm{mK}$. Top: linear polarization $p = 0$, bottom: circular polarization $p = +1$. The dressed states are labeled as $\{|j_\tau, m_{j_\tau}\rangle|n\rangle\}$.

transition, but slightly blue detuned. We use $B = 2.089\,662\,8\,\mathrm{GHz}$ [84] so that the resonance energy is at $2\,B/k_B = 200.6\,\mathrm{mK} \rightarrow \Delta = 3.4\,\mathrm{mK}$. In the following, we will omit the division by k_B in the notations for the quantities expressed in Kelvin. We used

$n = 0, \pm 1$ for the calculations. The color of the curves indicates the value of $m_{tot} = 0, \pm 1$ for $p = 0$ and $m_{tot} = 0, \pm 1, \pm 2$ for $p = +1$. The solid lines correspond to a rotational basis set $j_\tau = 0, 1$ while the dashed curves correspond to a rotational basis set $j_\tau = 0, 1, 2$. One can see that the $j_\tau = 0, 1$ is sufficient to converge the energies for $E < 1\,\mathrm{kV\,cm^{-1}}$, considered later in the chapter. For $E = 0\,\mathrm{kV\,cm^{-1}}$, the eigenenergies tend well to the energies ϵ_α given in Eq. 4.2.18. Moreover, from the zoom on the plots, it is clear that the state $|1, 0\rangle\,|-1\rangle$ is slightly below the state $|0, 0\rangle\,|0\rangle$ because the molecules have absorbed a photon slightly blue-detuned. Let's focus now on the $\{|0, 0\rangle\,|0\rangle\}$ state for $E \neq 0\,\mathrm{kV\,cm^{-1}}$:

- For $p = 0$, the state $\{|0, 0\rangle\,|0\rangle\}$ is shifted to higher energies as the value of the electric field increases. It is mainly repelled by the lower state $\{|1, 0\rangle\,|-1\rangle\}$ with which it is coupled by the microwave field. The states $\{|1, \pm 1\rangle\,|-1\rangle\}$ are not directly coupled with it (by conservation of m_{tot}) and are not too much affected by the field.
- For $p = +1$, this state is also repelled but in this case this is via its coupling with $\{|1, +1\rangle\,|-1\rangle\}$. A calculation with $p = -1$ would give the same curve but the coupling would be with $\{|1, -1\rangle\,|-1\rangle\}$. These differences are a consequence of the conservation of m_{tot}.

A change of p will therefore entail different composition of the dressed states, hence different dynamics properties of the molecules during the collision.

4.2.4 Collisions of two molecules in an electromagnetic field

Asymptotic basis

The Hamiltonian for two molecules is given by:

$$\hat{h} = \hat{h}_{\mathrm{rot}_1} + \hat{h}_{\mathrm{rot}_2} + \hat{h}^p_{m_1.f} + \hat{h}^p_{m_2.f} + \hat{h}_f. \tag{4.2.19}$$

As we will study collisions of identical molecules, we will use the symmetrized internal wave function given in Eq. 3.6.3 whose expression is recalled below:

$$|j_1, m_{j_1}, j_2, m_{j_2}; \eta\rangle\,|n\rangle = \frac{1}{\sqrt{2(1 + \delta_{j_1,j_2}\delta_{m_{j_1},m_{j_2}})}}\Big[|j_1, m_{j_1}, j_2, m_{j_2}\rangle + \eta|j_2, m_{j_2}, j_1, m_{j_1}]\Big]\,|n\rangle \tag{4.2.20}$$

with $\eta = \pm 1$ for respectively symmetric and anti-symmetric combinations of the initial rotational states and where the quantum state $|n\rangle$ has been added. With this basis set, the eigenvectors are $\left|\tilde{j}_1, \tilde{m}_{j_1}, \tilde{j}_2, \tilde{m}_{j_2}; \eta\right\rangle |\tilde{n}\rangle$ and will be noted $\{|j_1, m_{j_1}, j_2, m_{j_2}\rangle_\pm\,|n\rangle\}$. The projection of the angular momentum of the symmetrized state is given by:

$$m_{1+2+f} = m_{j_1} + m_{j_2} + n \times p \tag{4.2.21}$$

and is a good quantum number. This dressed state picture can be used asymptotically as the characteristic time of the Rabi oscillations is much shorter than the characteristic

time between two collisions as explained in details in appendix. A.1.

We show in Fig. 4.3 the energy of two separated bosonic $^{23}Na^{87}Rb$ molecules as a function of the electric field E, for the same conditions than in Fig. 4.2. We can see that for $p = 0$, the dressed state $\{|0,0,0,0\rangle_+ |+1\rangle\}$ is highly coupled with $\{|0,0,1,0\rangle_+ |-1\rangle\}$ while for $p = 1$ it is highly coupled with $\{|0,0,1,+1\rangle_+ |-1\rangle\}$. This change will cause the adiabatic energy curves to behave differently in function of the polarization chosen (cf. discussion in section 4.3).

Collisional study

When the molecules are getting closer, the centrifugal energy and the long-range interactions must be treated using the collisional formalism described in the previous section. The collisional channels are then defined by:

$$\begin{aligned} |i\rangle &\equiv |\tilde{\alpha}\rangle |l, m_l\rangle \\ &= |\tilde{j}_1, \tilde{m}_{j_1}, \tilde{j}_2, \tilde{m}_{j_2}\,; \eta\rangle |\tilde{n}\rangle |l, m_l\rangle \\ &= \left\{|j_1, m_{j_1}, j_2, m_{j_2}\rangle_\pm |n\rangle\right\} |l, m_l\rangle. \end{aligned} \tag{4.2.22}$$

The projection of the total angular momentum of the system is described by the quantum number:

$$M_J = m_{1+2+f} + m_l = m_{j_1} + m_{j_2} + n \times p + m_l \tag{4.2.23}$$

which is conserved during the collision. As demonstrated in the previous chapter, the symmetrization of the total collisional basis gives:

$$\hat{P}_{12}\{|j_1, m_{j_1}, j_2, m_{j_2}\rangle_\pm |n\rangle\} |l, m_l\rangle = \eta(-1)^l \{|j_1, m_{j_1}, j_2, m_{j_2}\rangle_\pm |n\rangle\} |l, m_l\rangle \,. \tag{4.2.24}$$

In the following, we will only deal with identical bosons then only even values of the orbital moment ($l = 0, 2, 4, ...$) are considered. This time-independent formalism can be safely employed even during a collision as the time of a collision is much longer than the period time of the Rabi oscillations as shown in appendix A.1 (see supplemental material of [103]).

Finally, the total Hamiltonian is given by:

$$\hat{H} = \hat{T} + \hat{V} + \hat{h}_{\mathrm{rot}_1} + \hat{h}_{\mathrm{rot}_2} + \hat{h}_{m_1.f} + \hat{h}_{m_2.f} + \hat{h}_f \tag{4.2.25}$$

with $\hat{T} = -\frac{\hbar^2}{2\mu}\nabla^2_{\vec{r}}$ and $\hat{V}$ is composed by:

$$\hat{V} = \hat{V}_{\mathrm{dd}} + \hat{V}_{\mathrm{el}}. \tag{4.2.26}$$

The first term $\hat{V}_{\mathrm{dd}}$ is derived from the multipolar expansion (Cf. Eq. 3.4.14) and describes the dipole-dipole interaction:

$$\langle i| \hat{V}_{\mathrm{dd}} |i'\rangle = \langle\tilde{\alpha}| \left(\frac{1 - 3\cos^2\theta_r^{SF}}{4\pi\epsilon_0 r^3}\right) \hat{d}_1\hat{d}_2 |\tilde{\alpha}'\rangle \, \delta_{n,n'} = \frac{C_3}{r_3}\zeta_{i,i'}(l, m_l, l', m_l'; E) \tag{4.2.27}$$

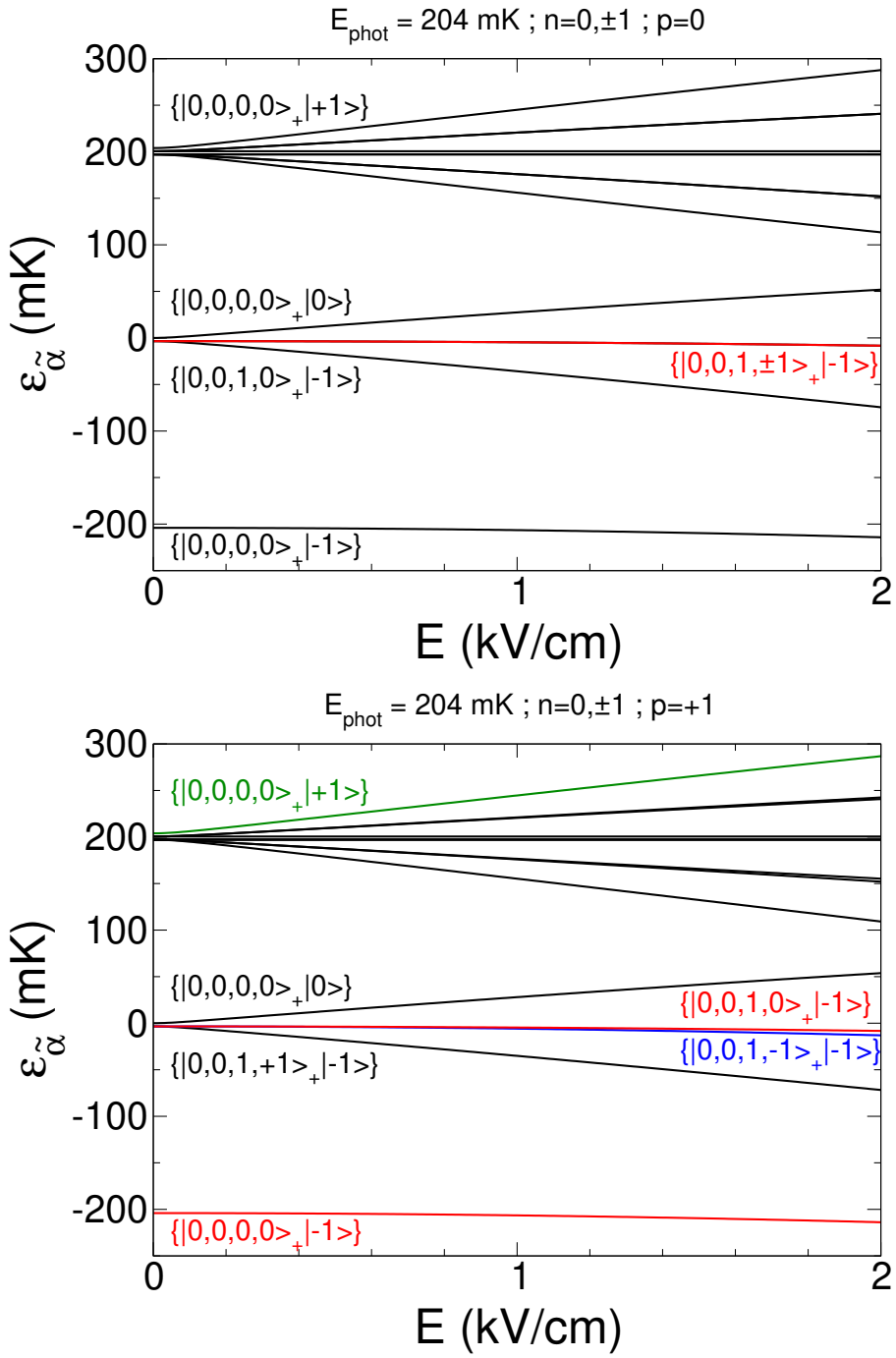

Figure 4.3: Energy of two separated bosonic ^{23}Na^{87}Rb molecules as a function of the electric field E of an electromagnetic wave for $E_{phot} = 204$ mK. Top: linear polarization $p = 0$, Bottom: circular polarization $p = +1$. Some of the dressed states are labelled as $\{|j_1, m_{j_1}, j_2, m_{j_2}\rangle_\pm |n\rangle\}$.

with $C_3 = \frac{\hat{d}_1 \hat{d}_2}{4\pi\epsilon_0}$ and $\zeta_{i,i'}(l, m_l, l', m'_l; E)$ a geometrical coefficient depending on the orbital

angular momentum as well as the rotational angular momentum via the dressed states. It also depends on the value of the electric field. We could include the quadripolar and octupolar terms but it was shown [97] that they are totally negligible at low energy. Moreover, for some convenient reasons, we do not take into account of the entire electronic structure of the molecules. We use an effective isotropic and dispersive potential $\propto r^{-6}$ whose matrix elements are given by:

$$\langle i|\,\hat{V}_{\rm el}\,|i'\rangle = \frac{C_6^{\rm el}}{r^6}\delta_{i,i'} \tag{4.2.28}$$

with $C_6^{\rm el} < 0$ the electronic van der Waals coefficient theoretically determined [183].

4.3 Shielding of NaRb + NaRb collisions

Now, we consider bosonic ^{23}Na^{87}Rb molecules prepared in their ground electronic state $^1\Sigma^+$, ground vibrational state $v = 0$ and ground rotational states $j = 0$ [184]. We want to apply an electromagnetic wave so that the $j = 0$ and $j = 1$ are coupled together. As in the previous part, we use a mode of the field with a corresponding photon energy $E_{phot} = 2\,B + 0.034\,B = 204\,\text{mK}$, using $B = 2.0896628$ GHz [84]. This is a photon slightly blue detuned with the $j = 0 \leftrightarrow j = 1$ transition as the detuning:

$$\Delta = E_{phot} - 2\,B \tag{4.3.1}$$

amounts to $0.034\,B$ in this case and is positive ($\Delta/2B \simeq 0.01$). The typical value of E_{phot} is characteristic of an electromagnetic wave in the microwave domain. To converge the results, we take the rotational quantum numbers $j_\tau = 0, 1$, the photon numbers $n = 0, \pm1, \pm2$, the orbital quantum numbers $l = 0, 2, 4$, and the total projection $M_J = 0$. We choose $r_{min} = 5\ a_0$, a full loss condition Eq. 3.5.11 at short-range, and we propagate $\mathbf{Z}$ up to $r_{max} = 35000\ a_0$ to get converged rate coefficients for the elastic, inelastic, loss and quenching processes.

In appendix A.3, we have shown that the effects related to hyperfine interactions can be neglected if we apply a sufficiently large magnetic field. For NaRb, we have estimated that this value is $B = 100$ G. We will consider that this magnetic field is always on for all the calculations made in this chapter so that we neglect all the effects related to the hyperfine structure.

Adiabatic energy curves

First, let's look what happens when the electric field is not yet swiched on. In Fig 4.4, we have represented the adiabatic energies as a function of r for $E = 0$, $p = 0$, $M_J = 0$ and $E_{phot} = 204$ mK.

When the field is zero, the quantum numbers n, j_τ and m_{j_τ} are good quantum numbers. Therefore, we can identify each adiabatic energy curve by a well defined set of quantum numbers. We represented the $n = 0, +1, -1, +2, -2$ curves respectively in black, blue, red, orange, green. The states whose internal states are identical but for

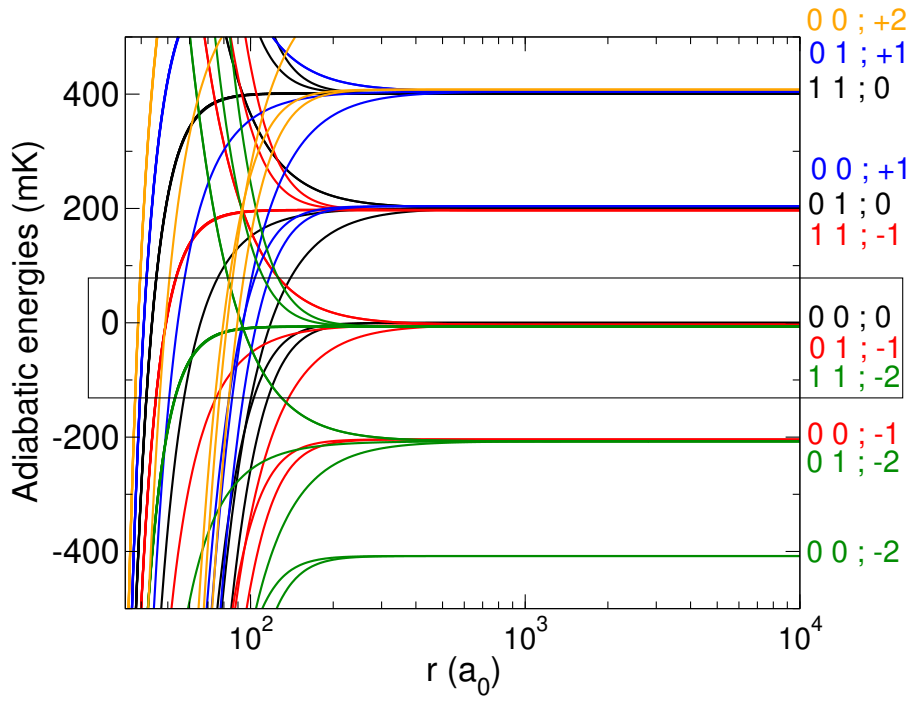

Figure 4.4: Adiabatic energies as a function of r for the bosonic ^{23}Na^{87}Rb + ^{23}Na^{87}Rb system for $E = 0$, $p = 0$, $\eta = +1$, $M_J = 0$ and $E_{phot} = 204$ mK. The $n = 0, +1, -1, +2, -2$ curves are plotted in black, blue, red, orange, green. The values $j_1, j_2 \,; n$ of $\left\{|j_1, m_{j_1}, j_2, m_{j_2}\rangle_+ |n\rangle\right\}$ labels the dressed states asymptotically. The box indicates what is shown in more details in Fig. 4.5-a.

which the quantum number n is different have the same adiabatic energy curves that shifted in energy via the presence of the term ε_n in the asymptotic energies given in Eq. 4.2.18. As E_{phot} is chosen so that it is almost in resonance with the $j = 0 \leftrightarrow j = 1$ transition, then one can see that the states $\left\{|0, 0, 0, 0\rangle_+ |0\rangle\right\}$, $\left\{|0, 0, 1, 0\rangle_+ | - 1\rangle\right\}$ and $\left\{|1, 0, 1, 0\rangle_+ | - 2\rangle\right\}$ are really close to each others, as indicated by the box. We have verified that they tend well asymptotically to the energies presented in Fig. 4.3.

If we zoom on the incident channel (Fig. 4.5-a), we observe the usual behavior of the centrifugal potential energy. Indeed, potential energy curves mainly composed of the s-wave partial wave ($\tilde{l} = 0$) have no centrifugal barrier and are attractive, whereas the potential energy curves mainly composed of the d-partial wave ($\tilde{l} = 2$) have a small centrifugal barrier before being attractive due to the van der Waals term. In these conditions, if two molecules start to collide with a low relative kinetic energy, their radial wave functions see the attractive $\tilde{l} = 0$ curve and are lost in the short-range domain. If the electromagnetic wave is turned on ($E = 0.2\,\mathrm{kV\,cm^{-1}}$, Fig. 4.5-b-c), the states start to be enough coupled to observe the shielding mechanism. n is not a good quantum number anymore and the curves have lost their color code. Let's distinguish the two cases:

- For $p = 0$, we observe that for the incident state, the corresponding $\tilde{l} = 2$ channel has become totally repulsive while the $\tilde{l} = 0$ channel remains attractive.

- For $p = +1$, we observe that for the incident state, both the channels $\tilde{l} = 0, 2$ become repulsive.

This difference is due to the specific selection rules in the matrix elements of the coupling matrix in Eq. 4.2.19, as found for Na + Na collisions [142]. Therefore, for $p = 0$ the shielding will not be efficient due to the presence of the attractive s-wave behavior in the $\tilde{l} = 0$ channel. On the contrary, the $p = 1$ polarization is a good candidate for shielding because the incident radial wave functions will see barriers at long-range in both $\tilde{l} = 0, 2$. The barriers are very high ($\sim$ K) compared to the collision energy ($\sim$ nK). As a result, we expect them to prevent the molecules to come into the short-range region (and the loss rate coefficient will decrease).

If one increases E to $E = 0.05$ kV/cm (Fig. 4.5-d), we observe that the more we increase the electromagnetic field the more the partial waves corresponding to our initial state move away from the curves corresponding to other states. We therefore expect a decrease in the inelastic collision rates to the other de-excitation channels when E increases.

4.3.1 Rate coefficients

The set of coupled equations (Eq. 3.4.10) adapted in the Flocket formalism are given by:

$$\left[-\frac{\hbar^2}{2\mu}\frac{d^2}{dr^2} + \frac{\hbar^2 l(l+1)}{2\mu r^2} + \epsilon_{\tilde{\alpha}} - E_{\text{tot}}\right] f_i(r) + \sum_{i'} V_{i,i'} f_{i'}(r) = 0 \tag{4.3.2}$$

where $V_{i,i'}$ includes the dipole-dipole interaction and the van der Waals interaction. After propagation of the log-derivative matrix (cf. section 3.5), we obtained the different rate coefficients. We present in Fig. 4.6 the elastic (red), inelastic (green), loss (black) and quenching (blue) rate coefficients as a function E for $E_{phot} = 204\,\text{mK}$, $p = +1$ and $E_{\text{k}} = 720\,\text{nK}$ (on the order of the temperatures reached in the CUHK NaRb experiment [184, 84, 157]). For the calculations, we used $M_J = 0, \pm1, \pm2, \pm3, \pm4$. Only the different contributions of M_J for the elastic rate coefficients are plotted (for visibility) and are represented by dashed lines. The solid lines represent the sum of the different contributions.

First, we can see that $M_J = 0$ is the main contribution for elastic collisions. This can be explained by the fact that the incident channel $\{|0,0,0,0\rangle_{\pm}|0\rangle\}\left|\tilde{0},0\right\rangle$ has its main couplings with $\{|0,0,1,+1\rangle_{\pm}|-1\rangle\}\left|\tilde{0},0\right\rangle$ and $\{|0,0,1,0\rangle_{\pm}|-1\rangle\}\left|\tilde{2},+1\right\rangle$ which are responsible of the repulsion of the incident channel (and they both correspond to $M_J = 0$). For low values of the electric field ($E < 0.02\,\text{kV cm}^{-1}$), the quenching rate coefficient is high because the barrier in the channel $\tilde{l} = 0$ has not yet appeared. For higher electric fields ($E > 0.02\,\text{kV cm}^{-1}$), the barrier appears and becomes higher as the electric field increases. This is why the loss rate coefficients in this electric field range decrease.

Secondly, we can note that for $E = 0\,\text{kV cm}^{-1}$, the inelastic collisions are zero because without field there is no coupling between the states and therefore no inelastic collisions are possible. As predicted in section 4.3, we can observe that as the field increases, the inelastic collision rate coefficients decrease. Indeed, the probability to go in an open channel which is moving away decreases.

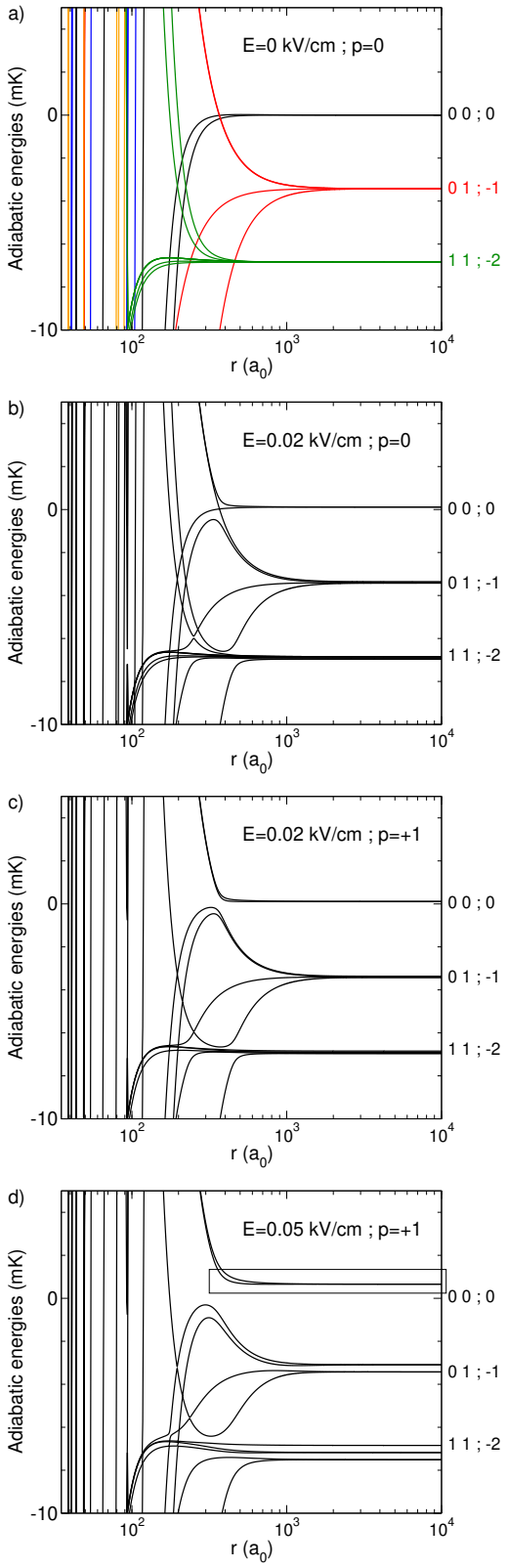

Figure 4.5: Same as Fig. 4.4. Panel a): $E = 0$ kV/cm and $p = 0$. Panel b): $E = 0.02$ kV/cm and $p = 0$. Panel c): $E = 0.02$ kV/cm and $p = +1$. Panel d): $E = 0.05$ kV/cm and $p = +1$. The content of the box in panel d) is shown in more details in Fig. 4.9.

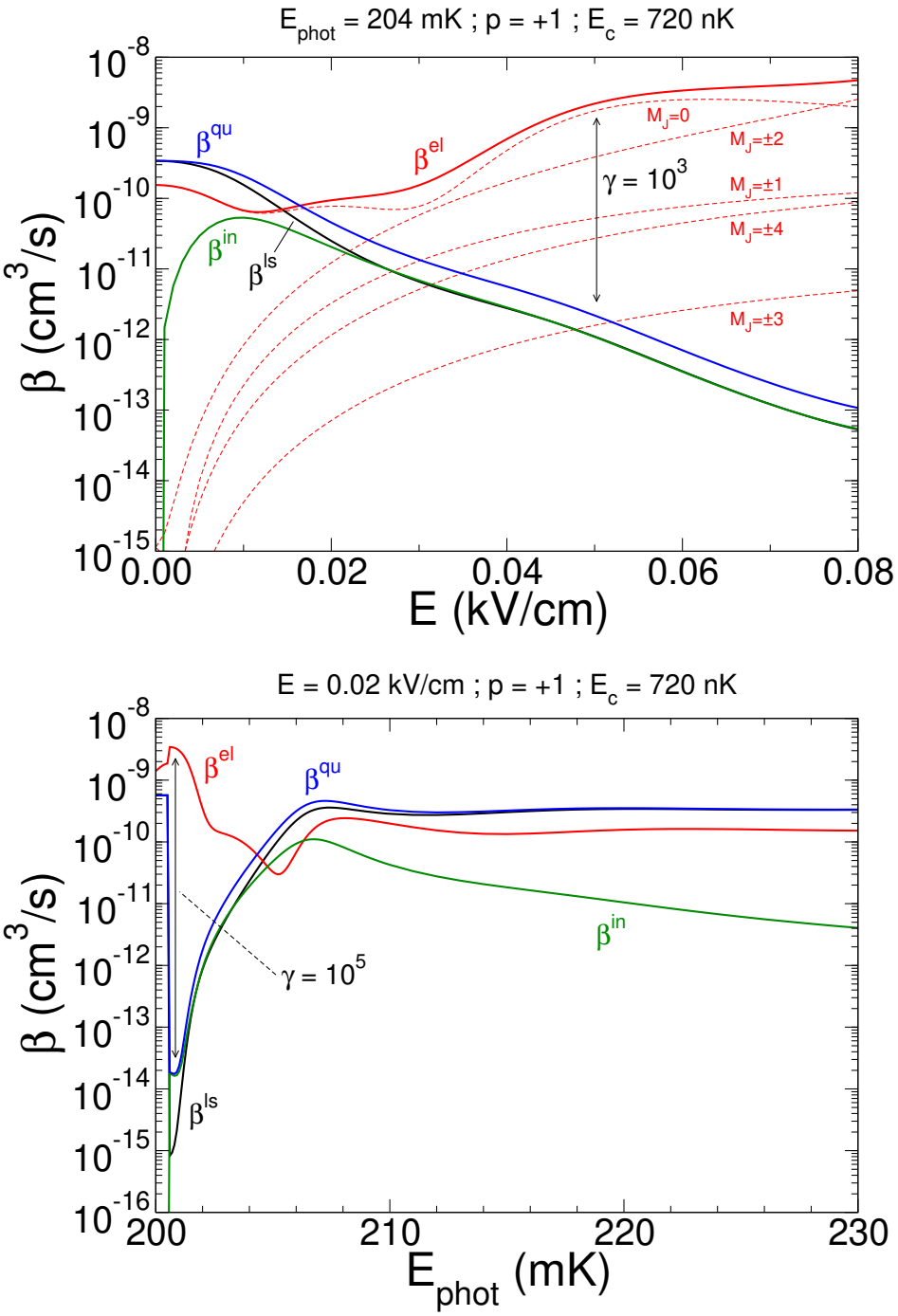

Figure 4.6: Rate coefficients for the bosonic ^{23}Na^{87}Rb + ^{23}Na^{87}Rb system for $p = +1$ and $E_{\rm k} = 720$ nK. Red curve: elastic process β^{el}, green curve: inelastic process β^{in}, black curve: loss process β^{ls}, blue curve: quenching process β^{qu} (inelastic + loss). The $M_J = 0, \pm1, \pm2, \pm3, \pm4$ components of the elastic process have also been shown as dashed lines. Top panel: as a function of E for $E_{phot} = 204$ mK. Bottom panel: as a function of E_{phot} for $E = 0.02$ kV/cm. The resonance energy is at $2\,B = 200.6$ mK.

When the electric is turned on, first the inelastic rate coefficient increases and then it decreases with E. As explained in section 4.3, when we increase the electric field, the energy gap between the channels increases. Therefore, the probability to go in a open channel which is moving away decreases.

Finally, for $E \geq 0.05\,\mathrm{kV\,cm^{-1}}$ a ratio $\gamma = \beta^{el}/\beta^{qu} \geq 10^3$ can be reached. This represents favorable conditions for evaporative cooling purpose. Note that at $E = 0$ kV/cm, the quenching rate coefficient tends to the value $\sim 3.4\ 10^{-10}$ cm^3/s, showing that we have calibrated well our short-range condition to the zero field experimental data. Note that for this range of microwave field intensity, the optical dipole trap remains deep enough to trap the molecules as shown in appendix A.2.

So far, we have studied the shielding mechanism for a fixed detuning. However, we believe that there is also an optimal value for the detuning, because the smaller the detuning, the closer will be the three states represented in Fig. 4.5 and the stronger the coupling between the states will be. This will affect the height of the potential barrier created and therefore the collision rate coefficients. In Fig. 4.6, we have plotted the collision rate coefficients as a function of the detuning for a fixed value of the microwave field $E = 0.02\,\mathrm{kV\,cm^{-1}}$. The transition $j = 0 \leftrightarrow j = 1$ is at $2\,B = 200.6$ mK. Therefore, when $E_{phot} < 200.6$ mK, we are in the case of a red detuned laser and no molecular states are below the incident ones. Our state will simply be pushed down by the states above and become even more attractive. This is why we observe that for this range of detuning, the elastic and quenching rate coefficients have similar values which is not interesting in term of shielding. When $E_{phot} > 200.6$ mK, we are in the case of a blue detuned laser and the effects of shielding start to appear in the collision rates. Indeed, we observe that the quenching rate coefficient drops drastically compared to the elastic ones when the field intensity increases. One can reach a ratio γ of 10^5 for the appropriate value of E_{phot}. When we move away from the crossing, one gets back to the normal situation where the photon is so off-resonance that the dressing has no effect on the molecules, and they collide as if they were no effect of the microwave field.

To produce molecular Bose-Einstein condensates, reaching temperatures in the Wigner regime is crucial. We have represented in Fig. 4.7 the evolution of the collision rate coefficient as a function of the collision energy E_k. We identify the Wigner regime area by looking to the laws of evolution of the different rate coefficients. Indeed, if we refer to the equations 3.5.26 and 3.5.27, the Wigner regime is characterized by inelastic collisions and loss rate coefficients which are independent of the collision energy whereas the elastic collision rate coefficients must be $\propto E_\mathrm{k}^{1/2}$. These behaviors are found in an area between $E_\mathrm{k} = 10^{-12} - 10^{-9}$ K which is represented by a blue box on the graph. Although shielding is very effective for NaRb molecules, if one wishes to study and use its dipolar properties in the ultracold range, very low temperatures must be reached.

4.3.2 Scattering length

We have seen that one can find values of E for which the quenching processes are suppressed, more exactly where the ratio γ gets large. This is an important value for the evaporative cooling process. However, another important quantity to control is the

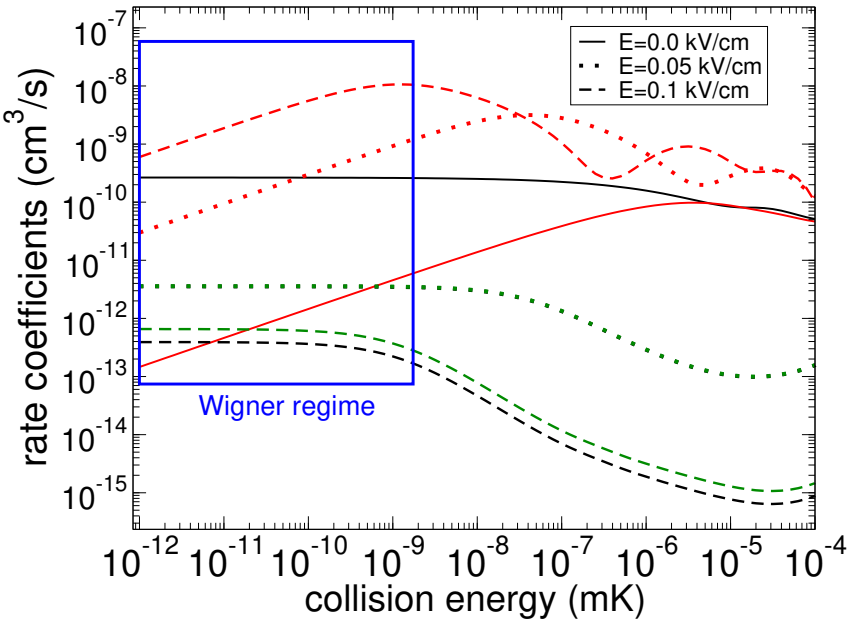

Figure 4.7: Rate coefficients for the bosonic ^{23}Na^{87}Rb + ^{23}Na^{87}Rb system for $p = +1$ in function of E_k for different value of the electric field E. Red curve: elastic process β^{el}, green curve: inelastic process β^{in}, black curve: loss process β^{ls}. The green and black dotted lines are superimposed. For $E = 0\,\mathrm{kV\,cm^{-1}}$, inelastic rate coefficients are 0 and are not represented here. The blue box represents the Wigner regime.

scattering length, more especially the real part of it, to form stable quantum degenerate gases such as Bose–Einstein condensates.

We have represented in Fig. 4.8, the evolution of the scattering length (real and imaginary part) as a function of the electric field for $E_\mathrm{k} = 10^{-12}\,\mathrm{K}$. As we can see on the insert, the imaginary part decreases with the electric field. As shown in Eq. 3.5.29, the imaginary part is only related to the quenching. The results are therefore in agreement with the behavior of the rate coefficients. However, we notice two resonance peaks in the real and imaginary part of the scattering length which were not transcribed in the collision rate coefficients calculated previously. By choosing properly the value of the electric field, we can control both the sign and the amplitude of the real part of the scattering length. The resonances are large enough to select a value of the scattering length allowing the formation of stable many-body gas.

Why do these resonance peaks appear?

The resonant features are explained by the apparition of a long-range, isolated shallow potential well in the entrance channel (indicated by a box in Fig. 4.5-d) when the intensity of the field is increased. The more intense the applied field, the deeper the well becomes. The resonances appear each time that the potential well can carry an additional bound states.

In Fig. 4.9, we zoomed in and plotted the long-range well for different values of E. For

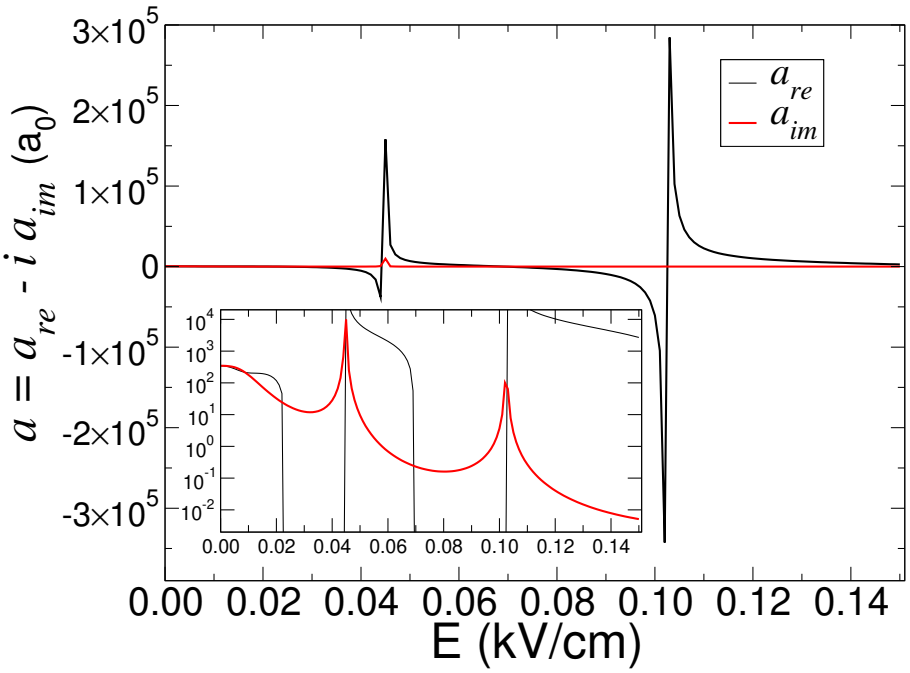

Figure 4.8: Scattering length as a function of E for the bosonic ^{23}Na^{87}Rb + ^{23}Na^{87}Rb system for $E_{phot} = 204\,\mathrm{mK}$ and $E_\mathrm{k} = 1\,\mathrm{pK}$. Black curve: real part, red curve: imaginary part.

$E < 0.02\,\mathrm{kV\,cm^{-1}}$, the shielding is not yet activated as the long-range potential barrier is not yet formed. For $E > 0.2\,\mathrm{kV\,cm^{-1}}$, we observe the presence of a small potential well whose depth increases with the field intensity. While the repulsive character comes from the electromagnetic wave dressing, the attractive character of the well at even more longer range comes from the unavoidable coupling between the $\tilde{l} = 0$ and higher $\tilde{l}$ curves of the same initial state. Indeed, the partial waves $\tilde{l} = 2$ and $\tilde{l} = 4$ are the only two channels above the partial wave $\tilde{l} = 0$ which can push it down.

We know that the scattering length depends on the position of the last bound state present in the potential well. It becomes large and positive ($a \to +\infty$) when the energy of the last bound state tends towards the dissociation limit. When the last bound state "comes out" of the potential and is lost, the scattering length becomes large and negative ($a \to -\infty$). Then, the resonances in Fig. 4.8 appear each time that the potential well can carry an additional bound states. To identify these bound states, I developed a numerical procedure based on the renormalized Numerov method [185]. As expected, for $E = 0.5\,\mathrm{kV\,cm^{-1}}$ (after the first peak) and $E = 0.15\,\mathrm{kV\,cm^{-1}}$ (after the second peak) the potential well contains respectively one and two bound states. These resonances are reminiscent of the so-called field-linked states [186, 187] in collisions of dipolar molecules in a static electric field.

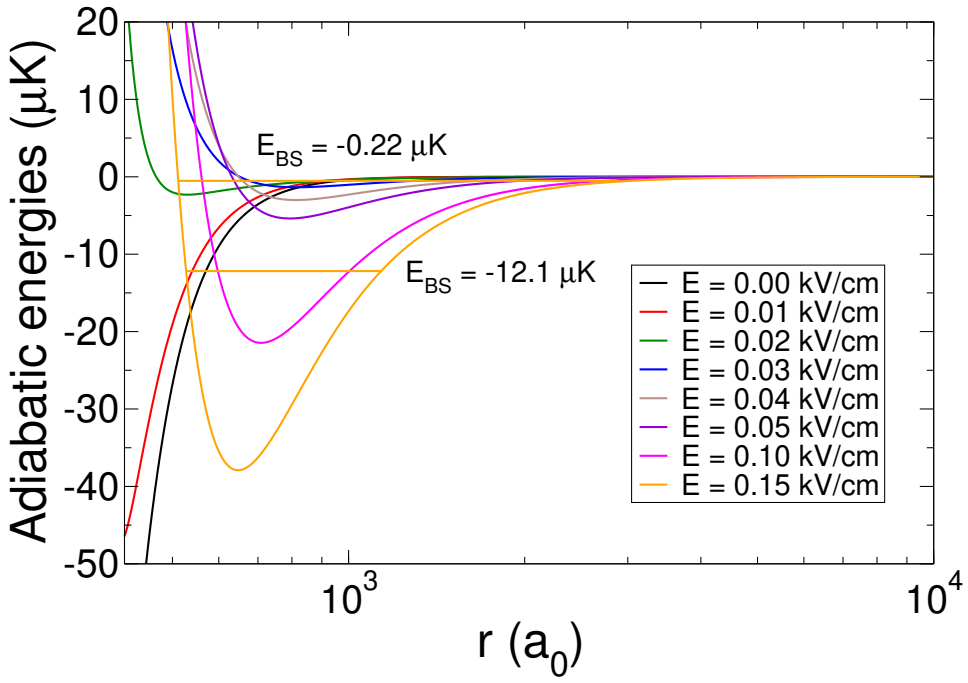

Figure 4.9: Depth of the long-range potentials inside the box of panel d) in Fig. 4.4, for different values of E. For $E = 0.15$ kV/cm (orange curve), the potential can carry two bound states at $E_{BS} = -12.1\,\mu$K and $E_{BS} = -0.22\,\mu$K.

4.4 Adimensional study

The aim of this part is to treat the microwave shielding through an adimensional approach. In a first part, we derive the parameters and equations that govern the dynamics of the system. In a second part, we present the results obtained and determine the molecules for which the shielding is effective. It is based on the formalism of [98] and adapted for collisions in presence of an electromagnetic field [103]. The transformation between atomic units and SI units are given in the caption of Table. A.1.

4.4.1 Quantum formalism

The shielding mechanism is based on the long-range dipole-dipole interaction. Its characteristic length [188] is given by:

$$s_{r_3} \equiv \frac{2\mu C_3}{\hbar^2} = \frac{2\mu}{\hbar^2}\frac{d^2}{4\pi\epsilon_0} = 2(\mu/\text{a.u.})(d/\text{a.u.})^2 \tag{4.4.1}$$

and the corresponding characteristic energy [188] is:

$$s_{E_3} \equiv \frac{\hbar^2}{2\mu s_{r_3}^2} = \frac{\hbar^6}{(2\mu)^3(d^2/4\pi\epsilon_0)^2} = [8(\mu/\text{a.u.})^3(d/\text{a.u.})^4]^{-1}. \tag{4.4.2}$$

Theses quantities scale up respectively as μ and μ^{-3}, then if the fictitious molecules are heavier, we expect the barrier appear at a longer distance and will be higher if their permanent dipole moment are similar. It is then possible to rescale the distance r and all the energies $\epsilon = \{E_{\rm tot}, \epsilon_{\tilde{\alpha}}, E_{\rm k}\}$ with respect to these characteristic quantities such as:

$$\tilde{r} = \frac{r}{s_{\rm r_3}} \qquad\qquad \tilde{\epsilon} = \frac{\epsilon}{s_{\rm E_3}}. \tag{4.4.3}$$

One can derive an adimensional set of coupled equations given by:

$$\sum_i \left[\left\{ -\frac{d^2}{d\tilde{r}^2} + \frac{l'(l'+1)}{\tilde{r}^2} + \tilde{\epsilon}_{\tilde{\alpha}} - \tilde{E}_{tot} \right\} \delta_{i,i'} + \left\{ \frac{\zeta_{i",i}(l", m_l", l', m_l'; E)}{\tilde{r}^3} \right\} \right] f_{i',i}^{\tilde{E}_{tot}}(\tilde{r}) = 0 \tag{4.4.4}$$

with $E_{\rm tot} = \varepsilon_{\tilde{\alpha}} + E_{\rm k}$ so that $\tilde{E}_{tot} = \tilde{\varepsilon}_{\tilde{\alpha}} + \tilde{E}_c$, then $\tilde{\varepsilon}_{\tilde{\alpha}'} - \tilde{E}_{tot} = (\tilde{\varepsilon}_{\tilde{\alpha}'} - \tilde{\varepsilon}_{\tilde{\alpha}}) - \tilde{E}_c$. By multiplying and dividing $(\tilde{\varepsilon}_{\tilde{\alpha}'} - \tilde{\varepsilon}_{\tilde{\alpha}})$ by B, one gets $((\varepsilon_{\tilde{\alpha}'} - \varepsilon_{\tilde{\alpha}})/B) \times (B/s_{E_3})$, then we obtain:

$$\sum_{i'} \left[\left\{ -\frac{d^2}{d\tilde{r}^2} + \frac{l'(l'+1)}{\tilde{r}^2} + \left(\frac{\varepsilon_{\tilde{\alpha}'} - \varepsilon_{\tilde{\alpha}}}{B} \right) \tilde{B} - \tilde{E}_c \right\} \delta_{i',i''} + \left\{ \frac{\zeta_{i'',i'}(l'', m_l'', l', m_l'\,; \tilde{E})}{\tilde{r}^3} \right\} \right] f_{i',i}^{\tilde{E}_{tot}}(\tilde{r}) = 0. \tag{4.4.5}$$

From the equation above, we can extract four key parameters. The first parameter is a rescaled rotational constant $\tilde{B}$ and is simply expressed as a function of the rotational constant, the electric dipole moment and the reduced mass of the system:

$$\tilde{B} = \frac{B}{s_{\rm E_3}} = \frac{8B\mu^3}{\hbar^6} \left(\frac{d^2}{4\pi\epsilon_0} \right)^2 = 8(B/\text{a.u.})(\mu/\text{a.u.})^3(d/\text{a.u.})^4. \tag{4.4.6}$$

In short, this quantity contains all the information necessary to describe a molecule. Another parameter is:

$$\frac{\varepsilon_{\tilde{\alpha}'} - \varepsilon_{\tilde{\alpha}}}{B}. \tag{4.4.7}$$

It represents the difference between the energy $\varepsilon_{\tilde{\alpha}'}$ of a molecular state $|\tilde{\alpha}'\rangle$ dressed by the quantized field and the energy $\varepsilon_{\tilde{\alpha}}$ of the initial one $|\tilde{\alpha}\rangle$, rescaled by the rotational constant. We introduced B in this parameter because the rescaled energies $\varepsilon_{\tilde{\alpha}}/B$ are obtained directly by dividing Eq. 4.2.19 by the rotational constant B on both sides:

$$\frac{\hat{h}}{B} = \frac{\hat{h}_{\rm rot_1} + \hat{h}_{\rm rot_2} + \hat{h}^p_{m_1.f} + \hat{h}^p_{m_2.f} + \hat{h}_f}{B}. \tag{4.4.8}$$

As the result, the two first Hamiltonians are independent of B. The molecule-field interactions $\hat{h}^p_{m_1.f} + \hat{h}^p_{m_2.f}$ give terms in $\hbar\Omega/B = dE/B$. Therefore, the rescaled energies

$\varepsilon_{\tilde{\alpha}}/B$ are implicit functions of $dE/B \equiv \tilde{E}$. Or equivalently, in term of the rescaled Rabi Frequency:

$$\tilde{\Omega} = \frac{\Omega}{B/\hbar} = \frac{dE}{B} \equiv \tilde{E} \tag{4.4.9}$$

which becomes the second parameter and identifies with the rescaled electric field. Finally, the quantized field hamiltonian $\hat{h}_f$ gives terms in $\hbar\omega/B = E_{phot}/B$. Then, the rescaled energies are also implicit functions of $E_{phot}/B \equiv \tilde{E}_{phot}$. Equivalently, they are functions of a rescaled detuning (relative to the $j = 0 \leftrightarrow j = 1$ transition):

$$\tilde{\Delta} = \frac{\Delta}{B} = \frac{E_{phot} - 2\,B}{B} = \tilde{E}_{phot} - 2 \tag{4.4.10}$$

which becomes the third parameter. In the following, we fix this third parameter to an arbitrary positive constant of $\tilde{\Delta} = 0.034$ (blue-detuned). We choose the values of $\tilde{\Delta}$ and $\tilde{\Omega}$ appropriately so that the blue-detuned microwave radiation does not lead to an anti-trapping effect of the molecules, see Appendix A.2. Finally, the fourth parameter is the rescaled collision energy:

$$\tilde{E}_c = \frac{E_\mathrm{k}}{s_{E_3}}. \tag{4.4.11}$$

4.4.2 Adding the electronic van der Waals interaction

As seen in the previous chapter, we must include the attractive van der Waal interaction in our calculations. In contrast to the dipole-dipole interaction, this interaction is $\propto r^{-6}$. Its characteristic length [188] is given by:

$$s_{r_6} = \left(\frac{2\mu C_6^{el}}{\hbar^2}\right)^{\frac{1}{4}} \neq s_{r_3}. \tag{4.4.12}$$

As a result, if we try to rescale $\hat{V}^{el}$, we cannot express it only in function of the previously defined adimensional quantities because the reduced mass and the dipole moment remain. Therefore, we cannot end up in general with a strictly adimensional study, i.e. without dependence on molecular parameters. Neglecting the electronic van der Waals term is also not possible given that in some cases the geometrical factor $\zeta_{i,i'}$ vanishes in the diagonal element of $\langle i|V_{dd}|i'\rangle$, such as for an incoming and outgoing s-wave $l = l' = 0$. As a consequence, instead of having an attractive s-wave in our adiabatic energy curves, we would have a curve equal to 0 for any value of r. However, the electronic van der Waals interactions play a negligible role for a lot a systems [98]. Roughly, this is valid for molecules for which:

$$C_6^{rot} \gg C_6^{el}. \tag{4.4.13}$$

This is why we solved the dimensional coupled equations for a fixed fictitious electronic coefficient $C_6^{el} \neq 0$ chosen in the same order or magnitude as for the molecules studied (Cf. section 4.5). Then, we appropriately come back to adimensional rescaled quantities. It turns out that for the sytems for which the shielding is efficient, this is a good approximation.

4.4.3 Adimensional observables

We consider the Bethe–Wigner regime as $E_\mathrm{k} \to 0$ and where the scattering length is independent of the collision energy. We can express the adimensional scattering length as [98]:

$$\tilde{a} = \tilde{a}_\mathrm{re} - i\,\tilde{a}_\mathrm{im} = \frac{\tilde{a}}{s_{\mathrm{r}_3}}. \tag{4.4.14}$$

It is then possible to reconstruct the cross sections and collision rate coefficients via the relations:

$$\tilde{\sigma}_\mathrm{el} = |\tilde{a}|^2\kappa, \qquad \tilde{\sigma}_\mathrm{qu} = \frac{\tilde{a}_\mathrm{im}}{\tilde{k}}\kappa, \tag{4.4.15}$$

$$\tilde{\beta}_\mathrm{el} = \tilde{k}|\tilde{a}|^2\kappa, \qquad \tilde{\beta}_\mathrm{qu} = \tilde{a}_\mathrm{im}\kappa, \tag{4.4.16}$$

with $\tilde{k} = \sqrt{E_\mathrm{k}/s_{\mathrm{E}_3}}$ and κ the coefficient related to the indiscernibility of the molecules.

Finally, it is possible to express the ratio γ of the elastic collision rate coefficient to the total loss rate coefficient via:

$$\gamma = \frac{\beta^\mathrm{el}}{\beta^{qu}} = \frac{|\tilde{a}|^2}{\tilde{a}_\mathrm{im}}\tilde{k}. \tag{4.4.17}$$

4.5 Numerical results

In the next two sections, we consider molecules initially prepared in their ground rotational state $|0,0,0,0\rangle_+|0\rangle$. Only the symmetric states $\eta = +1$ exist for same, indistinguishable states and are coupled to other symmetric states. To get converged results, we use $j_\tau = 0, 1$, $n = 0, \pm1, \pm2$, $l = 0, 2, 4$ and $M_J = 0$. We will solve the dimensional equations for a fictitious molecule $(XY)^*$ for which we fix the rotational constant $B^* = 10^{-7}$ a.u. (~ 0.022 cm^{-1}) and electric dipole moment $d^* = 1$ a.u. (~ 2.54 Debye) while the mass μ^* is varied. In this way, the parameter $\tilde{B} = 8(B^*/\text{a.u.})(\mu^*/\text{a.u.})^3(d^*/\text{a.u.})^4$ in Eq. 4.4.6 only varies with μ^*. Fixing B^* and d^* is also convenient for varying the rescaled field $\tilde{E} = d^*E/B^*$, since it is sufficient to vary the electric field E only. We consider the scattering properties at collision energies $E_c^* = 100$ nK so that the third parameter $\tilde{E}_c$ is fixed. We used $r_{min} = 5\,a_0$ and r_{max} is chosen so that $k^*\,r^*_{max} \sim 5$. As the mass μ^* is changed here to vary the parameter $\tilde{B}$, k^* changes accordingly, and so does r^*_{max}. Most of the systems investigated in experiments are diatomic dipolar molecules of alkali atoms for which the electronic C_6^{el} coefficients belongs to the range $3000 \leq C_6^{el} \leq 20000$ a.u [189, 190, 183, 191]. In this study we use a fixed value of $C_6^{el,*} = 10000$ a.u. between two molecules $(XY)^*$.

4.5.1 Ratio γ

In Fig. 4.10, we present the quantity $|\tilde{a}|^2/\tilde{a}_\mathrm{im}$ which represents the ratio γ when $\tilde{k} = 1$, that is at a typical collision energy of $E_\mathrm{k} = E_3$. To get the ratio at $E_\mathrm{k} > E_3$, one has to multiply this quantity by $\tilde{k}$. For evaporative cooling techniques, γ has to reach a factor of 10^3 or more for the process to be highly efficient. Therefore, the regions of the graph in yellow, orange and red correspond to favorable conditions for evaporative cooling.

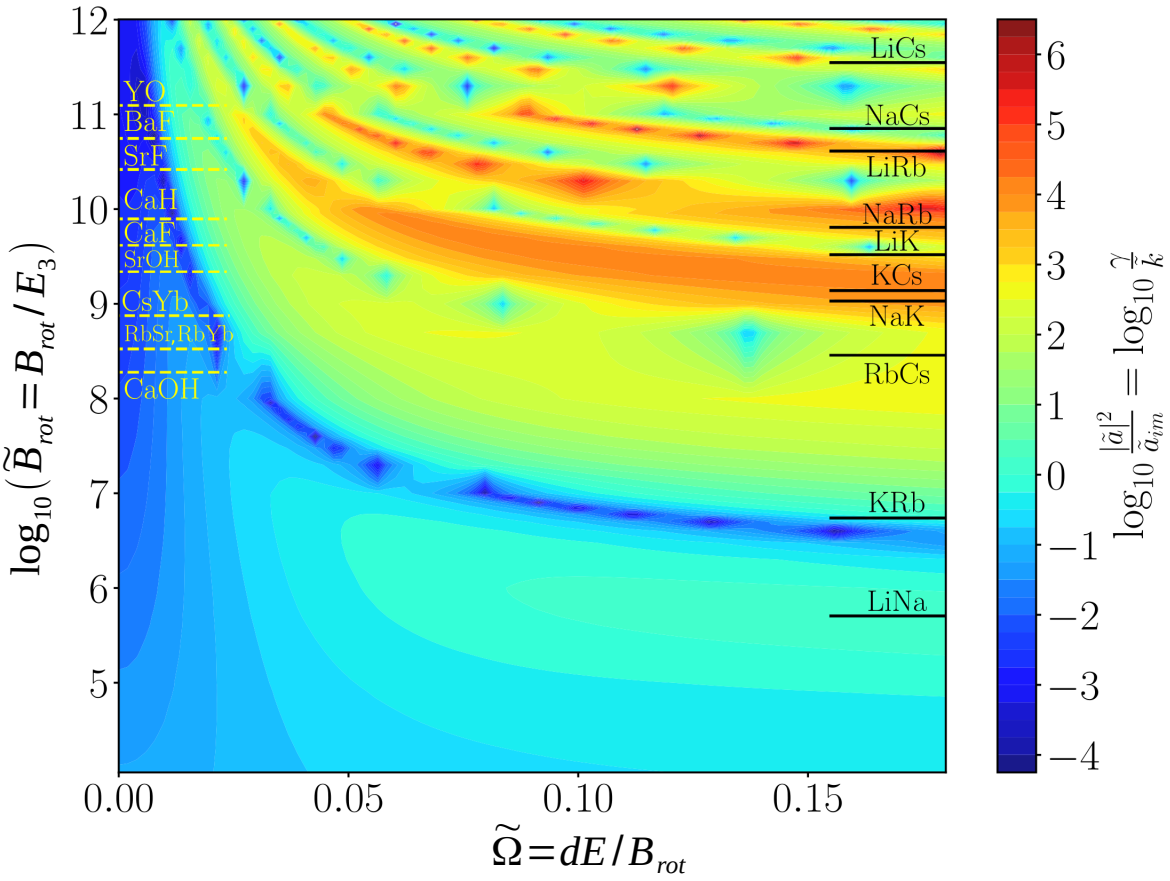

Figure 4.10: $|\tilde{a}|^2/\tilde{a}_{\rm im} \equiv \gamma/\tilde{k}$ as a function of $\tilde{B}$ and $\tilde{\Omega}$ for a constant rescaled detuning of $\tilde{\Delta} = 0.034$. The color scale, presented at the right of the picture, goes from 10^{-4} to 10^{6}. The $\tilde{B}$ values of some characteristic dipolar molecules are reported on the figure. Edited from [103].

The regions in green and blue correspond to unfavorable conditions. The rescaled Rabi frequency is plotted in abscissa and represents the amount of the field applied. The rescaled rotational constant is plotted in ordinate and uniquely characterizes a molecule, see table A.1 in appendix A.4. The values of the dipolar alkali molecules have been reported. For indication, we also report values for $^2\Sigma^+$ molecules of experimental interest [192, 193, 194, 195, 196, 197, 198, 199, 200, 201, 202, 203, 204]. Looking at the general feature of the figure, one can distinguish two main regions for the dipolar molecules: a region for which $\tilde{B} > 10^8$ where the ratio can globally reach 10^3 or more, and a region for which $\tilde{B} < 10^7$ where the ratio barely reach 10^2. The former region includes the molecules RbCs, NaK, KCs, LiK, NaRb, LiRb, NaCs, LiCs and determines the good candidates for the microwave shielding. The latter region includes the molecules KRb and LiNa for which the microwave shielding will be not efficient for the present range of $\tilde{\Omega}$. This is due to an unfortunate combination of μ, d and B yielding a too low value of $\tilde{B}$.

These previous results are in agreement with the ones given for NaRb molecules in the previous section. To be convinced of this, we have represented in Fig. 4.11-a the rescaled adiabatic energy curves as a function of the rescaled distance $\tilde{r}$ between the molecules, for $\tilde{B} = 10^{10}$ and $\tilde{\Omega} = 0.18$. We find the strong repulsive curves arising in the initial entrance channel $\{|0\,0, 0\,0\rangle_+ |0\rangle\}$ (indicated by an arrow) which prevents the molecules to come close to each other and being lost at short-range. This explains the decrease of the quenching rate coefficients and the increase of the ratio γ.

Let's note that the hyperfine structure of the $^1\Sigma$ molecules and that the fine and hyperfine structure of the $^2\Sigma$ molecules have not been included in our calculations. Indeed, it is not possible to consider them while keeping an adimentional study approach. However, neglecting the fine or hyperfine structure of the molecules is a good assumption as far as the electronic and the nuclear spins act as spectators, or in other words when they are decoupled enough from the rotational structure. This can be done applying a magnetic field as explained in appendix A.3.

4.5.2 Scattering length

In Fig. 4.12-a, we plot $\tilde{a}_{\text{re}}$ and $\tilde{a}_{\text{im}}$ as a function of $\tilde{\Omega}$ for a value $\tilde{B} = 10^{10}$ ($\sim$NaRb). There are values of $\tilde{\Omega}$, hence of the field, for which the real part $\tilde{a}_{\text{re}}$ can take large positive and negative values while the imaginary part $\tilde{a}_{\text{im}}$ remains low. Then, the elastic cross sections which are proportional to $\tilde{a}_{\text{re}}$ (see Eq. 3.5.28 and Eq. 3.5.29 in chapter 3) if $a_{\text{im}} \to 0$ can be tuned to any desired values up to the maximal value given by the unitarity limit $2 \times \pi/k^2$ for indistinguishable molecules. The imaginary part globally decreases when $\tilde{\Omega}$ increases, confirming that the quenching rate coefficients, which are proportional to $\tilde{a}_{\text{im}}$, also decreases. The resonant features are explained by the apparition of a long-range, isolated shallow potential well in the entrance channel when $\tilde{\Omega}$ is increased. This is illustrated in Fig. 4.11-b which is a close-up of the lowest entrance channel of Fig. 4.11-a. At $\tilde{\Omega} = 0.18$ (black curve), the well can support three bound states shown on the figure. If $\tilde{\Omega}$ is decreased, the depth of the well also decreases and those bound states can disappear. For example down at $\tilde{\Omega} = 0.08$ (red curve), the well supports now only two bound states

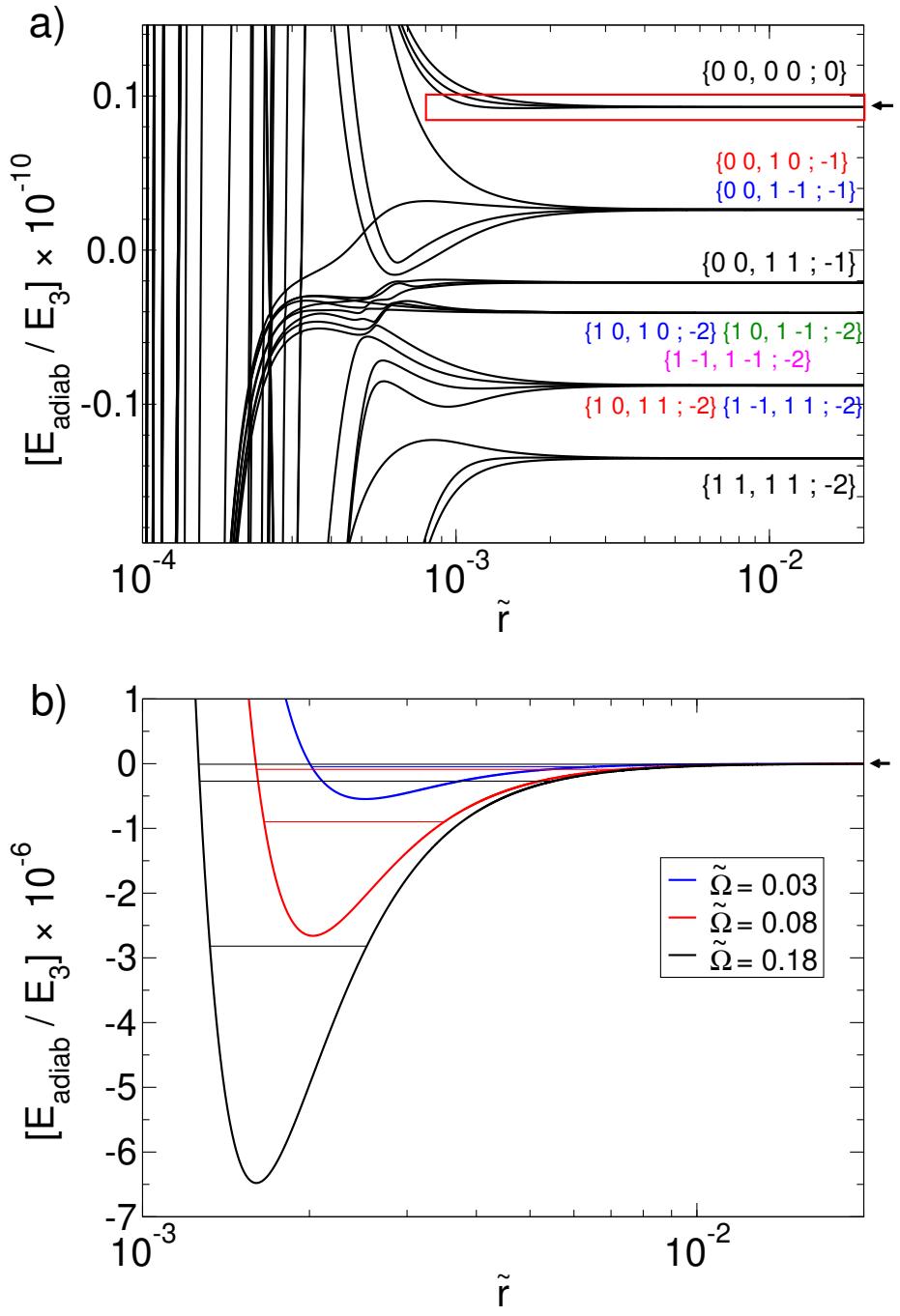

Figure 4.11: Left panel: Long-range rescaled adiabatic energies as a function of the rescaled distance between the molecules for $\tilde{B} = 10^{10}$, $\tilde{\Omega} = 0.18$, and σ^+ circularly polarized field $p = +1$. The region in the red box is shown in the right panel. The notation $\{j_1\, m_{j_1}, j_2\, m_{j_2}; n\}$ is used to represent the asymptotic dressed states with $\eta = +1$. The labels in black (resp. red, blue, green, magenta) corresponds to values of $m_{1+2+f} = m_{j_1} + m_{j_2} + n \times p = 0$ (resp. -1, -2, -3, -4). Right panel: Close-up of the long-range potential well in the lowest entrance channel for $\tilde{B} = 10^{10}$ and $\tilde{\Omega} = 0.18$ (black), $\tilde{\Omega} = 0.08$ (red), $\tilde{\Omega} = 0.03$ (blue) together with the corresponding bound states energies they can support. Edited from [103].

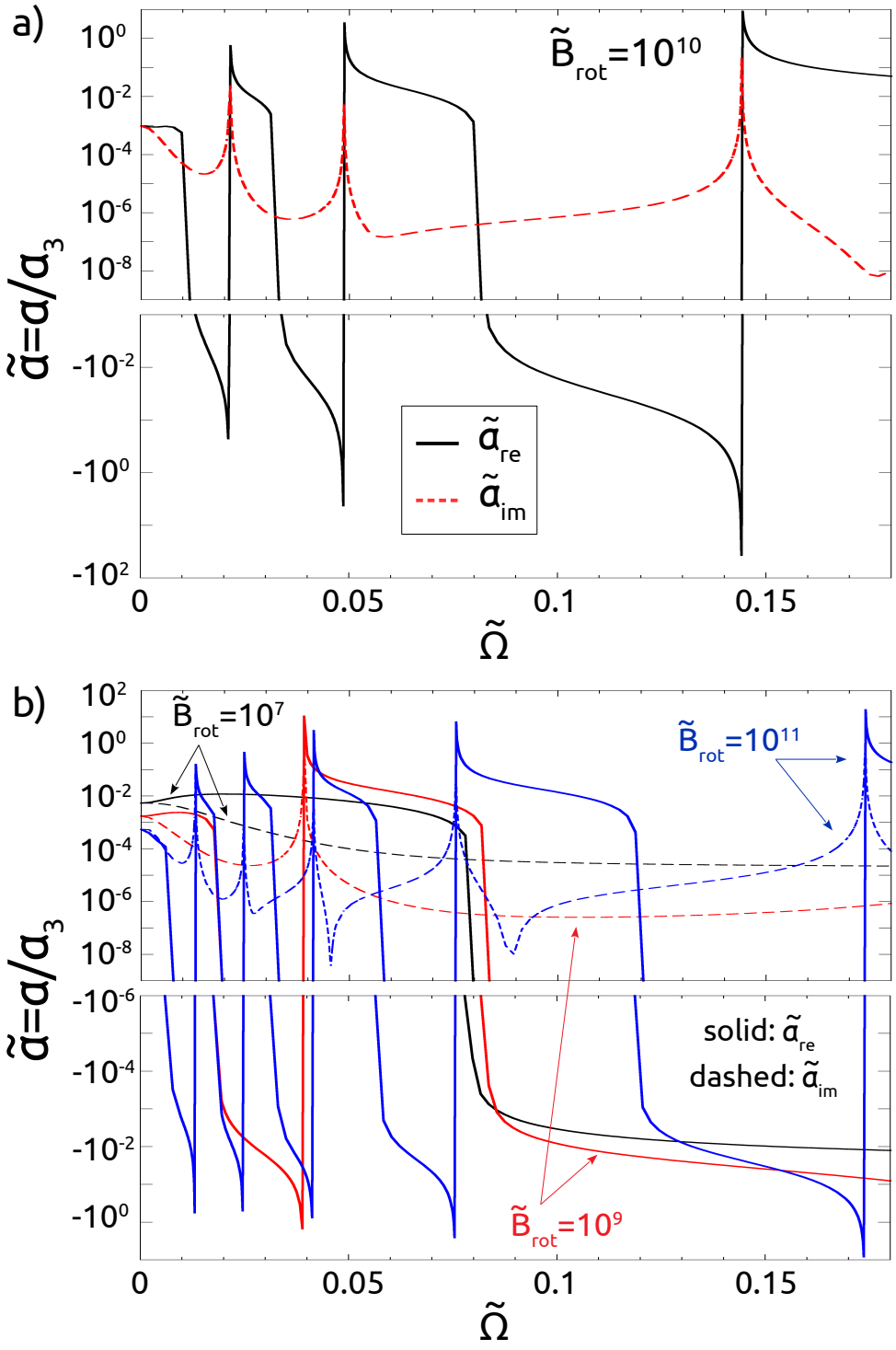

Figure 4.12: Top panel: Rescaled scattering length $\tilde{a}$ as a function of $\tilde{\Omega}$ for $\tilde{B} = 10^{10}$ ($\sim$NaRb). Bottom panel: Same for $\tilde{B} = 10^{7}$ ($\sim$KRb), $\tilde{B} = 10^{9}$ ($\sim$NaK, KCs), $\tilde{B} = 10^{11}$ ($\sim$NaCs). Edited from [103].

and at $\tilde{\Omega} = 0.03$ (blue curve), it supports only one. When the bound states are localized at the zero energy threshold, typically for values of $\tilde{\Omega}$ slightly below 0.18, 0.08, 0.03, $\tilde{a}_{\rm re}$ turns from a large and positive value to a large and negative value, as seen in Fig. 4.12-a.

We present in Fig. 4.12-b the trend of the scattering length for increasing values of $\tilde{B} = 10^7, 10^9, 10^{11}$. For a small value of $\tilde{B} = 10^7$ ($\sim$ KRb, black curves), one cannot see any resonant features of $\tilde{a}$ for the present range of $\tilde{\Omega}$. When $\tilde{B}$ is increased, typically for $\tilde{B} \geq 10^8$, the long-range wells are deep enough to support bound states, and resonant features appear in the scattering length as in Fig. 4.12-a. This is shown for $\tilde{B} = 10^9$ ($\sim$ NaK, KCs, red curves) and $\tilde{B} = 10^{11}$ ($\sim$ NaCs, blue curves). These long-range bound states are actually reminiscent of the field-linked states [186, 187] in collisions of dipolar molecules in a static electric field as I mentioned above. The presence of these microwave field-linked states in the long-range wells, when the condition $\tilde{B} \geq 10^8$ is satisfied, is therefore responsible for the control of the scattering length of dipolar molecules.

In contrast to the static electric field shielding method that we will introduce in the next chapter, this method provides two tools to control both the real part of the scattering length (i.e. the stability of the Bose-Einstein condensate) and its imaginary part (i.e. the short-range losses). The detuning can be used to bring the states into resonance, and thus control the shielding process, while the field intensity can be used to increase the depth of the potential well, and thus control the real part of the scattering length.

For that purpose, we have used recently the NaRb molecule as an example (especially Fig. 4.8). Applying in addition a static electric field, we can control both the real and imaginary part of the scattering length as well as the dipolar length. This is very important when the density increases for many-body physics and new states of matter (quantum droplets, super-solid states). We are currently preparing a draft on that [205].

Chapter 5

Simplified static electric field shielding

In the presence of a static electric field, dipolar molecules orient themselves along the applied electric field. Therefore, their dipole moments in the laboratory-fixed frame are no longer zero and can be controlled varying the strength of the applied electric field. Through the control of these so-called *induced dipole moments*, one can control the long-range dipole-dipole interaction and by extension short-range losses. This method was proposed initially in 2006 [96] for non-lossy molecules, using a non-absorbing repulsive hard wall at short-range. It has been extended to lossy molecules in 2015 [97] and generalized in 2017 [98] using an adimensional approach similar to that developed in chapter 4. Recently, static electric field shielding has been observed experimentally in a quasi two-dimensional geometry [206] and then in a three-dimensional molecular quantum gas of KRb molecules [100]. One of my goals is to extend this shielding method to three-body collisions. However, the complete quantum calculations require a large number of rotational levels and partial waves which are numerically too cumbersome when switching to three-body collisions.

In this chapter, we will start with a brief summary of the results already obtained for the static electric field shielding. Then, we will simplify the existing model by extracting the essential physics while preserving a moderate and exploitable numerical effort. We will present the different simplifications used and we will compare them to the complete quantum calculations.

To illustrate our point, we will consider KRb molecules prepared in their ground electronic $X^1\Sigma^+$ and vibrational $v = 0$ states.

5.1 Complete quantum calculation and formalism

In this section, we will describe the main lines of the two-body shielding using a static electric field: we will make the link between the formalism presented in the last two chapters and the one used here, then we will report the main results obtained in the last years with this method while identifying its drawbacks.

5.1.1 Theoretical formalism

The collision formalism used is broadly the same as the one used in the chapter 4. The electric field is treated in a semi-classical way and is no longer quantified (i.e. we drop the $|n\rangle$ states). As a result, the collision channels are given by:

$$|i\rangle \equiv |\tilde{j}_1, m_{j_1}, \tilde{j}_2, m_{j_2}\,; \eta\rangle\, |l, m_l\rangle\,. \tag{5.1.1}$$

As in the microwave shielding case, the tildes correspond to a certain admixture of different rotational quantum numbers due to the interaction of the molecules with the electric field. This interaction is described by the stark effect $V_S = -\vec{d}.\vec{E}$ whose matrix elements are given by:

$$\begin{aligned}\langle j_\tau, m_{j_\tau}|\, V_S \left|j'_\tau, m'_{j_\tau}\right\rangle = -dE\, \delta_{m_{j_\tau}, m'_{j_\tau}} (-1)^{m_{j_\tau}} \sqrt{2j_\tau + 1}\sqrt{2j'_\tau + 1} \\ \times \begin{pmatrix} j_\tau & 1 & j'_\tau \\ 0 & 0 & 0 \end{pmatrix} \begin{pmatrix} j_\tau & 1 & j'_\tau \\ -m_{j_\tau} & 0 & m'_{j_\tau} \end{pmatrix}.\end{aligned} \tag{5.1.2}$$

In this study, the total Hamiltonian (Eq. 4.2.25) is given by:

$$\hat{H} = \hat{T} + \hat{V} + \hat{h}_{\mathrm{rot}_1} + \hat{h}_{\mathrm{rot}_2} + V_S \tag{5.1.3}$$

where $\hat{T}$, $\hat{V}$, $\hat{h}_{\mathrm{rot}_1}$ and $\hat{h}_{\mathrm{rot}_2}$ have already be defined in the previous chapters. The set of coupled equations obtained is very similar to the one given in Eq. 4.3.2 and are solved using the short-range loss condition given in Eq. 3.5.11 and by propagating the Z-matrix.

To understand the next results, it is useful to define the induced dipole moment along the electric field direction in the laboratory-fixed frame:

$$d_{\mathrm{ind}}(E_0) = \left\langle \tilde{j}_\tau, m_{j_\tau}\right| \vec{d}.\hat{z} \left|\tilde{j}'_\tau, m'_{j_\tau}\right\rangle\Big|_{E_0} = -\frac{d\epsilon_{\tilde{\alpha}_\tau}}{dE}\bigg|_{E_0}. \tag{5.1.4}$$

This represents the mean value of the projection of the permanent dipole moment on the axis of quantification $\hat{z}$ between the dressed state $\left|\tilde{j}_\tau, m_{j_\tau}\right\rangle$ at a given electric field E_0. The larger its value, the more the dipole is oriented along the electric field. If the dipole moment is positive then the dipole is oriented in the same direction as the electric field and oppositely if its sign is negative. Note that this quantity is equal to to the opposite of the derivative of the energy with the electric field at E_0. This equality is known as the Hellmann-Feynman theorem [207, 208].

To be consistent with the article [97], we use the experimental values of the rotational constant $B = 1.113\,950\,\mathrm{GHz}$ from Ospelkaus *et al.* for the fermionic $^{40}\mathrm{K}^{87}\mathrm{Rb}$ molecules and $B = 1.095\,362\,\mathrm{GHz}$ from Aikawa *et al.* for the bosonic $^{41}\mathrm{K}^{87}\mathrm{Rb}$ molecules. We use the experimental value of the dipole moment $d = 0.574\,\mathrm{D}$ [209] and the theoretical van der Waals coefficient $C_6^{el} = 12636$ a.u [183].

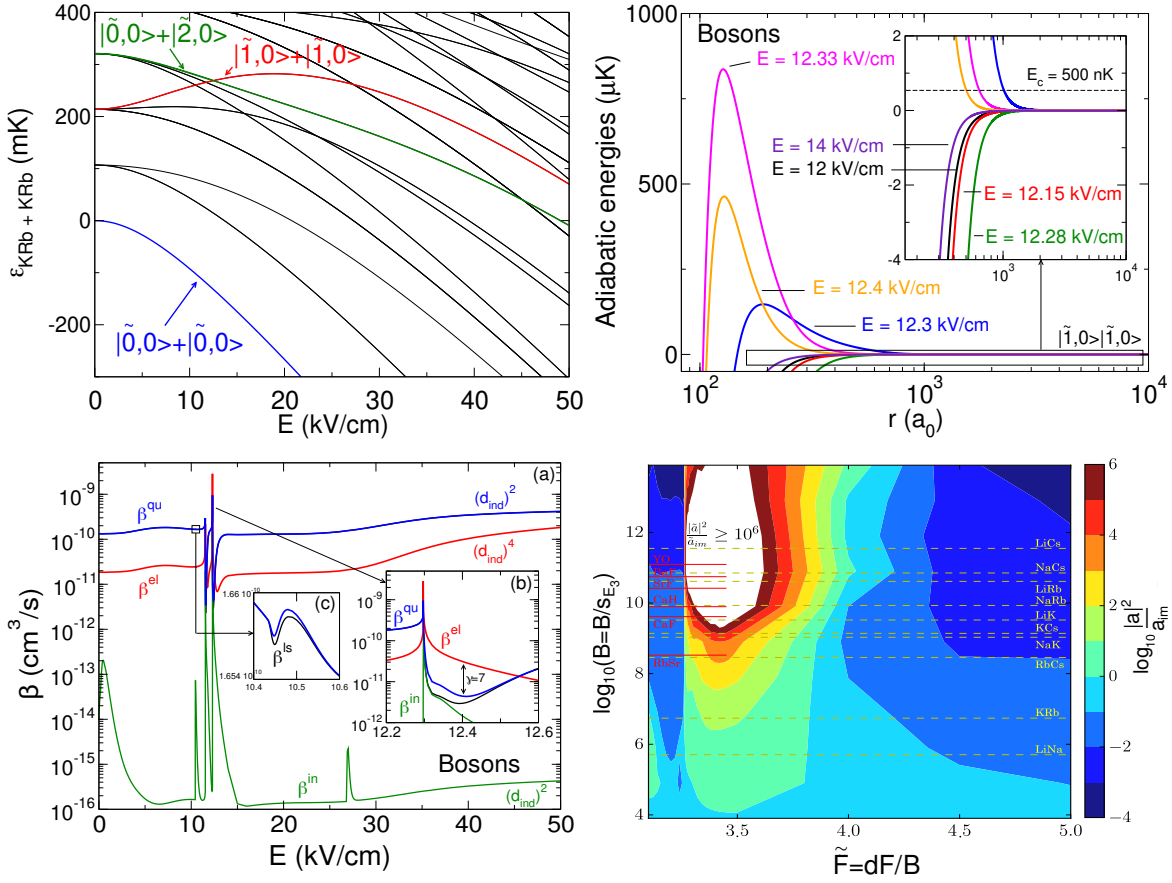

Figure 5.1: The figures have been taken from [97, 98]. (top-left) Energy of ^{41}K^{87}Rb+^{41}K^{87}Rb as a function of the electric field. (top-right) Lowest incident channel taken from the adiabatic energies for the initial colliding state $\left|\tilde{1},0\right\rangle + \left|\tilde{1},0\right\rangle$ at various electric fields (relative to the initial threshold energy) for bosonic collisions. (bottom-left) Rate coefficient for the inital colliding state $\left|\tilde{1},0\right\rangle + \left|\tilde{1},0\right\rangle$ at various electric field. The collision energy if fixed at $E_{\mathrm{k}} = 500\,\mathrm{nK}$ (bottom-right) $|\tilde{a}|^2/a_{im} = \gamma/\tilde{k}$ as a function of $\tilde{B}$ and $\tilde{F}$. The white area corresponds to values $\gamma > 10^6$.

5.1.2 Physical principle and results

As seen in chapter 4, three conditions must be met to achieve an effective shielding. Firstly, we must be able to put two molecular states in quasi-resonance using an external field. Secondly, the coupling elements of the dipole-dipole interaction between the two molecular states must be large enough to create a long-range barrier. Thirdly, we have to check that the inelastic collisions do not become too large compared to the elastic ones.

The first condition can be investigated by looking at Fig. 5.1 (top-left panel). We represented the Stark effect on the asymptotic bosonic molecular states. In contrast to the microwave shielding case, the state $\left|\tilde{0},0\right\rangle + \left|\tilde{0},0\right\rangle$ doesn't cross any other state. As a result, it cannot be used as the incident channel. On the other hand, the states $\left|\tilde{1},0\right\rangle + \left|\tilde{1},0\right\rangle$ cross three states: $\left|\tilde{0},0\right\rangle + \left|\tilde{2},\pm2\right\rangle$, $\left|\tilde{0},0\right\rangle + \left|\tilde{2},\pm1\right\rangle$ and $\left|\tilde{2},0\right\rangle + \left|\tilde{1},0\right\rangle$ at respectively

$E_1^* \sim 10.5\,\mathrm{kV\,cm^{-1}}$, $E_2^* \sim 11.5\,\mathrm{kV\,cm^{-1}}$ and $E_3^* \sim 12.3\,\mathrm{kV\,cm^{-1}}$ for bosons. A similar behaviour is obtained for fermions but for $E_1^* \sim 10.6\,\mathrm{kV\,cm^{-1}}$, $E_2^* \sim 11.7\,\mathrm{kV\,cm^{-1}}$ and $E_3^* \sim 12.5\,\mathrm{kV\,cm^{-1}}$. The first condition is then fulfilled with $\left|\tilde{1},0\right\rangle + \left|\tilde{1},0\right\rangle$ as incident channel because it can be brought into resonance with other states for reasonable electric field values.

The second condition can be checked by looking at the adiabatic energy curves. On Fig. 5.1 (top-right panel), the $\tilde{l} = 0$ partial wave of the incident channel for different values of the electric field $E \sim E_3^*$ is plotted. When the electric field is higher than E_3^*, the adiabatic energy curves become fully repulsive. This means that the dipole-dipole interaction is sufficiently strong compared to the attractive van der Waals term. By varying the value of the applied electric field, we can control the height of the barrier and by extension the collision rate coefficients. As the barriers ($\sim 800\,\mu\mathrm{K}$) involved are much higher than the typical collision energy $E_\mathrm{k} = 500\,\mathrm{nK}$, we expect the short-range losses to be strongly reduced but the propagation and the extraction of the different rate coefficients must be performed.

In Fig. 5.1 (bottom-left), we can observe three different peaks in the elastic, inelastic and loss rate coefficients by varying the electric field. The first one at $E \sim E_1^*$ result from the crossing between the incident channel and the state $\left|\tilde{0},0\right\rangle + \left|\tilde{2},\pm 2\right\rangle$. The impact of the resonance on the different rate coefficients is weak because there is no direct coupling between the two states. The next two peaks are obtained at E_2^* and E_3^* as expected. It was shown that it is possible to get a maximum ratio of elastic over quenching rate coefficients $\gamma = \frac{\beta^{el}}{\beta^{qu}} = 7$ at $E = 12.4\,\mathrm{kV\,cm^{-1}}$ for $^{41}\mathrm{K}^{87}$ Rb collisions (Bosons) and $\gamma = 20$ at $E = 12.65\,\mathrm{kV\,cm^{-1}}$ for $^{40}\mathrm{K}^{87}\mathrm{Rb}$ collisions (Fermions). For these optimal values of the electric field, we can see that the quenching rate coefficient is quasi equal to the loss rate coefficient. As a result, we can easily neglect inelastic collisions for these values of electric field. However, this is no longer the case closer to the resonance where inelastic collisions are dominant. It can be noted that the range of electric field for which the shielding is optimal is quite small but can be reached experimentally. These sharp and rapidly changing structures confirm that shielding is a resonant process whose collision rate coefficients are uniquely driven by the barrier height in the incident channels.

An adimensional point of view, similar to the one used in chapter 4 has been used to illustrate the effect of the static electric field on different molecules as shown in Fig. 5.1 (bottom-right). The y-axis and the color labels correspond to the same quantities as the ones defined in chapter 4, i.e. they represent respectively a parameter identifying the molecules and the elastic to quentching ratio. The coordinate on the x-axis describes the applied electric field strength. The shielding is considered effective when yellow, orange, red and white colored regions are plotted. We can see that for a large number of molecules, one can find a value of the electric field for which the shielding is efficicent.

This method seems to be very efficient for a large number of molecules, however, to obtain the collision rates presented above, several hundred of channels must be propagated. If one wishes to extend this study to three-body collisions, one must find some simplification as illustrated in the next section.

5.2 A simplified model

The previous calculations [97, 98] have been carried out taking no restrictions on the rotational structure. They used $j = [0, 5]$ with $l = 0, 2, 4$ for bosons and $l = 1, 3, 5$ for fermions which corresponds to 956, 923 and 857 channels for respectively $M_{\text{tot}} = 0, 1, 2$. Extending this study to three-body collisions would be impossible because the number of channels would be too large to be solved numerically. For this reason, we have developed a simplified model that we first checked on two-body collisions (by comparing the results obtained with our model to the one given by the complete calculations) before extending it to three-body systems.

5.2.1 The $m_{j_1} = m_{j_2} = m_l = 0$ approximation

The two molecular states of interest are $\left|\tilde{0}, 0\right\rangle \left|\tilde{2}, 0\right\rangle$ and $\left|\tilde{1}, 0\right\rangle \left|\tilde{1}, 0\right\rangle$ whose angular projections m_{j_1} and m_{j_2} are both zero. For bosons, the partial wave $l = 0$ dominates the physical behavior of the rate coefficients at ultralow energies (especially in the shielding process because it is the only partial wave without a centrifugal barrier). For fermions, the lowest partial wave $l = 1$, $m_l = 0$ corresponds mainly to head-to-tail collisions while the projections $m_l = \pm 1$ correspond mainly to side-by-side collisions. As we can see on Fig. 5.7, if the molecules are both oriented along the same direction, the head-to-tail configuration is intuitively more attractive (Cf. discussion in section. 5.2.2). Consequently, the losses are mainly due to the head-to-tail configuration, i.e. the one described by $m_l = 0$. For these reasons, we will perform our first calculations with $m_{j_1} = m_{j_2} = m_l = 0$ (i.e. $M_{\text{tot}} = 0$) as explored in [98, 210]. Under this approximation, we can reduce the number of states to 63. The adiabatic energy curves obtained are plotted in red in Fig. 5.2 (bosons) for the optimal value of the electric field $E = 12.4\,\text{kV}\,\text{cm}^{-1}$. As expected, we can see that the red curves are less numerous than the black ones which correspond to the complete quantum calculations. We then expect to underestimate the inelastic collision rate coefficients compared to the complete calculation. Let's now focus on the two resonant states (zoom in on the graph). We note that in both cases, the partial wave $\tilde{l} = 0$ remains repulsive. The black and red curves overlap perfectly at long-range but a mismatch appears when the intermolecular distance decreases. Indeed, the barrier seems to be more quickly repulsive in the complete calculation when r decreases. This is because when all m_{j_τ} projections are considered, there is a larger density of states (not taken into account in our model) below and near the incident channel that push our channel upwards. However, as we work with very low collision energy $E_{\text{k}} = 500\,\text{nK}$, the collision rate coefficients are mainly sensitive to the long-range part of the potential (where the overlap is good). As a result, we expect to have elastic and loss collision rate coefficients similar to the complete calculation.

On Fig 5.3–5.4 , we superimposed the elastic, inelastic and loss collision rate coefficients obtained with the $m_{j_1} = m_{j_2} = m_l = 0$ approximation (dashed lines) and with the complete calculation (solid lines) for collisions of respectively identical bosons (Fig. 5.3) and fermions (Fig. 5.4). Note that the complete calculations showed a very good agreement with a recent experimental observation of the shielding for a three-dimensional gas

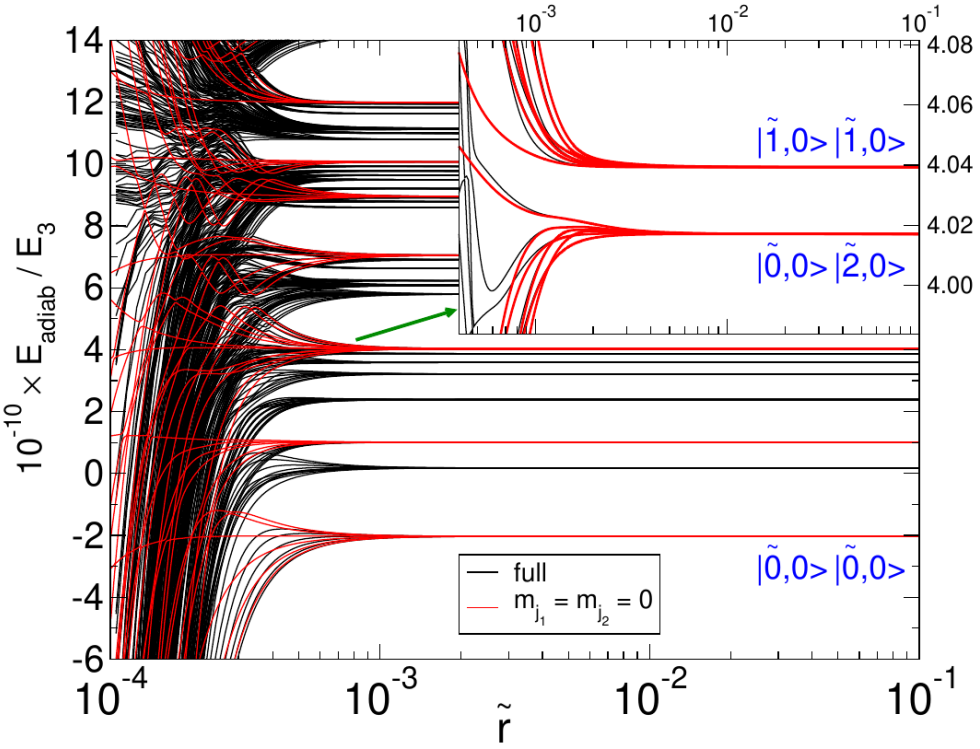

Figure 5.2: Adiabatic energy curves as a function of the inter-molecular separation for the $M = 0$ component. Solid black lines: complete treatment. Solid red lines: Simplified model with only $m_{j_1} = m_{j_2} = m_l = 0$ Insert: Zoom in on the two states $|\tilde{1}, 0\rangle + |\tilde{1}, 0\rangle$ and $|\tilde{2}, 0\rangle + |\tilde{0}, 0\rangle$. Taken from [98].

of fermionic $^{41}K^{87}Rb$ molecules (see Fig.2 from [100]). With our model, the two peaks at E_1^* and E_2^* do not appear because they correspond to states whose projections $m_{j_\tau} = \pm 1$ $\pm 2 \neq 0$ which are not considered in our model. We can notice that the inelastic collision rate coefficients are identical at resonance because the closest and most coupled state $|\tilde{2}, 0\rangle + |\tilde{0}, 0\rangle$ is conserved in our model. When we move away from the resonance, inelastic collisions are slightly underestimated as expected. Note that the elastic and loss rate coefficients are almost identical between the two models because the curves for the lowest partial waves $\tilde{l} = 0$ (bosons) and $\tilde{l} = 1$ (fermions) are mostly unchanged at long-range. For electric fields $E > 14\,\mathrm{kV\,cm^{-1}}$, the curves of the two models match perfectly because we are far from any avoided crossings. The incident channel can be considered as isolated and is mainly gouverned by the van der Waals interaction. The rate coefficients follow the threshold laws developed in [211, 212, 213]:

$$\begin{aligned} \beta^{\mathrm{el}} &\propto d_{\mathrm{ind}}^4 && \text{For Bosons and Fermions} \\ \beta^{\mathrm{in}} \propto \beta^{\mathrm{qu}} &\propto d_{\mathrm{ind}}^2 && \text{For Bosons} \\ \beta^{\mathrm{in}} \propto \beta^{\mathrm{qu}} &\propto d_{\mathrm{ind}}^6 && \text{For Fermions} \end{aligned} \tag{5.2.1}$$

which depend on the value of the induced dipole moments. Although this approximation $M = 0$ allows to drastically reduce the number of states used, it remains unusable when

studying a three-body system because the number of states remains too large. In the following section, we will present a model that is limited to the study of only two molecular states.

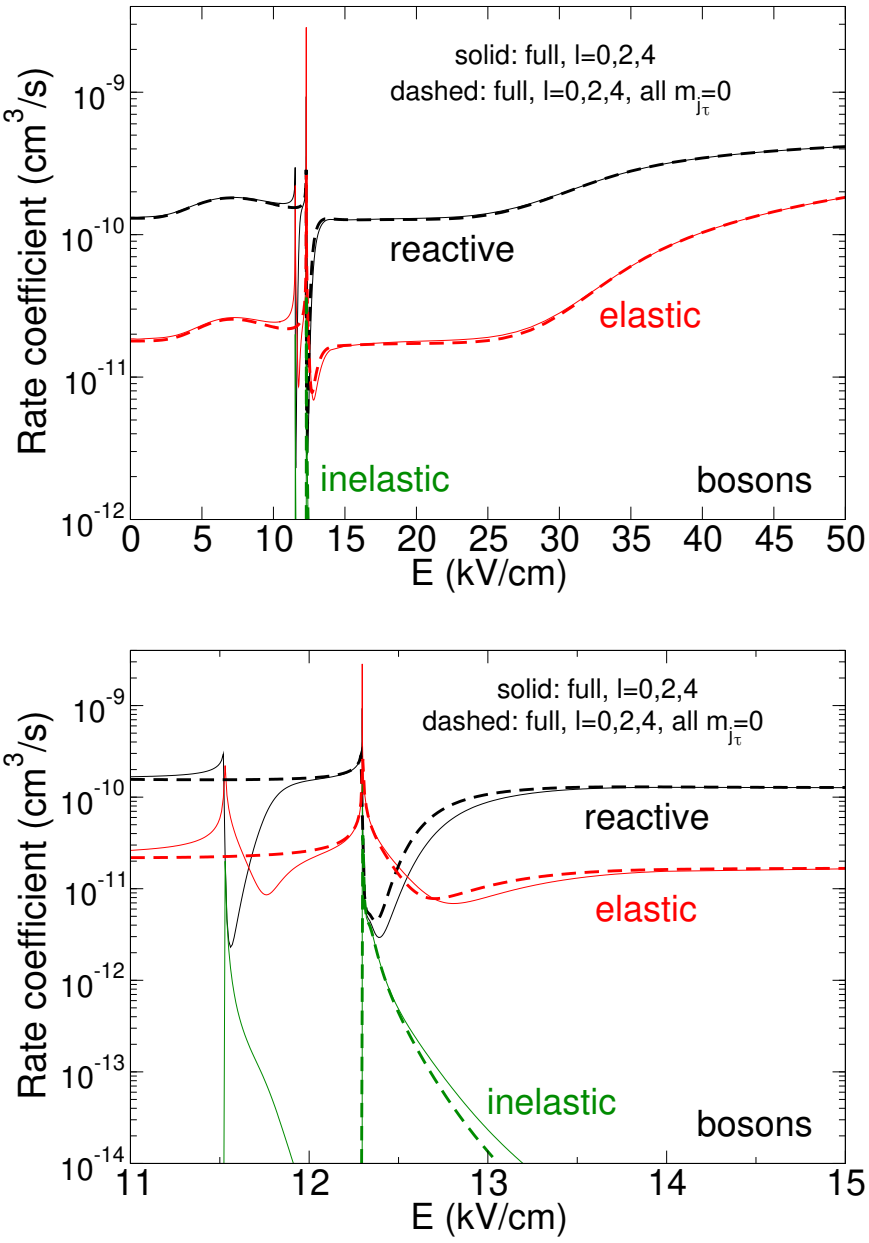

Figure 5.3: Rate coefficients as a function of the electric field for bosonic $^{41}K^{87}Rb$ for a collision energy $E_k = 500\,nK$. Black line: reactive process, red line: elastic process, green line: inelastic process. Solid lines: complete treatment, dashed lines: complete treatment but with all $m_{j_\tau} = 0$.

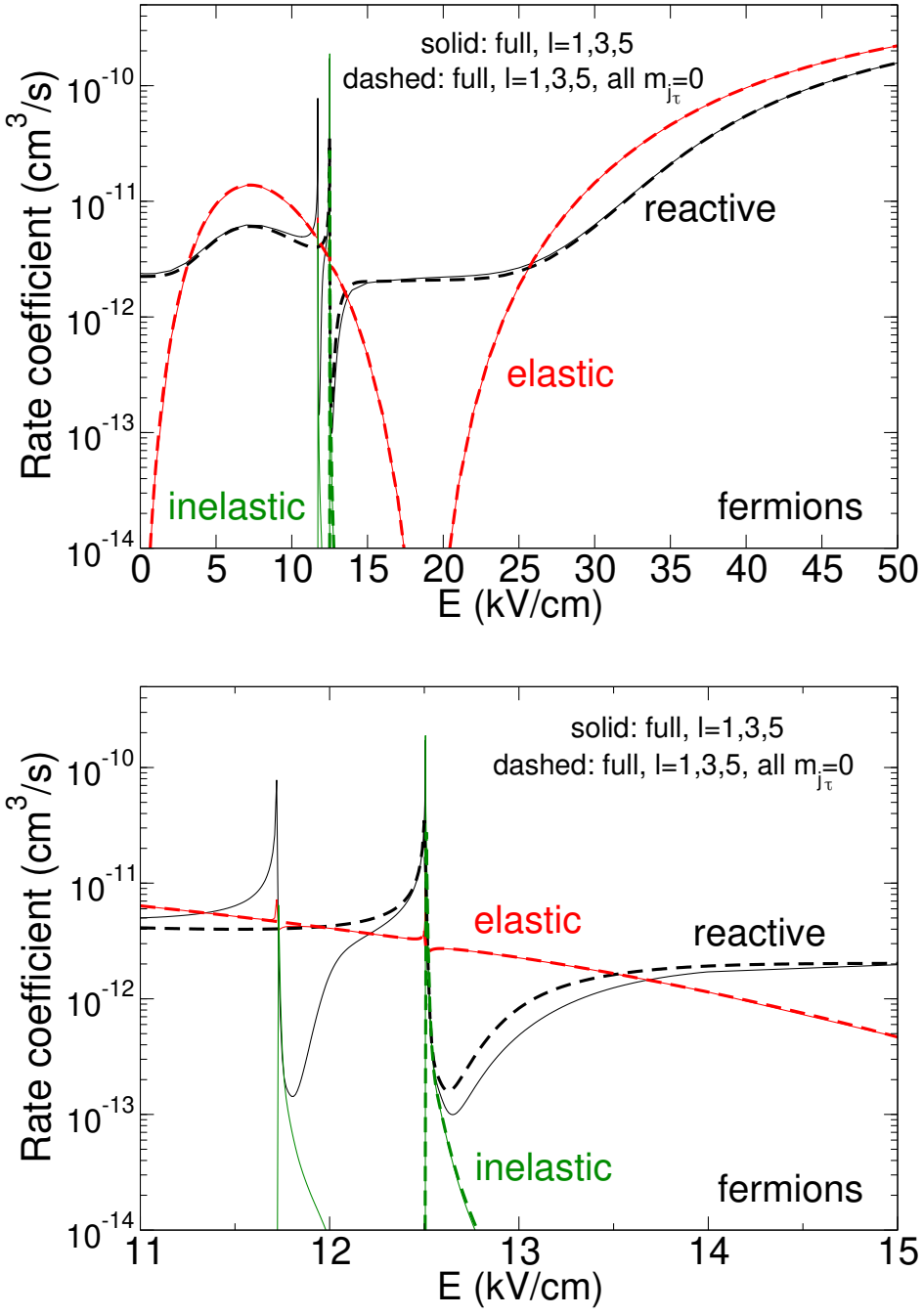

Figure 5.4: Same as Fig. 5.3 but for fermionic ^{40}K^{87}Rb.

5.2.2 A two-level model

The idea is to develop a two-state model that qualitatively reproduces the shielding mechanism while preserving the orders of magnitude of the collision rate coefficients previously obtained. First, we will present the notations used and show how to separate the internal structure from the collisional angular part. We will explain how to reduce the problem to the study of a two-level system. Before integrating on the partial waves, we will diagonalize the potential matrix and show why the two eigenenergy surfaces V_+ and V_- are useful to understand the core of the shielding mechanism. We will show that by integrating these diagonalized energy surfaces on only the first partial wave, we can reduce the complete study to a single channel problem. We will conclude by comparing our model to the complete quantum calculation.

Notations and removal of the rotational structure

The approximation $m_{j_\tau} = 0$ having been previously verified and validated, we will compact the notation so that we omit the m_{j_τ} quantum numbers in the following:

$$\left|\tilde{j}_1, 0\right\rangle \left|\tilde{j}_2, 0\right\rangle \rightarrow \left|\tilde{j}_1, \tilde{j}_2\right\rangle . \tag{5.2.2}$$

We will deal only with the two symmetrized molecular states of interest, the initial one:

$$\left|1\right\rangle = \left|\tilde{1}, \tilde{1}\right\rangle_+ = \left|\tilde{1}\right\rangle \left|\tilde{1}\right\rangle \tag{5.2.3}$$

and the resonant one:

$$\left|2\right\rangle = \left|\tilde{0}, \tilde{2}\right\rangle_+ = \frac{1}{\sqrt{2}} \left\{ \left|\tilde{0}\right\rangle \left|\tilde{2}\right\rangle + \left|\tilde{2}\right\rangle \left|\tilde{0}\right\rangle \right\} \tag{5.2.4}$$

whose corresponding energies $E_{\tilde{1}\tilde{1}}(E) = \epsilon_{\tilde{1}} + \epsilon_{\tilde{1}}$ and $E_{\tilde{0}\tilde{2}}(E) = \epsilon_{\tilde{0}} + \epsilon_{\tilde{2}}$ depend on the applied electric field.

To remove the rotational structure from the formalism and to simplify (future) calculations of three-body collisions, we employ the definition of a generalized induced dipole moment (whose derivation is given in appendix B) between a state $\tilde{j}$ and tilde $\tilde{j}'$, that includes as well the transition dipole moments [214]:

$$d^{\tilde{j}_\tau \rightarrow \tilde{j}'_\tau} = d_\tau \times \sum_{j_\tau, j'_\tau} \langle j_\tau \,|\, \tilde{j}_\tau \rangle \, \langle j'_\tau \,|\, \tilde{j}'_\tau \rangle \, \sqrt{2j_\tau + 1} \sqrt{2j'_\tau + 1} \begin{pmatrix} j_\tau & 1 & j'_\tau \\ 0 & 0 & 0 \end{pmatrix}^2 , \tag{5.2.5}$$

where d_τ is the permanent dipole moment of the molecule τ, j_τ and j'_τ represent the index of the bare rotational states, $\langle j_\tau \,|\, \tilde{j}_\tau \rangle$ and $\langle j'_\tau \,|\, \tilde{j}'_\tau \rangle$ are the coefficients of development of the dressed states onto the bare states for a given electric field E. When $j = j'$ these are the induced dipole moments and when $j = j'$ these are the transition dipole moments. We represent in Fig. 5.5 the induced and transition dipole moments as a function of the electric field for different transitions $\tilde{j} = 0, 1, 2 \rightarrow \tilde{j}' = 0, 1, 2$. For the optimal value of the electric field, we see that the two induced dipole moments for the incident channel are both negative, hence oriented in the opposite direction of the electric field ($\downarrow\downarrow$) while the induced dipoles corresponding to the second state are not oriented in the same direction ($\uparrow\downarrow$). The effects of the non-diagonal terms are described in the next section.

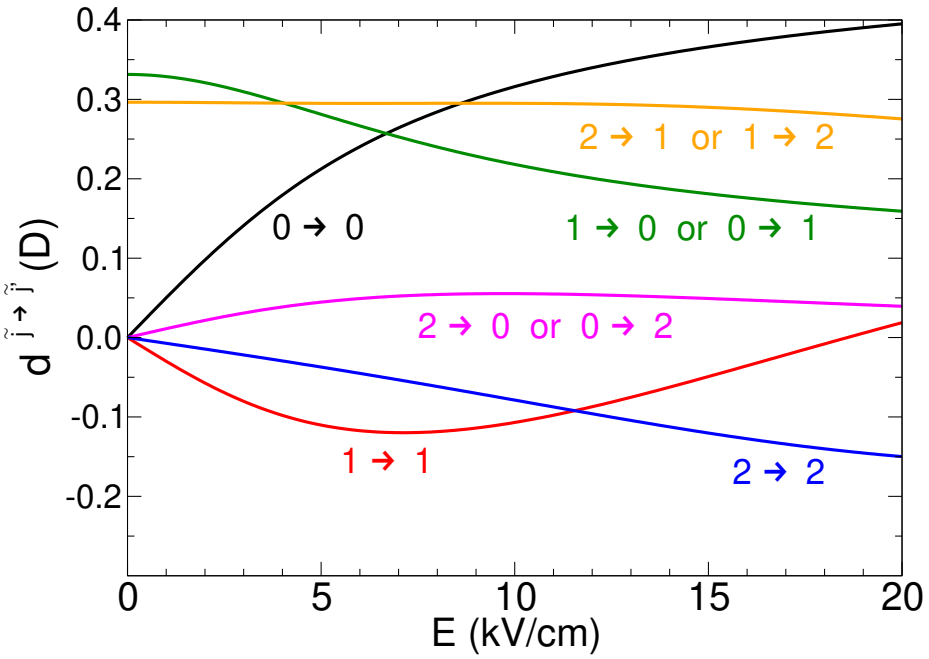

Figure 5.5: Induced ($j = j'$) and transition ($j \neq j'$) dipole moments as a function of the electric field for different values of $j \to j'$.

Definition of two potential energy surfaces V^+ and V^-

We can now use a classical dipole-dipole expression [97, 212], even for collisions involving inelastic transitions, such as the ones in the collisional shielding [206]. Using the definition in Eq. 5.2.5, the classical expression of the dipole-dipole interaction between a dressed rotational state $\tilde{j}$ and $\tilde{j}'$ for molecule 1 and for molecule 2 (Cf. appendix B) can be written as:

$$V_{dd}^{\tilde{j}_1 \to \tilde{j}'_1, \tilde{j}_2 \to \tilde{j}'_2}(r) = \frac{d^{\tilde{j}_1 \to \tilde{j}'_1} \, d^{\tilde{j}_2 \to \tilde{j}'_2}}{4\pi\varepsilon_0 \, r^3} \left(1 - 3\cos^2\theta\right) \tag{5.2.6}$$

and includes now the off-diagonal elements, responsible for the inelastic transitions.

In the specific conditions of the collisional shielding, the physical picture is rather a strong dipolar interaction first (this can persist at long-range as the two energy levels of the molecular states become more and more degenerate), then a subsequent coupling between partial waves. It is therefore physically intuitive to first look at the effect of the dipolar interaction (mediated by the rotational levels), then to treat the effect on the orbital motion at a second stage, as a pertubation. This is in essence what was proposed and employed in [102] where Born-Oppenheimer-like potentials were introduced to investigate similar studies of shielding. Therefore, we first diagonalize the following

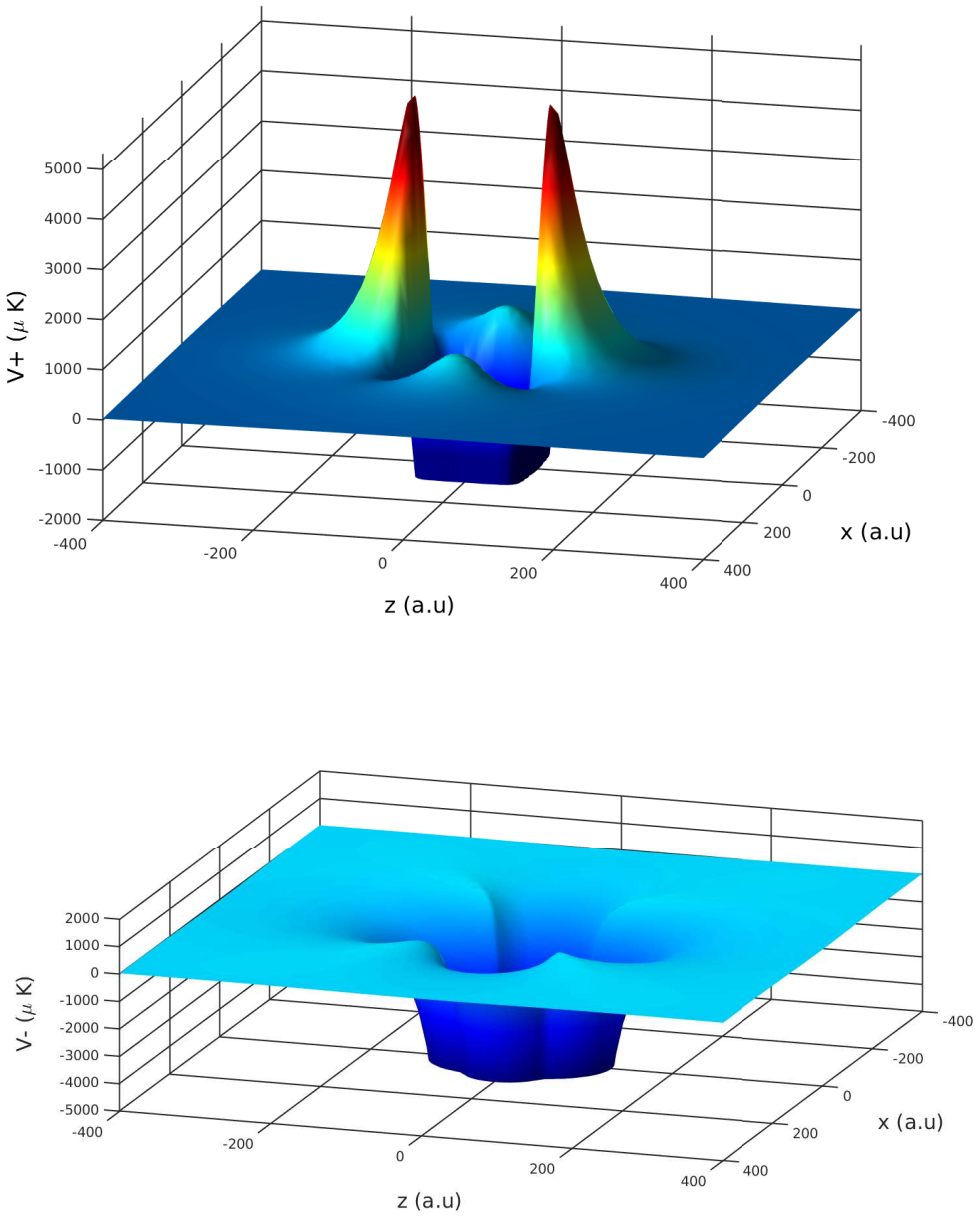

Figure 5.6: Potential model V_+ (top) and V_- (bottom) as a function of the polar coordinates $x = r\sin\theta$ and $z = r\cos\theta$. They are calculated for fermionic ^{40}K^{87}Rb molecules at respectively $E = 12.7\,\mathrm{kV\,cm^{-1}}$ and $E = 12.5\,\mathrm{kV\,cm^{-1}}$. They include the dipole-dipole interaction, the van der Waals interaction and the $l = 1$ centrifugial barrier.

matrix:

$$\begin{bmatrix} \frac{d^{\tilde{1}\to\tilde{1}}\,d^{\tilde{1}\to\tilde{1}}}{4\pi\varepsilon_0\,r^3}\left(1-3\cos^2\theta\right)+E_{\tilde{1}\tilde{1}} & \sqrt{2}\,\frac{d^{\tilde{1}\to\tilde{0}}\,d^{\tilde{1}\to\tilde{2}}}{4\pi\varepsilon_0\,r^3}\left(1-3\cos^2\theta\right) \\ \sqrt{2}\,\frac{d^{\tilde{1}\to\tilde{2}}\,d^{\tilde{1}\to\tilde{0}}}{4\pi\varepsilon_0\,r^3}\left(1-3\cos^2\theta\right) & \frac{d^{\tilde{0}\to\tilde{0}}\,d^{\tilde{2}\to\tilde{2}}+d^{\tilde{0}\to\tilde{2}}\,d^{\tilde{0}\to\tilde{2}}}{4\pi\varepsilon_0\,r^3}\left(1-3\cos^2\theta\right)+E_{\tilde{0}\tilde{2}} \end{bmatrix} \tag{5.2.7}$$

and obtain two surface functions of eigenvalues in r and θ:

$$E_{\pm}(r,\theta) = \frac{1}{2}(E_a + E_b) \pm \frac{1}{2}\sqrt{(E_a - E_b)^2 + 4W^2}, \tag{5.2.8}$$

with:

$$\begin{aligned} E_a &\equiv \frac{d^{\tilde{1}\to\tilde{1}}\, d^{\tilde{1}\to\tilde{1}}}{4\pi\varepsilon_0\, r^3}\,(1 - 3\cos^2\theta) + E_{\tilde{1}\tilde{1}} \\ E_b &\equiv \frac{d^{\tilde{0}\to\tilde{0}}\, d^{\tilde{2}\to\tilde{2}} + d^{\tilde{0}\to\tilde{2}}\, d^{\tilde{0}\to\tilde{2}}}{4\pi\varepsilon_0\, r^3}\,(1 - 3\cos^2\theta) + E_{\tilde{0}\tilde{2}} \\ W &\equiv \sqrt{2}\,\frac{d^{\tilde{1}\to\tilde{2}}\, d^{\tilde{1}\to\tilde{0}}}{4\pi\varepsilon_0\, r^3}\,(1 - 3\cos^2\theta). \end{aligned} \tag{5.2.9}$$

To get a more accurate picture of what is going on, we include the van der Waals interaction and the centrifugal barrier of the lowest partial wave such that:

$$V_+(r,\theta) = E_+(r,\theta) - \frac{C_6}{r^6} + \frac{C_2}{2\mu r^2} \qquad V_-(r,\theta) = E_-(r,\theta) - \frac{C_6}{r^6} + \frac{C_2}{2\mu r^2}. \tag{5.2.10}$$

To illustrate the discussion, we consider the case of fermions in the following so:

$$C_2 = \hbar^2 l(l+1) \underset{l=1}{=} 2\hbar^2. \tag{5.2.11}$$

When $E_{\tilde{1}\tilde{1}} > E_{\tilde{0}\tilde{2}}$, the model potential curve for the initial state will be $V(r,\theta) \equiv V_+(r,\theta)$. We represented in Fig. 5.6 (top panel), the potential energy surface $V_+(r,\theta)$ in polar coordinates defined as:

$$z = r\cos(\theta) \qquad\qquad x = r\sin(\theta) \tag{5.2.12}$$

for $E = 12.72\,\mathrm{kV\,cm^{-1}} > E_3^*$. For a fixed intermolecular distance r_0, the potential $V(r_0,\theta)$ corresponds to a circle of radius r_0 on the potential energy surface. Then, we observe that in the short-range domain (circle of small radius), the van der Waals interaction dominates the physical process and the interaction is purely attractive. If we focus on the long-range part, we observe four repulsive peaks which are signatures of the dipole-dipole interaction. The two peaks along $z = 0$ are coming from side-by-side collisions (i.e. $\theta = \pi/2$) whereas the two peaks along $x = 0$ are coming from the head-to-tail collisions (i.e. $\theta = 0$). The difference in height between the two configurations will be explained in Sec. 5.2.2. For $\theta \approx 54°$, we have a zero because $1 - 3\cos^2\theta = 0$. As we will average our potential energy surface over the partial wave $l = 1$, hence over θ, then for a circle whose perimeter hits all four peaks, the interaction remains globally repulsive.

When $E_{\tilde{1}\tilde{1}} < E_{\tilde{0}\tilde{2}}$, the model potential curve becomes $V(r,\theta) \equiv V_-(r,\theta)$. We represented this potential energy surface in Fig. 5.6 (bottom panel) for $E = 12.5\,\mathrm{kV\,cm^{-1}}$. We obviously obtain an attractive potential at short-range because of the attractive van der Waals interaction. The small repulsive parts are coming from the centrifugal $l = 1$ barrier for the configuration where $1 - 3\cos^2\theta = 0$. Unfortunately, these small barriers are not high enough to prevent losses in average.

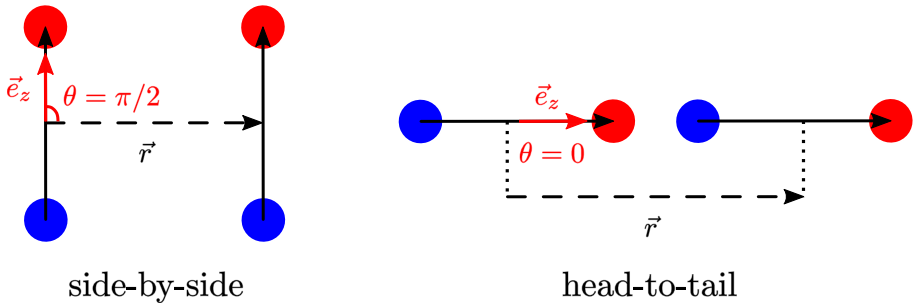

Figure 5.7: Side-by-side and head-to-tail configurations. An external electric field is applied along $\vec{e}_z$ where the induced dipole moments are oriented.

Illustration of the PES's angular dependence

By looking at the Fig. 5.7, it is intuitive to understand that the side-by-side configuration is more repulsive than the head-to-tail configuration. Indeed, in the first case, the dipole moments approach pointing in the same direction, whereas in the second case they approach pointing in opposite directions.

However, when we look at the $V_+(r,\theta)$ surface presented earlier, the barriers corresponding to the head-to-tail configuration are the most repulsive. To understand this difference, we have plotted on Fig 5.8 the diabatic potential energy surfaces (then before diagonalization of the matrix 5.2.7) and the adiabatic ones as a function of the intermolecular distance for the two configurations $\theta = 0$ and $\theta = \pi/2$. To understand the difference between the diabatic curves, we recall here the two terms describing the upper and the lower diabatic states:

$$E_a \equiv \frac{d^{\tilde{1}\to\tilde{1}}\, d^{\tilde{1}\to\tilde{1}}}{4\pi\varepsilon_0\, r^3}\,(1-3\cos^2\theta) + E_{\tilde{1}\tilde{1}} \tag{5.2.13}$$

$$E_b \equiv \frac{d^{\tilde{0}\to\tilde{0}}\, d^{\tilde{2}\to\tilde{2}} + d^{\tilde{0}\to\tilde{2}}\, d^{\tilde{0}\to\tilde{2}}}{4\pi\varepsilon_0\, r^3}\,(1-3\cos^2\theta) + E_{\tilde{0}\tilde{2}}. \tag{5.2.14}$$

For:

- the incident channel E_a, the term $d^{\tilde{1}\to\tilde{1}} d^{\tilde{1}\to\tilde{1}}$ is obviously positive. The overall sign of the expression then depends only on the sign of $(1-3\cos^2\theta)$ which is positive when $\theta = \pi/2$ and negative when $\theta = 0$. This is why the black curves corresponding to the incident channel are attractive for $\theta = 0$ and repulsive for $\theta = \pi/2$ on Fig 5.8.

- the lowest channel E_b, the term $d^{\tilde{0}\to\tilde{0}}\, d^{\tilde{2}\to\tilde{2}}$ is large and negative while the term $d^{\tilde{0}\to\tilde{2}}\, d^{\tilde{2}\to\tilde{0}}$ is small and positive (cf. Fig 5.5): the total is then negative. Following the same reasoning as before, the diabatic energies for this state must be repulsive for $\theta = 0$ and attractive for $\theta = \pi/2$.

We end up with two diabatic curves which are crossing for the head-to-tail configuration while the two curves do not cross for the side-by-side configuration. After diagonalization

of the total matrix, an avoided crossing appears for the $\theta = 0$ case due to the off-diagonal element W. As a consequence, at the beginning of the collisional process, the two molecules are aligned in the same direction. When they are enough close to each other, the incident channel is strongly mixed with the channel bellow and takes on its character. Then, the induced dipole of one of the molecule changes to an opposite direction which prevents the molecules to approach to each other due to the creation of a repulsive barrier. When molecules move back apart, the molecules orient themselves again in the same direction. When the molecules collide via a side-by-side configuration ($\theta = \pi/2$), the two molecules stay aligned along the same direction during the entire collisional process.

Finally, the difference in the height of the barriers between the two configurations explained by the fact that W is proportional to $(1 - 3\cos^2\theta)$ which is two times stronger for $\theta = 0$ than for $\theta = \pi/2$.

Average over the orbital angular momentum

To obtain a more quantitative comparison, we will present in this section the adiabatic energy curves obtained after averaging over the partial waves and we will compare them to those obtained with the complete quantum calculation.

As seen in the theoretical part, partial waves are just spherical harmonics whose polar and azimuthal angular parts are separable $\mathcal{Y}_l^{m_l}(\theta,\phi) = \Theta_l^{m_l}(\theta)\,\Phi_{m_l}(\varphi)$. The integral of the model potential over the partial wave $\mathcal{Y}_l^{m_l}(\theta,\phi)$ is given by:

$$\left\langle V(r)\right\rangle_{l,m_l} = \left\langle l, m_l \middle| V(r,\theta) \middle| l', m_l' \right\rangle = \int \left[\mathcal{Y}_l^{m_l}(\theta,\phi)\right]^* V(r,\theta)\, \mathcal{Y}_{l'}^{m_l'}(\theta,\phi) \sin\theta \, d\theta \, d\phi. \quad (5.2.15)$$

Note that this is not analytical anymore, one cannot use 3-j symbols, but for each intermolecular distance r one must numerically compute the integrals. We will only consider the first partial wave in our model so $l = l' = 0$ for bosons and $l = l' = 1$. Moreover, since the potential is independent of ϕ, $m_l = m_l'$ and we can simply perform a one-dimensional integral over θ:

$$\left\langle V(r)\right\rangle_{l,m_l} = \int_0^\pi \left[\Theta_l^{m_l}(\theta)\right]^* V(r,\theta)\, \Theta_l^{m_l}(\theta) \sin\theta \quad (5.2.16)$$

with

$$\Theta_l^{m_l}(\theta) = (-1)^{m_l} \sqrt{\frac{2l+1}{2}} \sqrt{\frac{(l-m_l)!}{(l+m)!}}\, P_l^{m_l}(\theta) \qquad \text{with:} \qquad m_l \geq 0 \quad (5.2.17)$$

$$\Theta_l^{m_l}(\theta) = (-1)^{|m_l|}\, \Theta_l^{|m_l|}(\theta) \qquad \text{with:} \qquad m_l < 0. \quad (5.2.18)$$

To compute the integral in Eq. 5.2.16, a Gauss-Legendre quadrature is well suited because the barriers are located at the edges of the integration domain of θ. For symmetry considerations, we have realized the quadrature only on $\theta \in [0, \pi/2]$. We used 200 points for the quadrature.

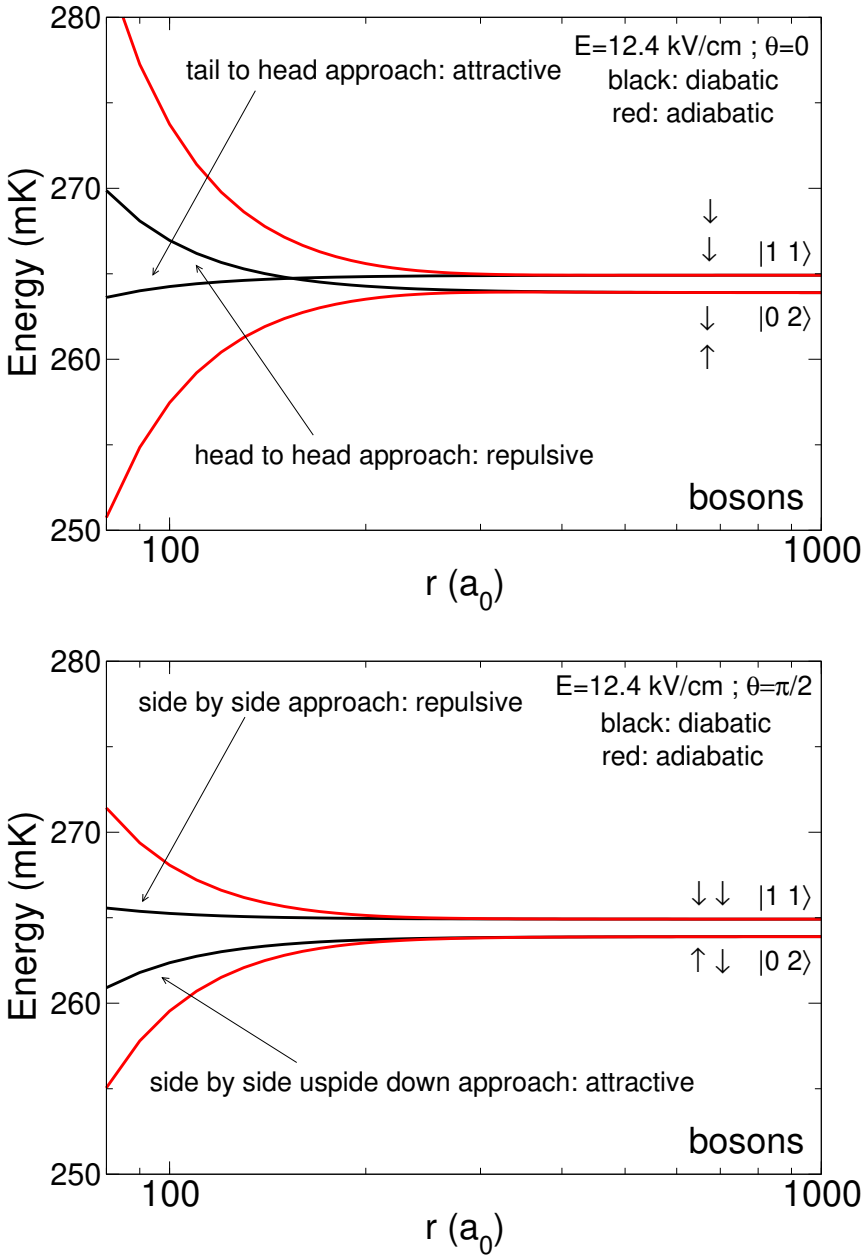

Figure 5.8: PES for $\theta = 0$ (top) and $\theta = \pi/2$ (bottom) as a function of the intermolecular distance r for $E = 12.4\,\mathrm{kV\,cm^{-1}}$.

For bosons, the first parial wave $|0,0\rangle$ is not degenerate. Then, we only have a one channel problem:

$$\big\langle V(r)\big\rangle_{0,0} = \big\langle 0,0\big|V(r,\theta)\big|0,0\big\rangle = \int_0^\pi \frac{1}{2}\,V(r,\theta)\,\sin\theta\,d\theta. \tag{5.2.19}$$

For fermions, the partial wave $l = 1$ has three corresponding projections $m_l = 0, \pm 1$:

$$\big\langle V(r)\big\rangle_{1,0} = \big\langle 1,0\big|V(r,\theta)\big|1,0\big\rangle = \int \frac{3}{2} V(r,\theta)\, \cos^2\theta\ \sin\theta\, d\theta \tag{5.2.20}$$

and:

$$\big\langle V(r)\big\rangle_{1,\pm 1} = \big\langle 1,\pm 1\big|V(r,\theta)\big|1,\pm 1\big\rangle = \int \frac{3}{4} V(r,\theta)\, (1-\cos\theta)^2\ \sin\theta\, d\theta. \tag{5.2.21}$$

Now, we can compare the adiabatic potential energy curves obtained to the previous model $m_{j_1} = m_{j_2} = m_l = 0$. We have superimposed in Fig. 5.9 the adiabatic energies of the lowest partial wave for the two models for different values of the electric field. The top panel corresponds to collisions of identical bosons while the bottom panel corresponds to identical fermions collisions. We can note that a long-range potential barrier is obtained so from a qualitative point of view, the physics of the shielding mechanism is preserved. From a quantitative point of view:

- For bosons, the barrier obtained for $E = 12.3\,\mathrm{kV\,cm^{-1}}$ is too large compared to the previous model. We can explain this difference by the fact that we are too close to the resonance. As a result, the partial waves $\tilde{l} = 2, 4$ of the incident state couple strongly with the partial waves of the other state and acquire their character. As these partial waves are strongly coupled to the partial wave $\tilde{l} = 0$ of the incident channel, the latter is pushed down. As our model uses only the partial wave $l = 0$, it is out of touch with reality under these conditions. However, for electric fields close to the optimum field, the barrier sizes are relatively well respected: partial waves act as perturbation. Furthermore, the curves match perfectly at long-range so we expect to obtain similar collision rate coefficients.

- For fermions, we remain in the same situation. The curves match relatively well except for the electric field $E = 12.55\,\mathrm{kV\,cm^{-1}}$ too close to the resonance and for the electric field $E = 12.85\,\mathrm{kV\,cm^{-1}}$ where the states are too far apart to use a two-level model.

We can note that the barriers presented in Fig. 5.9 in the adiabatic energy curves are much smaller than the barriers presented in Fig. 5.6. This is because one type of barriers are averaged over the angles, including the presence of a $\sin\theta$ term in the Jacobian of the integral in Eq. 5.2.16 and the other type of barriers come directly from the PES, with no averaging over the angles.

We then found a way to reproduce well the barriers for the optimal values of the electric field.

Rate coefficients

In this part, we use the model adiabatic barriers to compute the rate coefficients. The idea of our model is to realize the dynamics on only the incident channel: we neglect any transition between the two surfaces V_+ and V_-. That's reminiscent to a Born–Oppenheimer-like approximation and we can compare with the complete calculation to

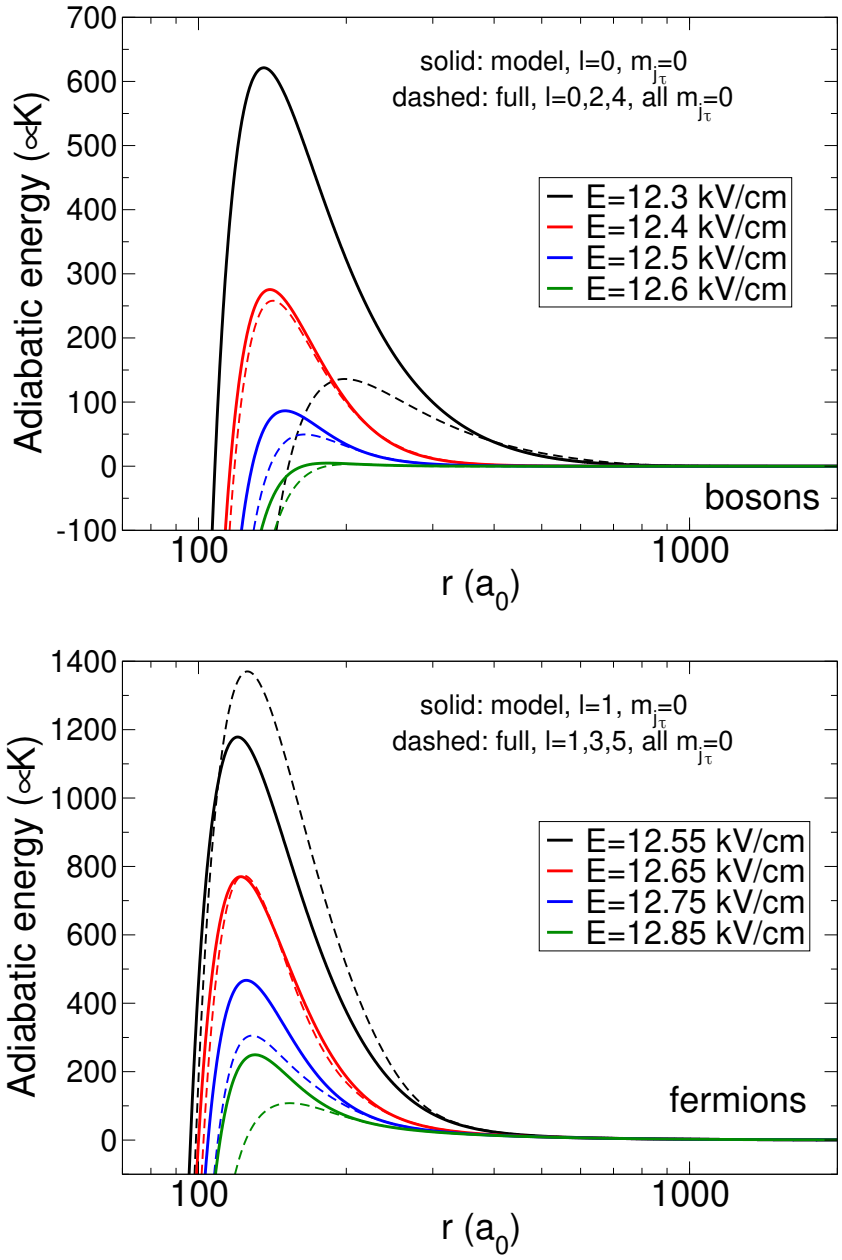

Figure 5.9: Adiabatic energy curves as a function of the inter-molecular separation for different electric fields for the $M = m_l = 0$ component. Solid lines: model, dashed lines: complete treatment with all $m_{j_\tau} = 0$. Upper panel: bosonic ^{41}K^{87}Rb, lower panel: fermionic ^{40}K^{87}Rb.

estimate its validity. Moreover, this approximation seems legitimate because we have previously shown that the inelastic collision rate coefficients are negligible at the optimal electric field. On the other hand, we know that if we are too close to resonance, our model will break down and will not reproduce reality.

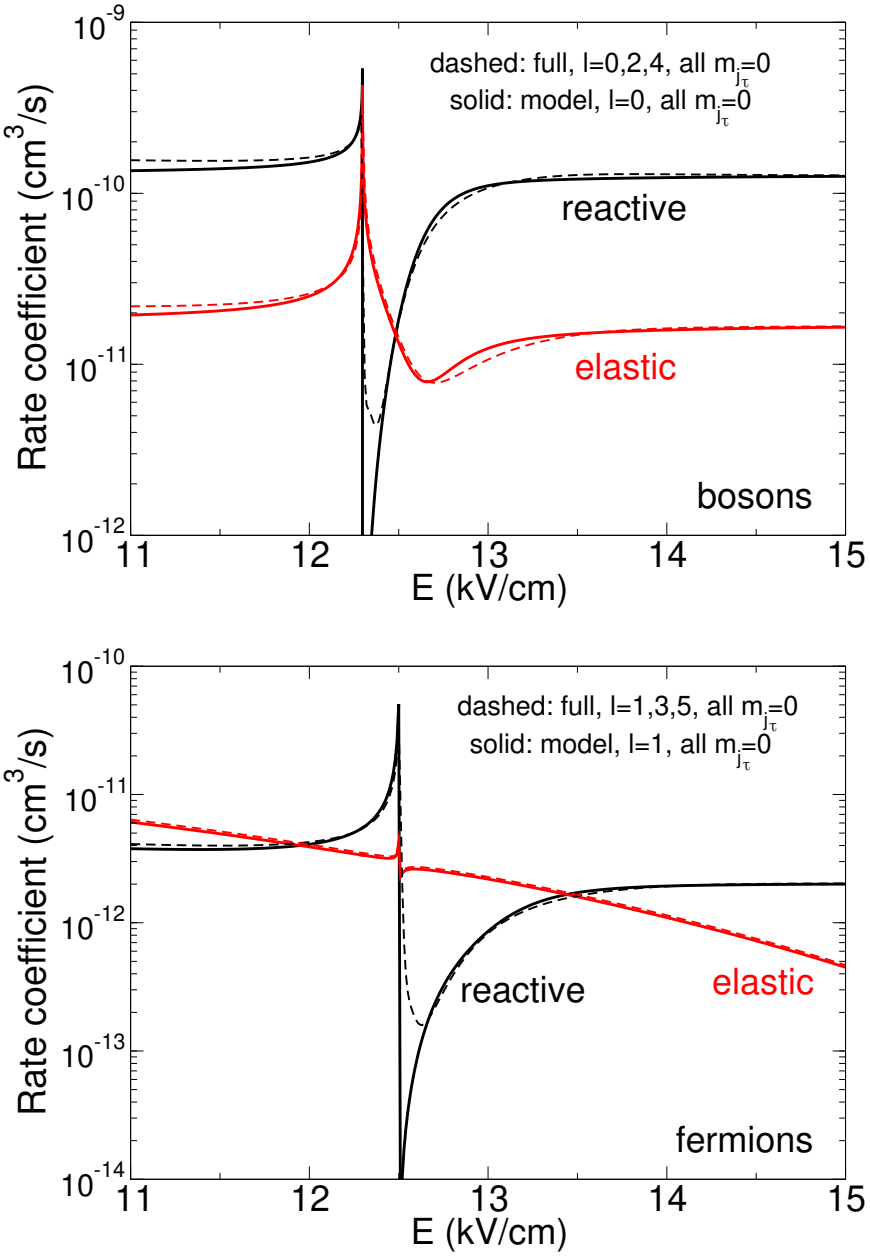

Figure 5.10: Rate coefficients as a function of the electric field for bosonic ^{41}K^{87}Rb (top panel) and fermionic ^{40}K^{87}Rb (bottom panel) at $E_{\mathrm{k}} = 500\,\mathrm{nK}$. Black line: reactive process, red line: elastic process, green line: inelastic process. Solid lines: complete treatment with all $m_{j_\tau} = 0$, dashed lines: model.

Let's focus on Fig. 5.10 (top panel) on which we represented the rate coefficients as a function of the electric field for the bosonic case. As shown above, very close to resonance, the potential barrier is overestimated, resulting in loss rate coefficients that are too low with our model. Moreover, inelastic collisions are not considered anymore as explained

before. On the other hand, for electric fields close to the optimal field for which the ratio γ is maximum, the loss and elastic rate coefficients are almost identical if they are computed using our model or using the complete calculations with $m_{j_1} = m_{j_2} = m_l = 0$. For higher electric fields, the rate coefficients are identical and follow the threshold laws (Cf. Eq. 5.2.1) because we can consider the incident channel as isolated. For fermions (bottom panel), our model match also very well with the complete calculations with $m_{j_1} = m_{j_2} = m_l = 0$ for a large range of values of the applied electric field especially for the values for which the ratio γ is maximum.

Without electric field, the characteristic time between two events of two-body collisions leading to losses (Cf. appendix C) is $\tau_{2B} = 0.03\,\mathrm{s}$ for bosons and $\tau_{2B} = 1.9\,\mathrm{s}$ for fermions. When the shielding is turn on and for the the electric field value for which the shielding is optimal, $\tau_{2B} = 0.90\,\mathrm{s}$ for bosons and $\tau_{2B} = 36\,\mathrm{s}$. These values depict how the gas lifetime increases when the shielding is activated. Experimentally, these electric field values are feasible and will provide favorable conditions for efficient evaporative cooling.

As a conclusion, the agreement between the complete calculations with $m_{j_1} = m_{j_2} = m_l = 0$ and the model is good in both magnitude and electric field dependence in the place where the shielding is efficient. Because the agreement between the complete calculation and the one with $m_{j_1} = m_{j_2} = m_l = 0$ (see Fig. 5.3) is semi-quantitatively good, then our model is also semi-quantitatively good when compared with the complete calculation. To get a correct estimation of the processes involved, it is then enough to treat the shielding problem with only the lowest collisional channel, provided that the PES has been pre-obtained after diagonalization. This model confirms that shielding is a resonant process where the dipole-dipole interaction plays the leading role. It was then correct to consider the effect of the orbital moment as perturbative. This model will serve as a strong basis for the more complicated shielding study of three-body collisions.

Part II

Three-body collisions

Chapter 6

Quantum reactive scattering theory for three-body collisions

Over the last twenty years, techniques for cooling and trapping atoms and molecules have progressed at a remarkable pace [1, 2, 3, 7, 53, 36]. Now, it is possible to prepare ultracold gases of molecules ($T < 1\,\mu K$) in a well defined rovibronic state [78, 40, 41, 42]. The development of new shielding methods [96, 97, 98, 99, 100, 103, 106, 107, 108] renewed the interest for reactive di-alkali-metal molecules where reactive collisions can occur even at ultralow energy [79]. As experimental techniques improve to accurately measure state-to-state differential cross sections and rate coefficients [215, 216, 217], three-body theoretical studies on these reactive molecules must be investigated.

For a long time, three-body calculations have been limited to ultracold collisions, where only a single partial wave is required. The studies were carried out on increasingly heavy systems as the computing capacities increased: H+D_2 [218] (2000), Na+Na_2 [219] (2002), K+K_2 [220] (2005), Li+Li_2 [221, 222, 154] (2005, 2007), K+KRb [223] (2017), Rb+K_2 [224] (2017), Li+LiNa [225] (2021). However, for higher collision energies, the calculations are much more difficult because several partial waves must be included. Therefore, three-body models have been improved and can now include several partial waves even for heavy alkali metal systems [152, 225]. The formalism is now well established to describe reactive or non-reactive processes such as:

$$\begin{cases} A + BC \rightarrow B + AC & \text{(Reactive collisions)} \\ A + B + C \rightarrow A + BC & \text{(Three-body recombination)} \\ A + BC \rightarrow A + B + C & \text{(Collision-induced dissociation)} \end{cases}$$

As we can see in the above equations, bonds can be formed and/or broken during a collision. For example, in the case of the first reaction equation shown above, the initial bond between atoms B and C has been broken whereas a bond between atoms A and C has been created. In the following, we will call *arrangement*, every atom-diatom combinations that can be formed during a collision. As shown in Fig. 6.1, we can only form three arrangements that we will label hereafter with the letters $\tau = A, B, C$. Therefore, the scattering wave function is now expressed as a linear combination of the existing internal states of each arrangement. If the initial and final arrangements remain identical

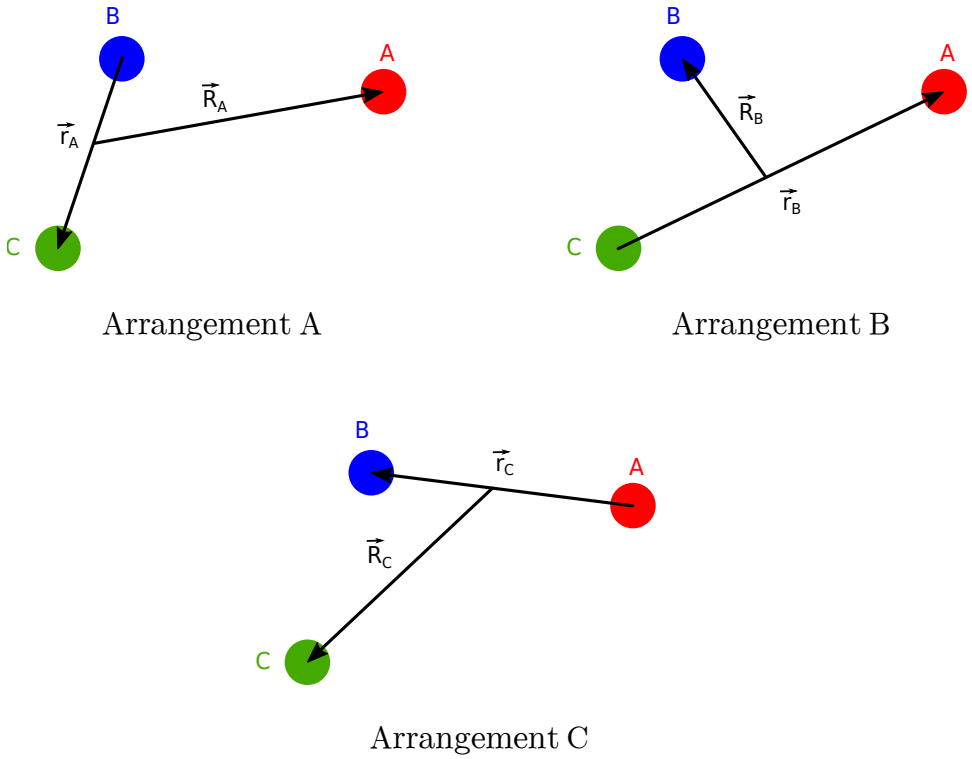

Figure 6.1: The three possible arrangements in Jacobi coordinates

during a collision, then we talk about a non-reactive collision whereas for a collision where the arrangements change, we talk about a reactive collision. We can note that for both cases, we can have a modification of the internal structure of the diatom (i.e. inelastic reactive collisions or inelastic non-reactive collisions). Various coordinate systems can be used to handle all these processes. Each has advantages and disadvantages that depend on the spatial configuration of the particles and on the system studied. However, they are all required for performing three-body studies, especially for the matching process.

In this chapter, we will present the different systems of coordinates: the mass-scaled Jacobi coordinates, the Delves hyperspherical coordinates [143, 144] and the principal axes hyperspherical coordinates (APH) developed initially by F. T. Smith and R. C. Whitten [146, 147] and employed by B. R. Johnson [148, 226, 227], R. T. Pack and G. A. Parker [150, 228], A. Kupperman [229] and J.-M. Launay [230]. Then, we will develop the time-independent formalism developed by B. Kendrick [152, 218] improving the accuracy of the calculations for any partial waves and adapt it for the case of three identical particles. Then, we will describe the matching procedure using mixed boundary conditions [231, 232] to extract the observables we want for atom-diatom collisions as well as for three-body recombination or collision-induced dissociation. This chapter is largely inspired by the PhD thesis of G. Quéméner [151] and by different papers [148, 150, 152].

6.1 Mass-scaled Jacobi coordinates

In the previous section, the two-body collisions were treated using Jacobi coordinates. We have shown that these coordinates are very convenient because they give a simple expression of the Hamiltonian in terms of the relative coordinates of the two particles.

In this section, we will introduce and adapt the Jacobi coordinates for the study of three-body systems. We will follow the same steps as in chapter. 3, i.e. we will give the three-body Hamiltonian, then the primitive basis on which the total wave function will be developed and finally we will present the set of coupled equations to be solved to extract the desired observables.

Jacobi coordinates

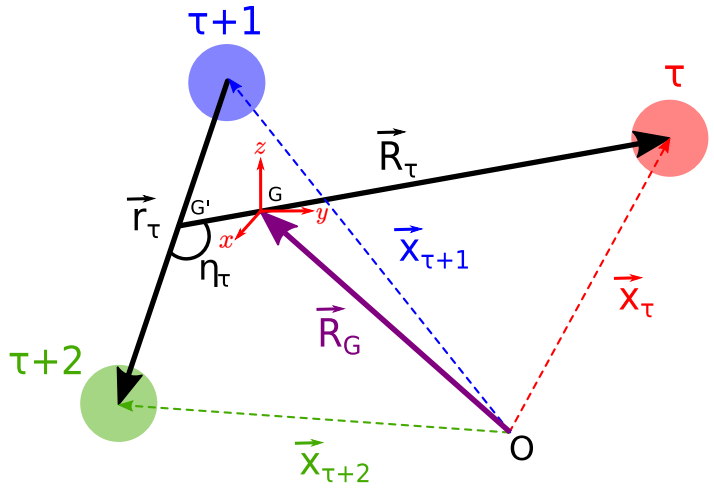

Figure 6.2: Jacobi coordinates for the arrangement τ. The vectors x_τ, $x_{\tau+1}$ and $x_{\tau+2}$ give the absolute position of the three particles from an arbitrary point O. The absolute position of the total center of mass G from the point O is given by $\vec{R}_G$. The Jacobi vectors $\vec{r}_\tau$ describes the relative position between the two atoms $\tau+1$ and $\tau+2$. The Jacobi vector $\vec{R}_\tau$ gives the relative position between the center of mass of the diatom G' and the atom τ. The internal angle η_τ corresponds to the angle between the two Jacobi vectors $\vec{r}_\tau$ and $\vec{R}_\tau$. The space-fixed frame is defined by $(\vec{e}_x, \vec{e}_y, \vec{e}_z)$.

Consider a system of three particles $\tau = A, B, C$ of mass m_τ described with individual position vectors $\vec{x}_\tau$ given from an arbitrary point O (Fig. 6.2). Following the example of the two-body formalism, we can build three sets of Jacobi coordinates $(\vec{r}_\tau, \vec{R}_\tau)$ step by step. First, we can define the relative position $\vec{r}_\tau$ between atoms[1] $\tau+1$ and $\tau+2$ and their center of mass G'_τ by:

[1]We obtain the atoms τ, $\tau+1$ and $\tau+2$ by doing a cyclic permutation of the three particles A, B and C.

$$\vec{r}_\tau = \vec{x}_{\tau+2} - \vec{x}_{\tau+1} \qquad \overrightarrow{OG'_\tau} = \frac{m_{\tau+1}\vec{x}_{\tau+1} + m_{\tau+2}\vec{x}_{\tau+2}}{m_{\tau+1} + m_{\tau+2}}. \quad (6.1.1)$$

Then, we can build the relative position $\vec{R}_\tau$ between the intermediate center of mass G'_τ and the atom τ and obtain the final center of mass G (which is by definition independent of the initial arrangement τ) such that:

$$\vec{R}_\tau = \vec{x}_\tau - \frac{m_{\tau+1}\vec{x}_{\tau+1} + m_{\tau+2}\vec{x}_{\tau+2}}{m_{\tau+1} + m_{\tau+2}} \qquad \overrightarrow{OG} = \frac{1}{M}\sum_\tau m_\tau \vec{x}_\tau \quad (6.1.2)$$

with $M = m_\tau + m_{\tau+1} + m_{\tau+2}$ the total mass of the system. Physically, $\vec{r}_\tau$ corresponds to the vibration (or dissociation) of the diatom and $\vec{R}_\tau$ corresponds to the distance from the center-of-mass of the diatom to the atom. They describe respectively the position of a fictitious atom-atom particle of mass $\mu_{\tau+1\,\tau+2}$ and the position of a fictitious atom-diatom particle of mass $\mu_{\tau\,-\,\tau+1\,\tau+2}$ given by:

$$\mu_{\tau+1\,\tau+2} = \frac{(m_{\tau+1}m_{\tau+2})}{(m_{\tau+1} + m_{\tau+2})} \qquad \mu_{\tau\,-\,\tau+1\,\tau+2} = \frac{m_\tau(m_{\tau+1} + m_{\tau+2})}{M}. \quad (6.1.3)$$

Because we will consider potentials that do not depend on the individual position of the particles, we can separate the center of mass from the relative coordinates. As a consequence, we will work in the center-of-mass frame (i.e. $\overrightarrow{OG} = \vec{0}$).

From an angular point of view, we will use spherical coordinates to describe the vectors $(\vec{r}_\tau, \vec{R}_\tau)$. Let us note $(\hat{r}_\tau^{\mathrm{SF}}, \hat{R}_\tau^{\mathrm{SF}})$ their angular components in the space-fixed frame (SF). Jacobi's coordinates are then fully described by two three-dimensional vectors:

$$\vec{r}_\tau = \{r_\tau, \hat{r}_\tau^{\mathrm{SF}} = (\theta_{r_\tau}^{\mathrm{SF}}, \phi_{r_\tau}^{\mathrm{SF}})\} \qquad \vec{R}_\tau = \{R_\tau, \hat{R}_\tau^{\mathrm{SF}} = (\theta_{R_\tau}^{\mathrm{SF}}, \phi_{R_\tau}^{\mathrm{SF}})\}. \quad (6.1.4)$$

The associated momentum operators are given by:

$$\vec{p}_\tau = -i\hbar\nabla_{\vec{r}_\tau} \qquad \vec{P}_\tau = -i\hbar\nabla_{\vec{R}_\tau} \quad (6.1.5)$$

and the angular momentum operators related to these two vectors are:

$$\hat{\vec{j}}_\tau = \hat{\vec{r}}_\tau \times \hat{\vec{p}}_\tau \qquad \hat{\vec{l}}_\tau = \hat{\vec{R}}_\tau \times \hat{\vec{P}}_\tau \quad (6.1.6)$$

where we omit the label SF in the angular momentum terms for more readability. At the end, we obtain the total angular momentum $\hat{\vec{J}} = \hat{\vec{j}}_\tau + \hat{\vec{l}}_\tau$ and the total angular momentum projection quantum number M (eigenvalue of $\hat{\vec{J}}_z$) which are both conserved for collisions without external fields.

Mass-scaled Jacobi coordinates

To simplify future calculations, let's introduce the mass-scaled Jacobi vectors $(\vec{s}_\tau, \vec{S}_\tau)$ defined such that:

$$\vec{s}_\tau = d_\tau^{-1}\vec{r}_\tau \qquad\qquad \vec{S}_\tau = d_\tau \vec{R}_\tau \tag{6.1.7}$$

with:

$$d_\tau = \left[\frac{m_\tau}{\mu}\left(1-\frac{m_\tau}{M}\right)\right]^{1/2} \qquad\qquad \mu = \left(\frac{m_\tau m_{\tau+1} m_{\tau+2}}{m_\tau + m_{\tau+1} + m_{\tau+2}}\right)^{1/2}. \tag{6.1.8}$$

The scale factor d_τ changes the length of the position Jacobi vectors but not their orientation ($\hat{r}_\tau^{\mathrm{SF}} = \hat{s}_\tau^{\mathrm{SF}}$ and $\hat{R}_\tau^{\mathrm{SF}} = \hat{S}_\tau^{\mathrm{SF}}$). As a result, Eq. 6.1–6.1.6 remain valid for the mass-scaled Jacobi coordinates. The set of mass-scaled Jacobi coordinates $\vec{x}^{\mathrm{SF}}$ is therefore given by:

$$\vec{x}^{\mathrm{SF}} \equiv s_\tau, S_\tau, \theta_{S_\tau}^{\mathrm{SF}}, \phi_{S_\tau}^{\mathrm{SF}}, \theta_{s_\tau}^{\mathrm{SF}}, \phi_{s_\tau}^{\mathrm{SF}}. \tag{6.1.9}$$

Total Hamiltonian

As a consequence of Eq. 6.1.7, the kinetic energy operators $\nabla^2_{\vec{s}_\tau}$ and $\nabla^2_{\vec{R}_\tau}$ both have the same reduced mass μ. The total Hamiltonian can then be written simply as a function of a single six-dimensional vector $\vec{\mathcal{R}}_\tau = (\vec{s}_\tau, \vec{S}_\tau)$:

$$\begin{aligned}\hat{H} &= -\frac{\hbar^2}{2\mu_{\tau+1-\tau+2}}\nabla^2_{\vec{r}_\tau} - \frac{\hbar^2}{2\mu_{\tau-\tau+1\tau+2}}\nabla^2_{\vec{R}_\tau} + V(\vec{r}_\tau, \vec{R}_\tau) \\ &= -\frac{\hbar^2}{2\mu}(\nabla^2_{\vec{s}_\tau} + \nabla^2_{\vec{S}_\tau}) + V(\vec{s}_\tau, \vec{S}_\tau) \\ &= -\frac{\hbar^2}{2\mu}\nabla^2_{\vec{\mathcal{R}}_\tau} + V(\vec{\mathcal{R}}_\tau)\end{aligned} \tag{6.1.10}$$

where $\nabla^2_{\vec{\mathcal{R}}_\tau}$ can be express in terms of radial derivatives and angular momenta:

$$\nabla^2_{\vec{\mathcal{R}}_\tau} = \frac{1}{S_\tau s_\tau}\left(\frac{\partial^2}{\partial S_\tau^2} + \frac{\partial^2}{\partial s_\tau^2} + \frac{1}{S_\tau^2}\hat{l}_\tau^2 + \frac{1}{s_\tau^2}\hat{j}_\tau^2\right) S_\tau s_\tau \tag{6.1.11}$$

with:

$$\begin{cases} \hat{l}_\tau^2 = -\dfrac{\hbar^2}{\sin\theta_{S_\tau}^{\mathrm{SF}}}\dfrac{\partial}{\partial\theta_{S_\tau}^{\mathrm{SF}}}\sin\theta_{S_\tau}^{\mathrm{SF}}\dfrac{\partial}{\partial\theta_{S_\tau}^{\mathrm{SF}}} + \dfrac{\hat{l}_{z_\tau}^2}{\sin^2(\theta_{S_\tau}^{\mathrm{SF}})} & \hat{l}_{z_\tau}^2 = -\hbar^2\dfrac{\partial^2}{\partial\phi_{S_\tau}^{\mathrm{SF}\,2}} \\ \hat{j}_\tau^2 = -\dfrac{\hbar^2}{\sin\theta_{s_\tau}^{\mathrm{SF}}}\dfrac{\partial}{\partial\theta_{s_\tau}^{\mathrm{SF}}}\sin\theta_{s_\tau}^{\mathrm{SF}}\dfrac{\partial}{\partial\theta_{s_\tau}^{\mathrm{SF}}} + \dfrac{\hat{j}_{z_\tau}^2}{\sin^2(\theta_{s_\tau}^{\mathrm{SF}})} & \hat{j}_{z_\tau}^2 = -\hbar^2\dfrac{\partial^2}{\partial\phi_{s_\tau}^{\mathrm{SF}\,2}}. \end{cases} \tag{6.1.12}$$

In this way, we can study the motion of only one fictitious super-particle of given reduced mass μ and described by a generalized six-dimensional vector $\vec{\mathcal{R}}_\tau$. As a consequence, a much more symmetric expression of the Hamiltonian is then obtained. Moreover, mass-scaled Jacobi coordinates are convenient because, to be transformed in another arrangement (i.e. $\vec{s}_\tau, \vec{S}_\tau \rightarrow \vec{s}_{\tau'}, \vec{S}_{\tau'}$), it is only required to perform a single kinematic rotation:

$$\vec{\mathcal{R}}_{\tau+1} = \mathbb{T}(\chi_{\tau\rightarrow\tau+1})\vec{\mathcal{R}}_\tau. \tag{6.1.13}$$

Here $\mathbb{T}(\chi_{\tau\to\tau+1})$ is a 6×6 matrix[2] which depends on the skew angle $\chi_{\tau\to\tau+1}$ between the arrangements τ and τ' such that:

$$\begin{aligned}\begin{pmatrix}\vec{S}_{\tau+1}\\ \vec{s}_{\tau+1}\end{pmatrix} &= \mathbb{T}(\chi_{\tau\to\tau+1})\begin{pmatrix}\vec{S}_{\tau}\\ \vec{s}_{\tau}\end{pmatrix}\\ &= \begin{pmatrix}\cos\chi_{\tau\to\tau+1}\mathbf{I} & \sin\chi_{\tau\to\tau+1}\mathbf{I}\\ -\sin\chi_{\tau\to\tau+1}\mathbf{I} & \cos\chi_{\tau\to\tau+1}\mathbf{I}\end{pmatrix}\begin{pmatrix}\vec{S}_{\tau}\\ \vec{s}_{\tau}\end{pmatrix}\end{aligned} \tag{6.1.14}$$

with $\mathbf{I}$ a 3×3 diagonal unit matrix. The skew angle between two adjacent arrangements τ and $\tau+1$ is the negative obtuse angle[3] given by:

$$\tan\chi_{\tau\to\tau+1} = \frac{m_{\tau+2}}{\mu} \qquad\qquad \chi_{\tau\to\tau+1}\in[-\pi,-\pi/2]. \tag{6.1.15}$$

The sum of the skew angles is then:

$$\chi_{\tau\to\tau+1}+\chi_{\tau+1\to\tau+2}+\chi_{\tau+2\to\tau} = -2\pi \tag{6.1.16}$$

or conversely:

$$\chi_{\tau+1\to\tau}+\chi_{\tau+2\to\tau+1}+\chi_{\tau\to\tau+2} = 2\pi. \tag{6.1.17}$$

One can be convinced of Eq. 6.1.14 looking at Fig. 6.3, where $S_{\tau+1}$ can be expressed as a linear combination of S_τ and s_τ. In the case of three identical particles, the three angles must be equal for obvious reasons of symmetry:

$$\chi_{\tau\to\tau+1}=\chi_{\tau+1\to\tau+2}=\chi_{\tau+2\to\tau}=\tan^{-1}\left(\frac{m}{\mu}\right)=\tan^{-1}\left(\sqrt{3}\right)=-\frac{2\pi}{3}. \tag{6.1.18}$$

Note also that for three identical particles, the reduced mass reduces to $\mu\to m/\sqrt{3}$ and $d_\tau\to\sqrt{2/\sqrt{3}}\approx 1.07457$. As a consequence, Jacobi coordinates slightly differ from the mass-scaled ones but their use greatly simplifies the formalism.

Jacobian

The Jacobian is given by:

$$\begin{aligned}\int\int d\vec{s}_\tau d\vec{S}_\tau F &= \int_0^\infty S_\tau^2 dS_\tau \int_0^\infty s_\tau^2 dr \int d\hat{s}_\tau^{\mathrm{SF}} \int d\hat{S}_\tau^{\mathrm{SF}} F\\ &= \int_0^\infty S_\tau^2 dS_\tau \int_0^\infty s_\tau^2 ds_\tau \int_0^\pi \sin\theta_{s_\tau}^{\mathrm{SF}} d\theta_{s_\tau}^{\mathrm{SF}} \int_0^{2\pi} d\phi_{s_\tau}^{\mathrm{SF}}\\ &\quad\times \int_0^\pi \sin\theta_{S_\tau}^{\mathrm{SF}} d\theta_{S_\tau}^{\mathrm{SF}} \int_0^{2\pi} d\phi_{S_\tau}^{\mathrm{SF}}\ F\end{aligned} \tag{6.1.19}$$

for any arbitrary function $F=F(\vec{s}_\tau,\vec{S}_\tau)$.

[2] We used a passive rotation convention. To get the equivalent formulas from an active point of view, one must replace $\chi_{\tau\to\tau+1}=-\chi_{\tau\to\tau+1}$.

[3] In [151] , it was defined as a positive obtuse angle then the sum of the three angles is equal to 4π. However, this does not affect the rest of the formalism.

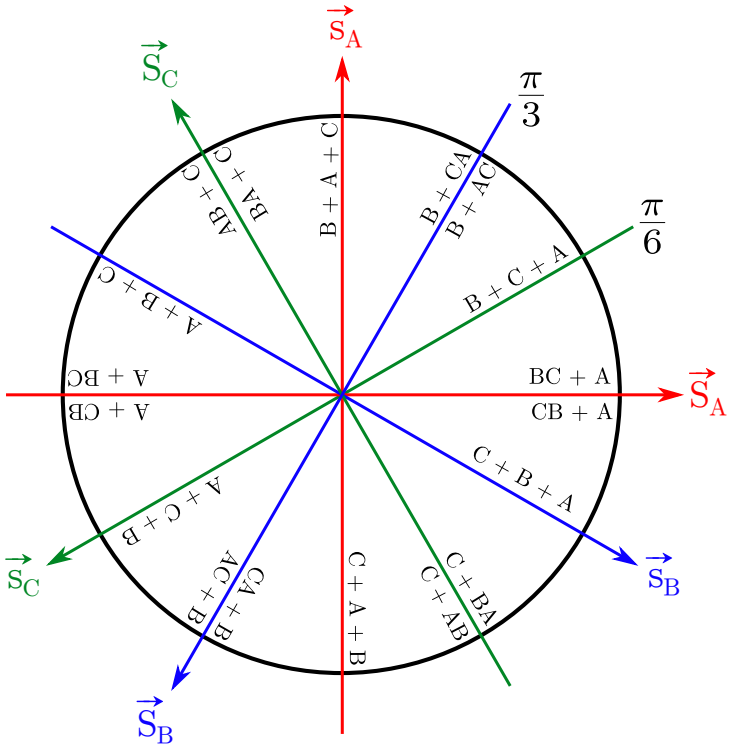

Figure 6.3: Skew angles for the three arrangements of a three-body linear configuration.

Partial waves expansion

As in the two-body formalism, it is possible to develop the total wave function for a given total energy E in terms of partial waves. To explain the basis functions on which the partial waves will be expanded, let us make the internal Hamiltonian of the diatom $\hat{h}_\tau$ explicit in Eq. 6.1.10:

$$\begin{aligned}\hat{H} &= -\frac{\hbar^2}{2\mu}\left[\frac{1}{S_\tau s_\tau}\left(\frac{\partial^2}{\partial S_\tau^2}+\frac{\partial^2}{\partial s_\tau^2}+\frac{1}{S_\tau^2}\hat{l}_\tau^2+\frac{1}{s_\tau^2}\hat{j}_\tau^2\right)S_\tau s_\tau\right]+V(\vec{s}_\tau,\vec{S}_\tau)\\ &=\left\{-\frac{\hbar^2}{2\mu}\left[\frac{1}{S_\tau}\left(\frac{\partial^2}{\partial S_\tau^2}S_\tau\right)+\frac{1}{S_\tau^2}\hat{l}_\tau^2\right]+U(\hat{s}_\tau,\hat{S}_\tau)\right\}+\left\{-\frac{\hbar^2}{2\mu}\left[\frac{1}{s_\tau}\left(\frac{\partial^2}{\partial s_\tau^2}s_\tau\right)+\frac{1}{s_\tau^2}\hat{j}_\tau^2\right]+v(s_\tau)\right\}\\ &=\left\{-\frac{\hbar^2}{2\mu}\left[\frac{1}{S_\tau}\left(\frac{\partial^2}{\partial S_\tau^2}S_\tau\right)+\frac{1}{S_\tau^2}\hat{l}_\tau^2\right]+U(\hat{s}_\tau,\hat{S}_\tau)\right\}+\hat{h}_\tau\end{aligned} \tag{6.1.20}$$

where we separated the potential of the diatomic in the arrangement τ to the other two-body potential energies and to the non-additive three-body interaction terms that we have regrouped indiscriminately in $U(\hat{s}_\tau,\hat{S}_\tau)$ such that:

$$V(\vec{s}_\tau,\vec{S}_\tau)=v(s_\tau)+U(\vec{s}_\tau,\vec{S}_\tau). \tag{6.1.21}$$

We will use the eigenfunctions of the operators $\{\hat{l}_\tau^2,\hat{j}_\tau^2,\hat{J}^2,\hat{J}_z,\hat{h}_\tau\}$ to form the angular basis functions on which the partial waves will be expanded. The eigenfunctions of the total angular momentum $\hat{J}$ are also eigenfunctions of the angular momentum $\hat{j}_\tau$ and $\hat{l}_\tau$.

We then note $\mathcal{Y}_{j_\tau l_\tau}^{JM}(\hat{S}_\tau^{\mathrm{SF}}, \hat{s}_\tau^{\mathrm{SF}})$ the coupled spherical harmonics of the arrangement τ which can be expressed as a linear combination of $\mathcal{Y}_{j_\tau}^{m_{j_\tau}}(\hat{s}_\tau)$ and $\mathcal{Y}_{l_\tau}^{m_{l_\tau}}(\hat{S}_\tau)$ such that:

$$\mathcal{Y}_{j_\tau l_\tau}^{JM}(\hat{S}_\tau^{\mathrm{SF}}, \hat{s}_\tau^{\mathrm{SF}}) = \sum_{m_{j_\tau}=-j_\tau}^{+j_\tau} \langle j_\tau, l_\tau; m_{j_\tau}, M - m_{j_\tau} \mid JM \rangle \, \mathcal{Y}_{j_\tau}^{m_{j_\tau}}\left(\hat{s}_\tau^{\mathrm{SF}}\right) \mathcal{Y}_{l_\tau}^{M-m_{j_\tau}}(\hat{S}_\tau^{\mathrm{SF}}) \quad (6.1.22)$$

where $\langle j_\tau, l_\tau; m_{j_\tau}, M - m_{j_\tau} \mid JM \rangle$ are the well known Clebsch–Gordan coefficients [182]. On one hand, the angular momentum verifies

$$\begin{cases} \hat{j}_\tau^2 \mathcal{Y}_{j_\tau}^{m_{j_\tau}} = \hbar^2 j_\tau(j_\tau+1)\mathcal{Y}_{j_\tau}^{m_{j_\tau}} & \hat{j}_{\tau_z} \mathcal{Y}_{j_\tau}^{m_{j_\tau}} = \hbar m_{j_\tau} \mathcal{Y}_{j_\tau}^{m_{j_\tau}} \\ \hat{l}_\tau^2 \mathcal{Y}_{l_\tau}^{m_{l_\tau}} = \hbar^2 l_\tau(l_\tau+1)\mathcal{Y}_{l_\tau}^{m_{l_\tau}} & \hat{l}_{\tau_z} \mathcal{Y}_{l_\tau}^{m_{l_\tau}} = \hbar m_{l_\tau} \mathcal{Y}_{l_\tau}^{m_{l_\tau}} \\ \hat{J}^2 \mathcal{Y}_{j_\tau l_\tau}^{JM} = \hbar^2 J(J+1)\mathcal{Y}_{j_\tau l_\tau}^{JM} & \hat{J}_z \mathcal{Y}_{j_\tau l_\tau}^{JM} = \hbar M \mathcal{Y}_{j_\tau l_\tau}^{JM} \end{cases} \quad (6.1.23)$$

and on the other hand, the Hamiltonian $\hat{h}_\tau$ has for solutions:

$$\left\{ -\frac{\hbar^2}{2\mu} \left[\frac{1}{s_\tau} \left(\frac{\partial^2}{\partial s_\tau^2} s_\tau \right) + \frac{1}{s_\tau^2} \hat{j}_\tau^2 \right] + v(s_\tau) \right\} \frac{\chi_{v_\tau j_\tau}(s_\tau)}{s_\tau} = \varepsilon_{v_\tau j_\tau} \frac{\chi_{v_\tau j_\tau}(s_\tau)}{s_\tau}$$

so that:

$$\left\{ -\frac{\hbar^2}{2\mu} \frac{\partial^2}{\partial s_\tau^2} + \frac{\hbar^2 j(j+1)}{2\mu s_\tau^2} + v(s_\tau) \right\} \chi_{v_\tau j_\tau}(s_\tau) = \varepsilon_{v_\tau j_\tau} \chi_{v_\tau j_\tau}(s_\tau). \quad (6.1.24)$$

These functions describe the rotational and vibrational motion of the diatom. To illustrate the shape of the $\chi_{v_\tau j_\tau}(s_\tau)$ functions, we have represented in Fig. 6.4 the $\chi_{00}(s_\tau)$, $\chi_{10}(s_\tau)$ and $\chi_{20}(s_\tau)$ functions, taking the $^7Li_2$ dimer as an example. The eigenfunctions and eigenenergies have been calculating solving Eq. 6.1.24 using the Numerov algorithm [185] already described in chapter 4. We can observe that the eigenfunctions are localized functions that are centered approximately at the same position as the minimum of the two-body potential well, i.e. at about $s_\tau = 7.5$ a_0 as described in chapter 8. We can note that the vibrational quantum number v gives directly the number of nodes of the wave functions.

The basis functions on which the partial waves will be expanded are then composed by the functions given in Eq. 6.1.22 and Eq. 6.1.24 such that:

$$\Phi_{\tau v j l}^{JME}(\hat{S}_\tau^{\mathrm{SF}}, \vec{s}_\tau) = \frac{1}{s_\tau} \chi_{vj}(s_\tau) \mathcal{Y}_{jl}^{JM}(\hat{S}_\tau^{\mathrm{SF}}, \hat{s}_\tau^{\mathrm{SF}}) \quad (6.1.25)$$

where $\tau v j l \equiv \tau v_\tau j_\tau l_\tau$ and where $E_{\mathrm{tot}} \equiv E$ for more readability. The total nuclear wave function can be expanded in function of these basis functions via:

$$\psi_{\tau v j l}^{JME}(\vec{S}_\tau, \vec{s}_\tau) = \sum_{\tau'' v'' j'' l''} \frac{1}{S_{\tau''}} \Phi_{\tau'' v'' j'' l''}^{JME}(\hat{S}_{\tau''}^{\mathrm{SF}}, \vec{s}_{\tau''}) F_{\tau'' v'' j'' l'', \tau v j l}^{JME}(S_{\tau''}). \quad (6.1.26)$$

As previously seen, J and M are conserved during the collision and are therefore good quantum numbers. For a given energy E_{tot}, the expansion of the total wave function is

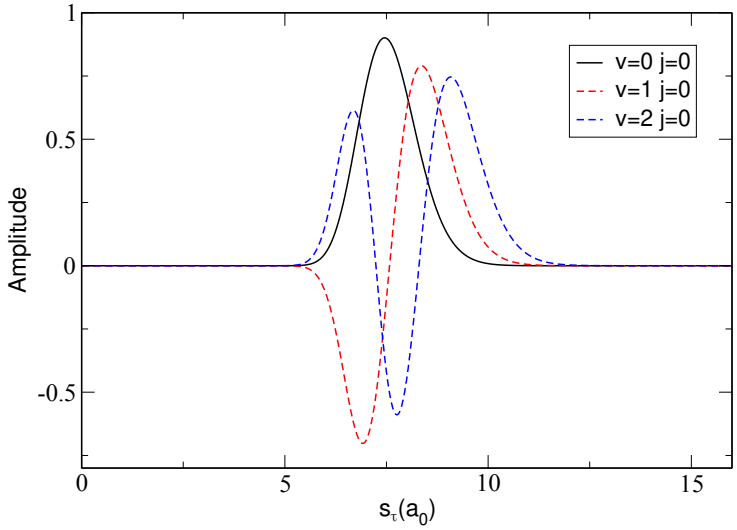

Figure 6.4: Normalized rovibrational eigenfunctions of the $^7Li_2$ dimer in function of the interatomic distance s_τ. The black solid curve, the red dashed curve and the blue dashed curve correspond respectively to $\chi_{00}(s_\tau)$, $\chi_{10}(s_\tau)$ and $\chi_{20}(s_\tau)$.

term of partial waves is therefore given by:

$$\Psi^E_{\tau v j m_j}(\vec{k}_{\tau vj}, \vec{s}_\tau, \vec{S}_\tau) = \sum_{JMlm_l jm_j} N_{JMlm_l jm_j}(\vec{k}_{\tau vj}) \psi^{JME}_{\tau vjl}(\vec{s}_\tau, \vec{S}_\tau) \tag{6.1.27}$$

where $N_{JMlm_l jm_j}(\vec{k}_{\tau vj})$ is a normalization factor and the wave vector $k_{\tau vj}$ is given by:

$$k_{\tau vj} = \sqrt{\frac{2\mu_{\tau-\tau+1\tau+2}(E_{\text{tot}} - \varepsilon_{\tau vj})}{\hbar^2}}. \tag{6.1.28}$$

Note that these equations are very similar to the one given in chapter 3 because the three-body wave functions are developed in terms of functions describing the collision of a diatom and an atom (which is very similar to a two body system: atom-diatom).

Coupled equations

If we insert the total wave function (Eq. 6.1.26) into the total Hamiltonian (Eq. 6.1.10), multiply on the left by $\left[\Phi^{JME}_{\tau vjl}(\hat{S}^{\text{SF}}_\tau, \vec{s}_\tau)\right]^*$ and integrate over the angular part, we get a set of coupled equations. By solving it numerically, we obtain the radial wave function $\mathbf{F}(R)$ (or the $\mathbf{Z}$ matrix) from which we can extract the different observables we need. These coupled equations are given by:

$$\left[-\frac{\hbar^2}{2\mu}\frac{d^2}{dS_{\tau'}^2}+\frac{\hbar^2 l'\left(l'+1\right)}{2\mu S_{\tau'}^2}+\varepsilon_{\tau' v' j'}-E_{\text{tot}}\right]F^{JME}_{\tau' v' j' l',\tau v j l}\left(S_{\tau'}\right) + \sum_{v'' j'' l''}\mathcal{U}^{JME\tau'}_{v' j' l',v'' j'' l''}\left(S_{\tau'}\right)F^{JME}_{\tau' v'' j'' l'',\tau v j l}\left(S_{\tau'}\right) + \sum_{\tau''\neq\tau'}\sum_{v'' j'' l''}\mathcal{W}^{JME}_{\tau' v' j' l',\tau'' v'' j'' l''}F^{JME}_{\tau'' v'' j'' l'',\tau v j l}\left(S_{\tau'}\right)=0 \quad (6.1.29)$$

with the coupling matrix elements:

$$\begin{aligned}\mathcal{U}^{JME\tau'}_{v' j' l',v'' j'' l''}(S_{\tau'}) &= \langle\Phi^{JME}_{\tau' v' j' l'}|U|\Phi^{JME}_{\tau' v'' j'' l''}\rangle_{\hat{S}^{\text{SF}}_{\tau'}\hat{s}^{\text{SF}}_{\tau'}} \\ &= \iint d\hat{S}^{\text{SF}}_{\tau'}d\vec{s}_{\tau'}\Phi^{JME}_{\tau' v' j' l'}(\hat{S}^{\text{SF}}_{\tau'},\vec{s}_{\tau'})U(\vec{S}_{\tau'},\vec{s}_{\tau'})\Phi^{JME}_{\tau' v'' j'' l''}(\hat{S}^{\text{SF}}_{\tau'},\vec{s}_{\tau'})\end{aligned} \quad (6.1.30)$$

and:

$$\mathcal{W}^{JME}_{\tau' v' j' l',\tau'' v'' j'' l''}F^{JME}_{\tau'' v'' j'' l'',\tau v j l}\left(S_{\tau'}\right)=S_{\tau'}\iint d\hat{S}^{\text{SF}}_{\tau'}d\vec{s}_{\tau'}\Phi^{JME}_{\tau' v' j' l'}(\hat{S}^{\text{SF}}_{\tau'},\vec{s}_{\tau'})(H-E) \frac{1}{S_{\tau''}}\Phi^{JME}_{\tau'' v'' j'' l''}(\hat{S}^{\text{SF}}_{\tau''},\vec{s}_{\tau''})F^{JME}_{\tau'' v'' j'' l'',\tau v j l}\left(S_{\tau''}\right). \quad (6.1.31)$$

This set of coupled integro-differential equations are impossible to solve numerically because the terms $\mathcal{W}^{JME}_{\tau' v' j' l',\tau'' v'' j'' l''}F^{JME}_{\tau'' v'' j'' l'',\tau v j l}\left(S_{\tau'}\right)$ require to know the radial functions $F^{JME}_{\tau'' v'' j'' l'',\tau v j l}\left(S_{\tau''}\right)$ whose dependence on $d\hat{S}^{\text{SF}}_{\tau'}d\vec{s}_{\tau'}$ is too complex. In fact, the mass-scaled Jacobi coordinates are not well adapted in the short-range region where the three arrangements coexist ($\tau'\neq\tau''$) or when the atoms are all far from each others.

However, the mass-scaled Jacobi coordinates will be useful for the matching procedure even if the Z-matrix will be obtained in another set of coordinates. In addition, these coordinates will help us to understand how less intuitive coordinates work such as the the Delves hyperspherical ones described in the next section.

6.2 SF-Delves Coordinates

As shown in the previous section, the mass-scaled Jacobi coordinates cannot be used during the propagation process. In this section, we will introduce another set of three-body coordinates, known as *Delves hyperspherical coordinates*. These coordinates are essential to make the link between the mass-scaled Jacobi coordinates and more subtle hyperspherical coordinates (as the ones used in section 6.4). We will follow the same structure as in the previous section: we will present the coordinates, the three-body Hamiltonian and the partial wave expansion of the total wave function.

SF-Delves Coordinates

For a given arrangement, we can define the hyperradius ρ and the Delves angle ω_τ such that:

$$\rho = \left(S_\tau^2 + s_\tau^2\right)^{1/2} \qquad \omega_\tau = \arctan\left(\frac{s_\tau}{S_\tau}\right) \tag{6.2.1}$$

with $\rho \in [0, +\infty[$ and $\omega_\tau \in [0, \pi/2]$. Note that the hyperradius is independent of the arrangement τ because the kinematic transformation from one arrangement to another is a unitary transformation and therefore:

$$\rho \equiv S_\tau^2 + s_\tau^2 = S_{\tau+1}^2 + s_{\tau+1}^2 = S_{\tau+2}^2 + s_{\tau+2}^2. \tag{6.2.2}$$

The relationship between Delves and mass-scaled Jacobi coordinates are similar as that of polar to Cartesian coordinates:

$$s_\tau = \rho \sin\omega_\tau \qquad S_\tau = \rho\cos\omega_\tau. \tag{6.2.3}$$

To complete the collective set of Delves coordinates, noted $\vec{x}_\tau^{\,\mathrm{SF}}$, we must add the four SF angles of the τ arrangement such that:

$$\vec{x}_\tau^{\,\mathrm{SF}} \equiv (\rho, \hat{\rho}_\tau^{\mathrm{SF}}) \equiv (\rho, \omega_\tau, \theta_{S_\tau}^{\mathrm{SF}}, \phi_{S_\tau}^{\mathrm{SF}}, \theta_{s_\tau}^{\mathrm{SF}}, \phi_{s_\tau}^{\mathrm{SF}}) \equiv (\rho, \omega_\tau, \hat{S}_\tau^{\mathrm{SF}}, \hat{s}_\tau^{\mathrm{SF}}). \tag{6.2.4}$$

Thus, for a fixed value of ρ, S_τ and s_τ are varied by changing the value of the Delves angle. As a consequence, a part of the radial variation has been transformed into an angular dependence (i.e. into the basis functions) which will simplify the final set of coupled equations. However, all the five angles presented here are those of one of the arrangement: the different arrangements are therefore not treated equivalently. For these reasons, we will only use Delves coordinates at large ρ, where the arrangement τ is approximately a good quantum number.

Total Hamiltonian

In the SF-Delves coordinates, the total Hamiltonian is given by:

$$\hat{H} = -\frac{\hbar^2}{2\mu\rho^5}\frac{\partial}{\partial\rho}\rho^5\frac{\partial}{\partial\rho} + \frac{\hat{\Lambda}^2\left(\hat{\rho}_\tau^{\mathrm{SF}}\right)}{2\mu\rho^2} + V\left(\rho, \hat{\rho}_\tau^{\mathrm{SF}}\right) \tag{6.2.5}$$

with:

$$\hat{\Lambda}^2\left(\hat{\rho}_\tau^{\mathrm{SF}}\right) = -\frac{\hbar^2}{\sin^2(2\omega_\tau)}\frac{\partial}{\partial\omega_\tau}\sin^2(2\omega_\tau)\frac{\partial}{\partial\omega_\tau} + \frac{\hat{l}_\tau^2}{\cos^2\omega_\tau} + \frac{\hat{j}_\tau^2}{\sin^2\omega_\tau} \tag{6.2.6}$$

the grand angular momentum operator. This operator, common to the different hyperspherical coordinates, has hyperspherical harmonics Y_λ as eigenfunctions and its eigenvalues are given by:

$$\hat{\Lambda}^2 Y_\lambda = \lambda(\lambda+4)Y_\lambda \tag{6.2.7}$$

with $\lambda = 0, 1, 2, ...$ and are highly degenerate [152].

Jacobian

The Jacobian is given by:

$$\begin{aligned}\iint d\vec{S}_\tau d\vec{s}_\tau F &= \frac{1}{4}\int_0^\infty \rho^5 d\rho \int_0^{\pi/2} \sin^2(2\omega_\tau)\, d\omega_\tau \int d\hat{S}_\tau^{\mathrm{SF}} \int d\hat{s}_\tau^{\mathrm{SF}} F \\ &= \frac{1}{4}\int_0^\infty \rho^5 d\rho \int_0^{\pi/2} \sin^2(2\omega_\tau)\, d\omega_\tau \int_0^\pi \sin\theta_{S_\tau}^{\mathrm{SF}} d\theta_{S_\tau}^{\mathrm{SF}} \\ &\quad \times \int_0^{2\pi} d\phi_{S_\tau}^{\mathrm{SF}} \int_0^\pi \sin\theta_{s_\tau}^{\mathrm{SF}} d\theta_{s_\tau}^{\mathrm{SF}} \int_0^{2\pi} d\phi_{s_\tau}^{\mathrm{SF}} F \end{aligned} \quad (6.2.8)$$

for any arbitrary function $F = F(\vec{x}_\tau^{\mathrm{SF}})$.

Partial waves expansion

One could use hyperspherical harmonics as basis functions, however it has been demonstrated that they are a poor basis set for representing localized functions. The basis functions usually used are rather:

$$\Phi_{\tau vjl}^{JME}\left(\hat{\rho}_\tau^{\mathrm{SF}};\rho\right) = \frac{2\chi_{\tau vjl}(\omega_\tau;\rho)}{\sin 2\omega_\tau} Y_{jl}^{JM}\left(\hat{S}_\tau^{\mathrm{SF}}, \hat{s}_\tau^{\mathrm{SF}}\right) \quad (6.2.9)$$

where the functions $Y_{jl}^{JM}(\hat{S}_\tau^{\mathrm{SF}})$ have already been defined in Eq. 6.1.22. The $\chi_{\tau vjl}(\omega_\tau;\rho)$ functions are solution of:

$$\begin{aligned}&\left[\frac{-\hbar^2}{2\mu\rho^2}\left(\frac{d^2}{d\omega_\tau^2} - \frac{j_\tau(j_\tau+1)}{\sin^2\omega_\tau} - \frac{l_\tau(l_\tau+1)}{\cos^2\omega_\tau}\right) + v(\omega_\tau;\rho)\right]\chi_{\tau vjl}(\omega_\tau;\rho) \\ &\qquad = \varepsilon_{\tau vjl}(\rho)\chi_{\tau vjl}(\omega_\tau;\rho)\end{aligned} \quad (6.2.10)$$

with $v(\omega_\tau;\rho)$ the potential of the diatom in the arrangement τ. This equation admits solutions $\varepsilon_{\tau vjl}(\rho) < 0$ which correspond to bound states well identified by the quantum numbers τvjl. Since $s_\tau = \rho\sin\omega_\tau$, for large values of ρ and small finite values of s_τ, we have $s_\tau \approx \rho\,\omega_\tau$. By replacing s_τ by $\rho\,\omega_\tau$ in Eq. 6.1.24 and after some mathematical manipulations [233], we have:

$$\frac{1}{\sqrt{\rho}}\chi_{\tau vjl}(\omega_\tau;\rho) \underset{\rho\to+\infty}{\longrightarrow} \chi_{\tau vj}(\rho\,\omega_\tau) \quad (6.2.11)$$

$$\varepsilon_{\tau vjl}(\rho) \underset{\rho\to+\infty}{\longrightarrow} \varepsilon_{\tau vj}, \quad (6.2.12)$$

which show that the Delves functions tend to the Jacobi ones at large distances. This can be verified by looking at Fig. 6.5 (a), where Delves wave functions (rescaled by a $1/\sqrt{\rho}$ factor) match perfectly with Jacobi functions for $^7Li_2$ diatom at $\rho = 60$ a_0.

The Eq. 6.2.10 also admits positive solutions $\varepsilon_{\tau vjl}(\rho) > 0$ that can describe:

- quasi-bound states where $\varepsilon_{\tau vjl}(\rho) \underset{\rho\to+\infty}{\longrightarrow}$ constant. These are manifestations of shape resonances because the centrifugal terms are at the origin of barriers that allow the existence of metastable states.

- continuum states (also called three-body breakup adiabats) where the distances between any two particles can approach infinity. Contrary to quasi-bound states, their energy approach 0 when ρ increase following:

$$\varepsilon_{\tau vjl}(\rho) \underset{\rho\to+\infty}{\longrightarrow} \frac{(\lambda+2)^2}{2\mu\rho^2} \tag{6.2.13}$$

  with $\lambda = 2v_\tau + j_\tau + l_\tau$. In this case, v_τ no longer refers to any vibration mode but is used to count the wave functions [231]. In Fig. 6.5 (b), we represented the two first positive solutions $\varepsilon_{\tau vjl}$ for $j = 0$ and $l = 0$. We can see that they are non-localized functions and it has been demonstrated that when the potential is fixed to 0, they correspond to hyperspherical harmonics [231].

The expansion of the partial waves are then given by:

$$\psi^{JME}_{\tau vjl} = \frac{2}{\rho^{5/2}} \sum_{\tau''v''j''l''} \frac{\chi_{\tau''v''j''l''}(\omega_{\tau''};\rho)}{\sin 2\omega_{\tau''}} Y^{JM}_{j''l''}\left(\hat{S}^{\mathrm{SF}}_{\tau''}, \hat{s}^{\mathrm{SF}}_{\tau''}\right) F^{JME(1,2)}_{\tau''v''j''l'',\tau vjl}(\rho). \tag{6.2.14}$$

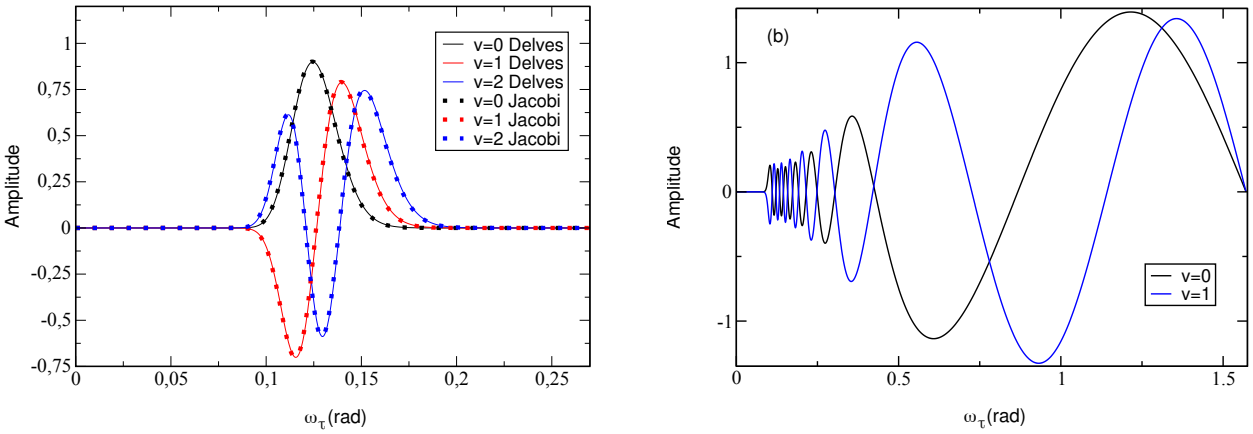

Figure 6.5: Left panel: Comparison of Delves renormalized functions $\frac{1}{\sqrt{\rho}}\chi_{\tau v00}(\omega_\tau;\rho = 60\,\text{a.u})$ (solid lines) and Jacobi functions $\chi_{\tau v0}(\rho\,\omega_\tau)$ (dotted lines) of $^7Li_2$ bound states with $v = 0$ (black), $v = 1$ (red) and $v = 2$ (blue). Right panel: Delves continuum functions $\chi_{\tau v00}(\omega_\tau;\rho = 60\,\text{a.u})$ for $v = 0$ (black) and $v = 1$ (blue).

6.3 BF$_\tau$-Delves Coordinates

As we can see in the Jacobian given in Eq. 6.2.8, there are four integrals over $\hat{s}_\tau^{\mathrm{SF}}$ and $\hat{S}_\tau^{\mathrm{SF}}$ which are numerically heavy. The passage to a mobile BF$_\tau$-frame implies a slightly more complicated formalism but the appearance of Wigner rotation matrices with well-known algebraically integrals alleviate numerical calculations. This is why we present the BF$_\tau$-Delves Coordinates in this section. As in the previous sections, we will present the coordinates, the three-body Hamiltonian, the partial wave expansion of the total wave function and the set of coupled equations describing the dynamics of the three-body system.

BF$_\tau$-Delves Frame

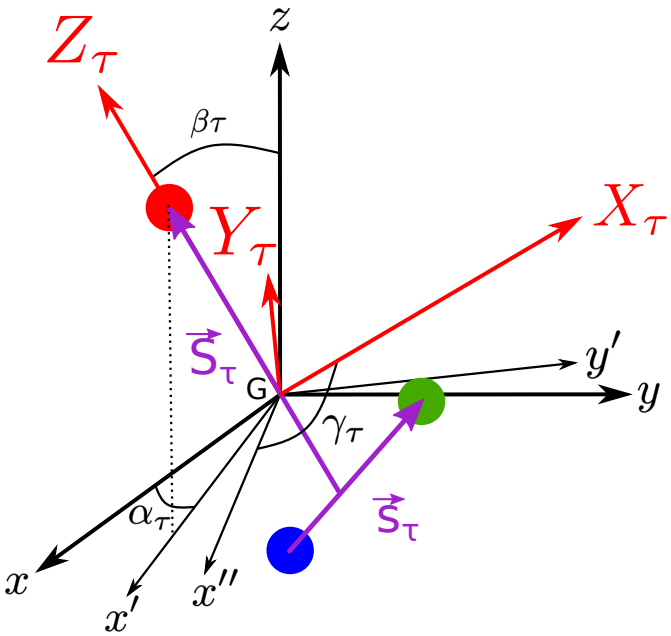

Figure 6.6: Passage from the space-fixed frame $(Gxyz)$ to the body-fixed frame $(GX_\tau Y_\tau Z_\tau)$. The axis x' and y' are the intermediate axis after the rotation of an angle α_τ around the axis z. The x'' axis comes from the rotation β_τ around the axis y'.

Let us note $(GX_\tau Y_\tau Z_\tau)$ the body-fixed (BF$_\tau$) frame shown in Fig. 6.6 [143, 144, 150, 151]. The (GZ_τ) axis is oriented along the $\vec{S}_\tau$ vector and the plane $(GX_\tau Z_\tau)$ contains the $\vec{s}_\tau$ vector. In Cartesian coordinates, the two vectors are given by:

$$\vec{S}_\tau^{\mathrm{BF}} = \begin{pmatrix} S_{X_\tau}^{\mathrm{BF}} \\ S_{Y_\tau}^{\mathrm{BF}} \\ S_{Z_\tau}^{\mathrm{BF}} \end{pmatrix} = \begin{pmatrix} 0 \\ 0 \\ S_\tau \end{pmatrix} \qquad \vec{s}_\tau^{\mathrm{BF}} = \begin{pmatrix} s_{X_\tau}^{\mathrm{BF}} \\ s_{Y_\tau}^{\mathrm{BF}} \\ s_{Z_\tau}^{\mathrm{BF}} \end{pmatrix} = \begin{pmatrix} s_\tau \sin\eta_\tau \\ 0 \\ s_\tau \cos\eta_\tau \end{pmatrix} \tag{6.3.1}$$

with:

$$\eta_\tau = \arccos\left(\frac{\vec{S}_\tau \cdot \vec{s}_\tau}{S_\tau s_\tau}\right) \tag{6.3.2}$$

the angle between $\vec{S}_\tau$ and $\vec{s}_\tau$. For $\eta = (0, \pi)$, the three particles are aligned while for $\eta = \pi/2$ the vectors $\vec{S}_\tau$ and $\vec{s}_\tau$ are orthogonal. In the following, we note the spherical components of the two mass-scaled Jacobi vectors in the BF_τ frame as:

$$\vec{S}_\tau = \left\{ S_\tau, \hat{S}_\tau^{\mathrm{BF}} = \left(\theta_{S_\tau}^{\mathrm{BF}}, \phi_{S_\tau}^{\mathrm{BF}}\right) \right\} \quad \vec{s}_\tau = \left\{ s_\tau, \hat{s}_\tau^{\mathrm{BF}} = \left(\theta_{s_\tau}^{\mathrm{BF}}, \phi_{s_\tau}^{\mathrm{BF}}\right) \right\} \tag{6.3.3}$$

with more specifically:

$$\left(\theta_{S_\tau}^{\mathrm{BF}}, \phi_{S_\tau}^{\mathrm{BF}}\right) = (0, 0) \qquad \left(\theta_{s_\tau}^{\mathrm{BF}}, \phi_{s_\tau}^{\mathrm{BF}}\right) = (\eta_\tau, 0). \tag{6.3.4}$$

Let $\mathbb{R}(\mathrm{BF}_\tau \leftarrow \mathrm{SF})$[4] be the ordinary spatial rotation operator that carries the initial space-fixed frame to the body-fixed one. This 6×6 matrix depends on the three Euler angles $(\alpha_\tau, \beta_\tau, \gamma_\tau)$ such that:

$$\mathbb{R}_{1\to 2}(\alpha_\tau, \beta_\tau, \gamma_\tau) = \begin{pmatrix} \mathbb{R} & 0 \\ 0 & \mathbb{R} \end{pmatrix} \tag{6.3.5}$$

with:

$$\mathbb{R} = \begin{pmatrix} \cos\alpha_\tau \cos\beta_\tau \cos\gamma_\tau - \sin\alpha_\tau \sin\gamma_\tau & \sin\alpha_\tau \cos\beta_\tau \cos\gamma_\tau + \cos\alpha_\tau \sin\gamma_\tau & -\sin\beta_\tau \cos\gamma_\tau \\ -\cos\alpha_\tau \cos\beta_\tau \sin\gamma_\tau - \sin\alpha_\tau \cos\gamma_\tau & -\sin\alpha_\tau \cos\beta_\tau \sin\gamma_\tau + \cos\alpha_\tau \cos\gamma_\tau & \sin\beta_\tau \sin\gamma_\tau \\ \cos\alpha_\tau \sin\beta_\tau & \sin\alpha_\tau \sin\beta_\tau & \cos\beta_\tau \end{pmatrix}.$$

As we want the Z_τ-axis to be along $\vec{S}_\tau$ and as we want $\vec{s}_\tau$ to be in the $(GX_\tau Z_\tau)$ plane, we need:

$$\alpha_\tau = \phi_{S_\tau}^{\mathrm{SF}} \qquad \beta_\tau = \theta_{S_\tau}^{\mathrm{SF}} \qquad \gamma_\tau = \varphi_\tau \tag{6.3.6}$$

with φ_τ chosen to get $\phi_{s_\tau} = 0$.

If we regroup the internal coordinates $(\rho, \omega_\tau, \eta_\tau)$ with the Euler angles $(\alpha_\tau, \beta_\tau, \gamma_\tau)$, we form the BF_τ-Delves hyperspherical coordinates:

$$\vec{x}^{\mathrm{BF}} \equiv (\rho, \omega_\tau, \eta_\tau, \alpha_\tau, \beta_\tau, \gamma_\tau). \tag{6.3.7}$$

Total Hamiltonian

In the BF_τ-Delves coordinates, the total Hamiltonian is given by:

$$\hat{H} = -\frac{\hbar^2}{2\mu\rho^5}\frac{\partial}{\partial\rho}\rho^5\frac{\partial}{\partial\rho} + \frac{\hat{\Lambda}^2\left(\hat{\rho}_\tau^{\mathrm{BF}}\right)}{2\mu\rho^2} + V\left(\rho, \hat{\rho}_\tau^{\mathrm{BF}}\right) \tag{6.3.8}$$

with:

$$\hat{\Lambda}^2\left(\hat{\rho}_\tau^{\mathrm{BF}}\right) = -\frac{\hbar^2}{\sin^2(2\omega_\tau)}\frac{\partial}{\partial\omega_\tau}\sin^2(2\omega_\tau)\frac{\partial}{\partial\omega_\tau} + \frac{\hat{l}_\tau^2}{\cos^2\omega_\tau} + \frac{\hat{j}_\tau^2}{\sin^2\omega_\tau} \tag{6.3.9}$$

with this time $\hat{l}_\tau^2$ and $\hat{j}_\tau^2$ expressed in the BF_τ-frame [151].

[4] To be consistent with Eq. 6.1.13, we keep a passive rotation convention.

Jacobian

The Jacobian is given by:

$$\begin{aligned}\iint d\vec{S}_\tau d\vec{s}_\tau F &= \frac{1}{4}\int_0^\infty \rho^5 d\rho \int_0^{\pi/2} \sin^2(2\omega_\tau)\, d\omega_\tau \int d\hat{S}_\tau^{\mathrm{BF}} \int d\hat{s}_\tau^{\mathrm{BF}} F \\ &= \frac{1}{4}\int_0^\infty \rho^5 d\rho \int_0^{\pi/2} \sin^2(2\omega_\tau)\, d\omega_\tau \int_0^{\pi} \sin\eta_\tau d\eta_\tau \\ &\quad \times \int_0^{2\pi} d\alpha_\tau \int_0^{\pi} \sin\beta_\tau d\beta_\tau \int_0^{2\pi} d\gamma_\tau F \end{aligned} \tag{6.3.10}$$

for any arbitrary function $F = F(\vec{x}_\tau^{\mathrm{BF}})$.

Partial wave expansion

The surface functions are given by [151]:

$$\Phi^{JME}_{\tau v j \Lambda_\tau}(\hat{\rho}_\tau^{\mathrm{BF}};\rho) = \frac{2\chi_{\tau v j}(\omega_\tau;\rho)}{\sin 2\omega_\tau} Y^{JM}_{j\Omega_\tau}(\hat{R}_\tau^{\mathrm{BF}}, \hat{r}_\tau^{\mathrm{BF}}) \tag{6.3.11}$$

where Λ_τ is the projection of $\hat{\vec{J}}$ on the (GZ_τ) axis. The expansion of the partial waves are given by:

$$\psi^{JME}_{\tau v j l} = \frac{2}{\rho^{5/2}} \sum_{\tau'' v'' j'' \Lambda''_{\tau''}} \frac{\chi_{\tau'' v'' j''}(\rho;\omega_{\tau''})}{\sin 2\omega_{\tau''}} \quad Y^{JM}_{j''\Lambda''_{\tau''}}\left(\hat{R}_{\tau''}^{\mathrm{BF}}, \hat{r}_{\tau''}^{\mathrm{BF}}\right) F^{JME(1,2)}_{\tau'' v'' j'' \Lambda''_{\tau''},\tau v j l}(\rho). \tag{6.3.12}$$

Coupled Equations

In the BF_τ-Delves coordinates, the set of coupled equations are given by:

$$\begin{aligned}&\left\{-\frac{\hbar^2}{2\mu}\frac{\partial^2}{\partial\rho^2} - \left[E_{\mathrm{tot}} + \frac{\hbar^2}{8\mu\rho^2}\right]\right\} F_{fi}(\rho) \\ &\qquad + \sum_n \left\langle f \left| -\frac{\hbar^2}{2\mu\rho^2}\left[\frac{\partial^2}{\partial\omega_\tau^2} - \frac{j_\tau(j_\tau+1)}{\sin^2\omega_\tau} - \frac{l_\tau(l_\tau+1)}{\cos^2\omega_\tau}\right]\right.\right. \\ &\qquad\qquad \left.\left. + V(\rho,\omega_\tau,\eta_\tau)\right| i \right\rangle F_{ni}(\rho) = 0 \end{aligned} \tag{6.3.13}$$

where $i = \{\nu_\tau, j_\tau, \ell_\tau\}_i$ are the initial quantum numbers, $n = \{\nu_\tau, j_\tau, \ell_\tau\}_n$ are intermediate quantum numbers, and finally $f = \{\nu_\tau, j_\tau, l_\tau\}_f$ are the final quantum numbers. Moreover, the total potential $V(\rho,\omega_\tau,\eta_\tau)$ is composed of the pairwise sum of two-body interaction terms and the non-additive interaction ones.

To solve this set of coupled equations, we can use a diabatic-by-sector representation where the surface functions $\Phi^{JME}_{\tau v j l}(\omega_\tau;\rho_{\max})$ are evaluated in the middle of each sector

$\left[\rho_\chi^l, \rho_\chi^r\right]$. In Eq. 6.3.13, if we multiply the elements in the sum by $(\rho_\chi^m/\rho_\chi^m)^2$ and if we add and subtract to the equation the term $\left[(\rho_\chi^m/\rho_\chi^m)^2\ V_\tau(\rho\sin\omega_\tau)\right]$, we have:

$$\left\{-\frac{\hbar^2}{2\mu}\frac{\partial^2}{\partial\rho^2} - \left[E_{\rm tot} + \frac{\hbar^2}{8\mu\rho^2}\right]\right\} F_{fi}(\rho) + \sum_n \left\langle f\left| -\left(\frac{\rho_\chi^m}{\rho}\right)^2 \frac{\hbar^2}{2\mu\rho_\chi^{m\,2}}\left[\frac{\partial^2}{\partial\omega_\tau^2} - \frac{j_\tau(j_\tau+1)}{\sin^2\omega_\tau} - \frac{l_\tau(l_\tau+1)}{\cos^2\omega_\tau}\right]\right.\right. + V(\rho,\omega_\tau,\eta_\tau) + (\rho_\chi^m/\rho_\chi^m)^2\ V_\tau(\rho\sin\omega_\tau) - (\rho_\chi^m/\rho_\chi^m)^2\ V_\tau(\rho\sin\omega_\tau)\left.\left|i\right\rangle F_{ni}(\rho) = 0. \quad (6.3.14)$$

We can make appear the energies $\varepsilon_{\tau vjl}(\rho_\chi^m)$ using Eq. 6.2.10:

$$\left\{-\frac{\hbar^2}{2\mu}\frac{\partial^2}{\partial\rho^2} - \left[E_{\rm tot} - \left(\frac{\rho_\chi^m}{\rho}\right)^2 \varepsilon_{\tau vjl}(\rho_\chi^m) + \frac{\hbar^2}{8\mu\rho^2}\right]\right\} F_{fi}(\rho) + \sum_n \left\langle f\left| V(\rho,\omega_\tau,\eta_\tau) - \left(\frac{\rho_\chi^m}{\rho_\chi}\right)^2 V_\tau(\rho\sin\omega_\tau)\right|i\right\rangle F_{ni}(\rho) = 0. \quad (6.3.15)$$

In this way, the coupled equations are simpler to solve because the terms of the kinetic operator are included in the energies $\varepsilon_{\tau vjl}(\rho_\chi^m)$ which are calculated at the same time as the basic functions. The overlap matrix elements:

$$O^{JME}_{\tau vjl\,,\tau' v' j' l'} = \left\langle \Phi^{JME}_{\tau vjl}(\hat{S}^{\rm SF}_\tau, \vec{s}_\tau; \rho_\chi)\middle| \Phi^{JME}_{\tau vjl}(\hat{S}^{\rm SF}_\tau, \vec{s}_\tau; \rho_{\chi+1})\right\rangle \quad (6.3.16)$$

and the coupling matrix elements:

$$\left\langle f\left| V(\rho,\omega_\tau,\eta_\tau) - \left(\frac{\rho_\chi^m}{\rho_\chi}\right)^2 V_\tau(\rho\sin\omega_\tau)\right|i\right\rangle \quad (6.3.17)$$

which are required for the propagation, are evaluated by numerical quadratures.

However, as we have seen previously, this kind of coordinates does not allow to treat all arrangements in an equivalent way and provides inaccurate results for many scattering calculations. We will use these coordinates only during the matching procedure or to realize propagation at large distances where the quantum number τ is a good quantum number.

6.4 Principal axes hyperspherical coordinates (APH)

In this section, we will describe the APH coordinates which are mainly used to describe three-body collisions. These coordinates are more subtle than the previous ones and involve, in particular, a BF-frame that is oriented along the main axes of inertia of the triatomic system. These coordinates are well-suited to describe collisions in the region where the three particles strongly interact. On the other hand, we will see that at larger distances, these coordinates are no longer adapted to describe atom-diatom collisions. This is why at large distances an intermediate propagation step can be realized in Delves coordinates.

6.4.1 Definition of χ_τ

The main idea of the APH coordinates is to find a frame which is independent of the initial set of coordinates chosen [150, 148, 151]. This is the reason why we want to create two vectors $\vec{Q}$ and $\vec{q}$ that obey the following equalities:

$$\begin{pmatrix} \vec{Q} \\ \vec{q} \end{pmatrix} = \mathbb{T}(\chi_A) \begin{pmatrix} \vec{S}_A \\ \vec{s}_A \end{pmatrix} = \mathbb{T}(\chi_B) \begin{pmatrix} \vec{S}_B \\ \vec{s}_B \end{pmatrix} = \mathbb{T}(\chi_C) \begin{pmatrix} \vec{S}_C \\ \vec{s}_C \end{pmatrix}, \tag{6.4.1}$$

where $\mathbb{T}(\chi_\tau)$ is the 6×6 transformation matrix given in Eq. 6.1.14 and χ_τ is now a continuous variable whose label τ defines only its origin. As we want the three arrangements to be treated equivalently, it is important that Eq. 6.4.1 remains valid regardless of the set of coordinates initially chosen. To express the angle χ_τ with an origin from an arrangement different from that originally chosen, we must use:

$$\chi_\tau = \chi_i - \chi_{i\to\tau} \tag{6.4.2}$$

with χ_i the total angle formed from the initial arrangement i. To illustrate the previous equations, let's take an example that we have represented on Fig. 6.7. By definition, $\vec{Q} = \cos\chi_\tau \vec{S}_\tau + \sin\chi_\tau \vec{s}_\tau$ can be expressed as a combination of the two mass-scaled Jacobi vectors. As we have not yet described how χ_τ is defined, let's place $\vec{Q}$ on the diagram in an arbitrary way. If we consider the arrangement A as the initial arrangement, then the corresponding angle between $\vec{S}_A$ and $\vec{Q}$ is that given by the angle χ_A. On the contrary, if the arrangement B is the initial arrangement then the corresponding angle is given by χ_B. The above equations simply tell us that $\vec{Q}$ can be obtained either via an appropriate combination of $\vec{S}_A$ and $\vec{s}_A$ or via a combination of $\vec{S}_B$ and $\vec{s}_B$. The two methods to obtain $\vec{Q}$ are equivalent because $\vec{S}_B$ and $\vec{s}_B$ can also be decomposed as a function of $\vec{S}_A$ and $\vec{s}_A$ as shown in Eq. 6.1.14. This can be verified mathematically by starting from the initial arrangement B and by expressing χ_B as a function of the initial angle χ_A:

$$\begin{aligned}
\mathbb{T}(\chi_B) \begin{pmatrix} \vec{R}_B \\ \vec{r}_B \end{pmatrix} &= \begin{pmatrix} \cos\chi_B & \sin\chi_B \\ -\sin\chi_B & \cos\chi_B \end{pmatrix} \begin{pmatrix} \vec{R}_B \\ \vec{r}_B \end{pmatrix} \\
&= \begin{pmatrix} \cos(\chi_A - \chi_{A\to B}) & \sin(\chi_A - \chi_{A\to B}) \\ -\sin(\chi_A - \chi_{A\to B}) & \cos(\chi_A - \chi_{A\to B}) \end{pmatrix} \begin{pmatrix} \vec{R}_B \\ \vec{r}_B \end{pmatrix} \\
&= \begin{pmatrix} \cos\chi_A & \sin\chi_A \\ -\sin\chi_A & \cos\chi_A \end{pmatrix} \begin{pmatrix} \cos\chi_{A\to B} & -\sin\chi_{A\to B} \\ \sin\chi_{A\to B} & \cos\chi_{A\to B} \end{pmatrix} \begin{pmatrix} \vec{R}_B \\ \vec{r}_B \end{pmatrix} \\
&= \begin{pmatrix} \cos\chi_A & \sin\chi_A \\ -\sin\chi_A & \cos\chi_A \end{pmatrix} \begin{pmatrix} \cos\chi_{B\to A} & \sin\chi_{B\to A} \\ -\sin\chi_{B\to A} & \cos\chi_{B\to A} \end{pmatrix} \begin{pmatrix} \vec{R}_B \\ \vec{r}_B \end{pmatrix} \\
&= \begin{pmatrix} \cos\chi_A & \sin\chi_A \\ -\sin\chi_A & \cos\chi_A \end{pmatrix} \begin{pmatrix} \vec{R}_A \\ \vec{r}_A \end{pmatrix} \\
&= \begin{pmatrix} \vec{Q} \\ \vec{q} \end{pmatrix}.
\end{aligned} \tag{6.4.3}$$

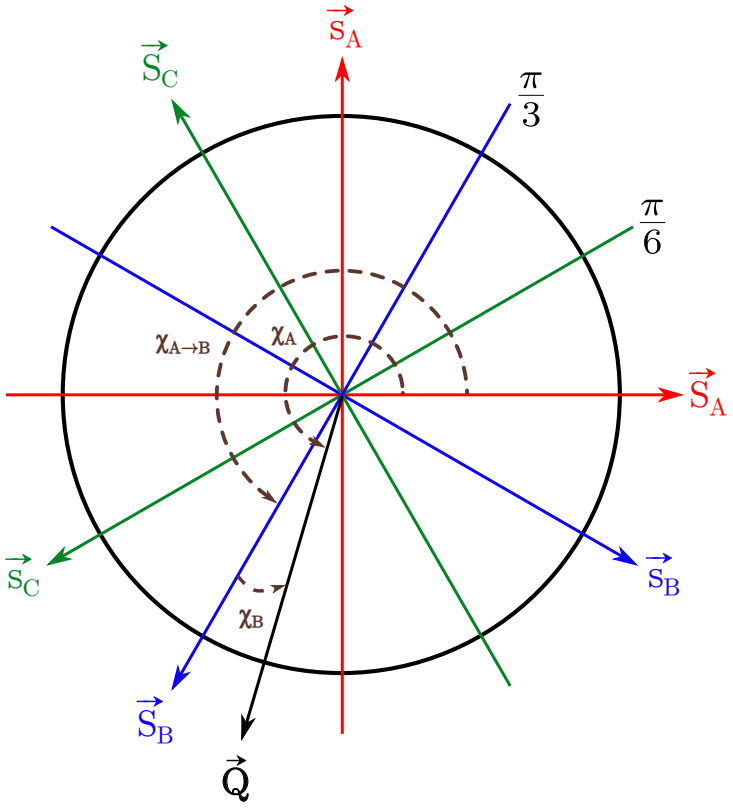

Figure 6.7: The vector $\vec{Q}$ in terms of kinematic rotation angles defined from different initial arrangements

As a result, whatever the initial arrangement chosen, we will find the same vectors $\vec{Q}$ and $\vec{q}$ at the end. If these two vectors are orthogonal, they will form, with a third vector perpendicular to the plane formed by $\vec{Q}$ and $\vec{q}$, a new body-fixed frame noted (BF_Q) oriented along the principal axes of inertia of the system. Under this condition, the χ_τ angle is no longer a parameter but a variable which fulfill the condition:

$$\vec{Q} \cdot \vec{q} = (\cos\chi_\tau \vec{S}_\tau + \sin\chi_\tau \vec{s}_\tau) \cdot (-\sin\chi_\tau \vec{S}_\tau + \cos\chi_\tau \vec{s}_\tau) = 0 \tag{6.4.4}$$

and whose solutions are given by:

$$\tan(2\chi_\tau) = \frac{2\vec{s}_\tau \cdot \vec{S}_\tau}{S_\tau^2 - s_\tau^2} \tag{6.4.5}$$

with $\chi_\tau \in [-\pi/2, +\pi/2]$. Note that unlike [150, 148, 230], we keep the natural definition of χ_τ and we don't double its domain of definition to prevent half-integer problems[5]. Finally, we will use $\phi = 2\chi_\tau$ with $\phi \in [-\pi, +\pi]$ in the following to be consistent with the choice of B. Kendrick [152]. Note that we have omitted the subscript τ because it simply refers to the arrangement chosen as origin.

[5]We will come back to this problem further.

We can also show that using this definition of ϕ leads to maximizing the amplitude Q^2 of $\vec{Q}$:

$$\frac{dQ^2}{d\phi} = 2\cos\phi \vec{S}_\tau \cdot \vec{s}_\tau + \sin\phi \left[s_\tau^2 - S_\tau^2\right] = 0 \tag{6.4.6}$$

because Eq. 6.4.6 leads to the same solutions as the ones given in Eq. 6.4.5. As a consequence, the BF_Q will adapt itself in function of the spatial configuration of the three particles. For example, if an atom τ' goes away from the other ones (i.e. $S_{\tau\prime} \gg s_{\tau\prime}$) then the $\vec{Q}$ vector gets closer to $\pm\vec{S}_{\tau\prime}$ (which belongs to the set of Jacobi coordinates, appropriate to use in this configuration). However, we can mention that $\vec{q}$ can't approach $\vec{s}_{\tau\prime}$ as the vector $\vec{q}$ is orthogonal to $\vec{Q}$ while the angle between the two vector $\vec{S}_\tau$ and $\vec{s}_\tau$ is given by $\eta_\tau \neq \pi/2$ in general. As a conclusion, the BF_Q is well adapted for the short-range domain but it is not physically relevant for asymptotic atom-diatom configurations (i.e. for $S_\tau \to \infty$). This is why, we will rather use the three BF_τ at long-range (especially at matching distances).

6.4.2 Construction of the BF_Q

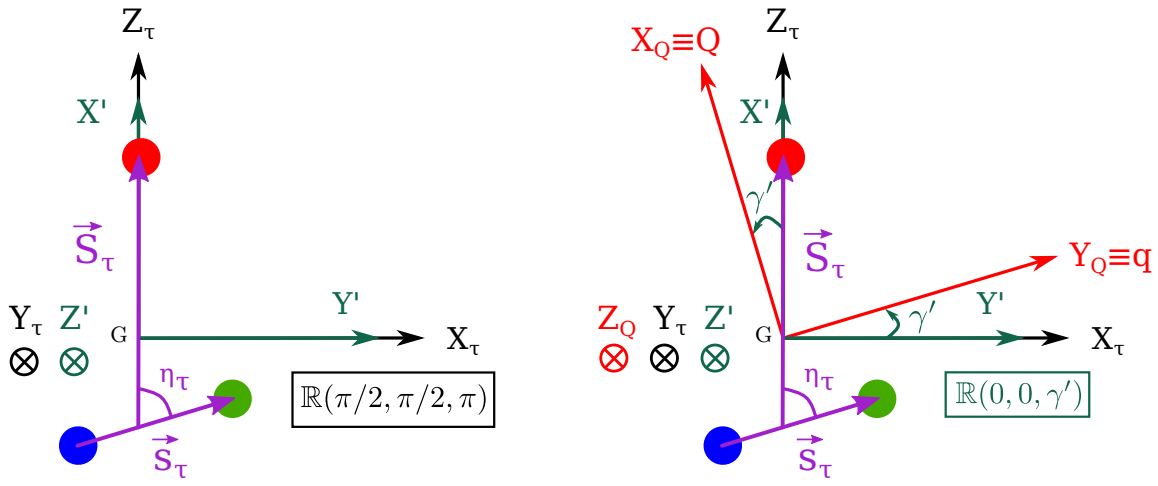

Figure 6.8: Transformation of the BF_τ into the intermediate frame $(GX'Y'Z')$ (left). Transformation of the intermediate frame $(GX'Y'Z')$ into the BF_Q (right).

As previously explained, we will use a new body-fixed frame BF_Q represented on Fig. 6.8. We will follow B. Kendrick's convention [152] using the unit vectors $\{\vec{u}_{X_Q}, \vec{u}_{Y_Q}, \vec{u}_{Z_Q}\} \equiv \{\vec{u}_Q, \vec{u}_q, \vec{u}_Z\}$ as basis with:

$$\vec{u}_Q = \frac{\vec{Q}}{Q} \qquad \vec{u}_q = \frac{\vec{q}}{q}. \tag{6.4.7}$$

To transform the BF_τ into the BF_Q, we can decompose the process into two steps:

- Let's transform first the BF_τ into an intermediate $(GX'Y'Z')$ frame where $X_\tau \to Y'$, $Y_\tau \to Z'$ and $Z_\tau \to X'$. To do this, one must apply the rotation operator

$\mathbb{R}(\pi/2, \pi/2, \pi)$ defined in Eq. 6.3.5 to the BF_τ axes. This transformation is represented in Fig. 6.8 (left).

- Then, one must do a rotation γ' around the axis Z' of the intermediate frame. As a consequence, the new X_Q axis will be superimposed on $\vec{Q}$ and the new Y_Q axis will be superimposed on $\vec{q}$ as illustrated in Fig. 6.8 (right).

These two steps can be combined by applying an unique rotation given by:

$$\begin{pmatrix} \vec{u}_Q \\ \vec{u}_q \\ \vec{u}_{Z_Q} \end{pmatrix} = \mathbb{R}(\pi/2, \pi/2, \pi + \gamma\prime) \begin{pmatrix} \vec{u}_{X_\tau} \\ \vec{u}_{Y_\tau} \\ \vec{u}_{Z_\tau} \end{pmatrix}. \tag{6.4.8}$$

To get the definition of the γ' angle, let's express the vector $\vec{Q}$ in the intermediate (X', Y', Z') frame:

$$\vec{Q} = \begin{pmatrix} Q_{X\prime} \\ Q_{Y\prime} \\ 0 \end{pmatrix} = \begin{pmatrix} S_\tau \cos(\phi/2) + s_\tau \sin(\phi/2) \cos\eta_\tau \\ s_\tau \sin(\phi/2) \sin\eta_\tau \\ 0 \end{pmatrix} \tag{6.4.9}$$

and in the BF_Q:

$$\vec{Q} = \begin{pmatrix} Q \\ 0 \\ 0 \end{pmatrix}. \tag{6.4.10}$$

By writing the transformation equation to go from one representation to the other:

$$\vec{Q} = \begin{pmatrix} Q \\ 0 \\ 0 \end{pmatrix} = \begin{pmatrix} \cos\gamma\prime & \sin\gamma\prime & 0 \\ -\sin\gamma\prime & \cos\gamma\prime & 0 \\ 0 & 0 & 1 \end{pmatrix} \begin{pmatrix} Q_{X\prime} \\ Q_{Y\prime} \\ 0 \end{pmatrix} \tag{6.4.11}$$

we can deduce the definition of the angle γ':

$$\sin\gamma\prime = \frac{s_\tau \sin(\phi/2) \sin\eta_\tau}{Q} \qquad \cos\gamma\prime = \frac{S_\tau \cos(\phi/2) + s_\tau \sin(\phi/2) \cos\eta_\tau}{Q} \tag{6.4.12}$$

which gives:

$$\tan\gamma\prime = \frac{s_\tau \sin(\phi/2) \sin\eta_\tau}{S_\tau \cos(\phi/2) + s_\tau \sin(\phi/2) \cos\eta_\tau}. \tag{6.4.13}$$

These relations are very important for the following because they make the link between the Jacobi, Delves and APH axis and are especially used in the matching procedure. Other conventions for the choice of the axes of the BF_Q can be chosen (such as choosing the Y_Q axis as being perpendicular to the plane formed by the three particles). To understand the difference between our choice and the other conventions, refer to the discussion in section 6.4.5.

6.4.3 Hyperspherical coordinates

In the orthogonal frame $\{\vec{u}_Q, \vec{u}_q, \vec{Z}_Q\}$, we can define[6]:

$$\rho = \left(Q^2 + q^2\right)^{1/2} \qquad q = \rho \sin(\theta/4) \tag{6.4.14}$$

$$\theta = 4 \arctan\left(\frac{q}{Q}\right) \qquad Q = \rho \cos(\theta/4) \tag{6.4.15}$$

with respectively $\rho \in [0, +\infty[$, $\theta \in [0, \pi]$ and $\phi \in [-\pi, \pi]$. These coordinates turn out to be very similar to the Delves hypersherical coordinates. Indeed, they both use equivalent definitions for ρ and the expression of the θ angle is very similar to what was done for ω_τ. As a result, while ρ describes the overall size of the ABC system, the bending angle θ and the arrangement angle ϕ describe its shape. These three variables (ρ, θ, ϕ) are commonly called *internal coordinates*.

To these three variables, we will add the three *external coordinates* $(\alpha_Q, \beta_Q, \gamma_Q)$ so that the set of hyperspherical coordinates we will use in the next are given by:

$$\vec{x} \equiv (\rho, \hat{\rho}_\tau^{\mathrm{BF}}) = (\rho, \theta, \phi, \alpha_Q, \beta_Q, \gamma_Q) \tag{6.4.16}$$

with the Euler angles given by:

$$\alpha_Q = \alpha_\tau + \pi/2 \quad \beta_Q = \beta_\tau + \pi/2 \quad \gamma_Q = \gamma_\tau + \gamma\prime + \pi \tag{6.4.17}$$

with $\alpha_Q \in [0, 2\pi]$, $\beta_Q \in [0, \pi]$ and $\gamma_Q \in [0, 2\pi]$. Because we consider all the spatial configurations and arrangements equivalently, these hyperspherical coordinates are called *democratic* to differentiate them from the Delves hyperspherical coordinates.

6.4.4 Passage relations

In summary, the relations for going from hyperspherical to mass-scaled Jacobi coordinates are given by[7]:

$$\begin{aligned}
\rho &= \left(\vec{S}_\tau^{\,2} + \vec{s}_\tau^{\,2}\right)^{\frac{1}{2}} \\
\theta &= 4 \arctan\left\{\left(\frac{(S_\tau^2 + s_\tau^2) - \left[(S_\tau^2 - s_\tau^2)^2 + \left(2\vec{S}_\tau \cdot \vec{s}_\tau\right)^2\right]^{1/2}}{(S_\tau^2 + s_\tau^2) + \left[(S_\tau^2 - s_\tau^2)^2 + \left(2\vec{S}_\tau \cdot \vec{s}_\tau\right)^2\right]^{1/2}}\right)^{1/2}\right\} \\
\phi &= \arctan\left(\frac{2\overrightarrow{S_\tau} \cdot \overrightarrow{s_\tau}}{S_\tau^2 - s_\tau^2}\right)
\end{aligned} \tag{6.4.18}$$

[6] Our angle θ is doubled compared to [150, 148, 230] to follow B. Kendrick's convention.

[7] Note that there is a typo in [151] for the second equation.

and the inverse relations:

$$\begin{aligned} S_\tau &= \frac{\rho}{\sqrt{2}}\left[1+\cos(\theta/2)\cos\left(\phi\right)\right]^{1/2} \\ s_\tau &= \frac{\rho}{\sqrt{2}}\left[1-\cos(\theta/2)\cos\left(\phi\right)\right]^{1/2} \\ \cos\eta_\tau &= \frac{\cos(\theta/2)\sin\phi}{\left[1-\cos^2(\theta/2)\cos^2\left(\phi\right)\right]^{1/2}}. \end{aligned} \tag{6.4.19}$$

We note that if $\theta = \pi$ (i.e. $\eta_\tau = \pi/2$), the system corresponds to an oblate top triangular configuration whereas if $\theta = 0$ (i.e. $\eta_\tau = 0$), it corresponds to a collinear configuration. This is why θ is also called the *configuration angle*. All these expressions are particularly useful to express potential energy surfaces, usually given in Jacobi coordinates, in hyperspherical coordinates or during the matching procedure as show in section 6.6.

6.4.5 Instantaneous principal axes of inertia

In this part, we will demonstrate that our BF_Q axis is well oriented along the instantaneous principal axes of inertia. To do this, let's express the Jacobi vectors ($\vec{S}_\tau$, $\vec{s}_\tau$) in the BF_Q inverting Eq. 6.1.13 and using the fact that $\mathbb{T}^{-1}(\phi/2) = \mathbb{T}(-\phi/2)$:

$$\begin{aligned} S_{\tau_Q} &= \left(\cos(\phi/2)\,\vec{Q} - \sin(\phi/2)\,\vec{q}\right)\cdot\vec{u}_Q & s_{\tau_Q} &= \left(\sin(\phi/2)\,\vec{Q} + \cos(\phi/2)\,\vec{q}\right)\cdot\vec{u}_Q \\ &= Q\cos(\phi/2) & &= Q\sin(\phi/2) \\ &= \rho\cos(\theta/4)\cos(\phi/2) & &= \rho\cos(\theta/4)\sin(\phi/2) \\ S_{\tau_q} &= \left(\cos(\phi/2)\,\vec{Q} - \sin(\phi/2)\,\vec{q}\right)\cdot\vec{u}_q & s_{\tau_q} &= \left(\sin(\phi/2)\,\vec{Q} + \cos(\phi/2)\,\vec{q}\right)\cdot\vec{u}_q \\ &= -q\sin(\phi/2) & &= q\cos(\phi/2) \\ &= -\rho\sin(\theta/4)\sin(\phi/2) & &= \rho\sin(\theta/4)\cos(\phi/2) \\ S_{\tau_{Z_Q}} &= 0 & s_{\tau_{Z_Q}} &= 0 \end{aligned} \tag{6.4.20}$$

where we well find that the two mass-scaled Jacobi vectors are in a plane perpendicular to the Z_Q axis. The inertia tensor in the BF_Q is derived using standard methods [234]:

$$\begin{aligned} I_Q &= \mu\left\{\left(S_{\tau_q}^2 + S_{\tau_{Z_Q}}^2\right) + \left(s_{\tau_q}^2 + s_{\tau_{Z_Q}}^2\right)\right\} & I_{Z_QQ} &= -\mu\Big\{S_{\tau_{Z_Q}}S_{\tau_Q} + s_{\tau_{Z_Q}}s_{\tau_Q}\Big\} \\ I_q &= \mu\left\{\left(S_{\tau_{Z_Q}}^2 + S_{\tau_Q}^2\right) + \left(s_{\tau_{Z_Q}}^2 + s_{\tau_Q}^2\right)\right\} & I_{Qq} &= -\mu\Big\{S_{\tau_Q}S_{\tau_q} + s_{\tau_Q}s_{\tau_q}\Big\} \\ I_{Z_Q} &= \mu\left\{\left(S_{\tau_Q}^2 + S_{\tau_q}^2\right) + \left(s_{\tau_Q}^2 + s_{\tau_q}^2\right)\right\} & I_{qZ_Q} &= -\mu\Big\{S_{\tau_q}S_{\tau_{Z_Q}} + s_{\tau_q}s_{\tau_{Z_Q}}\Big\}. \end{aligned} \tag{6.4.21}$$

This gives a diagonal tensor matrix of inertia:

$$\begin{pmatrix} I_Q & I_{Qq} & I_{QZ_Q} \\ I_{qQ} & I_q & I_{qZ_Q} \\ I_{Z_QQ} & I_{Z_Qq} & I_{Z_Q} \end{pmatrix} = \begin{pmatrix} \mu q^2 & 0 & 0 \\ 0 & \mu Q^2 & 0 \\ 0 & 0 & \mu\left(Q^2+q^2\right) \end{pmatrix} \tag{6.4.22}$$

which shows that the BF_Q is always oriented along the principal axes of inertia for a given $(\rho, \theta, \chi_\tau)$ spatial configuration. As the three particles stay in the plane perpendicular to the (GZ_Q) axis then $I_{Z_Q} = I_Q + I_q$ is the axis of largest inertia. The axis of least inertia is I_Q because q^2 is minimized while I_q is the intermediate axis of inertia because Q^2 is maximized (according to the initial definition of χ_τ chosen). We then have generally $0 \leq q \leq Q < \infty$ which corresponds to an asymmetric rotor. When $Q \gg q$, which occurs when the three atoms are close to a linear configuration (i.e. when θ approaches 0) or when one of the atoms is very far from the two others (as in the asymptotic zone), one has:

$$I_Q \ll I_q \approx I_Y \tag{6.4.23}$$

and the system approaches a prolate symmetric top with the axis (GQ) as axis of symmetry. When $Q \approx q$ (i.e. when θ approaches $\pi/2$), we get:

$$I_Q \approx I_q < I_Y \tag{6.4.24}$$

and the system approaches an oblate symmetric top (T-shaped configuration)[8] whose axis (GY) is the axis of symmetry.

As a conclusion, these coordinates describe more directly the inertia tensors of the system (which adiabatically adjust to follow any atom which leaves the other two) than its coordinates. This is why they are called Principal Axes Hyperspherical (APH) coordinates.

R. T. Pack and Parker [150] and J.-M. Launay [230, 151] use the GY_Q as the perpendicular axis to the plane of the three particles whereas we follow the convention of B. Kendrick [152] which uses GZ_Q as the perpendicular one. This choice will have a strong impact on the matrix elements of the grand angular moment operator which depend on the projections of $\vec{J}$ on the three axes X_Q, Y_Q and Z_Q. As the quantization axis can be chosen along a single axis, the matrix elements of the grand angular momentum operator will be defined differently. This will affect the scattering results if the singularities which appear in the grand angular momentum operator are not treated perfectly (Cf. section 6.5.2). However, if the calculations of the grand angular moment matrix elements are exact (as shown in our method) the scattering results will be similar regardless of the initial BF_Q axis chosen. However, our choice of BF is particularly convenient to (i) implement the inversion parity (Cf. section 6.5.1) (ii) optimize the parallelization of the calculations as explained in [152].

6.4.6 Total Hamiltonian

In APH coordinates, the total Hamiltonian looks like the ones in hyperspherical Delves coordinates:

$$\hat{H} = -\frac{\hbar^2}{2\mu\rho^5}\frac{\partial}{\partial\rho}\rho^5\frac{\partial}{\partial\rho} + \frac{\hat{\Lambda}^2}{2\mu\rho^2} + V(\rho, \theta, \phi). \tag{6.4.25}$$

[8] The T-shaped configuration corresponds to an equilateral triangle for equal mass particles.

However, the grand angular momentum operator is now expressed in terms of the APH coordinates [226, 227]:

$$\frac{\hat{\Lambda}^2}{2\mu\rho^2} = \frac{-8\hbar^2}{\mu\rho^2}\left[\frac{\partial^2}{\partial\theta^2} + \cot\theta\frac{\partial}{\partial\theta} + \frac{1}{2(1+\cos\theta)}\frac{\partial^2}{\partial\phi^2}\right] + \frac{1}{\mu\rho^2}\left[\frac{J_X^2}{(1-\cos\theta/2)} + \frac{J_Y^2}{(1+\cos\theta/2)} + \frac{J_Z^2}{(1+\cos\theta)}\right] + \frac{4\sin\theta/2}{\mu\rho^2(1+\cos\theta)}J_Z\frac{\hbar}{i}\frac{\partial}{\partial\phi} \quad (6.4.26)$$

with $J_X \equiv J_Q$, $J_Y \equiv J_q$ and $J_Z \equiv J_{Z_Q}$ the components of the total angular moment operator $\hat{\vec{J}}$ in the BF_Q. If we take a closer look of Eq. 6.4.26, we can see that many terms contain singularities [235] either when $\theta \to 0$ or either when $\theta \to \pi$. These so-called *Eckart singularities* are characteristic of all instantaneous principal axes systems and must be treated carefully to get correct results. Indeed, B. Kendrick [152] demonstrated that some scattering calculations done by A. Kuppermann and Y.-S. M. Wu [236, 237, 238], J.-M. Launay [230] and R. T. Pack and Parker [150] didn't reproduce experimental data for high collision energies where partial waves $J > 0$ are required. Indeed, the basis sets used were not adapted to perform accurate numerical cancellations of these singularities.

To prevent these errors, C. Eckart [239] proposed to use another body-fixed frame oriented along the principal axes of the equilibrium configuration [240]. In fact, this idea is well adapted for non-linear molecules executing small vibrations. However, for the other configurations the singularities remains and this is why we didn't choose this option.

Another solution could have been to use directly the hyperspherical harmonics as basis set but it is not convenient for three reasons. First, a simple analytic functional form of the hyperspherical harmonics (HHs) is still unknown[9] (for every partial waves J). Secondly, HHs are non-localized functions and are not efficient to represent localized wave functions such as dimer bound states. Thirdly, HHs are not a direct product basis of θ and ϕ which prevents the use of discrete variable representations which alleviate numerical calculations (Cf. next section).

For all these reasons, B. Kendrick has developed a basis set treating all Eckart's singularities in an accurate way. For more details, see [152]. If we define the axes of the BF_Q in a different way [150, 230, 151], then the terms $J_X \equiv J_Q$, $J_Y \equiv J_q$ and $J_Z \equiv J_{Z_Q}$ are switched. Therefore, the singular terms are distributed differently and the method of B. Kendrick is no longer valid and must be adapted.

6.4.7 Jacobian

The Jacobian is given by:

$$\int d\vec{S}d\vec{s}\,F = \frac{1}{32}\int_0^\infty \rho^5 d\rho \int_{-\pi}^{\pi} d\phi \int_0^{\pi} \sin\theta d\theta \int_0^{2\pi} d\alpha \int_0^{\pi} \sin\beta d\beta \int_0^{\pi} d\gamma F \quad (6.4.27)$$

[9] However some numerical procedures exist such as the one developed by L. Wolniewicz [241] but they are very complicated to implement.

for any arbitrary function $F = F(\vec{x})$.

6.4.8 Coupled equations

The total nuclear wave function[10] is expanded as:

$$\Psi_i^{JMpq}(x) = 4\sqrt{2}\sum_t \rho^{-5/2}\psi_{it}^{Jpq}(\rho)\Phi_t^{JMpq}\left(\omega;\rho_\xi^m\right) \tag{6.4.28}$$

with $\Phi_t^{JMpq}\left(\omega;\rho_\xi^m\right)$ the angular five-dimensional surface functions explicitly given in the diabatic-by-sector representation and $\psi_{it}^{Jpq}(\rho)$ the radial wave functions. p refers to the inversion parity and q refers to the particle exchange symmetry. As in the previous part, if we insert the total wave function into the Schrodinger equation, multiply by $[\Phi_t^{JMpq}\left(\omega;\rho_\xi^m\right)]^*$ on the left and integrate over the angular part, we obtain the following set of coupled equations:

$$\left[\frac{\partial^2}{\partial\rho^2} + \frac{2\mu}{\hbar^2}E\right]\psi_{it}^{Jpq}(\rho) = \frac{2\mu}{\hbar^2}\sum_{t'}\left\langle\Phi_t^{JMpq}\middle|H_c\middle|\Phi_{t'}^{JMpq}\right\rangle\psi_{it'}^{Jpq}(\rho) \tag{6.4.29}$$

with:

$$\left\langle\Phi_t^{JMpq}\middle|H_c\middle|\Phi_{t'}^{JMpq}\right\rangle \equiv \langle\Phi_t^{JMpq}|\left(\frac{\rho_\xi^m}{\rho}\right)^2\mathcal{E}_t^{Jpq}\left(\rho_\xi^m\right) + V(\rho,\theta,\phi) - \left(\frac{\rho_\xi^m}{\rho}\right)^2 V\left(\rho_\xi^m,\theta,\phi\right)\left|\Phi_{t'}^{JMpq}\right\rangle. \tag{6.4.30}$$

The five-dimensional surface functions $\Phi_t^{JMpq}\left(\omega;\rho_\xi^m\right)$ are evaluated at the center of each sector via:

$$\left[\frac{\hat{\Lambda}^2}{2\mu{\rho_\xi^m}^2} + \frac{15\hbar^2}{8\mu{\rho_\xi^m}^2} + V\left(\rho_\xi^m,\theta,\phi\right)\right]\Phi_t^{JMpq}\left(\omega;\rho_\xi^m\right) = \mathcal{E}_t^{Jpq}(\rho_\xi^m)\Phi_t^{JMpq}\left(\omega;\rho_\xi^m\right) \tag{6.4.31}$$

where $\mathcal{E}_t^{Jpq}(\rho_\xi^m)$ are the adiabatic energies and the term $15\hbar^2/8\mu{\rho_\xi^m}^2$ comes from the second derivative of Eq. 6.4.28.

Now that the main equations are established, we must:

- Choose a basis set on which we will extend the $\Phi_t^{JMpq}\left(\omega;\rho_\xi^m\right)$ surface functions. This set must treat accurately the Eckart singularities and it must give quickly converged calculations.
- Solve Eq. 6.4.31 obtaining the angular surface functions and the adiabatic energies.
- Compute the coupling matrix elements in Eq. 6.4.30 and the overlap matrix using the surface functions previously obtained.
- Propagate until $\rho_{\max}$ and do the matching[11].

[10] The term $\rho^{-5/2}$ is used to only keep second derivative terms in ρ in the set of coupled equations. The prefactor $4\sqrt{2}$ cancels with the one in Eq. 6.4.27 to give orthonormal surface functions.

[11] In some systems, we must perform an intermediate propagation in Delves ($\rho_{\max}^{\text{Delves}} \geq \rho_{\max}$) before doing the matching.

6.5 Correct basis set and numerical methods

As seen previously, the initial choice of the axes forming the BF_Q distribute the singularities differently on the terms J_X, J_Y and J_Z. If the primitive basis functions on which the surface functions will be expanded are not carefully chosen, the Eckart singularities should strongly affect the matrix elements and the scattering results. However, for some systems, singularities are well treated without making any particular effort on the choice of primitive basis functions. For example, for equilateral configurations (i.e. $\theta = \pi/2$), the system approaches an oblate symmetric top where the Z_Q axis is the symmetry axis of the top. Thus, for molecules which favor this configuration (such as Li_3) the matrix elements of J_Z are diagonal as the quantization axis is chosen along Z_Q for our choice of BF_Q. If we truncate the number of Ω values used to express the total Hamiltonian, we reduce the impact of the singularities coming from the non-diagonal term coming from J_X and J_Y and the solutions obtained are quite accurate. For linear geometries (i.e. $\theta = 0$), the system approaches a prolate symmetric top with the X_Q axis being the symmetry axis of the top. Thus, for molecules which favor this configuration (such as HD_2) the matrix elements of J_X are diagonal for the choice of BF_Q axes used by [150, 230] as their quantization axis is chosen along X_Q. If they use the same procedure as the one described above, they can get quite accurate results for these systems. Thus, the choice of the BF_Q axes made in the past was directly related to the kind of system one wanted to study.

In this section, we will develop a method that treats all singular terms accurately so that all configurations are treated perfectly. We will present the primitive basis functions that we will use to expand the surface functions, then we will show how to treat Eckart singularities and finally we will present some numerical methods to solve the three body problem as optimally as possible.

6.5.1 The basis set

In the first studies of three-body collisions [150, 230, 238], the surface functions were expanded in terms of a direct product basis of Legendre polynomials in θ and cosine/sine functions in ϕ. But as we will show later, these basis sets can't give an accurate representation of all the HHs and can lead to errors in the scattering results. As a consequence, we will expand the five-dimensional surface functions in terms of the following orthonormalized basis set [152]:

$$\Phi_t^{JMp}(\omega;\rho_\xi) = \sum_{l=\mu}^{l_{\max}} \sum_{m=-m_{\max}}^{m_{\max}} \sum_{\Omega=-\Omega_{\max}}^{\Omega_{\max}} b_t^{lm\Omega} d_{\mu,\nu}^l(\theta) \frac{e^{im\phi}}{\sqrt{2\pi}} \widetilde{D}_{\Omega M}^J(\alpha,\beta,\gamma) \tag{6.5.1}$$

where the functions $d_{\mu,\nu}^l(\theta)$ are expressed in terms of Jacobi polynomials [170]:

$$d_{\mu,\nu}^l(\theta) = \sqrt{\frac{2l+1}{2}} \left[\frac{(l+\mu)!(l-\mu)!}{(l+\nu)!(l-\nu)!}\right]^{1/2} (\cos\theta/2)^{\mu+\nu} (\sin\theta/2)^{\mu-\nu} P_{l-\mu}^{(\mu-\nu,\mu+\nu)}(\cos\theta). \tag{6.5.2}$$

The two indices (μ, ν) will be appropriately chosen to treat the singularities at the two poles $\theta = 0$ and $\theta = \pi$ as explained in section 6.5.2. The renormalized Wigner functions

$\widetilde{D}^J_{\Omega M}(\alpha,\beta,\gamma)$ can be expressed in terms of the usual Wigner functions via:

$$\tilde{D}^J_{\Omega M}(\alpha,\beta,\gamma) = \sqrt{\frac{2J+1}{8\pi^2}} D^J_{\Omega M}(\alpha,\beta,\gamma) \tag{6.5.3}$$

so that:

$$\int_0^{2\pi} d\alpha \int_0^{\pi} \sin\beta\, d\beta \int_0^{2\pi} d\gamma\ \tilde{D}^{J_1*}_{\Omega_1 M_1}(\alpha,\beta,\gamma)\tilde{D}^{J_2}_{\Omega_2 M_2}(\alpha,\beta,\gamma) \ = \ \delta_{J_1 J_2}\,\delta_{\Omega_1\Omega_2}\,\delta_{M_1 M_2}. \tag{6.5.4}$$

Moreover, if we apply the inversion operator on the $\widetilde{D}$ functions, we have:

$$\mathcal{I}\widetilde{D}^J_{\Omega M} = (-1)^{\Omega}\widetilde{D}^J_{\Omega M}. \tag{6.5.5}$$

Therefore, to get well defined inversion parity surface functions, Ω must take only even values for even parity (i.e. $p=1$) and only odd values for odd parity (i.e. $p=0$). In the following, all sums over Ω (such as the one in Eq. 6.5.1) will be done either on the even or on the odd blocks according to the superscript p in the surface function studied.

By combining all the previous equations with the Jacobian from Eq. 6.4.27, we obtain orthonormalized surface functions:

$$\int_{-\pi}^{\pi} d\phi \int_0^{\pi} \sin\theta d\theta \int_0^{2\pi} d\alpha \int_0^{\pi} \sin\beta d\beta \int_0^{\pi} d\gamma \times \left[\Phi^{JMp}_t\left(\omega;\rho^m_\xi\right)\right]^* \Phi^{JMp}_{t'}\left(\omega;\rho^m_\xi\right) = \delta_{tt'}. \tag{6.5.6}$$

6.5.2 How to treat Eckart singularities?

To treat the Eckart singularities, one must appropriately choose the different sets (μ,ν) so that the singularities at the two poles $\theta\to 0$ and $\theta\to\pi$ vanish. To illustrate the method, let's consider the grand angular momentum operator when we approach to a linear configuration:

$$\hat{\Lambda}^2(\theta\to\pi) \approx -16\hbar^2\left[\frac{\partial^2}{\partial\theta^2} + \cot\theta\frac{\partial}{\partial\theta}\right] + \frac{2}{(1+\cos\theta)}\left(J_Z - i2\hbar\frac{\partial}{\partial\phi}\right)^2. \tag{6.5.7}$$

If we split the integral over θ to separate the two poles from the well defined parts:

$$\int_0^{\pi}\sin\theta d\theta = \int_0^{\theta_0}\sin\theta d\theta + \int_{\theta_0}^{\theta_\pi}\sin\theta d\theta + \int_{\theta_\pi}^{\pi}\sin\theta d\theta \tag{6.5.8}$$

and if we use the fact that the functions $d^l_{\mu,\nu}(\theta)$ satisfy:

$$\left[\frac{\partial^2}{\partial\theta^2} + \cot\theta\frac{\partial}{\partial\theta}\right] d^l_{\mu,\nu}(\theta) = \left[\frac{1}{\sin^2\theta}\left(\mu^2+\nu^2-2\mu\nu\cos\theta\right) - l(l+1)\right] d^l_{\mu,\nu}(\theta) \tag{6.5.9}$$

then the matrix elements of Eq. 6.5.7 are given by:

$$\Lambda^2(\theta \to \pi)^{JMp}_{ll'mm'\Omega\Omega'} \approx -8\hbar^2 \int_{\theta_\pi}^{\pi} \sin\theta \, d\theta \, d^l_{\mu\nu}(\theta) \, \frac{1}{(1+\cos\theta)} \, d^{l'}_{\mu\nu}(\theta) \times \left[(\mu+\nu)^2 - \left(\frac{\Omega}{2} + m \right)^2 \right] \delta_{m\,m'} \delta_{\Omega\,\Omega'}. \quad (6.5.10)$$

To prevent the term $\frac{1}{(1+\cos\theta)}$ in Eq. 6.5.10 from diverging, they are two possibilities. Either, the term $d^l_{\mu\nu}(\theta) \times d^{l'}_{\mu\nu}(\theta)$ cancels the term that diverges when we replace the functions $d^l_{\mu\nu}(\theta)$ by their definition given in Eq. 6.5.2 (but this is not always the case). Or, the term in brackets must be zero:

$$\left[(\mu+\nu)^2 - \left(\frac{\Omega}{2} + m \right)^2 \right] = 0 \quad (6.5.11)$$

and cancels the diverging matrix element. By separating the two squared terms in Eq. 6.5.11 and applying a square root to each side, we get the following condition:

$$|\mu+\nu| = \left| \frac{\Omega}{2} + m \right|. \quad (6.5.12)$$

Since the functions $d^l_{\mu,\nu}$ can be expanded exactly in terms of $d^{l'}_{\mu',\nu'}$ where $\mu' = \mu \,(\mathrm{mod}2)$ and $\nu' = \nu \,(\mathrm{mod}2)$ by definition, we can separately treat the cases for which $|\mu+\nu|$ is even or odd, i.e. one can only consider $|\mu+\nu| = 0$ or $1 \;(\mathrm{mod}2)$.

If $|\mu+\nu| = 0$, the functions $d^l_{\mu,\nu}(\theta) \underset{\theta\to+\pi}{\longrightarrow}$ constant and do not cancel the singular term. As a consequence, Eq. 6.5.12 must be satisfied which implies:

$$\left| \frac{\Omega}{2} + m \right| = 0 \pmod 2. \quad (6.5.13)$$

In other words, the quantity $\left(\frac{\Omega}{2} + m\right)$ must be even.

If $|\mu+\nu| = 1$, the term $d^l_{\mu,\nu}(\theta) \times d^{l'}_{\mu,\nu}(\theta) \underset{\theta\to+\pi}{\longrightarrow} 1+\cos\theta$ cancels naturally the singularities. Therefore, no condition on Ω and m seems necessary. However, if we allow even values of $\left(\frac{\Omega}{2} + m\right)$, we get for the off-diagonal matrix elements in $\mu\,\mu'$ and $\nu\,\nu'$:

$$\hat{\Lambda}^2(\theta \to \pi)^{JMp}_{\mu\mu'\nu\nu'll'mm'\Omega\Omega'} \approx -8\hbar^2 \int_{\tilde{\theta}_\pi}^{\pi} \sin\theta \, d\theta \, d^l_{\mu\nu}(\theta) \frac{1}{(1+\cos\theta)} d^{l'}_{\mu'\nu'}(\theta) \times \left[(\mu'+\nu')^2 - \left(\frac{\Omega}{2} + m \right)^2 \right] \delta_{mm'} \, \delta_{\Omega\Omega'}. \quad (6.5.14)$$

If $|\mu+\nu| = 1$ and $|\mu'+\nu'| = 0$, we are in the same case than Eq. 6.5.13 and then $\left(\frac{\Omega}{2} + m\right)$ must be even. On the contrary, if $|\mu+\nu| = 0$ and $|\mu'+\nu'| = 1$, the Eckart

singularities are no longer naturally canceled and $\left(\frac{\Omega}{2}+m\right)$ must be odd. Therefore, although no condition on μ and ν must be used for the diagonal matrix elements $\mu\,\mu$ and $\nu\,\nu$, we impose to use $|\mu+\nu|=1$ for $\left(\frac{\Omega}{2}+m\right)$ odd to cancel the divergent terms in the non-diagonal elements. As a conclusion, the singularities are perfectly canceled using:

$$|\mu+\nu|=0 \text{ for } \left(\frac{\Omega}{2}+m\right) \text{even} \qquad |\mu+\nu|=1 \text{ for } \left(\frac{\Omega}{2}+m\right) \text{odd}. \tag{6.5.15}$$

When approaching to an equilateral configuration, the grand angular momentum operator is given by:

$$\hat{\Lambda}^2(\theta\to 0)^{JMp}_{ll'mm'\Omega\Omega'} \approx -8\hbar^2 \int_0^{\theta_0} \sin\theta d\theta d^l_{\mu\nu}(\theta)\frac{1}{(1-\cos\theta)}d^{l'}_{\mu\nu}(\theta) \times \left[(\mu-\nu)^2\delta_{\Omega\Omega'} - \left\langle \tilde{D}^J_{\Omega M}\left|\frac{J^2_{X_Q}}{\hbar^2}\right|\tilde{D}^J_{\Omega' M}\right\rangle\right]\delta_{mm'} \tag{6.5.16}$$

and involves matrix elements of the squared projection J_{X_Q} of the total angular momentum on the X_Q axis. If we follow the same procedure than for the linear configuration case, the condition which must be satisfied to cancel the singular terms is given by:

$$|\mu-\nu|\delta_{\Omega\Omega'} = \left|\left\langle \widetilde{D}^J_{\Omega M}\left|\frac{J^2_{X_Q}}{\hbar^2}\right|\widetilde{D}^J_{\Omega' M}\right\rangle\right|^{1/2} \quad (\text{mod}2). \tag{6.5.17}$$

However, this term is not diagonal in Ω and cannot be satisfied for all values of J. The Eckart singularities cannot therefore be perfectly canceled. However, as demonstrated in section 8.1.2, the singular terms are numerically treated (but not perfectly canceled) using adapted values of (μ,ν). B. Kendrick showed that we need in total four different sets (μ,ν) to treat all the singularities [152]. In order to show the J, Ω and m dependence on (μ,ν), we replace the labels (μ,ν) by the parameter k^a_Ω which depends explicitly on Ω and where $a=E$ when m is even and $a=O$ when m is odd. The parameter k^a_Ω can then take four values $k^a_\Omega=[1-4]$ corresponding to the four sets (μ,ν) which have been chosen to cancel the singularities. To know which value of $k^a_\Omega=[1-4]$ to use for a given value of J, Ω and m, we must refer to the table 6.1. Then, to know to which values of (μ,ν) corresponds the number $k^a_\Omega=[1-4]$, we must refer to the table 6.2. For example, if we consider the case of $J=2$, $\Omega=4$ and $m=1$, then we must look on table 6.1 the column corresponding to even J and to odd m and note the number corresponding to the line $\Omega=4$ (i.e. $k^a_\Omega=2$). Finally, we check on table 6.2 the function corresponding to the number 2. Then, we must use the $d^l_{1/2,1/2}(\theta)$ as primitive basis functions for $J=2$, $\Omega=4$ and $m=1$. In the following we will use $d^l_{k^a_\Omega}(\theta)$ instead of $d^l_{\mu,\nu}(\theta)$ to explicitly show that the functions used are the chosen ones to treat the singularities.

It should be noted that for $p=0$, the values of m are half-integers while there are integers for $p=1$. Thus, we did not double the domain of definition for the angle ϕ (contrary to [148, 150, 230]) because these half-integer numbers are required to treat Eckart singularities for odd parities. As a result, according to Eq. 6.5.1, there are $(l_{\max}-\mu+1)$ values of l and $(2m_{\max}+1)$ values of m when $p=1$ and $(2m_{\max})$ values of m when $p=0$.

	Even J		Odd J	
	Even m	Odd m	Even m	Odd m
Ω	k_Ω^E	k_Ω^O	k_Ω^E	k_Ω^O
$\vdots$	$\vdots$	$\vdots$	$\vdots$	$\vdots$
$+4$	1	2	3	4
$+2$	2	1	4	3
$+0$	1	2	3	4
-2	2	1	4	3
-4	1	2	3	4
$\vdots$	$\vdots$	$\vdots$	$\vdots$	$\vdots$
$\vdots$	$\vdots$	$\vdots$	$\vdots$	$\vdots$
$+3$	4	3	2	1
$+1$	3	4	1	2
-1	4	3	2	1
-3	3	4	1	2
$\vdots$	$\vdots$	$\vdots$	$\vdots$	$\vdots$

Table 6.1: For a given value of J, the choice of d function depends upon the value of Ω and whether m is even or odd. The number k_Ω^a labels the type of d function (see Table 6.2). Even and odd Ω correspond to even and odd inversion parity, respectively. For odd Ω, even m refers to $m = -1/2, +3/2, -5/2, ...$ and odd m refers to $m = +1/2, -3/2, +5/2, ...$ This table is edited form [152].

	$\lvert\mu-\nu\rvert = 1$	$\lvert\mu-\nu\rvert = 0$
$\lvert\mu+\nu\rvert = 1$	$d^l_{1,0}(4)$	$d^l_{1/2,1/2}(2)$
$\lvert\mu+\nu\rvert = 0$	$d^l_{1/2,-1/2}(3)$	$d^l_{0,0}(1)$

Table 6.2: The appropriate d functions which are needed to remove the Eckart singularities are determined by the values of $|\mu+\nu|(\text{mod}2)$ and $|\mu-\nu|(\text{mod}2)$. The value $|\mu+\nu| = 0$ correspond to even m and the value $|\mu+\nu| = 0$ correspond to odd m. The value $|\mu-\nu| = 0$ correspond to even Λ (the eigenvalue of J_x) and $|\mu-\nu| = 1$ correspond to odd value of Λ (Cf. [152]). The numbers in parenthesis label each type of d function (see Table 6.1). This table is edited form [152].

6.5.3 A Finite Basis Representation (FBR)

In the finite basis representation, the five-dimensional surface functions are given by:

$$\left|\Phi_t^{JMp}\left(\rho_\xi^m\right)\right\rangle = \sum_{lm\Omega} b_t^{lm\Omega} |l\rangle_{k_\Omega^a} \otimes |m\rangle \otimes |J\Omega M\rangle. \tag{6.5.18}$$

In the $\langle\theta| \otimes \langle\phi| \otimes \langle\alpha,\beta,\gamma|$ representation, the surface functions are given by:

$$\begin{aligned}\Phi_t^{JMp}\left(\omega;\rho_\xi^m\right) &\equiv \langle\theta| \otimes \langle\phi| \otimes \langle\alpha,\beta,\gamma \mid \Phi_t^{JMp}\left(\rho_\xi^m\right)\rangle \\ &= \sum_{lm\Omega} b_t^{lm\Omega}\, d_{\mu\nu}^l(\theta) \frac{e^{im\phi}}{\sqrt{2\pi}} \tilde{D}_{\Omega M}^J(\alpha,\beta,\gamma).\end{aligned} \tag{6.5.19}$$

To obtain the coefficients $b_t^{lm\Omega}$, one must express the matrix elements of Eq. 6.4.31 in the primitive base $|l\rangle_{k_\Omega^a} |m\rangle |J\Omega M\rangle$ and then diagonalize the total matrix. As, J, M, and p are good quantum numbers, we can diagonalize each block (J, M, p) independently. For a given block (Ω, Ω'), the matrix elements, noted ${}^{5\mathrm{D}}\mathbf{H}_{\Omega\Omega'}^{JMp}$, are given by:

$$\begin{aligned}{}^{5\mathrm{D}}\mathbf{H}_{\Omega\Omega'}^{JMp} = &\begin{pmatrix} {}^{k_\Omega^E}\mathbf{K}_\theta \otimes {}^{E}\mathbf{I}_\phi & 0 \\ 0 & {}^{k_\Omega^O}\mathbf{K}_\theta \otimes {}^{O}\mathbf{I}_\phi \end{pmatrix} \delta_{\Omega\Omega'} + \begin{pmatrix} {}^{k_\Omega^E}\mathbf{B}_\theta \otimes {}^{E}\mathbf{K}_\phi & 0 \\ 0 & {}^{k_\Omega^O}\mathbf{B}_\theta \otimes {}^{O}\mathbf{K}_\phi \end{pmatrix} \delta_{\Omega\Omega'} \\ &+ \begin{pmatrix} {}^{k_\Omega^E k_{\Omega'}^E}\mathbf{K}_{J^2} \otimes {}^{E}\mathbf{I}_\phi & 0 \\ 0 & {}^{k_\Omega^O k_{\Omega'}^O}\mathbf{K}_{J^2} \otimes {}^{O}\mathbf{I}_\phi \end{pmatrix} + \begin{pmatrix} {}^{k_\Omega^E}\mathbf{C}_\theta \otimes {}^{E}\mathbf{C}_\phi & 0 \\ 0 & {}^{k_\Omega^O}\mathbf{C}_\theta \otimes {}^{O}\mathbf{C}_\phi \end{pmatrix} \delta_{\Omega\Omega'} \\ &+ \frac{15}{8\mu\rho_\xi^{m\,2}} \begin{pmatrix} {}^{E}\mathbf{I}_\theta \otimes {}^{E}\mathbf{I}_\phi & 0 \\ 0 & {}^{O}\mathbf{I}_\theta \otimes {}^{O}\mathbf{I}_\phi \end{pmatrix} \delta_{\Omega\Omega'} + \begin{pmatrix} {}^{EE}_{\Omega}\mathbf{V} & {}^{EO}_{\Omega}\mathbf{V} \\ {}^{OE}_{\Omega}\mathbf{V} & {}^{OO}_{\Omega}\mathbf{V} \end{pmatrix} \delta_{\Omega\Omega'}\end{aligned} \tag{6.5.20}$$

with:

$$\begin{aligned}{}^{k_\Omega^a}K_\theta^{l'} &\equiv -\frac{8\hbar^2}{\mu\rho_\xi^2}\left\langle d_{k_\Omega^a}^l \left| \frac{\partial^2}{\partial\theta^2} + \cot\theta\frac{\partial}{\partial\theta} \right| d_{k_\Omega^a}^{l'} \right\rangle & {}^{a}K_\phi^{m_a m_a'} &\equiv \hbar^2 m_a^2 \delta_{m_a m_a'} \\ {}^{k_\Omega^a}C_\theta^{ll'} &\equiv \frac{4}{\mu\rho_\xi^2}\left\langle d_{k_\Omega^a}^l \left| \frac{\sin\theta/2}{(1+\cos\theta)} \right| d_{k_{\Omega'}^a}^{l'} \right\rangle \hbar\Omega & {}^{a}C_\phi^{m_a m_a'} &\equiv \hbar m_a \delta_{m_a m_a'} \\ {}^{a}I_\theta^{ll'} &\equiv \delta_{ll'} & {}^{a}I_\phi^{m_a m_a'} &\equiv \delta_{m_a m_a'} \\ {}^{k_\Omega^a}B_\theta^{ll'} &\equiv \frac{4}{\mu\rho_\xi^2}\left\langle d_{k_\Omega^a}^l \left| \frac{1}{(1+\cos\theta)} \right| d_{k_\Omega^a}^{l'} \right\rangle k_\Omega^a k_{\Omega'}^a. & &\end{aligned} \tag{6.5.21}$$

The term:

$$\begin{aligned}K_{J^2}^{ll'} \equiv \frac{1}{\mu\rho_\xi^2}\Bigg[&\left\langle d_{k_\Omega^a}^l \left| \frac{1}{(1-\cos\theta/2)} \right| d_{k_{\Omega'}^a}^{l'} \right\rangle \left\langle \widetilde{D}_{\Omega M}^J \left| J_X^2 \right| \widetilde{D}_{\Omega' M}^J \right\rangle + \left\langle d_{k_\Omega^a}^l \left| \frac{1}{(1+\cos\theta/2)} \right| d_{k'_{\Omega'}}^{l'} \right\rangle \\ &\times \left\langle \widetilde{D}_{\Omega M}^J \left| J_Y^2 \right| \widetilde{D}_{\Omega' M}^J \right\rangle + \left\langle d_{k_\Omega^a}^l \left| \frac{1}{(1+\cos\theta)} \right| d_{k_\Omega^a}^{l'} \right\rangle \hbar^2\Omega^2\delta_{\Omega\Omega'} \Bigg]\end{aligned} \tag{6.5.22}$$

depends on J_X^2 and J_Y^2 for which the matrix elements with respect to the Wigner functions are well known analytically [182]. All the terms in Eq. 6.5.21–6.5.22 are computed using a Gauss-Legendre quadrature with 500 points whatever the system studied as recommended by B. Kendrick [152]. These matrix elements can be computed only once and are re-used for each sector.

Finally, the potential matrix elements are given by:

$$\overset{ab}{\Omega}\bar{V}^{ll'}_{mm'} \equiv \int_0^{+\pi} d\theta \sin\theta \int_{-\pi}^{+\pi} d\phi d^l_{k^a_\Omega}(\theta) \frac{e^{-im_a\phi}}{\sqrt{2\pi}} V\left(\rho^m_\xi, \theta, \phi\right) \frac{e^{im_b\phi}}{\sqrt{2\pi}} d^{l'}_{k^b_\Omega}(\theta) \tag{6.5.23}$$

where $a = E, O$ and $b = E, O$ label the even and odd m blocks of $\mathbf{V}$. However, the double integrals involved are too heavy numerically. For this reason, B. Kendrick proposed to use a FBR method in ϕ and a discrete variable representation in θ (Cf. next section). This so-called *Hybrid FBR/DVR representation* greatly reduces the calculation time of the potential matrix elements[12].

6.5.4 The Discrete Variable Representation

In this section, we will explain what is the Discrete Variable Representation (DVR) that we will use in the next section [242]. We will consider a one-dimensional system to simplify the discussion.

Usually, we use a set of N basis functions $\{\phi_i\}$ in which the different operators can be expressed. The vectors satisfy the orthonormality and closure relations:

$$\langle\phi_i|\phi_{i'}\rangle = \int \phi_i^*(x)\phi_{i'}(x)dx = \delta_{ii'} \qquad \sum_{i=1}^{N} |\phi_i\rangle\langle\phi_i| = \mathbf{1}. \tag{6.5.24}$$

To evaluate an integral numerically, we will use the Gauss quadrature method [170], transforming the continuous integral into a discrete sum:

$$\langle\phi_i|\phi_{i'}\rangle \approx \sum_{\alpha=1}^{N} \omega_\alpha \, \phi_i^*(x_\alpha)\phi_{i'}(x_\alpha) \tag{6.5.25}$$

where the continuous variable x is now a set of N points $\{x_\alpha\}$ and where $\langle x_\alpha|\phi_i\rangle \equiv \phi_i(x_\alpha)$. In our case, we will use more precisely a Gauss-Legendre quadrature [170] where the N points x_α are the roots of the N-th Legendre polynomial and where the weights ω_α are given by:

$$\omega_\alpha = \frac{2}{(1-x_\alpha^2)} P'_n(x_\alpha). \tag{6.5.26}$$

The idea of the discrete variable representation is to use the N points $\{x_\alpha\}$ as primitive basis. The associated state vectors in the DVR representation are given by:

$$|\tilde{x}_\alpha\rangle = \sqrt{\omega_\alpha}\,|x_\alpha\rangle \tag{6.5.27}$$

[12] A full DVR method for both ϕ and θ can't be used because the matrix elements of the Hamiltonian become complex and consequently, it doubles the size of the matrices used [152].

and verify the closure and orthogonality relations:

$$\langle \tilde{x}_\alpha | \tilde{x}_{\alpha'} \rangle = \delta_{\alpha,\alpha'} \qquad \sum_{\alpha=1}^{N} |\tilde{x}_\alpha\rangle \langle \tilde{x}_\alpha| = \mathbf{1}. \tag{6.5.28}$$

If we rewrite Eq. 6.5.24 by making the DVR vectors appear:

$$\begin{aligned} \langle \phi_i | \phi_{i'} \rangle = \langle \phi_i | \left[\sum_{\alpha=1}^{N} |\tilde{x}_\alpha\rangle \langle \tilde{x}_\alpha| \right] |\phi_{i'}\rangle &= \sum_{\alpha=1}^{N} \omega_\alpha \langle \phi_i | \tilde{x}_\alpha \rangle \langle \tilde{x}_\alpha | \phi_i \rangle \\ &= \sum_{\alpha=1}^{N} \omega_\alpha \, \phi_i^*(x_\alpha) \phi_{i'}(x_\alpha), \end{aligned} \tag{6.5.29}$$

we then find back Eq. 6.5.25 and make appear the passage matrix that relates the FBR representation to the DVR one:

$$T_x^{\alpha i} = \langle \tilde{x}_\alpha | \phi_i \rangle = \sqrt{\omega_\alpha}\, \phi_i(x_\alpha) \tag{6.5.30}$$

where the superscripts α and i are the indices of the matrix. We have chosen this notation to be consistent with the one used by B. Kendrick [152]. The inverse passage matrix is given by:

$$[\, T_x^{\alpha i} \,]^{-1} = T_x^{i\alpha} = \langle \phi_i | \tilde{x}_\alpha \rangle = \sqrt{\omega_\alpha}\, \phi_i^*(x_\alpha). \tag{6.5.31}$$

The advantage of using a DVR basis is that the potential V is diagonal in this representation and does not involve any integral:

$$\langle \tilde{x}_\alpha | \, V(x) \, | \tilde{x}_\alpha \rangle \approx V(x_\alpha) \delta_{\alpha\alpha'}. \tag{6.5.32}$$

This is the reason why we will apply a DVR representation for the hyperangle θ.

6.5.5 The Hybrid representation

In the Hybrid representation, the five-dimensional surface functions are given by:

$$\left| \Phi_t^{JMp} \left(\rho_\xi^m \right) \right\rangle = \sum_{im\Omega} \tilde{b}_t^{im\Omega} \left| \tilde{\theta}_i \right\rangle \otimes |m\rangle \otimes |J\Omega M\rangle \tag{6.5.33}$$

where $\tilde{b}_t^{im\Omega}$ are the coefficients in the Hybrid representation and $\left|\tilde{\theta}_i\right\rangle$ is the new state in the DVR representation expressed in terms of the Gauss-Legendre weights:

$$\left| \tilde{\theta}_i \right\rangle = \sqrt{\omega_i} \left| \theta_i \right\rangle. \tag{6.5.34}$$

To obtain the matrix elements ${}^{5\mathrm{D}}\tilde{\mathbf{H}}_{\Omega\Omega'}^{JMp}$ of Eq. 6.5.20 in the new Hybrid representation, we must express the matrix $\mathbf{K}_\theta$, $\mathbf{B}_\theta$, $\mathbf{K}_{J^2}$,$\mathbf{C}_\theta$, $\mathbf{I}_\theta$ and $\mathbf{V}$ in the new representation using the passage matrix:

$${}^{k_\Omega^a}T_\theta^{il} = \sqrt{\omega_i}\, d_{k_\Omega^a}^l(\theta_i). \tag{6.5.35}$$

We do not compute these elements directly in the hybrid representation because some terms have angular derivatives. We then obtain for the matrix elements of the grand angular momentum:

$$
\begin{aligned}
{}^{k^a_\Omega}\tilde{K}^{ii'}_{\theta} &= \sum_{ll'} {}^{k^a_\Omega}T^{il}_{\theta}\left({}^{k^a_\Omega}K^{ll'}_{\theta}\right){}^{k^a_\Omega}T^{i'l'}_{\theta} & {}^{k^a_\Omega}\tilde{B}^{ii'}_{\theta} &= \sum_{ll'} {}^{k^a_\Omega}T^{il}_{\theta}\left({}^{k^a_\Omega}B^{ll'}_{\theta}\right){}^{k^a_\Omega}T^{i'l'}_{\theta} \\
{}^{k^a_\Omega k^a_{\Omega'}}\tilde{K}^{ii'}_{J^2} &= \sum_{ll'} {}^{k^a_\Omega}T^{il}_{\theta}\left({}^{k^a_\Omega k^a_{\Omega'}}K^{ll'}_{J^2}\right){}^{k^a_\Omega}T^{i'l'}_{\theta} & {}^{k^a_\Omega}\tilde{C}^{ii'}_{\theta} &= \sum_{ll'} {}^{k^a_\Omega}T^{il}_{\theta}\left({}^{k^a_\Omega}C^{ll'}_{\theta}\right){}^{k^a_\Omega}T^{i'l'}_{\theta} \\
{}^{k^a_\Omega}\tilde{I}^{ii'}_{\theta} &= \delta_{ii'}
\end{aligned}
\tag{6.5.36}
$$

and for the potential energy matrix elements:

$$
{}^{ab}\tilde{V}^{ii'}_{mm'} \equiv \int_{-\pi}^{+\pi} \frac{d\phi}{2\pi} e^{-im_a\phi} V\left(\rho^m_\xi, \widetilde{\theta}_i, \phi\right) e^{im'_b\phi}\delta_{ii'}. \tag{6.5.37}
$$

Note that switching to the DVR representation has transformed the double integral into a single integral which considerably reduces the calculation time. On the other hand, we must use the same number of quadrature points as the number of functions $d^l_{k^a_\Omega}$ which may involves a large basis set for highly localized states.

To obtain the five-dimensional surface functions, we first compute the FBR elements of Eq. 6.5.21 with 500 quadrature points (omitting the ρ^m_ξ terms). Then, we transform these matrix elements into the DVR representation using Eq. 6.5.36. These elements are independent of the hyper-radius and are only computed once. Then, we compute the total matrix at the center of each sector ρ^m_ξ. Using parallel programming (OPENMP), 40 sectors can be diagonalized simultaneously by assigning a single thread to each sector[13]. Once the diagonalization is done, we store the energy independent eigenenergies and eigenvectors in binary files that can be reused later.

6.5.6 The Sequential Diagonalization Truncation (SDT)

Another advantage of using the Hybrid FBR/DVR approach is that we can perform a Sequential Diagonalization Truncation (SDT) to reduce the size of the total Hamiltonian before diagonalization. The first step is to compute an one-dimensional Hamiltonian ${}^{1D}\hat{H}(\theta_i)$ for each value θ_i such that:

$$
{}^{1D}\hat{H}(\theta_i) \equiv -\frac{4\hbar^2}{\mu {\rho^m_\xi}^2(1+\cos\theta_i)}\frac{\partial^2}{\partial\phi^2} + V(\rho^m_\xi, \theta_i, \phi). \tag{6.5.38}
$$

As we can see, we keep only the term of the grand angular momentum for which (J, M, p, l, Ω) are good quantum numbers. As a consequence, we need to compute the matrix elements which involve an integral over ϕ:

$$
\langle m'|\,{}^{1D}\hat{H}(\theta_i)\,|m\rangle = \frac{4\hbar^2}{\mu {\rho^m_\xi}^2(1+\cos\theta_i)} m^2\delta_{m'm} + \langle m'|\,V(\rho^m_\xi, \theta_i, \phi)\,|m\rangle\,. \tag{6.5.39}
$$

[13] One could easily adapt the code with a hybrid parallel approach using both OPEN-MP and MPI on supercomputers.

The first term is analytically obtained whereas the second one involves integrals which have already been computed and stored. For each possible value of θ_i, we diagonalize ${}^{1\mathrm{D}}\hat{\mathbf{H}}(\theta_i)$:

$$\left(\mathbf{Q}^i\right)^T {}^{1\mathrm{D}}\hat{\mathbf{H}}(\theta_i)\ \mathbf{Q}^i = {}^{1\mathrm{D}}\mathbf{E}^i \tag{6.5.40}$$

where $\mathbf{E}^i$ are the eigenenergies and $\mathbf{Q}^i$ are their corresponding eigenvectors. The second step is to keep the n_i eigenvectors whose energies are below a cut-off energy ${}^{1\mathrm{D}}E_{\mathrm{cut}}$ defined via convergence studies:

$${}^{1\mathrm{D}}E_n^i \leqslant {}^{1\mathrm{D}}E_{\mathrm{cut}}. \tag{6.5.41}$$

In total, we obtain $(l_{\max}-\mu+1)$ truncated vectors stored in $N^{1D}\times n_i$ rectangular matrices. The third step is to transform the total Hamiltonian into a truncated Hamiltonian, noted ${}^{5\mathrm{D}}\overline{\mathbf{H}}^{JMp}_{\Omega\Omega' ii'}$ obtained via the transformation:

$${}^{5\mathrm{D}}\overline{\mathbf{H}}^{JMp}_{\Omega\Omega' ii'} = \left(\mathbf{Q}^i\right)^T {}^{5\mathrm{D}}\tilde{\mathbf{H}}^{JMp}_{\Omega\Omega' ii'}\ \mathbf{Q}^{i'}. \tag{6.5.42}$$

We then have a new Hamiltonian whose dimensions are highly reduced (by a factor of about two). Moreover, the computation time of the whole SDT procedure is much lower than the total Hamiltonian diagonalization, then this method is indispensable, especially for large values of J.

Finally, we can express the five-dimensional surface functions in the new SDT-Hybrid representation:

$$\left|\Phi_t^{JMp}\left(\rho_{\tilde{\xi}}\right)\right\rangle = \sum_{in\Omega} \bar{b}_t^{in\Omega}\,|\theta_i\rangle' \otimes |n\rangle_i \otimes |J\Omega M\rangle \tag{6.5.43}$$

where $|n\rangle_i$ are the truncated states. We can express them in terms of the initial ones via:

$$|n\rangle_i \equiv \sum_m Q^i_{mn}|m\rangle. \tag{6.5.44}$$

We can express the coefficients $\tilde{b}_t^{im\Omega}$ of the Hybrid representation to those of the truncated representation $\bar{b}_t^{in\Omega}$ by inserting Eq. 6.5.44 into Eq. 6.5.43:

$$\tilde{b}_t^{im\Omega} = \sum_n \bar{b}_t^{in\Omega} Q^i_{mn}. \tag{6.5.45}$$

This equation is useful to calculate the overlap matrix elements for which the truncated eigenvectors do not have the same size from one sector to another.

6.5.7 Identical particle permutation symmetry

It is complicated to symmetrize the primitive basis set before diagonalization while preserving an accurate cancellation of Eckart singularities. It is then preferable to diagonalize the total Hamiltonian and then extract the symmetrized surface functions by applying a projection operator. In our studies, we will deal with collisions of three identical particles and it is here that our formalism deviates from B. Kendrick's which deals

with $A + B_2$ collisions.

Let $\mathcal{P}_{AB}$, $\mathcal{P}_{BC}$ and $\mathcal{P}_{CA}$ be the two-body permutation operators and $\mathcal{P}_{ABC}$ and $\mathcal{P}_{ABC}^{-1}$ be the cyclic and anti-cyclic three-body ones. We can show that they only affect the hyperangle ϕ and the three Euler angles such that:

$$\begin{aligned}
P_{BC}: &\quad (\theta_i, \phi, \alpha, \beta, \gamma) \to (\theta_i, -\phi, \pi + \alpha, \pi - \beta, -\gamma) \\
P_{AB}: &\quad (\theta_i, \phi, \alpha, \beta, \gamma) \to (\theta_i, -\phi + 4\pi/3, \pi + \alpha, \pi - \beta, -\gamma) \\
P_{CA}: &\quad (\theta_i, \phi, \alpha, \beta, \gamma) \to (\theta_i, -\phi - 4\pi/3, \pi + \alpha, \pi - \beta, -\gamma) \\
P_{ABC}: &\quad (\theta_i, \phi, \alpha, \beta, \gamma) \to (\theta_i, \phi + 4\pi/3, \alpha, \beta, \gamma) \\
P_{ABC}^{-1}: &\quad (\theta_i, \phi, \alpha, \beta, \gamma) \to (\theta_i, \phi - 4\pi/3, \alpha, \beta, \gamma).
\end{aligned} \tag{6.5.46}$$

We can show that the P_{BC} operator inverts the Z_Q and Y_Q axis:

$$X_Q \to X_Q \qquad Y_Q \to -Y_Q \qquad Z_Q \to -Z_Q \tag{6.5.47}$$

which can be verified explicitly by substituting the above transformation of the Euler angles into Eq. 6.3.5. The other transformations involve an additional kinematic rotation that enables us to move from one arrangement to another. The symmetrization operations are then very easy to set up in this choice of hyperspherical coordinates.

We must apply the operator $\sigma_\pm$:

$$\sigma_\pm = \frac{1}{6}\left(1 \pm P_{BC} \pm P_{AB} \pm P_{CA} \pm P_{ABC} \pm P_{ABC}^{-1}\right) \tag{6.5.48}$$

on the surface functions:

$$\Phi_t^{JMPq=\pm}(\omega; \rho_\xi^m) = \sigma_\pm \Phi_t^{JMp}(\omega; \rho_\xi^m) \tag{6.5.49}$$

to extract fully symmetric (+) or anti-symmetric (-) surface functions. For example, to extract the surface functions of symmetry $q = +$, we must apply σ_+ on every surface functions Φ_t^{JMp} (i.e. every t). However, every non-symmetrized surface functions t can't form a $q = +$ surface function. We must then test each function Φ_t^{JMpq} formed by computing their norm:

$$\left\langle \Phi_t^{JMpq} \middle| \Phi_t^{JMpq} \right\rangle. \tag{6.5.50}$$

If the norm = 1 then we keep the surface function because it has good symmetry. If the norm = 0, this means that the surface functions t correspond to another symmetry and is not kept. Since the surface functions are linear combinations of Wigner functions, the following symmetry property:

$$\tilde{D}^J_{\Omega M}(\pi + \alpha, \pi - \beta, -\gamma) = (-1)^J \tilde{D}^J_{\Omega M}(\alpha, \beta, \gamma) \tag{6.5.51}$$

are used to simplify the calculations of the elements in Eq. 6.5.50.

6.5.8 Propagation

To solve the set of coupled equations (Eq. 6.4.29), we use the same method as for the two-body part. We propagate the logarithmic derivative $\mathbf{Z}$ of the radial wave function over $[\rho_{\min}, \rho_{\max}]$ by dividing the total interval into sub-sectors. The distance $\rho = \rho_{\max}$ is the distance at which the matching is performed and is chosen large enough so that the different channels have reached their asymptotic behavior. At $\rho = \rho_{\min}$, we are in the classically forbidden zone where the wave functions is zero. Therefore the initial condition of the Z-matrix is given by:

$$Z_{t,t'}(\rho_{\min}) = \infty\, \delta_{tt'}. \tag{6.5.52}$$

We can note that this condition can be applied if the potential energy surface is known at short distance and if no loss conditions similar to the ones used in chapters 4 and 5 are applied.

Finally, to complete the propagation process, we evaluate the overlap matrix elements:

$$O_{tt'}^{Jp\pm} \equiv \left\langle \Phi_t^{JMp\pm}\left(\rho_\xi^m\right) \middle| \Phi_{t'}^{JMp\pm}\left(\rho_{\xi+1}^m\right) \right\rangle \tag{6.5.53}$$

and the potential coupling matrix elements:

$$\left\langle \Phi_t^{JMp\pm}(\rho_\xi^m) \middle| V(\rho,\theta,\phi) - \left(\frac{\rho_\xi^m}{\rho}\right)^2 V(\rho_\xi^m,\theta,\phi) \middle| \Phi_{t'}^{JMp\pm}(\rho_{\xi+1}^m) \right\rangle \tag{6.5.54}$$

by paralleling the integral over ϕ. The matrix elements of the overlap matrices and ofthe potential coupling matrices are computed once (for all value of ρ) and can be re-used for studies in function of the collision energy E_k.

6.6 Matching

Once the propagation has been carried out to a distance large enough so that the potential has reached its asymptotic form, the boundary conditions on the radial wave functions can be applied. As in Delves coordinates (Cf. section 6.2), we can distinguish three kinds of state asymptotically. The first two correspond to bound and quasi-bound states whose adiabatic energy curves:

$$\mathcal{E}_t^{Jp\,q}(\rho) \underset{\rho\to+\infty}{\longrightarrow} \varepsilon_{\tau vjl} \tag{6.6.1}$$

where $\varepsilon_{\tau vjl}$ are the solutions of Eq 6.2.10. The bound states are characterized by negative energies $\varepsilon_{\tau vjl} < 0$ while the quasi-bound states are characterized by positive energies $\varepsilon_{\tau vjl} > 0$ (which are manifestations of shape resonances of a free diatomic molecule in an excited rotational state). These two states correspond to the configuration where $S_\tau \underset{\rho\to+\infty}{\longrightarrow} +\infty$ while s_τ remains finite. Physically, they correspond to the simple continuum of an

atom and a diatom. This is why they are usually called *simple continuum states*. The last kind of states are the ones whose adiabatic energy curves vanish asymptotically following:

$$\mathcal{E}_t^{Jp\,q}(\rho) \underset{\rho\to+\infty}{\longrightarrow} \frac{\lambda(\lambda+4)+15/4}{2\mu\rho^2} \tag{6.6.2}$$

where $\lambda = 0, 1, 2, ...$ as explained in section 6.2. These states correspond to the case where the three particles are all far from each others, i.e. the two conditions $S_\tau \underset{\rho\to+\infty}{\longrightarrow} +\infty$ and $s_\tau \underset{\rho\to+\infty}{\longrightarrow} +\infty$ are both satisfied. This is why they are usually called *double continuum states*.

As explained in the discussion below Eq. 6.4.6, APH coordinates are not adapted when $S_\tau \gg s_\tau$ (i.e. asymptotic atom-diatom configurations) because the vector $\vec{q}$ does not match with the vector $\vec{s}_\tau$ by definition. Therefore, we will apply a mixed-boundary condition [231, 232] where the asymptotic atom-diatom radial wave functions will be given in Jacobi coordinate while the asymptotic continuum functions will be given in APH coordinates.

6.6.1 Asymptotic boundary conditions for simple continuum states

The asymptotic form of the radial wave functions in mass-scaled Jacobi coordinates is obtained by solving the asymptotic form of Eq. 6.1.29. At large distances, these equations are no longer coupled and are similar to Eq. 3.5.12 (obtained in the two-body part) where we changed $r \to S_\tau$ and where the reduced mass used here is the three-body one:

$$\left[-\frac{\hbar^2}{2\mu}\frac{d^2}{dS_\tau^2} + \frac{\hbar^2 l\,(l+1)}{2\mu S_\tau^2} + \varepsilon_{\tau vj} - E_{\text{tot}}\right] F^{JME}_{\tau vjl,\tau vjl}\,(S_\tau) = 0. \tag{6.6.3}$$

The general solutions $\mathbf{F}$ of Eq. 6.6.3 are a combination of two independent solutions $\mathbf{F}^{(1)}$ and $\mathbf{F}^{(2)}$ such that:

$$\mathbf{F} = \mathbf{F}^{(1)}\mathbf{A} + \mathbf{F}^{(2)}\mathbf{B}\big|_{\rho=\rho_{\max}} \tag{6.6.4}$$

where $\mathbf{A}$ and $\mathbf{B}$ are normalization factors. For open channels (i.e. $E > \varepsilon_{\tau vj}$), their matrix elements are similar to Eq. 3.5.14:

$$\begin{aligned} F^{(1)\,JME}_{\tau'v'j'l',\tau vjl}\,(S_{\tau'}) &= S_{\tau'}\sqrt{k_{\tau'v'j'}}\,j_{l'}(k_{\tau'v'j'}S_{\tau'})\,\delta_{\tau'v'j'l',\tau vjl} \\ F^{(2)\,JME}_{\tau'v'j'l',\tau vjl}\,(S_{\tau'}) &= S_{\tau'}\sqrt{k_{\tau'v'j'}}\,n_{l'}(k_{\tau'v'j'}S_{\tau'})\,\delta_{\tau'v'j'l',\tau vjl} \end{aligned} \tag{6.6.5}$$

where $k^2_{vjl} = 2\mu(E_{\text{tot}} - \varepsilon_{\tau vj})/\hbar^2$. As in the two-body study, they are expressed in function of the Ricatti-Bessel (j_l) and Ricatti-Neumann (n_l) functions [170]. For closed channels, one must replace j_l by i_l and n_l by k_l which are the modified Bessel functions of integer order [170].

However, since the Z-matrix is obtained in APH coordinates, we must transform the asymptotic mass-scaled Jacobi radial wave functions into APH coordinates following two steps.

From mass-scaled Jacobi coordinates to SF$_\tau$–Delves coordinates

The first step consists in transforming the asymptotic functions $\mathbf{F}^{(1)}$ and $\mathbf{F}^{(2)}$ given in Eq. 6.6.5 into the SF$_\tau$–Delves coordinates. For a given atom-diatom channel $\{\tau, v, j, l\}$, the partial wave in mass-scaled Jacobi coordinates (Eq. 6.1.26) is given by:

$$\begin{aligned}\psi^{JME}_{\tau vjl} &= \sum_{\tau'' v'' j'' l''} \frac{1}{S_{\tau''}} \Phi^{JME}_{\tau'' v'' j'' l''}\left(\hat{S}^{\mathrm{SF}}_{\tau''}, \vec{s}^{\,\mathrm{SF}}_{\tau''}\right) F^{JME(1,2)}_{\tau'' v'' j'' l'', \tau v j l}\left(S_\tau\right)\Big|_{\rho=\rho_{\max}} \\ &= \frac{1}{S_\tau}\frac{\chi_{\tau vj}\left(s_\tau\right)}{s_\tau} Y^{JM}_{jl}\left(\hat{S}^{\mathrm{SF}}_{\tau}, \hat{s}^{\mathrm{SF}}_{\tau}\right) F^{JME(1,2)}_{\tau vjl, \tau vjl}\left(S_\tau\right)\Big|_{\rho=\rho_{\max}} \\ &= \frac{2}{\rho^2}\frac{\chi_{\tau vj}\left(s_\tau\right)}{\sin 2\omega_\tau} Y^{JM}_{jl}\left(\hat{S}^{\mathrm{SF}}_{\tau}, \hat{s}^{\mathrm{SF}}_{\tau}\right) F^{JME(1,2)}_{\tau vjl, \tau vjl}\left(S_\tau\right)\Big|_{\rho=\rho_{\max}}.\end{aligned} \tag{6.6.6}$$

In the SF$_\tau$–Delves coordinates, the same partial wave is given by Eq. 6.2.14:

$$\psi^{JME}_{\tau vjl} = \frac{2}{\rho^{5/2}} \sum_{\tau'' v'' j'' l''} \frac{\chi_{\tau'' v'' j'' l''}\left(\omega_{\tau''}; \rho_{\max}\right)}{\sin 2\omega_{\tau''}} Y^{JM}_{j'' l''}\left(\hat{S}^{\mathrm{SF}}_{\tau''}, \hat{s}^{\mathrm{SF}}_{\tau''}\right) F^{JME(1,2)}_{\tau'' v'' j'' l'', \tau v j l}(\rho). \tag{6.6.7}$$

By multiplying Eq. 6.6.6 and Eq. 6.6.7 on the left by $\left[\chi_{\tau' v' j' l'}\left(\omega_{\tau'}; \rho_{\max}\right) Y^{JM}_{j' l'}\left(\hat{S}^{\mathrm{SF}}_{\tau'}, \hat{s}^{\mathrm{SF}}_{\tau'}\right)\right]^*$, then integrating over all the angular coordinates and finally after identifying them, we obtain for the radial wave functions:

$$\begin{aligned}F^{JME(1,2)}_{\tau' v' j' l', \tau v j l}\left(\rho; \rho_{\max}\right) = \rho^{1/2} \left\langle \chi_{\tau' v' j' l'}\left(\omega_{\tau'}; \rho_{\max}\right) \Big| \chi_{\tau vj}\left(s_\tau\right) F^{JME(1,2)}_{\tau vjl, \tau vjl}\left(S_\tau\right) \right\rangle_{\omega_\tau}\Big|_{\rho=\rho_{\max}} \\ \times \delta_{j' j}\delta_{l' l}\delta_{\tau' \tau}\end{aligned} \tag{6.6.8}$$

where the index ω_τ means that we must perform an integral over the ω_τ angle. For the radial derivatives functions, we have:

$$\begin{aligned}&\left(F^{JME(1,2)}_{\tau' v' j' l', \tau v j l}\left(\rho; \rho_{\max}\right)\right)' \\ &\quad= \frac{\partial}{\partial \rho}\left\{\rho^{1/2} \left\langle \chi_{\tau' v' j' l'}\left(\omega_{\tau'}; \rho_{\max}\right) \Big| \chi_{\tau vj}\left(s_\tau\right) F^{JME(1,2)}_{\tau vjl, \tau vjl}\left(S_\tau\right) \right\rangle_{\omega_\tau}\right\}\Big|_{\rho=\rho_{\max}} \delta_{j' j}\delta_{l' l}\delta_{\tau' \tau} \\ &= \left\langle \chi_{\tau' v' j' l'}\left(\omega_{\tau'}; \rho_{\max}\right) \Big| \frac{\partial}{\partial \rho}\left\{\rho^{1/2} \chi_{\tau vj}\left(s_\tau\right) F^{JME(1,2)}_{\tau vjl, \tau vjl}\left(S_\tau\right)\right\} \right\rangle_{\omega_\tau}\Big|_{\rho=\rho_{\max}} \delta_{j' j}\delta_{l' l}\delta_{\tau' \tau}.\end{aligned} \tag{6.6.9}$$

For Eq. 6.6.9, the surface functions in Delves coordinates are evaluated at a fixed value of $\rho = \rho_{\max}$ whereas the Jacobi internal wave functions and the radial wave functions depend respectively on s_τ and S_τ which have a dependence on ρ. This leads to non-zero radial derivative terms. They are calculated using the following expression:

$$\begin{aligned}\frac{\partial}{\partial \rho}\left\{\rho^{1/2} \chi_{\tau vj}\left(s_\tau\right) F^{JME(1,2)}_{\tau vjl, \tau vjl}\left(S_\tau\right)\right\} &= \rho^{1/2}\left\{\cos\omega_\tau \chi_{\tau vj}\left(s_\tau\right) \frac{\partial F^{JME(1,2)}_{\tau vjl, \tau vjl}\left(S_\tau\right)}{\partial S_\tau}\right. \\ \left. + \sin\omega_\tau \frac{\partial \chi_{\tau vj}\left(s_\tau\right)}{\partial s_\tau} F^{JME(1,2)}_{\tau vjl, \tau vjl}\left(S_\tau\right)\right\} &+ \frac{1}{2\rho^{1/2}} \chi_{\tau vj}\left(s_\tau\right) F^{JME(1,2)}_{\tau vjl, \tau vjl}\left(S_\tau\right).\end{aligned} \tag{6.6.10}$$

From SF$_\tau$–Delves coordinates to APH coordinates

The second step consists in projecting the Delves functions onto the symmetric functions of the hyperspherical surfaces defined in Eq. 6.4.31. B. Kendrick defines the transformation matrix to go from APH coordinates to Delves coordinates in [218]:

$$U^{Jpq}_{\tau vjl,t} \equiv \frac{4\sqrt{2}}{2}\int_0^{\pi/2} \mathrm{d}\omega_\tau \sin(2\omega_\tau)\int_0^{+\pi} \mathrm{d}\eta_\tau \sin(\eta_\tau)\,\chi_{\tau' v' j' l'}(\omega_{\tau'};\rho_{\max}) \times \sqrt{\frac{2l+1}{2J+1}}\sum_\Lambda \left(1+(-1)^{p+j+l+1}\right) C(jlJ;\Lambda 0\Lambda)\hat{P}_{j\Lambda}(\eta_\tau)\,F^{Jpq}_{\Lambda t}(\omega_\tau,\eta_\tau) \quad (6.6.11)$$

where

$$F^{Jpq}_{\Lambda t}(\omega_\tau,\eta_\tau) \equiv \frac{(-1)^{p+1}}{\sqrt{2\pi}}\sum_{lm\Omega} b^{lm\Omega}_t d^l_{\mu\nu}(\theta(\omega_\tau,\eta_\tau)) \times d^J_{\Omega\Lambda}(\pi/2) i^\Lambda F^\Lambda_{m\Omega}(\omega_\tau,\eta_\tau) \quad (6.6.12)$$

and

$$F^\Lambda_{m\Omega}(\omega_\tau,\eta_\tau) = \begin{cases} N_\Lambda \cos\left[m\phi(\omega_\tau,\eta_\tau)+\Omega\gamma_Q\right] \\ \quad (q+\Lambda \text{ even}) \\ \\ iN_\Lambda \sin\left[m\phi(\omega_\tau,\eta_\tau)+\Omega\gamma_Q\right] \\ \quad (q+\Lambda \text{ odd}) \end{cases} \quad (6.6.13)$$

with $N_\Lambda = 2$ for $\Lambda > 0$ and $N_0 = 1$. The integer Λ denotes the projection of $\mathbf{J}$ along the BF$_\tau$–Delves Z_τ axis. The $C(jlJ;\Lambda 0\Lambda)$ are Clebsch-Gordan coefficients [170] and the $\hat{P}_{j\Lambda}$ are given by:

$$\hat{P}_{j\Lambda}(\eta_\tau) \equiv \sqrt{2\pi} Y_{j\Lambda}(\eta_\tau, 0) \quad (6.6.14)$$

where the $Y_{j\Lambda}$ are spherical harmonics. The $d^J_{\Omega\Lambda}(\pi/2)$ term and the $\Omega\gamma_Q$ term come from the rotation to go from the BF$_Q$ to the BF$_\tau$ [218].

To transform the SF$_\tau$–Delves radial wave function into APH coordinates, one must use the inverse matrix $\mathbf{U}^{-1}$ whose elements will be noted $U^{Jpq}_{t,\tau vjl}$. We then obtain:

$$F^{JME(1,2)}_{t,\tau vjl}(\rho;\rho_{\max}) = \sum_{\tau' v' j' l'} U^{Jpq}_{t,\tau' v' j' l'} F^{JME(1,2)}_{\tau' v' j' l',\tau vjl}(\rho;\rho_{\max}) \quad (6.6.15)$$

and:

$$\left(F^{JME(1,2)}_{t,\tau vjl}(\rho;\rho_{\max})\right)' = \sum_{\tau' v' j' l'} U^{Jpq}_{t,\tau' v' j' l'}\left(F^{JME(1,2)}_{\tau' v' j' l',\tau vjl}(\rho;\rho_{\max})\right)' \quad (6.6.16)$$

which are the non-diagonal elements that we will use in Eq. 6.6.18 for the matching.

6.6.2 Asymptotic boundary conditions for double continuum states

For the open continuum channels [243, 231, 232], the asymptotic radial functions are given by:

$$\begin{aligned} F^{JME(1,2)}_{t',t}(\rho;\rho_{\max}) &= \delta_{fi}\sqrt{\frac{\pi\rho}{2}} J_{\lambda_f+2}(k_f\rho) \\ F^{JME(1,2)}_{t',t}(\rho;\rho_{\max}) &= \delta_{fi}\sqrt{\frac{\pi\rho}{2}} Y_{\lambda_f+2}(k_f\rho) \end{aligned} \quad (6.6.17)$$

where $\lambda_f = 2\nu_f + j_f + \ell_f$ [231, 232] and $k_f^2 = 2\mu E_{\rm tot}/\hbar^2$. The functions J_n are the regular Bessel function of integer order, and Y_n are the irregular Bessel function of integer order.

The closed channels are obtained by replacing J_{τ_f+2} by I_{τ_f+2} and Y_{τ_f+2} by K_{τ_f+2} which are the modified Bessel functions of integer order [170].

6.6.3 K-matrix and S-matrix

As in the two-body part, we relate the K-matrix to the Z-matrix via:

$$\mathbf{K} = \left\{\mathbf{Z}\mathbf{F}^{(2)} - \mathbf{F}'^{(2)}\right\}^{-1}\left\{\mathbf{Z}\mathbf{F}^{(1)} - \mathbf{F}'^{(1)}\right\}\Big|_{\rho=\rho_{\max}}. \tag{6.6.18}$$

The S-matrix is obtained from the K-matrix using:

$$\mathbf{S} = \frac{\mathbf{I} + i\mathbf{K}}{\mathbf{I} - i\mathbf{K}}. \tag{6.6.19}$$

and the T-matrix is given by:

$$\mathbf{T} = \mathbf{S} - \mathbf{I}. \tag{6.6.20}$$

6.7 Observables

The elastic cross sections between atom-diatom are given by [151]:

$$\sigma_{el} = \sigma_{\tau vj\to\tau vj} = \frac{\pi}{(2j+1)k^2_{\tau vj}}\sum_{J,l}(2J+1)\left|T^J_{\tau vjl,\tau vjl}\right|^2. \tag{6.7.1}$$

The $(2j+1)$ term come from the fact that we have averaged the cross sections over the initial magnetic states m_j. The inelastic cross sections between bound states are given by:

$$\begin{aligned}\sigma_{in} &= \sum_{\tau'v'j'\neq\tau vj}\sigma_{\tau vj\to\tau'v'j'}\\ &= \sum_{\tau'v'j'\neq\tau vj}\frac{\pi}{(2j+1)k^2_{\tau vj}}\sum_{J,l,l'}(2J+1)\left|T^J_{\tau'v'j'l',\tau vjl}\right|^2\\ &= \frac{\pi}{(2j+1)k^2_{\lambda vj}}\sum_{J,l,l'}(2J+1)\left(1-\left|S^J_{\lambda vjl,\lambda vjl}\right|^2\right).\end{aligned} \tag{6.7.2}$$

The elastic β^{el} and inelastic β^{in} collision rate coefficients are given by:

$$\beta_{el} = \sigma^{el}\cdot v = \sigma^{el}\sqrt{\frac{2E_{\rm k}}{\mu_{\tau-\tau+1\,\tau+2}}} \quad \beta_{in} = \sigma^{in}\cdot v = \sigma^{in}\sqrt{\frac{2E_{\rm k}}{\mu_{\tau-\tau+1\,\tau+2}}} \tag{6.7.3}$$

where v denotes the relative velocity of the two particles, $\mu_{\tau-\tau+1\,\tau+2}$ is the atom-diatom reduced mass defined in Eq. 6.1.3 and $E_{\rm k}$ is the relative kinetic energy.

The three-body recombination rate coefficient, usually noted K_3, is given by [244]:

$$K_3 = \sum_{i,f} \frac{192(2J+1)\pi^2}{\mu k^4} \left| S^J_{f \leftarrow i} \right|^2 \tag{6.7.4}$$

where i and f label the incident (three-body continuum) and outgoing (two-body recombination) channels with $k_f^2 = 2\mu E/\hbar^2$ and where μ is the three-body reduced mass.

Chapter 7

Three-body static electric field shielding

In the two-body part, we studied two techniques for reducing short-range losses. Both methods aim to create a long-range potential barrier in the incident channel by taking advantage of the properties of the dipole-dipole interaction. The first method uses a circularly polarized electromagnetic wave while the second one uses a static electric field. Although the first method allows an interesting control of the scattering length, the number of states involved is much larger due to the additional quantum number n which must be considered. In this chapter, we focus on the static electric field shielding, which seems easier to implement numerically for three-body collisions.

Do three-body collisions really matter in ultracold experiments?

Since the shielding techniques have proven to be experimentally effective, the next challenge is to reach quantum degeneracy regimes. Although evaporative cooling ejects the hottest molecules, the densities involved increase and three-body collisions can become significant. Let's take the example of the experience at JILA [100]. They can cool down gases of KRb molecules to typical temperatures $T \approx 500\,\mathrm{nK}$ with densities $n_0 \approx 2.5 \times 10^{11}$ molecules/cm^3. As the characteristic time between two events of three-body collisions scales as $\tau^{3\mathrm{B}} \propto n_0^{-2}$ (Cf. appendix C), three-body loss processes can become significant, preventing the creation of degenerate quantum gases. In addition, if we reach quantum degeneracy regimes, some many-body states (droplets or many exotic supersolid states) can only appear in density ranges where three-body collisions dominate [245]. For all these reasons, it is crucial to find a method to reduce three-body losses while preserving two-body shielding.

In this chapter, we study the asymptotic three-body energies and show that two three-body internal states are resonant for the same electric field value as the one used for two-body shielding. We show that the number of states required for a complete study is too large to get converged results. Hence, we present a simplified model adapted from chapter 5 to extract the three-body rate coefficients. Finally, we discuss the results and present the validity domain of the model.

7.1 Asymptotic three-body rotational states

The general principle of the three-body shielding remains identical to that of the two-body one: only the mathematical formalism must be adapted to consider the effect of the third molecule. The objective is to create a long-range potential barrier by exploiting the dipole-dipole-dipole interaction. In the following, we only consider collisions between three identical bosonic ^{40}K^{87}Rb molecules.

The first step is to find two three-body rotational states that can be brought to resonance by applying an external static electric field. In Fig. 7.1, we represent the evolution of the asymptotic energies (i.e. when r_A, r_B and $r_C \to \infty$) as a function of the electric field. We restrict to the projections $m_{j_\tau} = 0$ for more visibility. Since the molecules are considered as isolated, the total internal energy $\varepsilon_{\tilde{\alpha}}$ can be divided as a sum of the individual energies of each molecule dressed by the electric field $\varepsilon_{\tilde{\alpha}} = \varepsilon_{\tilde{\alpha}_1} + \varepsilon_{\tilde{\alpha}_2} + \varepsilon_{\tilde{\alpha}_3}$. If we consider a third molecule excited in its first rotational state, this implies shifting all two-body energy levels by the same constant $\varepsilon_{\tilde{\alpha}_3}$. The three-body asymptotic states $\{|\tilde{1},0\rangle\,|\tilde{1},0\rangle\} \otimes |\tilde{1},0\rangle$ and $\{|\tilde{0},0\rangle\,|\tilde{2},0\rangle\} \otimes |\tilde{1},0\rangle$ therefore cross at the same electric field value as if the third molecule was spectator, i.e. $E_3^* = 12.3\,\mathrm{kV\,cm^{-1}}$. Therefore, a simultaneous two-body and three-body shielding seems to be feasible.

We can observe a second crossing (purple box) for an electric field $E < E_3^*$. This crossing could have been interesting from an experimental point of view since it requires a weaker electric field. Nevertheless, it corresponds to the intersection between the two states $|\tilde{1},0\rangle\,|\tilde{1},0\rangle\,|\tilde{2},0\rangle$ and $|\tilde{0},0\rangle\,|\tilde{0},0\rangle\,|\tilde{3},0\rangle$ which cannot be used because it is hard in an experimental point of view to prepare molecules in different states.

7.2 Complete three-body problem

In this section, we apply and adapt the formalism presented in chapter 6 to three-body shielding. First, we present the basis set and the potential used. Then, we show through the adiabatic energy curves that we are not able to get converged results, even using an adapted SDT method.

7.2.1 Formalism

Symmetrization of the internal states

As we consider indistinguishable molecules, one must symmetrize the internal states $|\tilde{j}_1,0\rangle\,|\tilde{j}_2,0\rangle\,|\tilde{j}_3,0\rangle$ with respect to the permutation operators previously presented. In this study, we only consider the two states $|\tilde{1},0\rangle\,|\tilde{1},0\rangle\,|\tilde{1},0\rangle$ and $|\tilde{0},0\rangle\,|\tilde{2},0\rangle\,|\tilde{1},0\rangle$. The first one corresponds to the special case of three indistinguishable states (i.e. $\tilde{j}_1 = \tilde{j}_2 = \tilde{j}_3$) then only internal states that are fully symmetric with respect to each permutation operator exist:

$$\begin{aligned} |\tilde{1},\tilde{1},\tilde{1}\rangle_+ &= \frac{1}{6}\Big[\,|\tilde{1},\tilde{1},\tilde{1}\rangle + |\tilde{1},\tilde{1},\tilde{1}\rangle + |\tilde{1},\tilde{1},\tilde{1}\rangle + |\tilde{1},\tilde{1},\tilde{1}\rangle + |\tilde{1},\tilde{1},\tilde{1}\rangle + |\tilde{1},\tilde{1},\tilde{1}\rangle\,\Big] \\ &= |\tilde{1},\tilde{1},\tilde{1}\rangle \end{aligned} \tag{7.2.1}$$

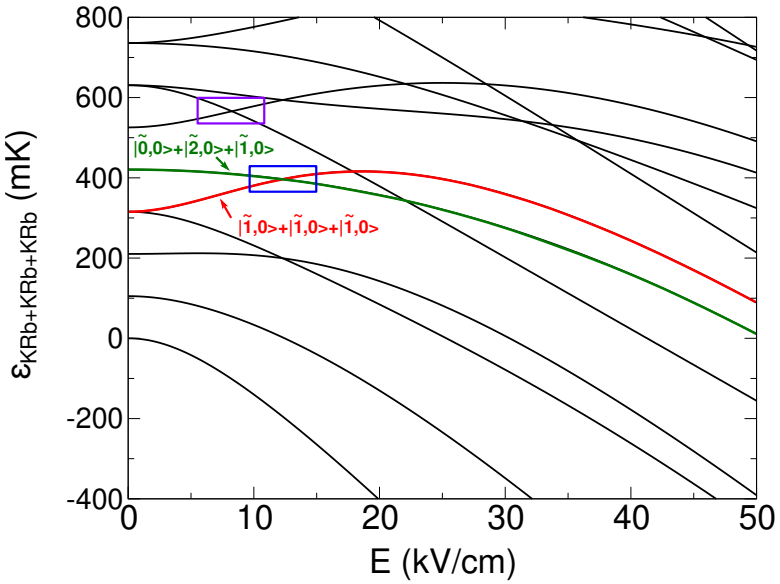

Figure 7.1: Energy of three bosonic $^{41}K^{87}Rb$ molecules as a function of the electric field. Only the curves corresponding to $m_{j_\tau} = 0$ are represented. Red curve: the initial state $\left|\tilde{1},0\right\rangle\left|\tilde{1},0\right\rangle\left|\tilde{1},0\right\rangle$, Green curve: the resonant state $\left|\tilde{0},0\right\rangle\left|\tilde{2},0\right\rangle\left|\tilde{1},0\right\rangle$. The blue box indicates the crossing at $E_3^* = 12.3\,\mathrm{kV\,cm^{-1}}$ between the two states we are interested. Purple box: Crossing not interesting from an experimental point of view.

where we omit $m_j = 0$ in the notations. We analogously form a fully symmetric state for the second internal state:

$$\left|\tilde{0},\tilde{1},\tilde{2}\right\rangle_+ = \frac{1}{\sqrt{6}}\Big[\left|\tilde{0},\tilde{1},\tilde{2}\right\rangle + \left|\tilde{0},\tilde{2},\tilde{1}\right\rangle + \left|\tilde{1},\tilde{0},\tilde{2}\right\rangle + \left|\tilde{1},\tilde{2},\tilde{0}\right\rangle + \left|\tilde{2},\tilde{0},\tilde{1}\right\rangle + \left|\tilde{2},\tilde{1},\tilde{0}\right\rangle\Big]. \quad (7.2.2)$$

To simplify the notations for the matrix elements, the state $\left|\tilde{1},\tilde{1},\tilde{1}\right\rangle_+$ will be identified by the index $i = 1$ while the second state $\left|\tilde{0},\tilde{1},\tilde{2}\right\rangle_+$ will correspond to the index $i = 2$.

Coupled Equations

The total Hamiltonian is given by:

$$\left[\begin{pmatrix}\hat{T} & 0\\ 0 & \hat{T}\end{pmatrix} + \begin{pmatrix}V_{11} & V_{12}\\ V_{21} & V_{22}\end{pmatrix}\right]\begin{pmatrix}\tilde{\psi}_1\\ \tilde{\psi}_2\end{pmatrix} = E\begin{pmatrix}\tilde{\psi}_1\\ \tilde{\psi}_2\end{pmatrix} \quad (7.2.3)$$

where the first diagonal term is the diabatic kinetic energy operator and V_{ij} are the potential matrix elements that couple the two internal states $i = 1, 2$ and $j = 1, 2$ via the dipole-dipole-dipole interaction. The total nuclear wave function $\Psi = \begin{pmatrix}\tilde{\psi}_1\\ \tilde{\psi}_2\end{pmatrix}$ is expanded within a given sector (see Eq. 6.4.28) as:

$$\Psi_i^{Mpq}(\rho,\theta,\phi,\alpha,\beta,\gamma) = 4\sqrt{2}\sum_t \rho^{-5/2}\psi_{it}^{pq}(\rho)\Phi_t^{Mpq}(\omega;\rho_\xi) \quad (7.2.4)$$

where J is no longer a good quantum number because the dipole-dipole-dipole interaction couples different partial waves (Cf. the section *Potential energy surface*). The surface functions ${}^{k}\Phi_t^{Mpq}(\omega;\rho_\xi)$ are now a linear combination of the two internal states:

$$\Phi_t^{Mpq}(\omega;\rho_\xi) = {}^{1}\Phi_t^{Mpq}(\omega;\rho_\xi)\otimes\left|\tilde{1},\tilde{1},\tilde{1}\right\rangle + {}^{2}\Phi_t^{Mpq}(\omega;\rho_\xi)\otimes\left|\tilde{0},\tilde{1},\tilde{2}\right\rangle \tag{7.2.5}$$

In the hybrid representation, these five-dimensional surface functions are given by (see Eq. 6.5.18):

$${}^{k}\Phi_t^{Mpq}(\omega;\rho_\xi) = \sum_{im\Omega J} {}^{k}b_t^{im\Omega J}|\theta_i\rangle'\otimes|m\rangle\otimes|J\Omega M\rangle \tag{7.2.6}$$

where a sum over the quantum number J is now required and where the subscript $k=1,2$ differentiates the two internal states.

Potential energy surface

The total potential can be accurately approximated by a pairwise sum of two-body interactions:

$$V_{ij} = v_{ij}(r_\tau) + v_{ij}(r_{\tau+1}) + v_{ij}(r_{\tau+2}) \tag{7.2.7}$$

where $i=1,2$ and $j=1,2$ represent the two internal states and where

$$v_{ij}(r_\tau) = v_{dd}^{ij}(r_\tau) + v_{vdw}(r_\tau) \tag{7.2.8}$$

is composed by the two-body dipole-dipole and van der Waals interactions. As in the two-body case, we employ the generalized definition of the induced dipole moment given in Eq. 5.2.5. To make the transition into hyperspherical coordinates easier, we express the dipole-dipole matrix elements in terms of spherical harmonics:

$$v_{dd}^{ij}(r_\tau) = -\frac{2}{4\pi\epsilon_0 r_\tau^3} d_{ij}^2 \sqrt{\frac{4\pi}{5}}\mathcal{Y}_{20}(\hat{r}_\tau^{SF}) \tag{7.2.9}$$

where the symmetrized matrix elements d_{ij}^2 are given by:

$$\begin{aligned}
d_{11}^2 &= d^{\tilde{1}\to\tilde{1}}d^{\tilde{1}\to\tilde{1}} \\
d_{22}^2 &= \frac{1}{3}\Big[d^{\tilde{0}\to\tilde{0}}d^{\tilde{1}\to\tilde{1}} + d^{\tilde{0}\to\tilde{1}}d^{\tilde{1}\to\tilde{0}} + d^{\tilde{0}\to\tilde{0}}d^{\tilde{2}\to\tilde{2}} + d^{\tilde{0}\to\tilde{2}}d^{\tilde{2}\to\tilde{0}} \\
&\qquad\qquad + d^{\tilde{1}\to\tilde{1}}d^{\tilde{2}\to\tilde{2}} + d^{\tilde{1}\to\tilde{2}}d^{\tilde{1}\to\tilde{2}}\Big] \\
d_{12}^2 &= \frac{\sqrt{6}}{3}\left[d^{\tilde{1}\to\tilde{0}}d^{\tilde{1}\to\tilde{2}}\right].
\end{aligned} \tag{7.2.10}$$

Then, we apply the renormalization relation $r_\tau = d_\tau^{-1}s_\tau$ and use the inverse relations from Eq. 6.1.7. The mass-scaled Jacobi coordinates are convenient because a simple kinematic rotation $\phi\to\phi\pm 4\pi/3$ allows to switch from one arrangement to another. Finally, we apply the spatial rotation:

$$\mathcal{Y}_{20}(\hat{s}_\tau^{\mathrm{SF}}) = \sum_{\omega_\lambda=-2}^{+2} D_{\omega_\lambda 0}^{2}(\alpha,\beta,\gamma)\mathcal{Y}_{2\omega_\lambda}(\hat{s}_\tau^{\mathrm{BF_Q}}) \tag{7.2.11}$$

to express the angular part of $\vec{s}_\tau$ in the BF_Q. By combining all these steps, we obtain:

$$\begin{aligned}
v_{dd}^{ij}(r_\tau) &= -\frac{2d_{ij}^2}{4\pi\epsilon_0}\frac{d_\tau^3 2^{3/2}}{\rho^3\left[1-\cos(\theta/2)\cos(\phi)\right]^{3/2}}\sqrt{\frac{4\pi}{5}}\sum_{\omega_\lambda=-2}^{+2}\tilde{D}^2_{\omega_\lambda 0}(\alpha,\beta,\gamma)\mathcal{Y}_{2\omega_\lambda}(\hat{s}_\tau^{\mathrm{BF}}) \\
v_{dd}^{ij}(r_{\tau+1}) &= -\frac{2d_{ij}^2}{4\pi\epsilon_0}\frac{d_{\tau+1}^3 2^{3/2}}{\rho^3\left[1-\cos(\theta/2)\cos\left(\phi+\frac{4\pi}{3}\right)\right]^{3/2}}\sqrt{\frac{4\pi}{5}}\sum_{\omega_\lambda=-2}^{+2}\tilde{D}^2_{\omega_\lambda 0}(\alpha,\beta,\gamma)\mathcal{Y}_{2\omega_\lambda}(\hat{s}_{\tau+1}^{\mathrm{BF}}) \\
v_{dd}^{ij}(r_{\tau+2}) &= -\frac{2d_{ij}^2}{4\pi\epsilon_0}\frac{d_{\tau+2}^3 2^{3/2}}{\rho^3\left[1-\cos(\theta/2)\cos\left(\phi-\frac{4\pi}{3}\right)\right]^{3/2}}\sqrt{\frac{4\pi}{5}}\sum_{\omega_\lambda=-2}^{+2}\tilde{D}^2_{\omega_\lambda 0}(\alpha,\beta,\gamma)\mathcal{Y}_{2\omega_\lambda}(\hat{s}_{\tau+2}^{\mathrm{BF}})
\end{aligned} \tag{7.2.12}$$

where $d_\tau = d_{\tau+1} = d_{\tau+2} \approx 1.07457$ for three identical molecules. Be careful, it corresponds to the renormalization coefficient to obtain the mass-scaled Jacobi vectors (see Eq. 6.1.7) and should not be confused with the dipole moment. In the BF_Q, the angular part of $\vec{s}_\tau$ is given by:

$$\begin{aligned}
\theta_{s_\tau} &= \pi/2 \qquad & \phi_{s_\tau} &= \tan^{-1}\left(\frac{\tan(\theta/4)}{\tan(\phi/2)}\right) \\
\theta_{s_{\tau+1}} &= \pi/2 \qquad & \phi_{s_{\tau+1}} &= \tan^{-1}\left(\frac{\tan(\theta/4)}{\tan(\phi/2+2\pi/3)}\right) \\
\theta_{s_{\tau+2}} &= \pi/2 \qquad & \phi_{s_{\tau+2}} &= \tan^{-1}\left(\frac{\tan(\theta/4)}{\tan(\phi/2-2\pi/3)}\right)
\end{aligned} \tag{7.2.13}$$

where $\theta_{s_\tau} = \pi/2$, $\theta_{s_{\tau+1}} = \pi/2$ and $\theta_{s_{\tau+2}} = \pi/2$ because the particles lie in the plane perpendicular to the Z_Q axis. Notice that the potential depends on the Euler angles (which is never the case for collisions without electric field) which leads to couplings between different partial waves J. This was predictable because the dipole-dipole interaction is an anisotropic interaction that depends on the orientation of the plane formed by the three molecules with respect to the orientation of the electric field. On Fig. 7.2, we took the example of three dipoles placed in an equilateral configuration for two different sets (α,β,γ) and for fixed values of (ρ,θ,ϕ). In the first case (left), two molecules collide in a side-by-side configuration while a third is coming from above. In the second case, we just applied $\beta \to \beta + \pi/2$ and the three molecules all collide in a side-by-side configuration. We can show the same behavior with the other angles, so it is natural that the dipole-dipole interaction depends on the three Euler angles.

If we follow the above procedure for the van der Waals interaction, we obtain:

$$\begin{aligned}
v_{vdw}(r_\tau) &= -\frac{C_6}{\rho^6}\frac{8\,d_\tau^6}{\left[1-\cos(\theta/2)\cos(\phi)\right]^3} \\
v_{vdw}(r_{\tau+1}) &= -\frac{C_6}{\rho^6}\frac{8\,d_{\tau+1}^6}{\left[1-\cos(\theta/2)\cos\left(\phi+\frac{2\pi}{3}\right)\right]^3} \\
v_{vdw}(r_{\tau+2}) &= -\frac{C_6}{\rho^6}\frac{8\,d_{\tau+2}^6}{\left[1-\cos(\theta/2)\cos\left(\phi-\frac{2\pi}{3}\right)\right]^3}.
\end{aligned} \tag{7.2.14}$$

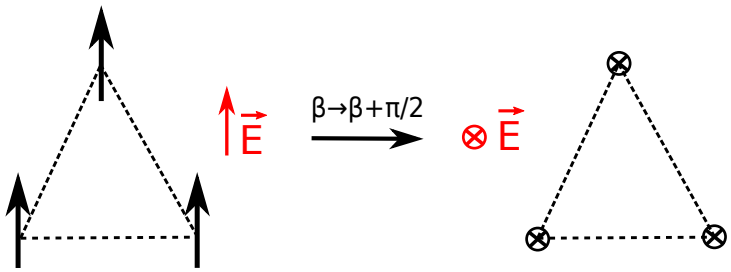

Figure 7.2: Orientation of three dipoles for two spatial configurations.

Unlike the dipole-dipole interaction, this interaction is isotropic and does not depend on the Euler angles: it is diagonal in J and Ω. However, the van der Waals matrix elements are non-diagonal in m and require to perform an integral in ϕ.

It is important to point out that the dipole-dipole and van der Waals interactions are derived from a multipole expansion of the potential. These equations remains valid at large distances, more precisely for intermolecular distances larger than the Leroy radius. This distance separates the region where the interacting particles keep their identity, i.e. their wave functions do not overlap, from the short distance region [246, 247]. In addition, we have shown through the two-body shielding studies that the long-range potential barrier prevents molecules from reaching short distances. The two-body short-range configurations are then considered as forbidden and are excluded by applying a cut-off condition for distances $r_\tau < r_{cut}$. This cutoff is chosen as the position of the barrier maximum in the two-body adiabatic energy curves. This choice is arbitrary because we do not know exactly where the two-body wave function vanishes in the potential barrier. However, the barrier height becomes to be higher than the typical collision energies involved in this study at larger distances than the position of the barrier maximum. We then take into consideration some configurations that should be forbidden, which increases the loss rate coefficients. Indeed, the loss rate coefficients will be slightly overestimated because the larger the cut-off distance, the less we consider the short distance region where the attractive van der Waals interaction dominates. Therefore, the model will provide an estimate of the lower value of the ratio $\gamma = \frac{\beta^{\rm el}}{\beta^{qu}}$ but we will show that it has no real impact on the final results. As we do not have any information on the short-range part, we will set the initial short-range loss condition at $\rho_{\rm min} \approx r_{\rm cut}$, i.e. at the position where the three additive terms are not considered anymore by the cut-off condition. If the wave function reaches distances $\rho < \rho_{\rm min}$, it will be considered as completely lost, which will increase the loss rate coefficients.

SDT

As we saw previously, the potential depends on the three Euler angles. The standard SDT method can therefore no longer be used because it is developed for a one-dimensional Hamiltonian. A first idea was to exclude the dipole-dipole-dipole interaction from the

SDT Hamiltonian:

$$^{1\mathrm{D}}\hat{H}(\theta_i) \equiv -\frac{4\hbar^2}{\mu\rho_\xi^{m\,2}(1+\cos\theta_i)}\frac{\partial^2}{\partial\phi^2} + v_{vdw}(r_\tau) + v_{vdw}(r_{\tau+1}) + v_{vdw}(r_{\tau+2}). \tag{7.2.15}$$

A second idea was to define an one-dimensional Hamiltonian based on the terms which are diagonal in Ω:

$$^{1\mathrm{D}}H_\Omega(\theta_i) \equiv {}^{1D}\hat{H}(\theta_i) + \frac{1}{\mu\rho_\xi^{m\,2}}\left[\frac{J_Z^2}{(1+\cos\theta_i)} + \frac{4\sin\theta_i/2}{(1+\cos\theta_i)}J_Z\frac{\hbar}{i}\frac{\partial}{\partial\phi}\right]. \tag{7.2.16}$$

The Ω term coming from the J_Z term shifts all energies upwards. After the application of the cutoff energy, more states are then excluded and the size of the total Hamiltonian decreases. Applying this method, we managed to achieve an additional decrease of about 15 % in the size of the total Hamiltonian compared to the first method.

Results

In Fig. 7.3, we show the adiabatic energy curves in the case of three-body ^{41}K^{87}Rb collisions. They are computed for $J = 0-2$, $l_{\max} = 40$ and $m_{\max} = 25$. The grand angular matrix elements in Eq. 6.5.21 are computed in FBR with 500 Gauss-Legendre quadrature points in θ, and then transformed into the DVR representation with the transformation matrix Eq. 6.5.30. Since its angular and radial parts are separable, the elements of the grand angular momentum are calculated once and reused for each sector. The potential matrix elements are computed with 400 quadrature points in ϕ and are diagonal in θ. As we deal with three-identical molecules, we can reduce the integral of ϕ on $[0, 4\pi/3]$ instead of $[-\pi, +\pi]$. The integral over the Euler angles are given analytically by:

$$\int_0^{2\pi} d\alpha \int_0^{\pi} d\beta \sin\beta \int_0^{2\pi} d\gamma D^{J_3}_{M_3M_3'}(\alpha,\beta,\gamma) D^{J_3}_{M_2M_2'}(\alpha,\beta,\gamma) D^{J_1}_{M_1M_1'}(\alpha,\beta,\gamma) = \frac{8\pi^2}{2J_3+1} C^{J_3M_3}_{J_1M_1J_2M_2} C^{J_2M_3'}_{J_1M_1'J_2M_2'} \tag{7.2.17}$$

where $C^{J_kM_k}_{J_iM_iJ_jM_j}$ are the Clebsch-Gordan coefficients [182] given by:

$$C^{J_kM_k}_{J_iM_iJ_jM_j} = (-1)^{j_i-j_j+m_k}\sqrt{2j_k+1}\begin{pmatrix} j_i & j_j & j_k \\ m_i & m_j & -m_k \end{pmatrix}. \tag{7.2.18}$$

Using this equation, we have shown that only states satisfying the condition $J' - J = \pm 2, \pm 4...$ can be coupled. Without SDT, we had 9840 states while the implementation of the SDT divided the size of the total Hamiltonian by about a factor 2. The other parameters used for the numerical calculation are grouped in Table 7.1.

We have zoomed on the initial state $\left|\tilde{1},\tilde{1},\tilde{1}\right\rangle$, while the curves coming from the lower part correspond to the continuum channels of the second internal state $\left|\tilde{0},\tilde{2},\tilde{1}\right\rangle$. It is impossible to draw any conclusions from these curves because a small increase of $l_{\max}$ changes radically the behavior of the adiabatic curves. This can be explained by the fact that we use a DVR for θ and that the number $l_{\max}$ is related to the number of quadrature points used if we were in a FBR. However, for long-range potentials, a large number of quadrature points is required to get accurate results. In conclusion, a complete quantum calculation is impossible and involves the development of a simplified model.

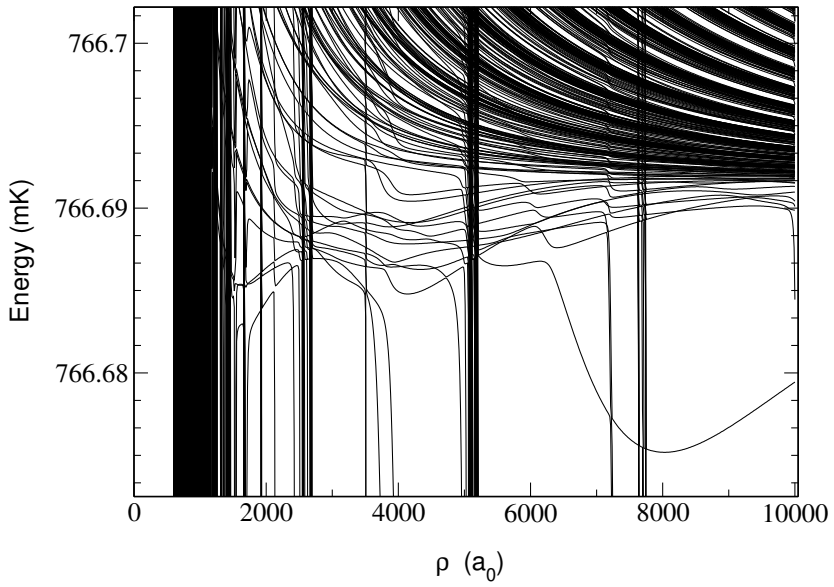

Figure 7.3: Adiabatic energy curves as a function of the hyperradius ρ for three-body bosonic ^{40}K^{87}Rb collisions obtained with $J = 0 - 2$, $l_{\max} = 40$ and $m_{\max} = 25$. The curves are not converged with respect to these parameters.

m_{KRb} (a.u.)	μ_{2B} (a.u.)	μ (a.u.)	B (a.u.)	d (D)	C_6 (a.u.)	E^* (kV/cm)	$\rho_{\min}$ (a_0)
233093	116547	134577	$1.67.10^{-7}$	0.226	-12636	12.3	140

Table 7.1: Parameters of ^{41}K^{87}Rb molecules useful for three-body numerical calculations. We provide useful conversion factors: 1 a.u. $\simeq$ 1822.88 a.m.u.; 1 a.u. $\simeq$ 219475 cm^{-1}; $1\,a_0 \simeq 0.529 \times 10^{-10}$ m.

7.3 A simplified model

In the previous section, we have demonstrated that the complete calculation of three-body shielding is not possible because too many states are required to get converged results. The aim of this part is to adapt the simplified model presented in section 5 to the three-body formalism. The characteristic parameters for ^{41}K^{87}Rb molecules are given in table 7.1.

7.3.1 A two-level system

As in the simplified two-body model, we only keep the two symmetric states $\left|\tilde{1},\tilde{1},\tilde{1}\right\rangle_+$ and $\left|\tilde{0},\tilde{1},\tilde{2}\right\rangle_+$. We can define the 2×2 interaction matrix:

$$\begin{bmatrix} V_{11}(\rho,\theta,\phi,\alpha,\beta,\gamma) + E_{\tilde{1}\tilde{1}\tilde{1}} & V_{12}(\rho,\theta,\phi,\alpha,\beta,\gamma) \\ V_{21}(\rho,\theta,\phi,\alpha,\beta,\gamma) & V_{22}(\rho,\theta,\phi,\alpha,\beta,\gamma) + E_{\tilde{0}\tilde{2}\tilde{1}} \end{bmatrix} \tag{7.3.1}$$

where $V_{ij}(\rho, \theta, \phi, \alpha, \beta, \gamma)$ are given by Eq. 7.2.7. Then, we diagonalize this matrix for each value of $(\rho, \theta, \phi, \alpha, \beta, \gamma)$ and obtain two orthogonal six-dimensional surfaces analytically given by:

$$E_{\pm}(r, \theta) = \frac{1}{2}(E_a + E_b) \pm \frac{1}{2}\sqrt{(E_a - E_b)^2 + 4W^2} \tag{7.3.2}$$

with:

$$\begin{aligned} E_a &\equiv V_{11}(\rho, \theta, \phi, \alpha, \beta, \gamma) + E_{\tilde{1}\tilde{1}\tilde{1}} \\ E_b &\equiv V_{22}(\rho, \theta, \phi, \alpha, \beta, \gamma) + E_{\tilde{0}\tilde{2}\tilde{1}} \\ W &\equiv V_{12}(\rho, \theta, \phi, \alpha, \beta, \gamma). \end{aligned} \tag{7.3.3}$$

To get a more accurate picture of the interaction, we also include the diagonal centrifugal term of the lowest partial wave such that:

$$V_{\pm}(\rho, \theta, \phi, \alpha, \beta, \gamma) = E_{\pm}(\rho, \theta, \phi, \alpha, \beta, \gamma) + \frac{\lambda(\lambda + 4) + 15/4}{2\mu\rho^2} \tag{7.3.4}$$

where $\lambda = 0$ for bosons. Note that unlike two-body collisions, the centrifugal term is non-zero for bosons.

7.3.2 A six-dimensional surface

To understand the role of the different angles, we plot the surfaces V_+ and V_- in function of two coordinates while keeping the other four fixed. We are not going to show and analyze all the possible combinations but only illustrative examples.

Internal coordinates

In Fig. 7.4, we show the surfaces V_+ and V_- in function of the two angles θ and ϕ for $\rho = 5000$ a_0 (top) and $\rho = 500$ a_0 (bottom) with $(\alpha = 0, \beta = 0, \gamma = 0)$. We observe that the three arrangements are centered on $\phi = 0$, $2\pi/3$ and $-2\pi/3$, i.e. for the kinematic angles transforming s_τ into $s_{\tau+1}$ and $s_{\tau+2}$. As we are in the case of three identical particles, the potential is equal whatever the arrangement considered. As a result, the integral can only be performed over $\phi \in [0, 2\pi/3]$ and then multiplied by 3. We can remark that the smaller the hyperradius, the closer the arrangements. For hyperradius $\rho < 500$ a_0, the arrangement overlap and τ is no longer a good quantum number. The extremums of the potential are mostly found around small values of θ because $s_\tau \to 0$ when ($\theta \to 0$, $\phi \to 0$) as expected from Eq. 6.4.19. Hence, we use a Gauss-Legendre quadrature where the integration points are more numerous at the boundaries of the integrals.

When the shielding is turned off, we have $E_{\tilde{1}\tilde{1}\tilde{1}} < E_{\tilde{0}\tilde{2}\tilde{1}}$. The potential surface for the initial state is therefore given by the lower attractive surface $V(\rho, \theta, \phi, \alpha, \beta, \gamma) \equiv V_-(\rho, \theta, \phi, \alpha, \beta, \gamma)$. In this case, the surface is pushed down by the state above and the attractive Van der Waals interaction is dominant. The potential is then on average strongly attractive, so the total wave function can reach short distances where losses dominate.

When the shielding is turned on, we have $E_{\tilde{1}\tilde{1}\tilde{1}} > E_{\tilde{0}\tilde{2}\tilde{1}}$. The potential surface for the initial state is therefore given by the upper repulsive surface $V(\rho, \theta, \phi, \alpha, \beta, \gamma) \equiv V_+(\rho, \theta, \phi, \alpha, \beta, \gamma)$. The barriers found by decreasing θ are the signatures of two-body shielding where each of the three barriers corresponds to the shielding between two different molecules. Let us point out that their height is of the order of a few tenths of mK (not shown on the figures), which is similar to those obtained for the two-body shielding (Cf. Fig. 5.6). On average, the barrier created could be large enough to reduce losses but the effect of the other angles (the Euler angles) has to be also investigated.

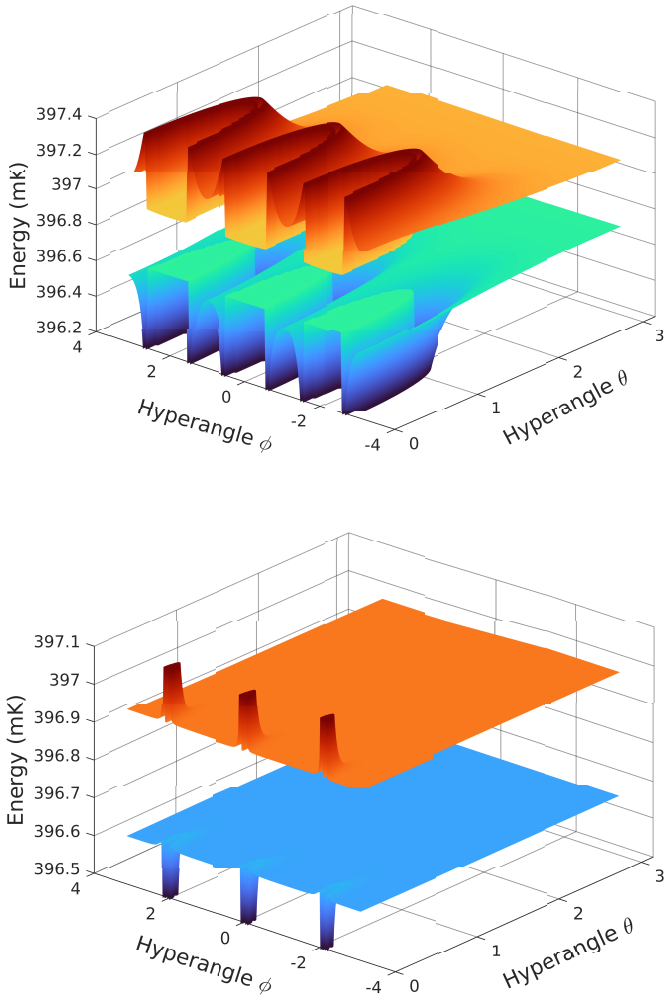

Figure 7.4: $V_+(\rho, \theta, \phi, \alpha = 0, \beta = 0, \gamma = 0)$ and $V_-(\rho, \theta, \phi, \alpha = 0, \beta = 0, \gamma = 0)$ for $\rho = 5000$ a_0 (top) and $\rho = 500$ a_0 (bottom). They are obtained diagonalizing Eq. 7.3.1.

Effect of the Euler angles

If we take a closer look at the expression of the potential, it involves a sum over the Wigner functions $D^J_{\omega_\lambda 0}(\alpha, \beta, \gamma) = e^{i\omega_\lambda \gamma} d^J_{\omega_\lambda 0}(\beta)$ which do not depend on the variable α.

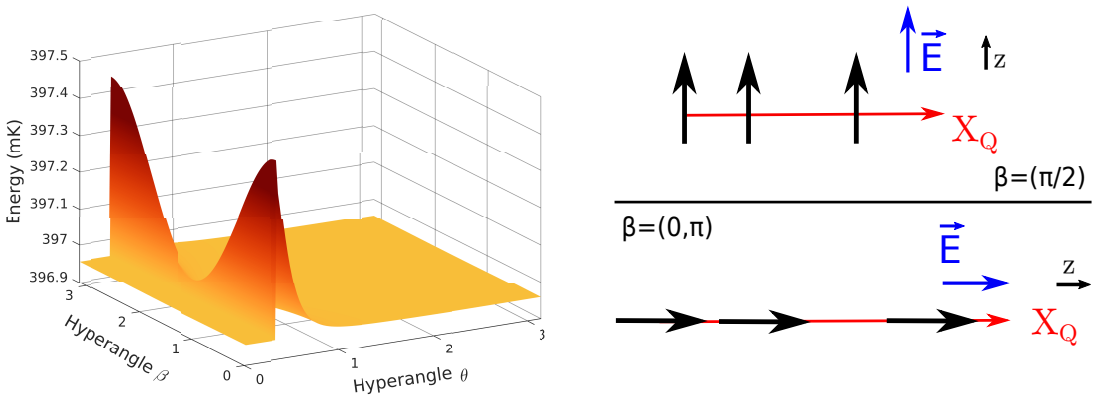

Figure 7.5: Left: Potential surface $V_+(\rho = 500 \text{ a.u.}, \theta, \phi = 0, \alpha = \pi/6, \beta, \gamma = 0)$ as a function of θ and β. Right: Orientation of three dipoles in a linear configuration for two configurations of β.

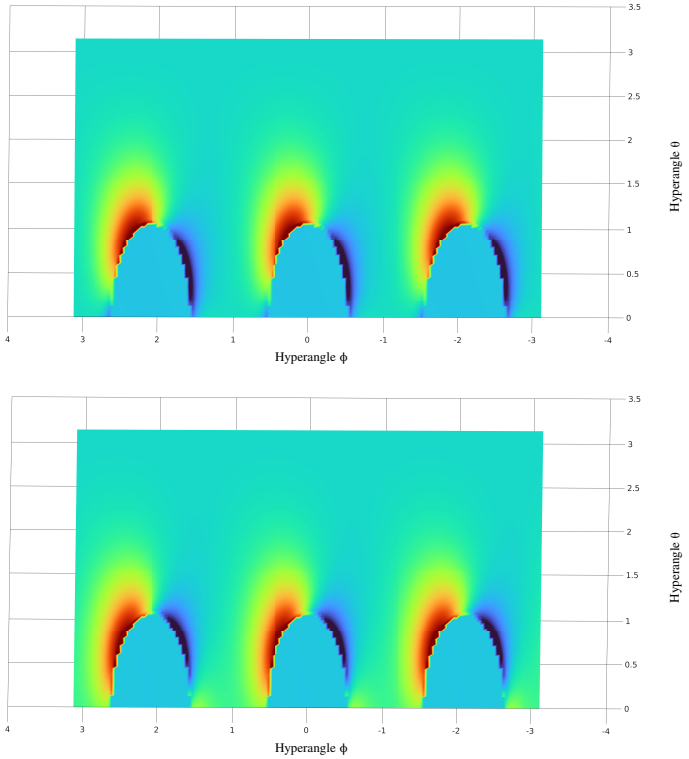

Figure 7.6: Potential surfaces $V_+(\rho = 500 \text{ a.u.}, \theta, \phi, \alpha = \pi/6, \beta = \pi/6, \gamma = 0)$ (top) and $V_+(\rho = 500 \text{ a.u.}, \theta, \phi, \alpha = \pi/4, \beta = \pi/6, \gamma = 0)$ (bot) in top view.

The numerical efforts are then minimized since there is one less integral to perform.

In Fig. 7.5 (left), we represent the potential surface V_+ in function of θ and β for $\rho = 500$ a.u, $\phi = 0$ and $\gamma = \pi/6$. We observe two maximums at $\beta = (0, \pi)$ and a minimum at $\beta = \pi/2$. To understand the shape of this surface, let's take the example of a linear configuration (i.e. $\theta = 0$) illustrated in Fig. 7.5 (right). In this configuration, the

three molecules are aligned along X_Q (Cf. Eq. 6.4.20) while the electric field is oriented along the space-fixed axis z. If the Z_Q axis is oriented in the same direction as the z axis, i.e. $\beta = (0, \pi)$, then the molecules collide in a head-to-tail configuration. On the other hand, if the two axis are orthogonal, i.e. $\beta = \pi/2$, then the molecules collide in a side-by-side configuration. In the simplified two-body model, we have shown that the barrier is much higher in a head-to-tail collision than in a side-by-side collision. This is why we find two maximums in Fig. 7.5(left) for $\beta = (0, \pi)$ (head-to-tail collision) and a minimum for $\beta = \pi/2$ (side-by-side collision). For symmetry reasons, the integral can be performed on $[0, \pi/2]$ and multiplied by 2. As the surface oscillates slowly, few quadrature points are needed.

In Fig. 7.6, we represent V_+ in function of θ and ϕ for $\gamma = \pi/6$ (top) and $\gamma = \pi/4$ (bottom) in a top view. The red parts correspond to repulsive parts and the blue parts to attractive ones. We see on both figures the anisotropic character of the dipole-dipole interaction. By changing γ, we modify the combination of spherical harmonics in Eq. 7.2.12 which changes the maximum and minimum positions. From another point of view, this is equivalent to rotating the plane including the three molecules around the axis Z and thus to modify the relative orientation of the molecules and by extension the dipole-dipole interaction. As $e^{i\gamma\omega_\lambda}$ can be negative, purely attractive regions can appear and counterbalance, the repulsive parts. One can show that the integral can be performed only on $[0, \pi]$ and multiplied by 2. As the surface oscillates slowly, few quadrature points are needed.

7.3.3 A one channel propagation

Average over the first partial wave

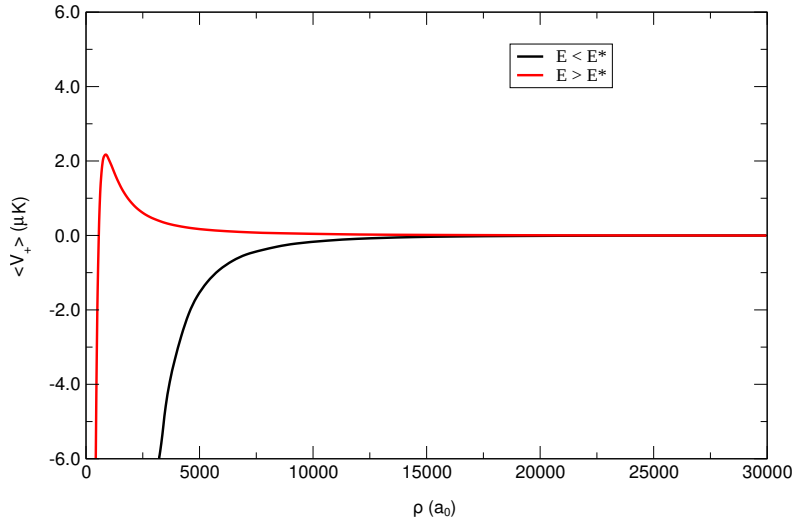

Figure 7.7: Energy curve $\langle V \rangle$ as a function of ρ obtained after integration of the initial potential surface on the partial wave $\lambda = 0$, for $E < E^*$ (black) and $E > E^*$ (red).

Once the energy surface corresponding to the initial state is conserved, we integrate it over the lowest partial wave, i.e. over the first hyperspherical harmonics. As in the case of

the two-body bosonic partial wave $l = 0$, it corresponds to an isotropic angular function equal to a constant: no direction is privileged. We have demonstrated numerically that it can be obtained by replacing $J = 0$, $M = 0$, $\Omega = 0$ $m = 0$ and $l = 0$ in Eq. 6.5.19. As in the two-body model, we obtain a single curve $\langle V \rangle$:

$$\begin{aligned}\langle V \rangle &= \int_{-\pi}^{\pi} \frac{d\phi}{2\pi} \int_0^{\pi} \sin\theta d\theta \int_0^{2\pi} \frac{d\alpha}{2\pi} \int_0^{\pi} \frac{1}{2} \sin\beta d\beta \int_0^{2\pi} \frac{d\gamma}{2\pi}\, V(\rho,\theta,\phi,\alpha,\beta,\gamma) \\ &= \int_0^{2\pi/3} \frac{3}{2\pi} d\phi \int_0^{\pi} \sin\theta d\theta \int_0^{\pi/2} \sin\beta d\beta \int_0^{\pi} \frac{d\gamma}{\pi}\, V(\rho,\theta,\phi,\beta,\gamma)\end{aligned} \tag{7.3.5}$$

for each value of ρ. Note that the factors in the first line of Eq. 7.3.5 come from the use of normalized Wigner functions. In the second line, the simplifications related to the symmetry of the potential surfaces and presented in the previous section have been applied. Unlike the complete quantum calculation, the integrals over the Euler angles are no longer algebraic because the Wigner functions are contained in the square root of Eq. 7.3.2. This implies numerically heavy integrals but in return, the selection rules no longer prohibit the transition $J = 0 \to J' = 0$. As in the two-body model, the model neglects the coupling between partial waves because the resonant phenomenon is considered as dominant. We computed the quadruple integral using Gauss-Legendre quadratures for each angle. We have distributed the calculation over 40 threads via the OPEN-MP library. We have used $n_\theta = 350, n_\phi = 350, n_\beta = 10, n_\gamma = 10$ to get converged collision rate coefficients.

On Fig. 7.7, we have represented the energy curve obtained $\langle V \rangle$ after integration for two values of electric field. The first curve (in black) was obtained for an electric field value $E < E^*$ where the internal state $|\tilde{1}, \tilde{1}, \tilde{1}\rangle$ is below $|\tilde{0}, \tilde{1}, \tilde{2}\rangle$. In this case, the shielding is not yet activated and the curve is purely attractive. If three molecules collide with a relative collision energy $E_\mathrm{k} > 0$, the total wave function will reach the short-range region and the losses will dominate.

The second curve (in red) was obtained for $E = 12.4\,\mathrm{kV\,cm^{-1}}$, i.e. for the optimal electric field value used in the two-body shielding. We observe the creation of a long-range barrier with a height of 2 μK. As we study collisions between ultracold molecules, the characteristic collision energy ($E_\mathrm{k} < 500$ nK) is much weaker than the barrier size. We then expect to strongly reduce the short-range losses. We can note that its height is much weaker than the barrier obtained in the surfaces in Fig. 7.4–7.5 due to the presence of the terms $\sin\theta$ and $\sin\beta$ in the Jacobian which reduce the most repulsive parts. This is also related to the presence of negative parts in the surface V_+ as shown in Fig. 7.6. To get an estimate of the loss reduction, we need to propagate the logarithmic derivative on this single curve and extract the collision rate coefficients from the S-matrix.

Propagation and Results

The propagation of the 1×1 Z-matrix is performed between $\rho \in [100, 40000]$ a_0 using 60000 sectors for a collision energy $E_k = 250\,\mathrm{nK}$ [100]. We apply the initial loss conditions at ρ_min. Therefore any part of the wave function reaching regions $\rho < \rho_\mathrm{min}$

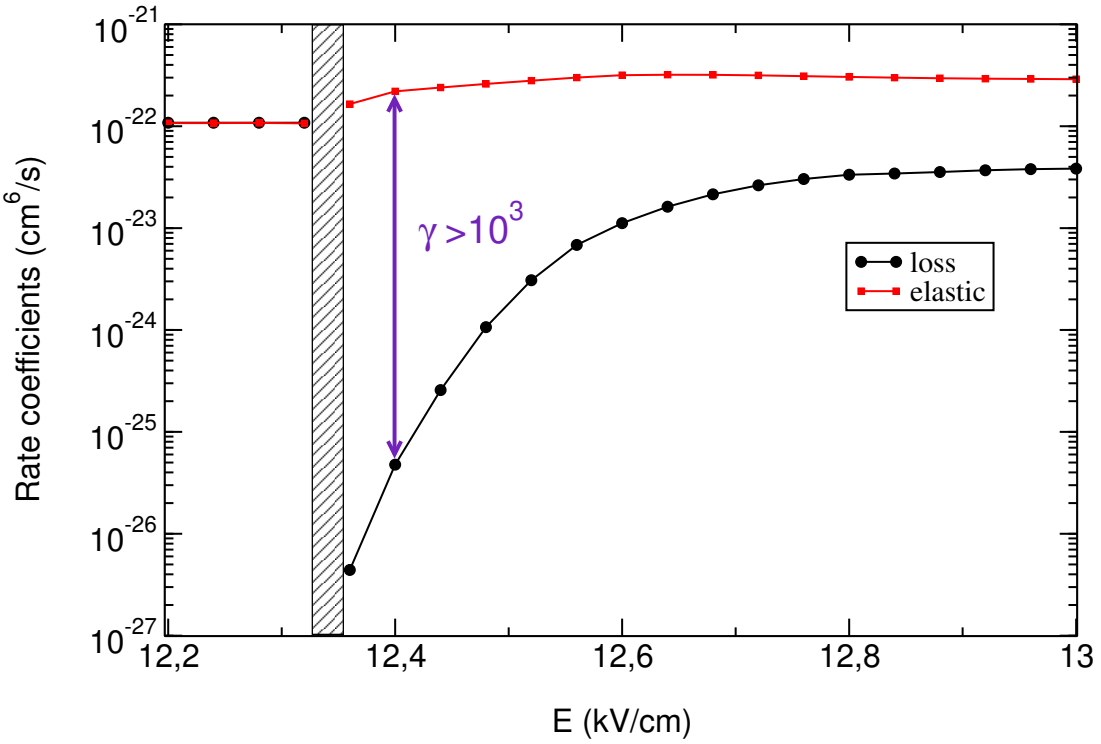

Figure 7.8: Elastic (red) and loss (black) collision rate coefficients as a function of the electric field for three-body bosonic ^{41}K^{87}Rb collisions for a collision energy $E_k = 250\,\text{nK}$. The hashed area corresponds to electric fields too close to the resonance so that the model can't give results as we don't consider inelastic collisions. The hatched region corresponds to the electric field range for which our model cannot provide any information as it is the region where inelastic collisions dominate.

will be considered as lost. Once the matching distance ρ_{max} is reached, we compute the K-matrix and the S-matrix via equations 3.5.18 and 3.5.19. As we have only one channel, these matrices have only one element. The asymptotic radial wave functions used are given by:

$$f_{11}^{(1)} = \left(\frac{\pi\rho_{\text{max}}}{2}\right)^{1/2} J_2(k\rho_{\text{max}}) \qquad f_{11}^{(2)} = \left(\frac{\pi\rho_{\text{max}}}{2}\right)^{1/2} Y_2(k\rho_{\text{max}}) \tag{7.3.6}$$

where $J_{\lambda+2}(k\rho)$ and $Y_{\lambda+2}(k\rho)$ are respectively the Bessel functions of the first and second kind [243]. Their derivative are given by:

$$\begin{aligned} f_{11}^{(1)} &= \left(\frac{\pi}{2}\right)^{1/2} \left(\frac{1}{2\sqrt{\rho_{\text{max}}}} J_2(k\rho_{\text{max}}) + \sqrt{\rho_{\text{max}}} k J_2'(k\rho_{\text{max}})\right) \\ f_{11}^{(2)} &= \left(\frac{\pi}{2}\right)^{1/2} \left(\frac{1}{2\sqrt{\rho_{\text{max}}}} Y_2(k\rho_{\text{max}}) + \sqrt{\rho_{\text{max}}} k Y_2'(k\rho_{\text{max}})\right) \end{aligned} \tag{7.3.7}$$

and give a unit Wronskian $W = f_{11}^{(1)} f_{11}^{(2)} - f_{11}^{(2)} f_{11}^{(1)} = 1$ because the two solutions are independent. Three-body rate coefficients [248, 243] are extracted from the S-matrix via:

$$\beta_{el} = \frac{192\pi^2}{\mu k^4}|T|^2 \qquad \beta_{ls} = \frac{192\pi^2}{\mu k^4}(1 - |S|^2). \tag{7.3.8}$$

with $k = \sqrt{\frac{2\mu E_k}{\hbar}}$ and μ the three-body reduced mass.

In Fig. 7.8, we represented the elastic rate coefficient β_{el} (red) and the loss rate coefficient β_{ls} (black) in function of the electric field. For electric fields $E < E_3^*$, we are in the situation where the shielding is not yet activated. The main part of the wave function reaches short distances and is lost, this is why the rate coefficients do not vary too much with the electric field. The rate coefficients $\beta_{el} \sim 10^{-22}$ cm^6/s and $\beta_{ls} = 10^{-22}$ cm^6/s obtained in this range of electric fields are not well estimated because they depend strongly on the value of the cut-off distance (Cf. discussion below). In Eq. C.2.3, we have linked the mean time between two events of three-body collisions resulting in losses to the density and the loss rate coefficients. In the unitary limit ($S^2 = 0$), we have:

$$\tau_{3B} = \frac{1}{2\beta_{ls} n_0^2} = 0.02\,\text{s} \tag{7.3.9}$$

where $\beta_{ls} = 2.8 \times 10^{-22}$ cm^6/s has been calculated setting $S^2 = 0$ in Eq. 7.3.8 and the density $n_0 = 2.5 \times 10^{11}$ molecules/cm^3 is taken from [100].

When the shielding is activated around $E \sim E_3^*$, there is an electric field interval (hatched region) for which our model cannot provide any information on the rate coefficients because inelastic collisions, which are not considered in our model, are dominant in this region.

Now we focus on $E > E_3^*$, especially at $E = 12.4\,\text{kV cm}^{-1}$, i.e. for the electric field value where the two-body model gave accurate results. We observe that the loss rate coefficient has been strongly reduced compared to the elastic collision rate coefficients. To describe the evaporative cooling efficiency, we usually use the ratio γ between elastic and loss rate coefficients. We consider that if it is greater than 10^2 then the losses are negligible and evaporative cooling will be effective. In our study, we reach $\gamma > 10^3$ for $E = E^*$, then we can consider that the shielding will be sufficient to protect bosonic ^{41}K^{87}Rb molecules.

We can note that for the two-body shielding, the ratio $\gamma_{2B} = 6$ was much worse. This can explained by the fact that for $\rho < 500$ a.u, the potential of the different arrangements overlap and add up. The areas which are normally purely attractive when considering a single arrangement (i.e. two molecules colliding and a third one far away) overlap with the repulsive parts of the other arrangements. We then have on average a more repulsive potential surface due to the non-additive nature of three-body collisions. In addition, the partial wave $\lambda = 0$ has a repulsive barrier (Cf. the second term of Eq. 7.3.4) which does not exist for the two-body case. The mean time between two events of three-body collisions resulting in losses is now given by:

$$\tau_{3B} = \frac{1}{2\beta_{ls} n_0^2} = 160\,\text{s} \tag{7.3.10}$$

with $\beta_{ls} = 5.0 \times 10^{-26}$ cm^6/s is the rate coefficient obtained for $E = 12.4\,\mathrm{kV\,cm^{-1}}$ and the density $n_0 = 2.5 \times 10^{11}$ molecules/cm^3 is taken from [100]. This time is much larger than when the shielding is not activated and thus shows that the shielding reduces the number of collisions leading to losses. For higher electric field values, we consider that our model is less relevant because the two-level model is no longer valid.

The simplified three-body model has two major differences from the simplified two-body model. First, when we vary θ and ϕ, we modify the position of the three molecules for a given ρ. Thus, some configurations correspond to A+A_2 collisions where the two molecules A_2 come too close to each other and must be considered as lost. On the other hand, for the same value of ρ, but with different values of θ and ϕ, some A+A+A configurations correspond to the case where all the distances $r_\tau, r_{\tau+1}, r_{\tau+2}$ are large enough that none of the molecules can be considered lost. However, the loss condition is only applicable for a given value of ρ, without differentiating the different configurations θ and ϕ. We then chose a hyperradius $\rho_{\min}$ large enough so that no configuration could be considered as lost beyond that. As a consequence, some of the configurations where $\rho < \rho_{\min}$ are considered lost when they should not be. On the other hand, no configuration that should be counted as lost is ignored. Therefore, our model slightly overestimates the losses and γ is expected to be higher than 10^3.

Moreover, the model implies the use of a cut-off function prohibiting the integral on two-body configurations which do not exist. We have chosen as cut-off distance the position of the maximum of the barrier in the two-body energy curves while at low energy, the wave function vanishes much further. We then integrate on forbidden configurations which increases the attractive side of the potential. We then underestimate the height of the three-body barrier and thus overestimate the losses. For the case $E < E_3^*$, we have used the attractive lower surface $V_-(\rho, \theta, \phi, \alpha, \beta, \gamma)$. In contrast to the case where the shielding is activated, the short-range configurations are no longer forbidden and must be considered. However, as we don't know the potential energy surface at short-range we keep the cut-off condition, and the estimated rates now depend somewhat on it. Nonetheless, we are not interested in computing the exact value of the rate coefficients there because we know that even the two-body shielding doesn't work for this range of electric fields. This is the reason why we have taken the unitary limit as the maximum value for our life-time estimation τ_{3B} in the unshielded part.

In conclusion, through this model, we have shown that the losses were highly reduced ($\gamma > 10^3$) for the same electric field value as the one used for the two-body shielding. This coefficient is still a pessimistic estimate that overestimates the losses, so shielding should be much more effective. This is an important result because it appears that evaporative cooling will be very efficient. This will allow to reach high enough densities to fill optical lattices (used in quantum simulation) or for the creation and the study of stable Bose-Einstein condensates.

Chapter 8

Application of the three-body formalism

For most of the ultracold molecular systems studied so far, inelastic and reactive collisions of a molecule with an atom or with another molecule follow universal rate laws which are independent of the short-range part as described in the experimental studies [249, 250, 251, 252, 253]. Indeed, in these cases, molecules are lost with unit probability in reactive or inelastic channels because too many open channels (or tetramer states) are energetically accessible. However, collision rate coefficients can behave differently from these universal laws if the density of open channels is low enough that inelastic and reactive collisions are no longer dominant. This scenario can occur with light atom-diatom systems as $H + H_2$ [254], $He + H_2$ [255], $He + Li_2$ [256], and $Li + Li_2$ [154], where a non-universal behavior for vibrational quenching has been theoretically predicted. However, the first experimental observation of non-universal rotational state dependence of chemical reactions has been observed in 2019 [257] for $Li + Li_2$ collisions and renewed the interest for three identical atomic collisions.

As sufficient product state resolution for collision energies below 1 K will become feasible in the next years, recent studies on heavier system and involving several partial waves are currently investigated. For example, many (non-universal) shape resonances in rotationally resolved rate coefficients have been predicted for Li + LiNa collisions [225]. The three-body numerical code we have developed can help to investigate these collisional systems involving three atoms.

The objective of this chapter is to apply our three-body numerical code to different systems. In a first part, we will verify that the Eckart singularities are well treated for partial waves $J \geq 0$ as in [152]. Then, we will study reactive and recombination collisions of three identical bosonic particles, taking a fictitious system with an arbitrary mass and potential. We will present the adiabatic energy curves and show how to extract the surface functions corresponding to three identical bosonic symmetries. Then, we will give the collision rate coefficients as a function of the collision energy and present the criteria to be checked to obtain well converged results. Finally, we will show that the code can extend to realistic studies such as $Li + Li_2$ collisions.

8.1 Eckart singularities and $J \geq 0$ Hyperspherical Harmonics

To demonstrate that the primitive basis in Eq. 6.5.33 correctly treats all the singularities, we will compute the adiabatic energies for different values of J where we dropped the $15\hbar^2/2\mu\rho_\xi^2$ term and set $V = 0$ in Eq. 6.4.31 and where we use an arbitrary mass. Under these conditions, the surface functions correspond to the well-known hyperspherical harmonics, with which we will compare them. This comparative study is important because without potential, no configuration of θ is privileged and the Eckart singularities at both poles $\theta = 0$ and $\theta = \pi$ are fully accessible. If they are badly treated, this will affect the surface functions obtained after diagonalization as well as their corresponding eigenenergies. We will compare the latter with the analytically known energies [152] given by:

$$\mathcal{E}_t^{Jp\,q}(\rho) \underset{\rho\to+\infty}{\longrightarrow} \frac{\lambda(\lambda+4)}{2\mu\rho^2} \tag{8.1.1}$$

with $\lambda = 0, 1, 2, 3, ...$ We also verify that the eigenfunctions match well with the hyperspherical harmonics (for the $J = 0$ case) but the results will not be presented here. If the basis can accurately reproduce the eigenvalues for the $V = 0$ case, then we expect that it will be the same for $V \neq 0$.

Without potential, the numerical efforts are lighter because there is no more term that couples different values of m such as described in Eq. 6.5.20. Thus, we will consider m as a good quantum number so each block m can be diagonalized independently. Moreover, no integral over ϕ will be required because the grand angular momentum matrix elements for a given value of m are known analytically. Consequently, the calculations will be done in the FBR.

Since inversion parity means that even and odd blocks of Ω can be diagonalized separately, there are $N^\Omega = J + 1$ values of Ω to consider for even J and $N^\Omega = J$ for odd J. As there are $N^\theta = (l_{\max} - \mu + 1)$ values of l to consider, the total size of the Hamiltonian to diagonalize (for a block J, p and m) is given by:

$$N^{\text{tot}} = N^\Omega \times N^\theta. \tag{8.1.2}$$

Thus, we can calculate the HHs up to $J = 55$, i.e. $N^{\text{tot}} < 9000$ which is the maximum size that a typical personal computer can diagonalize (without using SDT).

To get well-converged results, all the following calculations are done with 500 quadrature points for θ.

8.1.1 J=0 case

In the case $J = 0$, the functions $d^l_{00}(\theta)$ are used for even values of m and the functions $d^l_{1/2\,1/2}(\theta)$ are used for odd values of m (Cf. tables 6.1–6.2). In this case, the functions

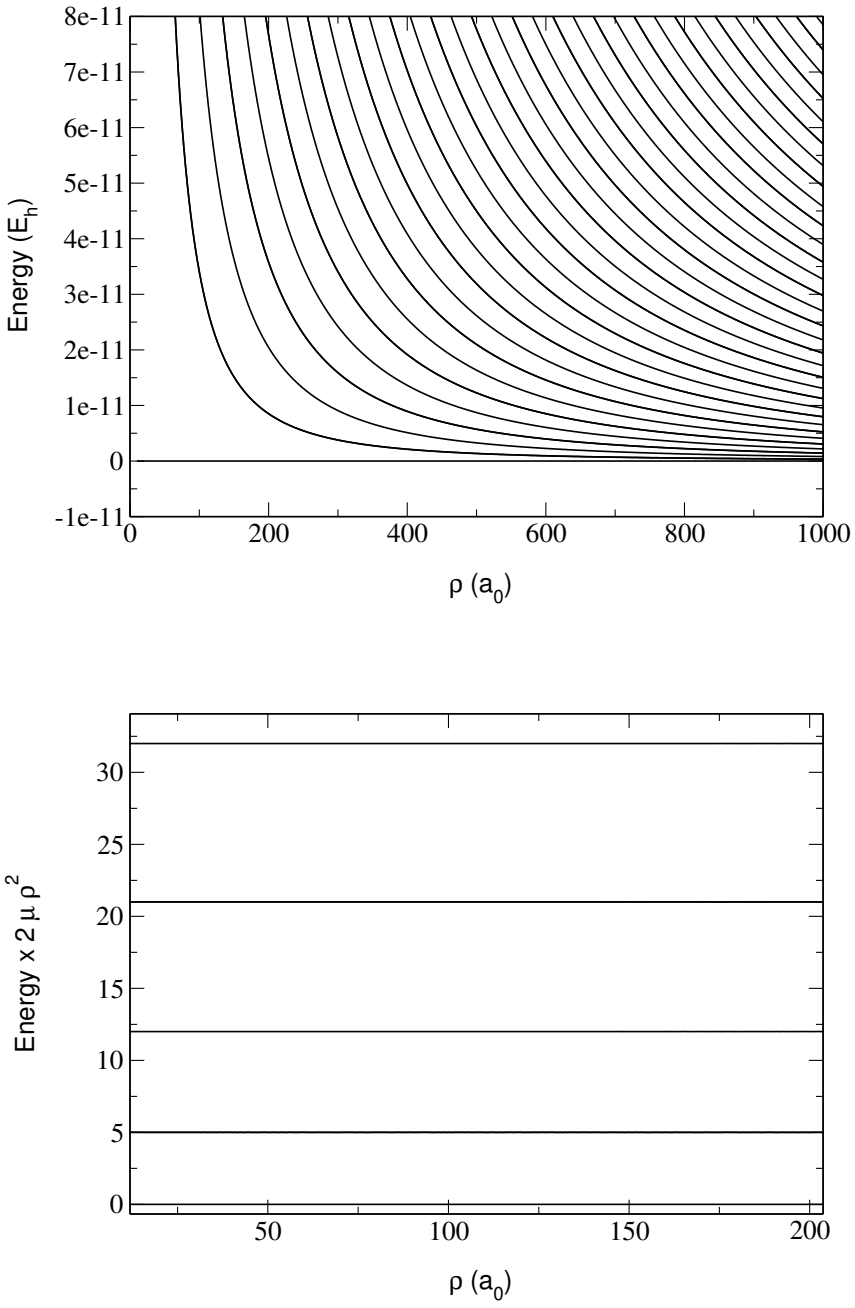

Figure 8.1: Adiabatic energies $\mathcal{E}_t^{Jpq}(\rho)$ as a function of ρ (top) and the dimensionless $\mathcal{E}_t^{Jpq}(\rho) \times 2\mu\rho^2$ term as a function of ρ (bottom). The surface functions associated to $\mathcal{E}_t^{Jpq}(\rho) \times 2\mu\rho^2$ are the Hyperspherical Harmonics.

remove exactly the Eckart singularities at the two poles $\theta = 0$ and $\theta = \pi$. Indeed, for

$\theta \to 0$, the conditions on μ and ν imposed to treat the singularities are given in Eq. 6.5.17:

$$|\mu - \nu|\, \delta_{\Omega\Omega'} = \left| \left\langle \widetilde{D}^J_{\Omega M} \left| \frac{J_x^2}{\hbar^2} \right| \widetilde{D}^J_{\Omega' M} \right\rangle \right|^{1/2} (\mathrm{mod} 2). \tag{8.1.3}$$

Since $J_x^2 = 0$ (because $J = 0$), the condition 8.1.3 is simplified and becomes:

$$|\mu - \nu| \delta_{\Omega\Omega'} = 0 (\mathrm{mod} 2). \tag{8.1.4}$$

This equation is always satisfied as $|\mu - \nu| = |0 - 0| = 0$ for even m and $|\mu - \nu| = |1/2 - 1/2| = 0$ for odd m (Cf. tables 6.1–6.2).

For $\theta \to \pi$, the conditions on μ and ν (already given in Eq. 6.5.15) are also simplified as $\Omega = 0$ and are given by:

$$|\mu + \nu| = 0 \text{ for even } m \qquad |\mu + \nu| = 1 \text{ for odd } m. \tag{8.1.5}$$

These equations are always satisfied as $|\mu + \nu| = |0 + 0| = 0$ for even m and $|\mu + \nu| = |1/2 + 1/2| = 1$ for odd m.

As the singularities are all perfectly removed, the eigenenergies are independent of $l_{\max}$ and match exactly with the energies given in Eq. 8.1.1. We represented on Fig. 8.1 (top) the adiabatic energies in function of the hyperradius for $J = 0$, $m = 0$ and $l_{\max} = 40$. We find that the lowest hyperspherical harmonic is zero ($\lambda = 0$) while the other curves follow a $1/2\mu\rho^2$ behavior. To convince ourselves of this, we have represented in Fig. 8.1 (bottom), the terms $\mathcal{E}_t^{Jp\,q}(\rho) \times 2\mu\rho^2$ in function of ρ. We can clearly identify horizontal curves at $0, 5, 12, 21...$ a.u. as obtained when replacing $\lambda = 0, 1, 2, 3...$ in $E_\lambda = \lambda(\lambda + 4)$.

8.1.2 J=2 and p=1 case

For $J \neq 0$, the matrix elements of J_X^2 given in Eq. 8.1.3 are no longer diagonal. Indeed, only the projection J_Z is diagonal for our choice of BF_Q axis (with Ω as associated quantum number) since only the Z_Q axis can be used as the quantization axis. As a result, the condition on the μ and ν numbers cannot be satisfied for all values of J. The Eckart singularities are then not exactly removed but B. Kendrick showed by a numerical study that the functions given in tables 6.1–6.2 are sufficient to cancel accurately (not perfectly) the singularities if $l_{\max}$ is large enough and if the same quadrature scheme is used for all singular matrix elements. In this section, we verify that the singularities are well canceled for $J = 2$ and $p = 1$ but a more complete study for other values of J is given in [152]. In Fig. 8.2, we represented the fractional errors:

$$\text{Fractional Error} \equiv \frac{\left[\mathcal{E}_t^{Jp\,q}(\rho) \times 2\mu\rho^2\right] - E_\lambda}{E_\lambda} \tag{8.1.6}$$

in function of $\left[\mathcal{E}_t^{Jp\,q}(\rho) \times 2\mu\rho^2\right]$ for $l_{\max} = 80$ (blue) and $l_{\max} = 160$ (black). The energies $E_\lambda = \lambda(\lambda+4)$ are the analytic energies associated to the HHs and can be degenerate. The

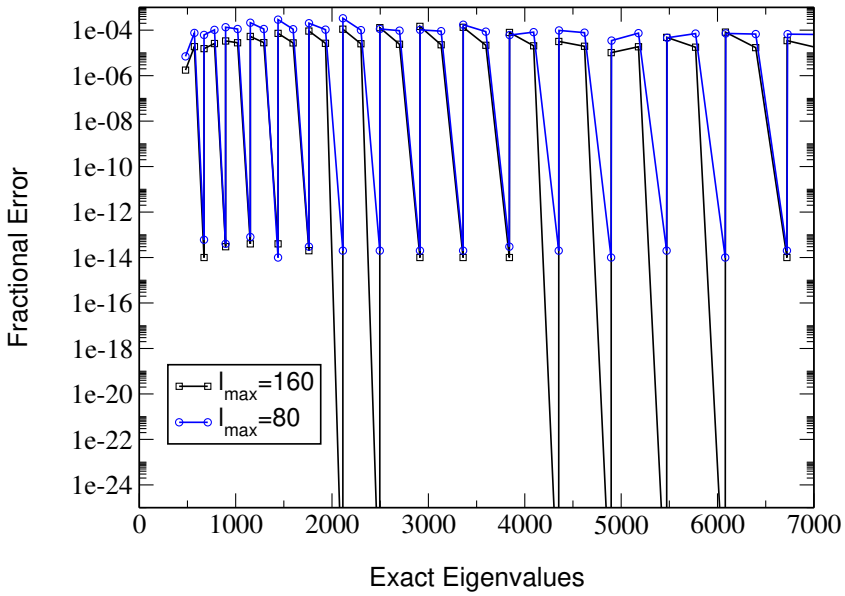

Figure 8.2: Fractional Errors in function of the exact eigenvalues $E_\lambda = \lambda(\lambda+4)$ for $l_{\max} = 80$ (blue) and $l_{\max} = 160$ (black).

smaller the fractional errors, the better the Eckart singularities are treated. We can see that for both values of $l_{\max} = 80, 160$, all the fractional errors are smaller that 10^{-4} which means that all the singular terms are pretty well treated. Moreover, the fractional errors are smaller than 10^{-13} for about half of the eigenvalues because some terms are better canceled than others. This comes from the fact that the functions given in tables 6.1–6.2 allow a more accurate treatment of singularities associated with smaller values of Λ (eigenvalues associated to J_{X_Q}) than for larger values of Λ. We note that for $l_{\max} = 160$, the singularities are better treated than for $l_{\max} = 80$, which is in agreement with what B. Kendrick demonstrated. As singularities are better treated when we increase $l_{\max}$, then we will know (when studying a real system) that the singularities no longer impact the results obtained when the results will remain unchanged for values $l > l_{\max}$. Kendrick compared the surface functions for HD_2 obtained using only the functions d^l_{00} or using the correct set of $d^l_{\mu\nu}$ functions and showed that the singularities can significantly affect the surfaces (and then the observables obtained), with differences which can reach few percents.

In this section, we have shown that Eckart singularities are well treated for $J = 0$ as well as for $J = 2$, $p = 1$ but a more detailed study [152] shows that the method works for any value of J. For $V = 0$, the singular terms at $\theta \to 0$ and $\theta \to \pi$ were fully accessible whereas in studies of real systems, the potential V may be sufficiently repulsive for some configurations of θ to limit the access to the wave functions at the singularities and thus reduce the errors associated to them. We have shown that for our choice of BF_Q axis, the

singularities at $\theta = \pi$ are perfectly removed because it involved only the projection J_{Z_Q} in the grand angular momentum matrix elements which are diagonal in Ω. However for $\theta = 0$ the numerical cancellation is not perfect because the condition given in Eq. 6.5.17 involves the operator J_{X_Q} which is not diagonal in our basis. If we had chosen another set of axes such as the one used by R. T. Pack and G. A. Parker or J.-M. Launay, then the singularities at $\theta \to 0$ could be treated perfectly (because our X_Q axis is chosen as their quantization axis) but conversely as the term J_{Z_Q} would no longer be diagonal, the singular terms at $\theta \to \pi$ would not be perfectly treated. A solution [152] could be to use Wigner rotation functions $\tilde{D}(\alpha, \beta, \gamma, \theta)$ depending on the hyperangle θ so that the BF_Q used is continuously optimal for each configuration θ, so that the choice of axis of B. Kendrick is rather used at/near $\theta = \pi$ and the one of R. T. Pack and G. A. Parker or J.-M. Launay is rather used at/near $\theta = 0$. This proposed scheme will be important for later numerical improvements of an optimal and adaptating choice of the BF_Q axis, related to corresponding "adaptating hyperspherical coordinates", to automatically treat the Eckart singularities.

8.2 Towards three-body recombination and collision induced dissociation

The objective of this part is to apply the formalism described in chapter 6 to study three-body recombination and collision induced dissociation on a fictitious system. We employ a fictitious system with a fictive mass and potential energy surface to investigate those prosesses on a desktop personal computer. Through this example, we will present all the steps to get well converged results. Later, one can use supercomputers to afford a more thorough study, investigating those processes on realistic systems with appropriate potential energy surface.

Let us consider a system composed of three identical bosons of arbitrary individual masses $m = 95$ a.m.u.[1]. The mass is chosen relatively large because coupled with a short-range and not too deep potential, the numbers of simple continuum state remains small while the double continuum states tend quickly to their asymptotic $1/2\mu\rho^2$ behavior. Therefore, the matching can be done at small distances $\rho_{\max} = 40$ a_0 for both reactive, recombination, or collision induced dissociation studies. In the following, we will only study the case where $J = 0$. As $|J - j_\tau| \leq l_\tau \leq |J + j_\tau|$, we will only consider $j_\tau = l_\tau$ states.

8.2.1 The potential energy surface

The potential energy surface used is a pairwise sum of two-body interactions given by:

$$V = v_{2B}(r_\tau) + v_{2B}(r_{\tau+1}) + v_{2B}(r_{\tau+2}) \tag{8.2.1}$$

with

$$v_{2B}(r_\tau) = D_0 \cosh(r_\tau / r_0)^{-2}. \tag{8.2.2}$$

[1] 1 a.m.u. (atomic mass unit) = 1022.88 a.u.

The distance r_0 is a parameter that defines the position of the potential well (and therefore its range) and D_0 controls the depth of the well and thus the number of rovibrational states of the diatom. We choose arbitrary values of $r_0 = 5$ a$_0$ and $D_0 = -3.480 \times 10^{-5}$ a.u. (~ -11 K). Let's note that no three-body non-additive terms have been included in the potential energy surface. The same steps as for Eq. 7.2.12 were followed to express the potential energy surfaces in APH coordinates.

8.2.2 The simple continuum states

Jacobi coordinates

In Fig. 8.3 (top), we have represented the term $v_{2B}(r) + \frac{j(j+1)}{2\mu r^2}$ from Eq. 6.1.24 in function of the distance between the two atoms composing the molecule. For the case $j = 0$, the potential energy surface has a depth of about 10 K. Using the same Numerov algorithm as the one used in section 4.3.2, we found that the vibrational quantum numbers range from $v = 0, 1, 2, 3, 4, 5$ and the maximum associated rotational quantum numbers are $j = 6, 4, 4, 2, 0, 0$ (only even values of j are considered). There are a total of 14 rovibrational states whose energies and wave functions are computed once and stored for the matching procedure. The energies are grouped in table 8.1.

In Fig. 8.3 (bottom), we have zoomed in on the long-range part of the curves. As j increases, the long-range barriers are higher. These barriers come from the centrifugal term $\frac{j(j+1)}{2\mu r^2}$ and allow the existence of quasi-bound states. The red line at 0.103 K represents the only quasi-bound state ($j = 6$, $v = 1$) of our system.

v	**j**	**Energy (K)**
0	0	-8.473
0	2	-5.493
0	4	-2.933
0	6	-0.856
1	0	-5.629
1	2	-3.231
1	4	-1.289
2	0	-3.358
2	2	-1.557
2	4	-0.256
3	0	-1.670
3	2	-0.473
4	0	-0.566
5	0	-2.939×10^{-2}

Table 8.1: Energies of the asymptotic bound states.

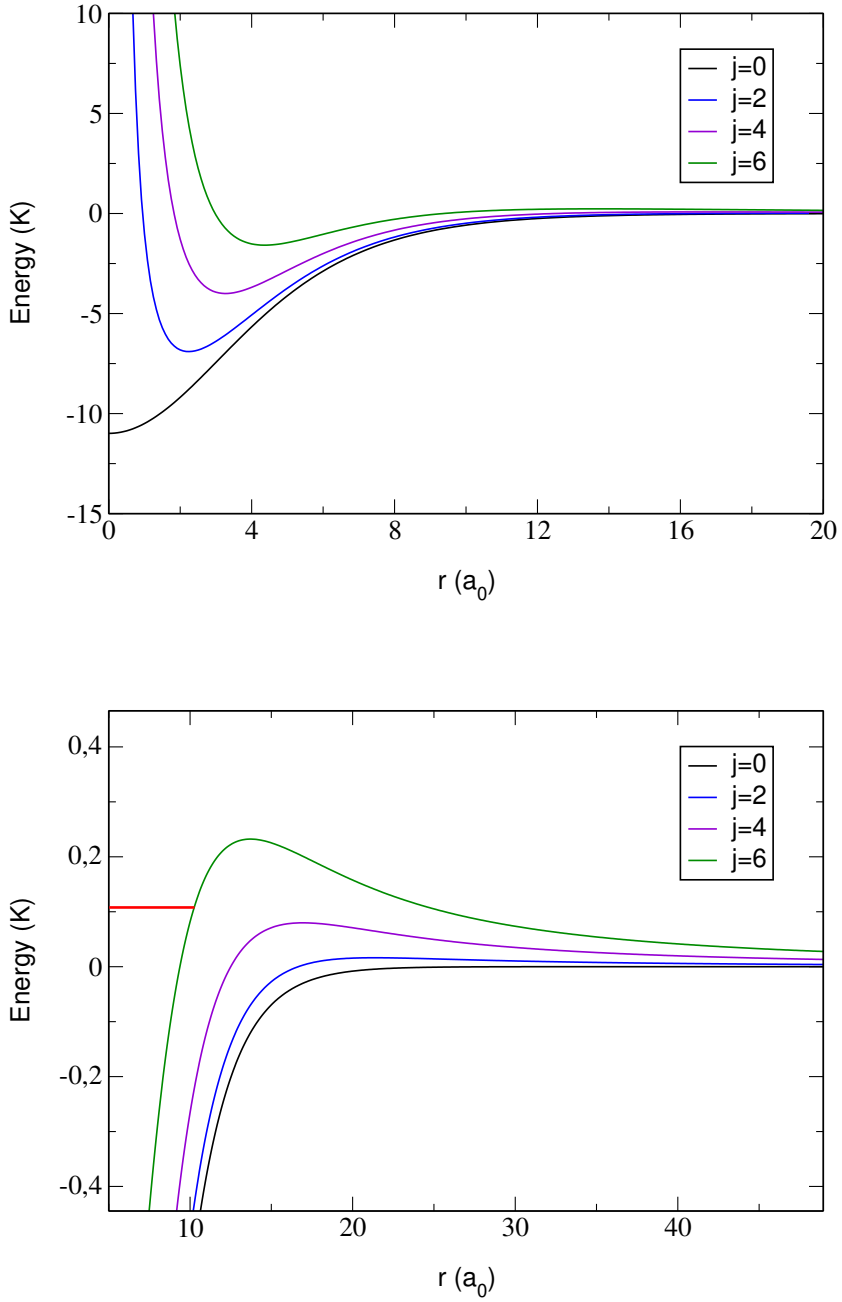

Figure 8.3: Total energy curve as a function of the interatomic distance r (top and bottom). The black curve corresponds to $j = 0$, the blue one to $j = 2$, the purple one to $j = 4$ and the green one to $j = 6$. The lower figure corresponds to a zoom on the long-range part. The red line corresponds to a quasi-bound state in the $j = 6$ potential energy curve.

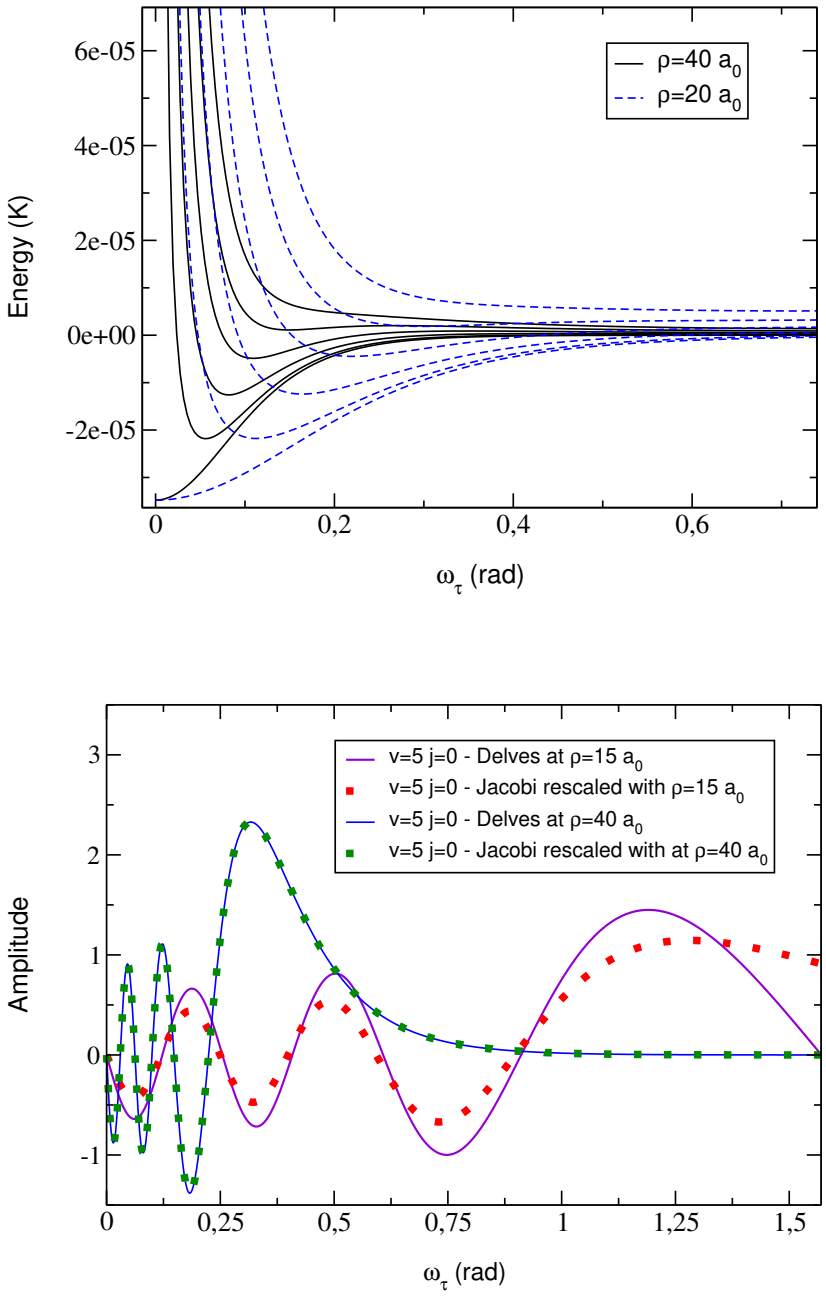

Figure 8.4: Top: Total energy curve obtained at $\rho = 40$ a$_0$ (black) and at $\rho = 20$ a$_0$ (blue) as a function of the Delves angle ω_τ. Bottom: $(v = 5, j = 0)$ simple continuum state in function of ω_τ. The solid lines have been calculated via Eq. 6.2.10 at $\rho = 15$ a$_0$ (purple) and at $\rho = 40$ a$_0$ (blue). The dotted lines have been calculated via Eq. 6.1.24 and rescaled using Eq. 6.2.11 with $\rho = 15$ a$_0$ (red) and with $\rho = 40$ a$_0$ (green).

Delves coordinates

In Fig. 8.4 (top), we represented the term from Eq. 6.2.10:

$$\frac{-\hbar^2}{2\mu\rho^2}\left(-\frac{j_\tau(j_\tau+1)}{\sin^2\omega_\tau}-\frac{l_\tau(l_\tau+1)}{\cos^2\omega_\tau}\right)+v\left(\omega_\tau;\rho\right) \tag{8.2.3}$$

in function of ω_τ for $\rho = 20$ a$_0$ (blue dashed lines) and for $\rho = 40$ a$_0$ (black solid lines). Note that unlike the Jacobi states, the Delves ones depend on the quantum number l_τ. This is explained by the fact that r_τ and R_τ are separable for the Jacobi coordinates while for the Delves ones $r_\tau = \rho\sin\omega_\tau$ and $R_\tau = \rho\cos\omega_\tau$ are mixed and are no longer separable.

Asymptotically, the Delves wave functions match with the Jacobi wave function following Eq. 6.2.11–6.2.12 because:

$$\frac{l_\tau(l_\tau+1)}{\cos^2\omega_\tau}\underset{s_\tau\to\infty}{\longrightarrow}0.$$

This is illustrated in Fig 8.4 (top) where we see that the more ρ increases, the more the potential is situated in a small zone close to $\omega_\tau = 0$. But if $\omega_\tau \to 0$ then $\rho^2\cos^2\omega_\tau \to \infty$ asymptotically (i.e. for $\rho \to \infty$) and the term in l_τ vanishes.

In Fig. 8.4 (bottom) we represented the first ($v = 5, j = 0$) wave functions obtained solving Eq. 6.2.10 in Delves coordinates for $\rho = 40$ a$_0$ (solid blue lines) and for $\rho = 15$ a$_0$ (solid purple lines). The Jacobi wave functions have been calculated via Eq. 6.1.24 and rescaled using Eq. 6.2.11 with $\rho = 15$ a$_0$ (dotted red lines) and with $\rho = 40$ a$_0$ (green dotted lines). We can note that the wave function in Delves and Jacobi coordinates match perfectly only at $\rho = 40$ a$_0$ because for lower distances (e.g. $\rho = 15$ a$_0$), the potential has not yet reached is asymptotic form. Therefore, by calculating the bound states wave functions in Delves and comparing them to the Jacobi ones we can have an estimate of the distance $\rho_{\max}$ that we will have to use in the calculations in APH coordinates. This is very important because if we choose a matching distance that is too small then we can find a number of bound states in Delves larger than the one asymptotically because asymptotic double continuum states can still have negative energies at these distances. This makes it impossible to compute the transformation matrix of Eq. 6.6.11 leading to errors in the matching process.

8.2.3 APH Adiabatic energies

In Fig. 8.5, we represented the adiabatic energies in function of the hyperradius. They are obtained solving Eq. 6.4.31 with $J = 0$, $l_{\max} = 51$ and $m_{\max} = 85$. As we use an adiabatic representation, we can observe a large number of avoided crossings, i.e. no curve ever crosses. These crossings are the consequence of coupling between states and are the source of the inelastic collisions.

We have represented the simple continuum states in blue, the double continuum states in black and the quasi-bound state in red. As expected, there are 14 bound states and one quasi-bound states whose asymptotic energies match with the ones given in table. 8.1. This is a good indication to know if the values of $l_{\max}$ and $m_{\max}$ are sufficient. For

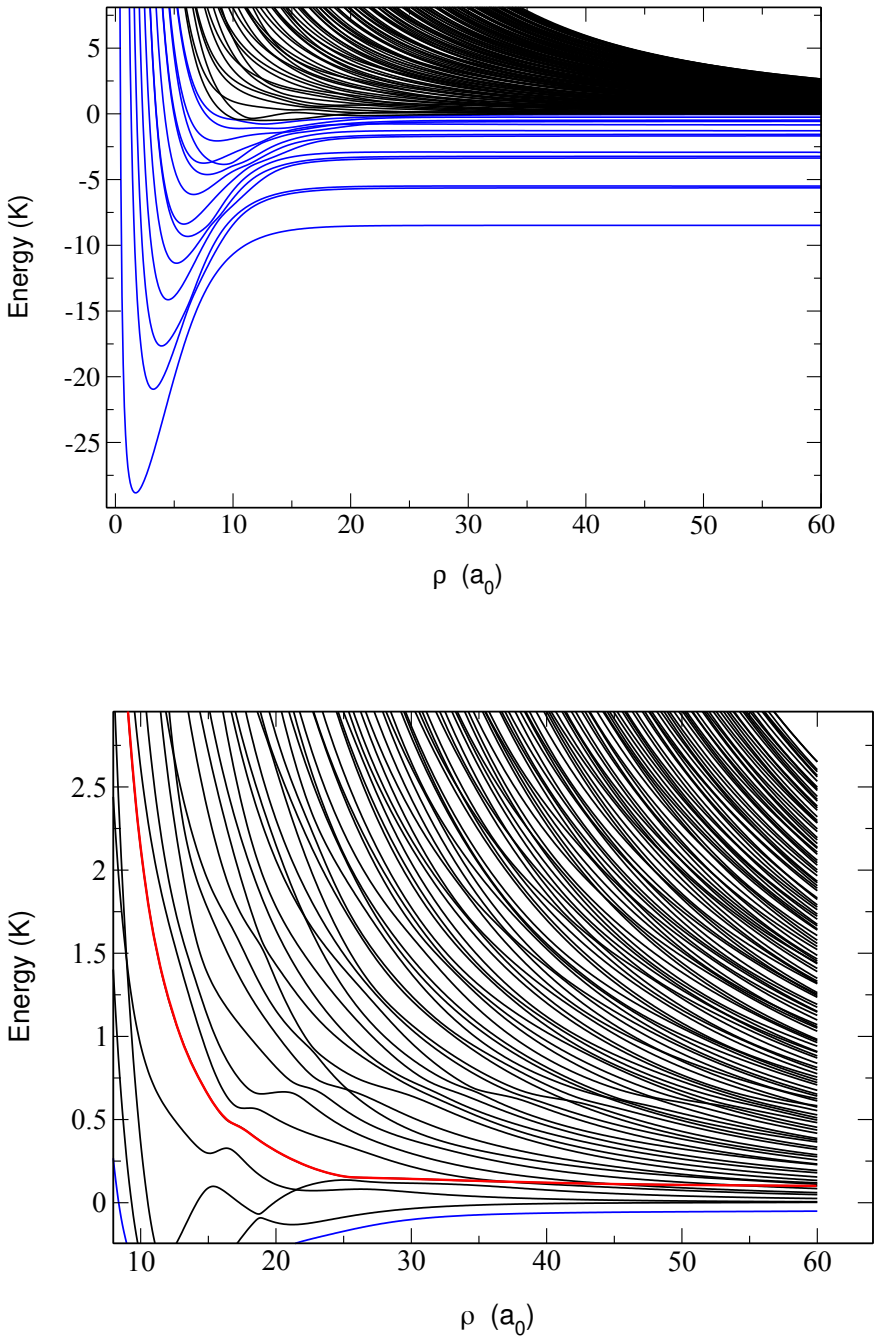

Figure 8.5: Top: Adiabatic energy curves as a function the hyperradius. Botton: A zoom on the double continuum channels. The blue curves correspond to the 14 bound states and the red curve corresponds to the quasi-bound state.

more complicated system, we can chose different values of $l_{\max}$ and $m_{\max}$ in function of the sector studied because we usually need less values of $l_{\max}$ and $m_{\max}$ at short-range. This can be explained by the fact that APH coordinates are not well suited for large distances. Indeed, when ρ becomes large, the regions of θ and ϕ corresponding to typical vibrational distances s_τ become small and the wave function become highly localized. Since the primitive basis is composed of not well localized functions, one must do a bigger linear combination to reproduce the wave function in these regions. Moreover, as we use a DVR in θ, the number $l_{\max}$ refers directly to the number of quadrature points in θ. However, if the potential becomes concentrated on a very small area, we need a larger number of points in this zone: we must therefore increase $l_{\max}$. We can note that the lowest adiabatic energy curve has a depth of $-25\,\mathrm{K}$ which corresponds to about three times the depth of the two-body potential well. This is consistent with the fact that we did the sum of the two-body potentials and that no three-body interactions are used.

If we look on Fig. 8.5 (bottom), we observed that the double continuum states go to 0 asymptotically following a $1/2\mu\rho^2$ behavior. Moreover, we can see that for low distances (for example $\rho = 20$ a$_0$), there are double continuum channels with negative energy. This means that the matching can't be done at this distance as explained in the previous section.

8.2.4 Discussion and results

How to get converged results?

The matching was done at $\rho_{\max} = 60\ a_0$. We took a total of 1200 sectors between $0.01\ a_0$ and $60\ a_0$. The size of a sector is then $0.05\ a_0$. We propagate a total of 200 channels to get well converged results (even when the study will be extended to recombination calculations). However, if we want to study only atom-diatom collisions for a total energy $E < 0$ then less channels could be used. This is what we will do in the next section where we will apply our numerical code to a realistic system. To be sure that our calculations are consistent, one must verify several things:

- The overlap matrix given in Eq. 6.3.16 must verify the property $\mathbf{O}^T\mathbf{O} = \mathbf{1}$. This matrix doesn't need to be symmetric but the diagonal elements must be close to 1.

- The coupling matrix given in Eq. 6.3.17 must be symmetric.

- The Z-matrix must be symmetric for the sub-matrix part which will be used for the matching. We must also verify that if we increase the number of channels propagated that the part used for the matching is unchanged. If we increase the collision energy, we must increase the number of channels propagated.

- The transformation matrix given in Eq. 6.6.11 must be close to a diagonal matrix and must verify $\mathbf{U}^T\mathbf{U} = \mathbf{1}$.

- The Delves wave functions computed at $\rho_{\max}$ must overlap well with the Jacobi wave functions renormalized using Eq. 6.2.11.

- The Wronskian matrix of the asymptotic solutions given in Eq. 6.6.15 and 6.6.16 must be equal to the identity matrix.
- The S-matrix must be unitary and must be equal to its conjugate transpose.

Rate coefficients in function of the hyperradius

In this part, we check that the collision rates are well converged for $\rho = \rho_{\max}$. In Fig. 8.6, we have represented the elastic (black curve) and inelastic (red curve) collision rate coefficients as a function of the matching distance. The curves were obtained for the initial state ($v = 6$, $j = 0$) with a collision energy $E_k = 500\,\mathrm{nK}$. We observe that the elastic collision rate coefficients are between 3.10^{-13} cm^3.s^{-1} and 4.10^{-13} cm^3.s^{-1} and remain relatively constant. For the inelastic collision rate coefficients, they are between 3.10^{-12} cm^3.s^{-1} and 4.10^{-12} cm^3.s^{-1}. In conclusion, the collision rates do not vary much with the hyperradius so we can consider that choosing $\rho_{\max} = 60$ a$_0$ is relevant. Note that if we do not perform the matching at a sufficiently large distance, we can observe oscillations in the collision rate coefficients (and more generally in the matrix elements of the S-matrix). In this case, it is possible to obtain a value close to the one obtained asymptotically by averaging over several oscillation cycles [231, 232].

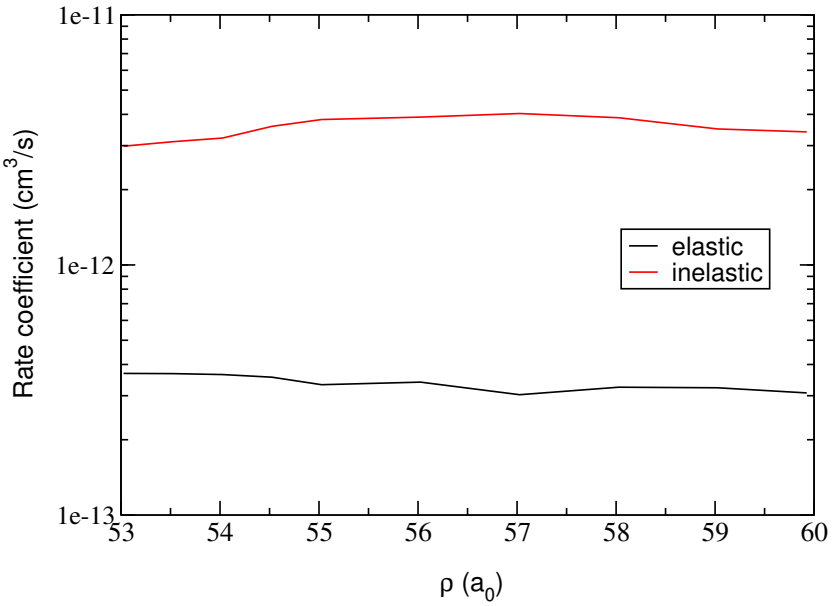

Figure 8.6: Elastic (black curve) and inelastic (red curve) rate coefficients as a function of the hyperradius. The initial channel chosen is ($v = 6$, $j = 0$) and the relative kinetic energy is $E_k = 500\,\mathrm{nK}$.

Current calculations are underway to investigate three-body recombination as well as collision induced dissociation with our numerical code. Future investigations will involve studies of these processes on a realistic system with a given potential energy surface.

8.3 Study of $Li + Li_2$ collisions

In this section, we will study collisions of three-identical bosonic atoms $^7Li\,(^2S)$ + $^7Li_2\,(^3\Sigma_u^+)$ at ultralow collision energies. Many theoretical studies have already been carried out on bosonic $^7Li + {}^7Li_2$ or fermionic $^6Li + {}^6Li_2$ collisions [221, 258, 154] as well as on heteronuclear lithium systems such as $^7Li + {}^7Li^6Li$ [222]. The lithium atoms are light enough (Cf. table 8.2) to get converged results while using a reasonable basis. In addition, this system is of experimental interest as a strong (non-universal) rotational dependence of the $v = 9$ state reaction rate coefficient has been recently observed [257].

In the following, we will limit our calculations on low initial rovibrational levels ($v = 0$ and $v = 1$) whose results will be compared with the existing theoretical ones, providing a benchmark for our numerical code. As for the previous fictitious case, we will limit to the partial wave $J = 0$.

8.3.1 Potential energy surface

system	^7Li	$^7Li_2$	$^7Li_3$
reduced mass (a.u.)	12789.4	6394.7	7384.0
electronic spin S	1/2	1	3/2
nuclear spin I	3/2	3	9/2
total spin F	1, 2	2, 3, 4	3, 4, 5, 6

Table 8.2: Parameters of the ^7Li atom and of the systems $^7Li_2$ and $^7Li_3$.

In contrast to shielding studies where no information on the short-range part of the potential surface was required to perform dynamics calculations, studying reactive collisions implies to know the total potential energy surface whose calculation is not as trivial as for the previous fictitious system. In this section, we will describe the potential energy surface that we will use in our calculations. It has been calculated in [259] and has already been used in [151] to which we will compare our calculations. It corresponds to the electronic quartet ground state of the lithium trimer and accounts for the conical intersection resulting from the crossing between the states $^4\Sigma_u^+$ and $^4\Pi_g$ in linear configuration. To get the potential energy surface for any configuration, an interpolation and extrapolation procedure [260] of ab initio points was used.

The potential energy surface can be developed into a sum of three terms:

$$V_{\text{tot}}\ (r_1, r_2, r_3) = V_{1B} + V_{2B}\,(r_1, r_2, r_3) + V_{3B}\,(r_1, r_2, r_3)\,. \tag{8.3.1}$$

The term V_{1B} corresponds to the dissociation energy of the three atoms (i.e. the sum of the energies of the three atoms when they are asymptotically separated). This is a constant set to zero in our calculations so that the double continuum states and the quasi-bound states have positive energies and the simple continuum states have negative energies. The term $V_{2B}\,(r_1, r_2, r_3)$ corresponds to a pairwise sum of two-body interactions such that:

$$V_{2B}\,(r_1, r_2, r_3) = v_{2B}\,(r_1) + v_{2B}\,(r_2) + v_{2B}\,(r_3) \tag{8.3.2}$$

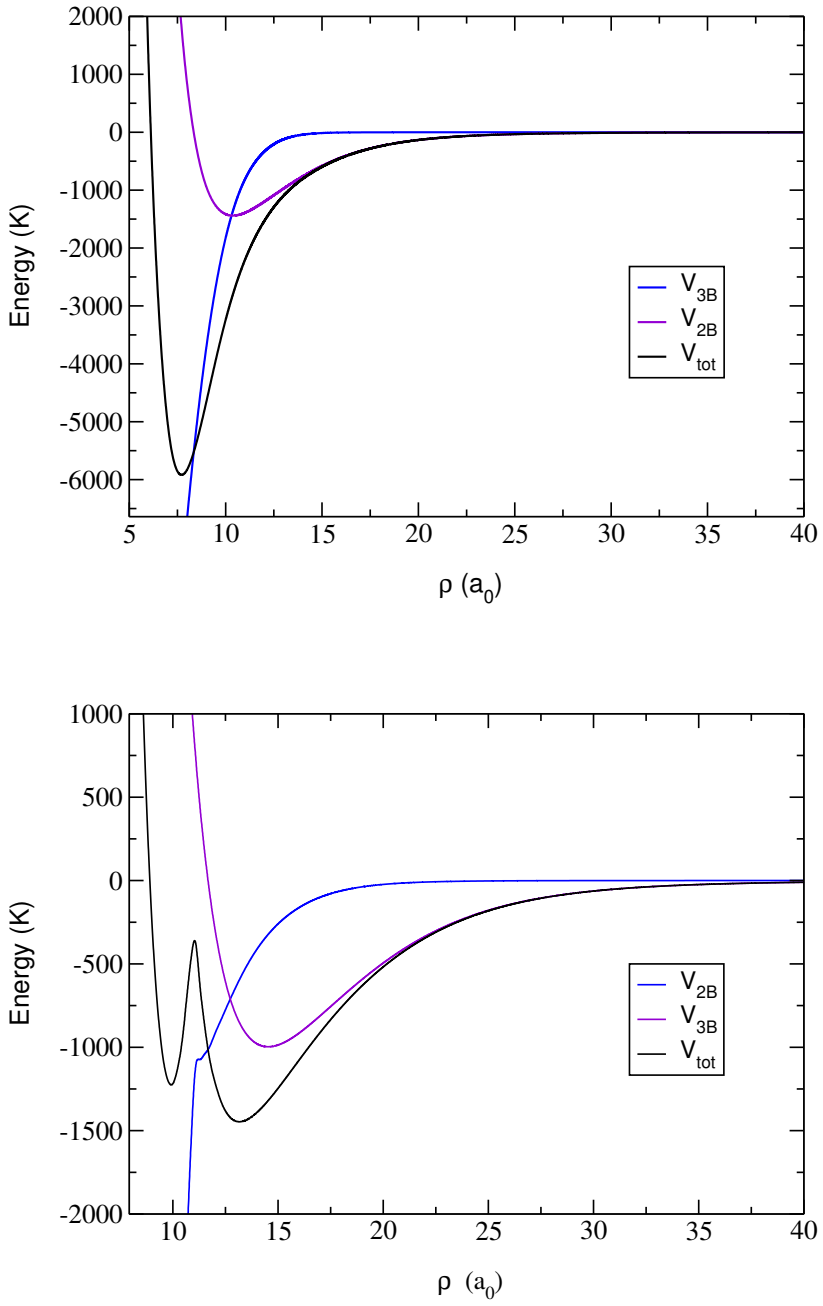

Figure 8.7: Potential energy surface for equilateral configuration (top) and linear configuration (botton) in function of the hyperradius.

where $v_{2B}(r_i)$ depends only on the interatomic distance between the two atoms considered. The ground electronic surface of the diatomic $^3\Sigma_u^+$ contains 11 vibrational levels $v = [0, 10]$. The term $V_{3B}(r_1, r_2, r_3)$ contains all the nonadditive three-body terms. The leading one is the Axilrod-Teller-Muto interactions (dipole-dipole-dipole) which fol-

lows a $\propto 1/(r_1^3 r_2^3 r_3^3)$ behavior at long-range. Note that more accurate potential energy surfaces were developed later and include higher order multipole terms such as the dipole-dipole-quadrupole, the dipole-quadrupole-quadrupole, the dipole-dipole-octupole, the quadrupole-quadrupole-quadrupole interactions [258].

In Fig. 8.7, we have represented the potential energy surface separating the different interaction terms (Cf. Eq. 8.3.1) in function of the hyperradius for the equilateral (top) and linear (bottom) configurations. For the equilateral configuration, we observe that the total potential has a localized minimum ($-5917\,\mathrm{K}$) at $\rho = 7.71\ \mathrm{a_0}$ while the two-body term has a minimum ($-1440\,\mathrm{K}$) at $\rho = 10.38\ \mathrm{a_0}$. This difference can be explained by the fact that the three-body interaction is more than four times stronger than the two-body interaction at the equilibrium distance. For the linear configuration, we observe that the potential energy curves behave differently for both the two-body and three-body parts compared to the equilateral configuration, leading to two distinct wells in the total potential energy curve. The first well ($-1225\,\mathrm{K}$) is located at $\rho = 9.92\ \mathrm{a_0}$ and the second well, which is the deepest one ($-1447\,\mathrm{K}$), is located at $\rho = 13.16\ \mathrm{a_0}$. The presence of this double well is related to the behavior of the two-body curve which rises back up slightly at $\rho = 11.28\,a_0$ and which comes from the fact that the two-body curves $^3\Sigma_u^+$ and $^3\Pi_u$ intersect at $r = 5.10\,a_0$.

8.3.2 Adiabatic energies

If we follow the same steps than section 8.2.2, we found that the vibrational quantum numbers of $^7Li_2$ range from $v = 0, 1, 2, ..., 10$ and the maximum associated rotational quantum numbers are $j = 34, 32, 28, 26, 24, 20, 18, 14, 10, 6, 2$. We consider atoms in their spin streched states as in [219, 222, 154, 258]. The nuclear spin wavefunction is then symmetric under interchange of two nuclei. The nuclear spatial part imposes a factor $(-1)^j$ when two nuclei are permuted while the electronic spatial wave function in the $^3\Sigma_u^+$ state is anti-symmetric when two nuclei are permuted. As the atoms ^{7}Li are bosons (while the nuclei are fermions), the total wave function must be anti-symmetric under the permutation of two nuclei. This is why we only deal with even values of j. Finally, we find a total of 118 rovibrational states in agreement with [230, 151] (Cf. appendix D.1).

We have split the calculation of the potential energy surfaces into 6 distinct sectors whose parameters $l_{\max}$, $m_{\max}$ and the number of sub-sectors n_ρ are given in table 8.3. As explained before, as ρ increases, the size of the base must be increased to represent the simple continuum states which are more and more localized.

$\rho\,(a_0)$	$l_{\max}$	$m_{\max}$	n_ρ
$[3, 13]$	50	67	250
$[13, 22]$	40	76	225
$[22, 26]$	50	85	100
$[26, 31]$	60	103	125
$[31, 34]$	60	112	75
$[34, 40]$	80	148	100

Table 8.3: Parameters for the numerical calculations.

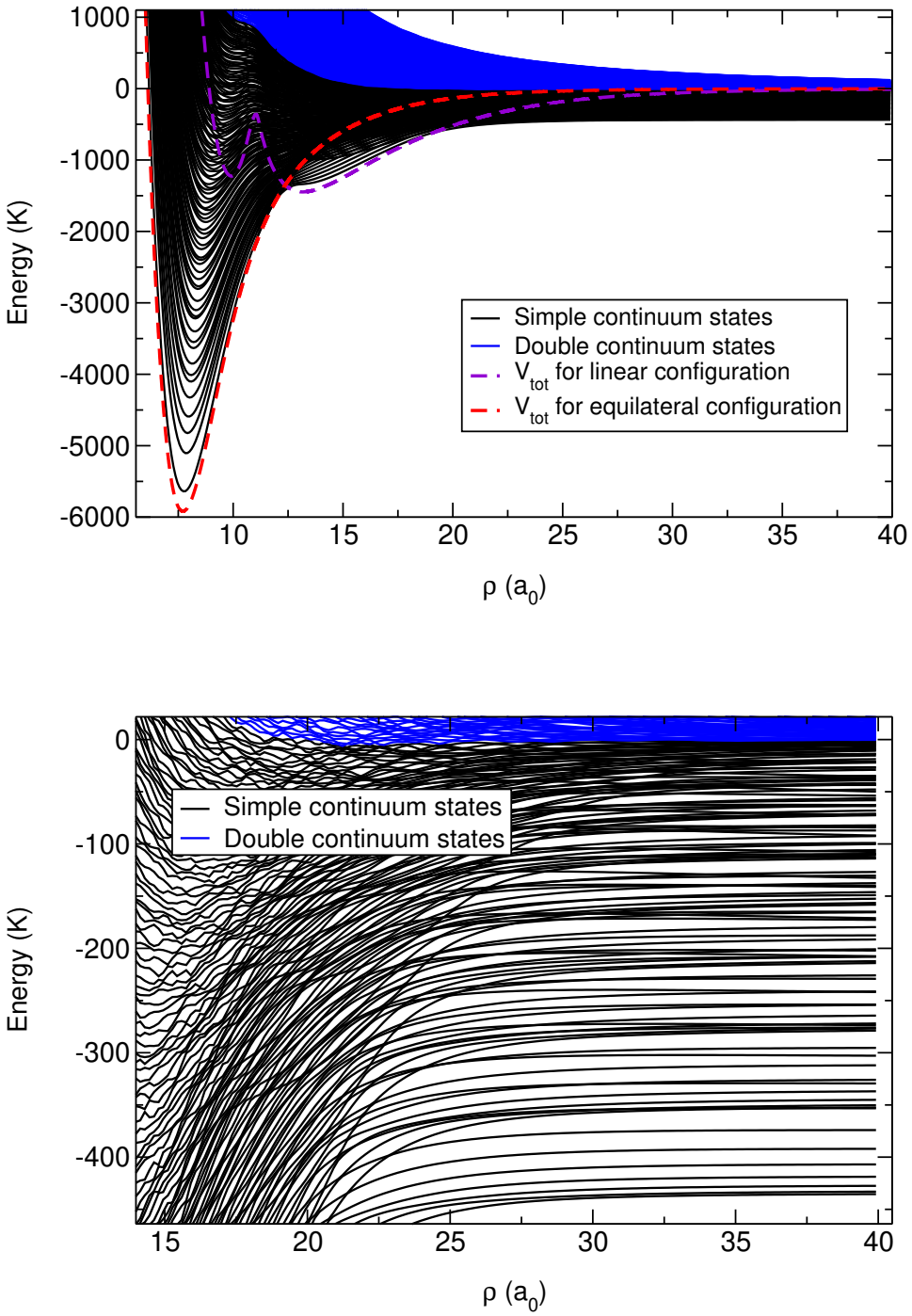

Figure 8.8: Top: Adiabatic energies as a function of the hyperradius. Bottom: A zoom on the bound states. The black curves match with the 118 simple continuum states and the blue ones correspond to the double continuum channels.

In Fig. 8.8 (top) we represented the adiabatic energies as a function of the hyperradius. The curves in black correspond to simple continuum states while the blue ones correspond to double continuum states. In red (dashed line), we have represented the total potential V_{tot} in the equilateral configuration initially described in Fig. 8.7. We notice that this configuration dominates at short-distance because the adiabatic energy curves are centered on the well previously described and located at $\rho = 7.71$ a$_0$. Note that the lowest adiabatic energy curve is slightly higher at the equilibrium distance than V_{tot} because on the one hand the other configurations disturb on average the effect of the equilateral configuration and on the other hand there is the three-body centrifugal energy to consider. We have also represented in purple the potential energy curve for the linear configuration. The latter dominates at greater distances (around $\rho = 14$ a$_0$) and the adiabatic energy curves follow the potential energy curve behavior.

In Fig. 8.8 (bottom), we zoomed in on the long-range part of the adiabatic energy curves. We find well 118 curves which tend to the rovibrational energies of the diatom. We observe a large number of avoided crossings around $\rho = 15$ a$_0$, which demonstrate the complexity of three-body studies and the importance of using relatively tight sector sizes to account for all these couplings (responsible for inelastic collisions).

8.3.3 Results

The matching was done at $\rho_{\max} = 40\ a_0$. We took a total of 875 sectors between 3 a_0 and 40 a_0. The size of the sectors is 0.04 a_0. Indeed, we can increase the size of the sectors once we are a bit far from the short-range part because the adiabatic energy curves do not vary much anymore. We propagate a total of 200 channels but this number must be increased if we study more exited vibrational states [151]. The matching is performed on 118 states because the highest ones were not necessary after convergence studies.

In Fig. 8.9 (top), we represented the elastic rate coefficient as a function of the collision energy for the initial $(v = 0, j = 0)$ state. For the initial collision energy $E_\mathrm{k} = 1\,\mathrm{nK}$, the elastic rate coefficient $\beta^{el} = 1.32 \times 10^{-13}\,\mathrm{cm^3\,s^{-1}}$ match with the one calculated in [154]. We note that for the range of initial collision energies $E_\mathrm{k} \in [1\ \mathrm{nK}, 0.1\ \mathrm{mK}]$, the elastic rate coefficient is linear on the logarithmic scale (it follows the red curve) with a slope of 1/2 in agreement with the Bethe-Wigner laws [172, 173] for elastic rate coefficients:

$$\beta^{el} \propto E_k^{2l+\frac{1}{2}}. \tag{8.3.3}$$

For $E_\mathrm{k} = 20\,\mathrm{mK}$ and $E_\mathrm{k} = 80\,\mathrm{mK}$, we observe drops in the elastic rate coefficient. As we are in the case $l = 0$, the elastic rate coefficient is proportional to the squared sine of the accumulated phase shift in the interaction zone:

$$\beta^{el} \propto \sin^2(\delta_0)\,. \tag{8.3.4}$$

When the phase shift is equal to 0 then the elastic rate coefficient goes to 0. This is equivalent to the "zeros" of the Ramsauer-Townsend effect but for atom-atom collisions in the s-wave ($l = 0$). However, these drops cannot be observed experimentally because they appear at collision energies high enough that the contributions of $J > 0$ partial

waves are large enough to wash them out.

In Fig. 8.9 (bottom), we represented the elastic (black) and the inelastic (pink) rate coefficients as a function of the collision energy for the initial $(v = 1, j = 0)$ state. As in the previous figure, we note that the elastic and inelastic collision rates obtained at collision energy $E_{\mathrm{k}} = 1\,\mathrm{nK}$ match with the ones calculated in [154]. We show that inelastic processes dominate over elastic processes by two orders of magnitude at very low energies. This means that the conditions for achieving evaporative cooling are not favorable as the ratio $\gamma < 10^2$ (i.e. inelastic collisions highly contribute to trap loss). The elastic rate coefficients have the same behavior as for the previous case at low energies and we still observe drops at higher collision energies. However, in this case the phase shift is complex (as there are inelastic processes), this is why the oscillations don't go to zero in contrast with case $(v = 0, j = 0)$. For the inelastic rate coefficient, we observe that they are constant up to collision energies $E_{\mathrm{k}} = 10\,\mu\mathrm{K}$, which is consistent with the Bethe–Wigner threshold law for inelastic collisions given by:

$$\beta^{\mathrm{in}} \propto E_k^l. \tag{8.3.5}$$

We observe that for high collision energies, the inelastic rate coefficients decrease because it follows the unitary regime.

As a conclusion, we have studied reactive $^7\mathrm{Li} + {}^7\mathrm{Li}_2$ bosonic collisions. We have computed the adiabatic energies curves and compared their behavior with the total potential energy curves for the linear and equilateral configurations. We have found all the 118 single continuum states and a large number of double continuum states had to be used to obtain well converged states. We have computed the elastic and inelastic rate coefficients for the initial states $(v = 0, j = 0)$ and $(v = 1, j = 0)$ in function of the initial collision energy. We have verified that our rate coefficients are in agreement with the ones calculated in [154] and with the Bethe–Wigner's threshold laws.

This study allowed us to verify that my numerical code works and gives consistent results by comparing my results with previous studies. The implementation of the code on supercomputers will allow us to explore other systems and may include several partial waves.

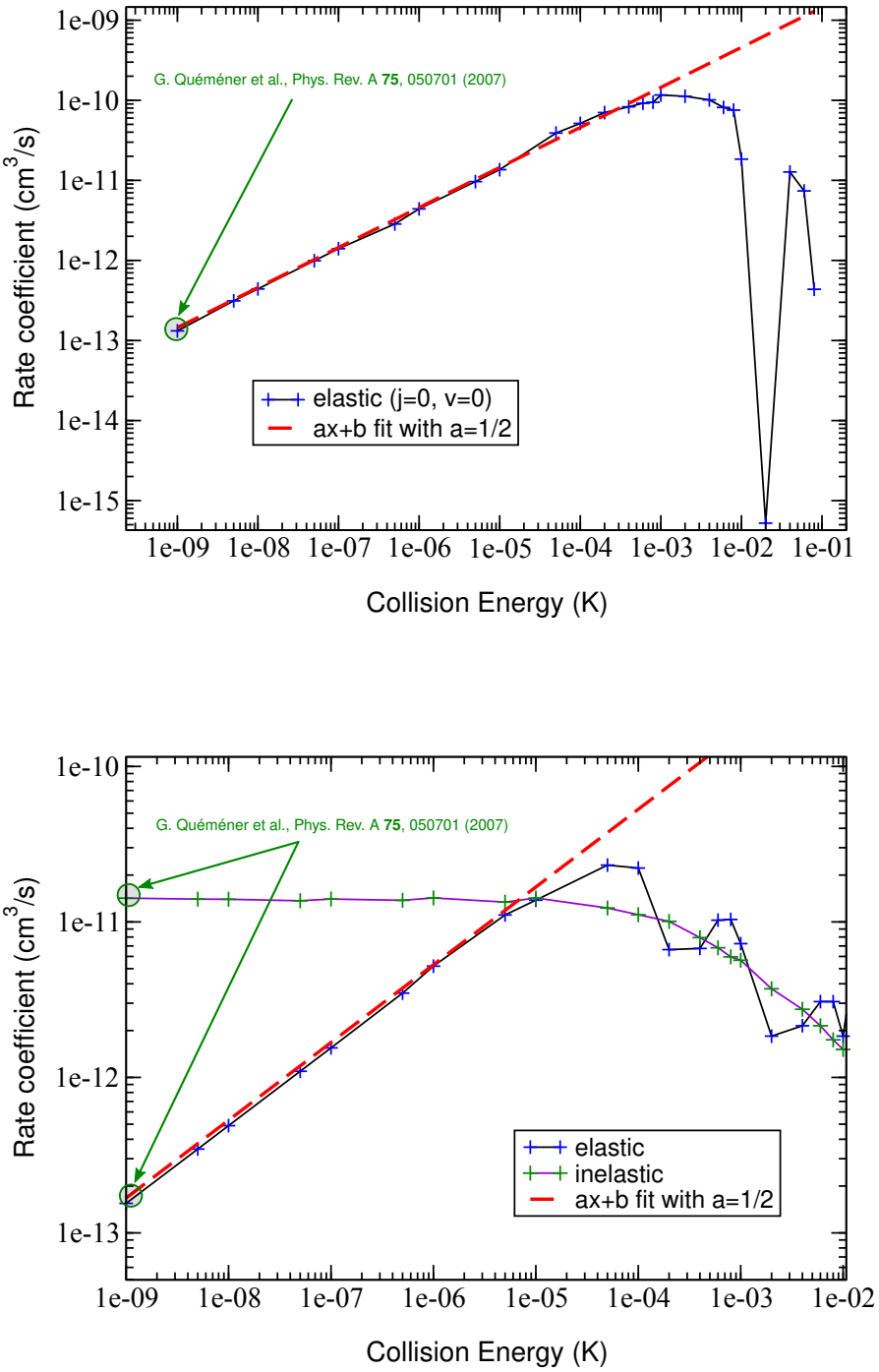

Figure 8.9: Top: Elastic (black curve) rate coefficients as a function of the collision energy for ^{7}Li+^{7}Li$_2$ ($v = 0, j = 0$). Bottom: Elastic (black curve) and inelastic (pink curve) rate coefficients as a function of the collision energy for ^{7}Li+^{7}Li$_2$ ($v = 1, j = 0$). For both plots, the crosses represent the numerically calculated point and the red curves correspond to linear fits of the elastic rate coefficients at low collision energies with $a = 1/2$ cm^3.s^{-1}.K^{-1}. The green circles are points taken from [154].

Chapter 9

Conclusions and perspectives

The work carried out in this thesis had two objectives. The first one was to develop shielding methods to reduce short-range molecular losses. The second one was to develop a numerical code involving collisions of three particles, suitable for studying atom-diatom collisions, three-body recombination or collision-induced dissociation and three-body shielding.

In the first part of the manuscript, I focused on two-body molecular collisions. In chapter 3, I presented the time-independent formalism required to study ultracold collisions. It is based on the expansion of the total wave function in terms of partial waves and on the S-matrix theory. In chapter 4, I developed the formalism of the two-body microwave shielding. First, I presented how to treat the electromagnetic wave from a time-independent point of view. Then, I showed that if one applies a circularly polarized microwave field whose frequency is slightly blue-detuned with respect to the transition $j = 0 \rightarrow j = 1$, one can engineer a long-range barrier by taking advantage of the dipole-dipole interaction. I demonstrated that for bosonic NaRb molecules, the barrier is high enough to prevent the total wave function from reaching short-range regions where processes (reactive or complex formation collisions) lead to the loss of molecules. By developing an adimensional approach, I showed that one can significantly reduce losses for a large number of molecules. Ratios between elastic and loss rate coefficients $\gamma > 10^3$ can be reached, leading to favorable conditions for evaporative cooling. A tiny potential well appears before the potential barrier at long-range. By varying both the intensity and the frequency of the applied microwave field, one can vary the depth of this well and make resonances appear in the real and imaginary parts of the scattering length. These resonances are large enough to adjust experimentally the sign and the magnitude of the scattering length. As the ability to control the molecule-molecule scattering length is not an easy task, this new method opens the door for a rich many-body physics for ultracold molecules, similar to that for ultracold atoms. We are preparing an article on the many-body physics of molecular Bose-Einstein condensates with strong dipole-dipole interactions [205]. By combining a microwave field with a static electric field, one can finely tune the two-body scattering length as well as the dipolar length of an ultracold molecular gas. This enables to set ideal conditions for the emergence of self-bound droplets, and explore phase diagrams that feature a variety of exotic supersolid states.

In chapter 5, I introduced the static electric field shielding method initially developed in our team [97, 98]. One can finely tune elastic, inelastic and reactive rate coefficients for a wide range of molecules prepared in their first rotational excited state. Our idea was to use this method for three-body collisions, but the method becomes difficult to implement because too many channels are required. Our objective was to develop a simplified model which would reproduce the complete calculation results while reducing the number of states used. First, I have shown that the two resonant states can be isolated from the other ones. Then, I diagonalized the interaction matrix for each spatial configuration (r, θ) and integrated the surface corresponding to the initial state over the lowest partial wave. After propagation of the single channel log-derivative matrix, collision rate coefficients are extracted from the S-matrix. I have shown that the elastic and loss rate coefficients, obtained for KRb molecular collisions, are in semi-quantitative agreement with those obtained from the complete calculations at the magic electric field value. Our simple model can then provide a good estimation of the elastic and loss rate coefficients, requiring only one collisional channel. As the model does not provide any information on the inelastic rate coefficients, it cannot reproduce well the results for other electric field values. Static electric field shielding has been observed for the first time experimentally in a three-dimensional gas and compared well with our model, as presented in our joint paper with the KRb JILA team [100]. We will present our model and the content of chapter 5 in a forthcoming paper.

In chapter 6, I developed the theoretical formalism required to study three-body collisions. First, I introduced the mass-scaled Jacobi coordinates which are mainly used at sufficiently large distances where all the arrangements are well separated. Then, I presented the Delves hyperspherical coordinates and show that they can be used as an intermediary between Jacobi coordinates and the APH coordinates. I showed that the latter are less intuitive to use, but in return they treat all the different arrangements equally even at short distances. They are closely related to the main axes of inertia of the system which implies the presence of singularities (the so-called Eckart singularities) in the grand angular momentum operator. Following the formalism developped by B. Kendrick [152], I explained how the primitive basis functions to accurately treat these divergent terms has been chosen. Then, I applied the SDT method to reduce the total size of the Hamiltonian and explained how the surface functions for three identical particles are extracted. Finally, I presented the matching method for the study of atom-diatom collisions and for the study of three-body recombination as well as collision induced dissociation.

In chapter 7, I illustrated that it is impossible to apply the three-body formalism from chapter 6 to the case of static electric field shielding. I have shown that the number of states involved is too large to get converged results. I have therefore applied and adapted the two-body model from chapter 5 to hyperspherical coordinates. I have demonstrated that one can get two five-dimensional surfaces via the diagonalization of the interaction matrix. By keeping only the surface corresponding to the initial state and integrating it over the first hyperspherical harmonics, one obtained a repulsive channel. After prop-

agation, I showed that the shielding is effective for the same electric field value as for the two-body shielding, which is very promising to achieve efficient evaporative cooling. Within the model, I can estimate a lower value of $\gamma = 10^3$, encouraging for suppressing three-body losses. All three-body results will be the subject of forthcoming articles.

In chapter 8, I applied my three-body numerical code for three systems. First, I studied the adiabatic energy curves when $V = 0$. By comparing the adiabatic energies obtained with my code with the analytic eigenvalues of the hyperspherical harmonics, I have estimated the errors resulting from the Eckart singularities. I have shown that the singularities are perfectly removed for $J = 0$ and the fractional errors do not exceed 10^{-4} in the worst cases for $J = 2$. These results are also valid for any value of J and the larger $l_{\max}$ is, the better the Eckart singularities are treated. Secondly, I have studied the atom-diatom collisions on a fictitious system for $J = 0$. I have shown how the adiabatic energy curves of good symmetry are extracted and presented the rate coefficients in function of the matching distance. Investigations are under way to apply the code for three-body recombination and collision-induced dissociation. Finally, I have used my numerical code for studying ^{7}Li+^{7}Li$_2$ bosonic collisions. I have presented the elastic and inelastic rate coefficients and showed that they were consistent with previous results. The numerical code is ready to be used on supercomputers to perform more complex calculations including partial waves $J \neq 0$.

As perspectives and now that I simplified the formalism of the static electric field shielding study for both two-body and three-body collisions, it might be interesting to see if this model can be applied to the microwave shielding case. Its implementation may be more challenging because the electromagnetic field is treated from a time-independent point of view, which implies more complicated interaction terms. Once set up, one must check the validity domains of the model, i.e. the sets of values E_{ac} and Δ for which the model best reproduces two-body complete calculations. Once the model is verified, it can be extended to three-body collisions.

A more detailed study of three-body static electric field shielding will have to be carried out. I plan to perform a comparative study between bosons and fermions in the case of KRb molecular collisions. The physical phenomenon will be explored for different systems by including molecules with a dipole moment larger than KRb, expecting the suppression to be larger as expected for two-body [98]. For this purpose, an adimensional study will be appropriate.

I developed during my PhD thesis a three-body code which can be brought to supercomputer platforms. We hope that the acquired skills on the development of coordinates, the treatment of singularities and on the implementation of numerical methods to reduce the computation time (SDT, hybrid representation) might open the way to study four-body systems, for which more and more four-body potential surfaces are developed [80, 261, 262, 263]. Since complex-mediated collisions are still not clearly understood [264, 265], these four-body studies would provide an opportunity to understand what happens in the short-range region when two reactive or non-reactive diatomic

molecules collide.

Appendix A

Microwave Shielding

A.1 Characteristic times of the problem

In this study, there are different characteristic times that we now compare in this section. The time-dependent microwave radiation applied to molecules initially prepared in the ground rotational state $j = 0$ is nearly resonant with the first excited state $j = 1$, with a detuning Δ. In this case, the time-dependent quantum state evolves between the $j = 0$ and the $j = 1$ bare states periodically, following Rabi oscillations with the generalized Rabi frequency:

$$\Omega_{gen} = \sqrt{(\Delta/\hbar)^2 + \Omega^2} \tag{A.1.1}$$

or in rescaled units:

$$\tilde{\Omega}_{gen} = \frac{\Omega_{gen}}{B_{rot}/\hbar} = \sqrt{\tilde{\Delta}^2 + \tilde{\Omega}^2}. \tag{A.1.2}$$

The characteristic time of a general process such as a stimulated emission or absorption (which is behind the shielding process and the control of the scattering length here) is on the order of the inverse of the generalized Rabi frequency [266]. A first characteristic time is then the period of those Rabi oscillations given by $t_{osc} = 2\pi/\Omega_{gen}$. If one looks at Fig. 4.10, the smallest typical value of $\tilde{\Omega}$ at which the microwave shielding is efficient and the long-range potential wells in Fig. 4.11 appear, depends on the molecules. Taking into account the typical rotational constants reported in table A.1, the fixed rescaled detuning $\tilde{\Delta} = 0.025$ and the smallest typical values of $\tilde{\Omega}$ of the different molecules, the oscillations times are on the order of $t_{osc} \sim 10^{-8}$ s or lower.

A second characteristic time is the time between collisions $T_{coll} = (\beta\, n)^{-1}$ [267, 266]. It depends on the density n of the gas and the two-body rate coefficients β. Typically, the rate coefficients (elastic or loss) are about $\beta \sim 10^{-10}$ cm^3/s for indistinguishable bosons [268]. The densities reach in typical experiments are about $n \sim [10^{10} - 10^{12}]$ molecules/cm^3 so that $T_{coll} \sim [0.01 - 1]$ s. The time between collisions is then far much longer than the period time of the Rabi oscillations, $T_{coll} \gg t_{osc}$. Therefore far from the collision, the dressed state picture {molecule + field} can be used. Asymptotically, the

molecules are well characterized by stationary quantum dressed states and the asymptotic form of the time-independent scattering wavefunction is well defined.

A third characteristic time is the time of a collision t_{coll} [266]. In our study, it is the time spent by two molecules in their intitial state when they go through the long-range potential well $V_{well}(r)$ shown in Fig. 4.11. We use a classical estimation given by:

$$t_{coll} = 2 \times \int_{r_{in}}^{r_{out}} \frac{dr}{v(r)} = 2 \times \int_{r_{in}}^{r_{out}} \frac{dr}{\sqrt{\frac{2[E_{\rm tot} - V_{well}(r)]}{\mu}}}. \tag{A.1.3}$$

$v(r)$ is the local velocity of the molecules at distance r given by:

$$v(r) = \sqrt{2\,E_k(r)/\mu} = \sqrt{2[E_{\rm tot} - V_{well}(r)]/\mu}. \tag{A.1.4}$$

r_{in} is the inner turning point given by the position of the wall of the potential and r_{out} is a typical distance at which the potential does not significantly change compared to the collision energy. The factor of 2 accounts for the way in and out. If the energy of the initial state of the molecules is taken as the zero of energy, $E_{\rm tot}$ identifies with the collision energy E_k. Taking into account the reduced mass μ and the potential well of different molecules, and taking a typical value of the collision energy $E_k = 500$ nK, we estimate t_{coll} to be on the order of 10^{-5} s or higher if the collision energy decreases. For a given molecule, highest values of Ω means deeper wells and fastest molecules, but also more distance to cover and at the end t_{coll} do not vary significantly with increasing values of Ω. The time of a collision is then much longer than the period time of the Rabi oscillations, $t_{coll} \gg t_{osc}$. The rapid evolution in time of the quantum state between the two bare states $j = 0$ and $j = 1$ can be averaged out during the collision, and therefore the time-independent dressed state picture formalism can be safely employed in our study.

Finally, other characteristic times are the lifetimes of the $j = 0$ or $j = 1$ states in the shielding mechanism. The advantage of the microwave shielding over the optical shielding lies in the fact that the molecules in $j = 1$ have generally long spontaneous emission times, on the order of $\sim 10^4$ s [98]. In addition, black-body radiation driving either rotational or vibrational excitations of the molecules at room temperature can be neglected as the lifetimes are on the order of $\sim 10^2$ s or more for alkali dipolar molecules [269]. These characteristic times are far much longer than the other characteristic times and those processes can be ignored.

A.2 Effect of the blue-detuned microwave radiation on the trapping of the molecules

When an electromagnetic wave is applied to a molecule with a permanent electric dipole moment in its ground rotational state $j = 0$, the energy level of the molecule will undergo an ac Stark shift [176], as a function of the energy $\hbar\omega$ and the ac field E or

similarly the intensity I of the radiation. Generally, $E = E(\rho, z)$ or $I = I(\rho, z)$ depends on cylindrical coordinates (ρ, z) and are given by a Gaussian beam profile [270]:

$$I(\vec{r}) = I(0) \times \frac{e^{-\frac{2\rho^2}{w^2}}}{1 + (z/z_R)^2}$$

where $w = w_0\sqrt{1 + (z/z_R)^2}$ is the spot size, w_0 is the beam waist and z_R is the Rayleigh parameter. In return, this gives rise to an effective dipolar potential $V_{dip}(\vec{r}) = \text{const.} \times \text{I}(\tilde{\text{r}})$. For a microwave field (MW), the potential has the form:

$$V^{MW}(\vec{r}) = V_0^{MW} \times \frac{e^{-\frac{2\rho^2}{(w^{MW})^2}}}{1 + (z/z_R^{MW})^2} \tag{A.2.1}$$

where V_0^{MW} corresponds to the ac Stark shift [176] at the corresponding ac field E or intensity I. If the energy shift is negative, the potential is attractive and becomes a trap, while if the energy shift is positive, the potential is repulsive. In our study, because of the blue-detuned microwave, the potential is repulsive. In addition to the MW potential, we consider that the molecules are trapped in an usual optical dipole trap (ODT). An ODT has a similar form than Eq. A.2.1:

$$V^{ODT}(\vec{r}) = V_0^{ODT} \times \frac{e^{-\frac{2\rho^2}{(w^{ODT})^2}}}{1 + (z/z_R^{ODT})^2} \tag{A.2.2}$$

where the energy shift V_0^{ODT} is negative due to a red-detuned optical radiation.

In Fig. A.1, we plot the total potential $V^{ODT} + V^{MW}$ as a function of ρ (we fix $z = 0$ for simplicity). We take typical experimental values of $V_0^{ODT} \simeq -10\,\mu$K [78], $w_0^{MW} \simeq 10\,$mm [270], $w_0^{ODT} \simeq 0.05\,$mm [36]. To estimate V_0^{MW}, we perform an adimensional calculation of the ac Stark shift energy levels of the alkali dipolar molecules for the parameters used in our study: $\tilde{\Omega} = 0.18$, $\tilde{\Delta} = 0.025$, circular polarization $p = +1$. We find an energy shift of $V_0^{MW} \simeq 0.04\,B_{rot}$ for the $j = 0$ state. We take as an example the LiK (resp. RbCs) molecule for which the MW potential is the most (resp. less) repulsive, as LiK (resp. RbCs) has the highest (lowest) value of B_{rot} (we exclude LiNa since the system is not appropriate for an efficient microwave shielding). This gives $V_0^{MW} \simeq 17\,$mK for LiK and $V_0^{MW} \simeq 1\,$mK for RbCs. For RbCs, we can see on the figure that the MW potential has no effect on the ODT trap as it remains $10\,\mu$K deep. For LiK, one can see a change of 20% in the depth of the ODT trap, from $10\,\mu$K to $8\,\mu$K, but this is still deep enough for the molecules to be trapped. This is mainly due to the different scale of the beam waists $w_0^{MW} \gg w_0^{ODT}$ so that the MW potential looks like just an overall constant shift in energy to the tiny ODT potential region. As the values V_0^{MW} of the other dipolar alkali molecules lie in between, then the molecules will not be affected by the MW repulsive potential for the range of $\tilde{\Omega} = [0 - 0.18]$ and $\tilde{\Delta} = 0.025$ chosen in the study. The MW potential can start to have an anti-trapping effect at some point if $\tilde{\Omega}$ is further increased and/or if $\tilde{\Delta}$ is further decreased, since in both cases the energy shift V_0^{MW} will increase and will lead to a more repulsive potential. In these conditions, the values of $\tilde{\Omega}$ and $\tilde{\Delta}$ would limit the efficiency of the shielding due to the anti-trapping effect that they can create.

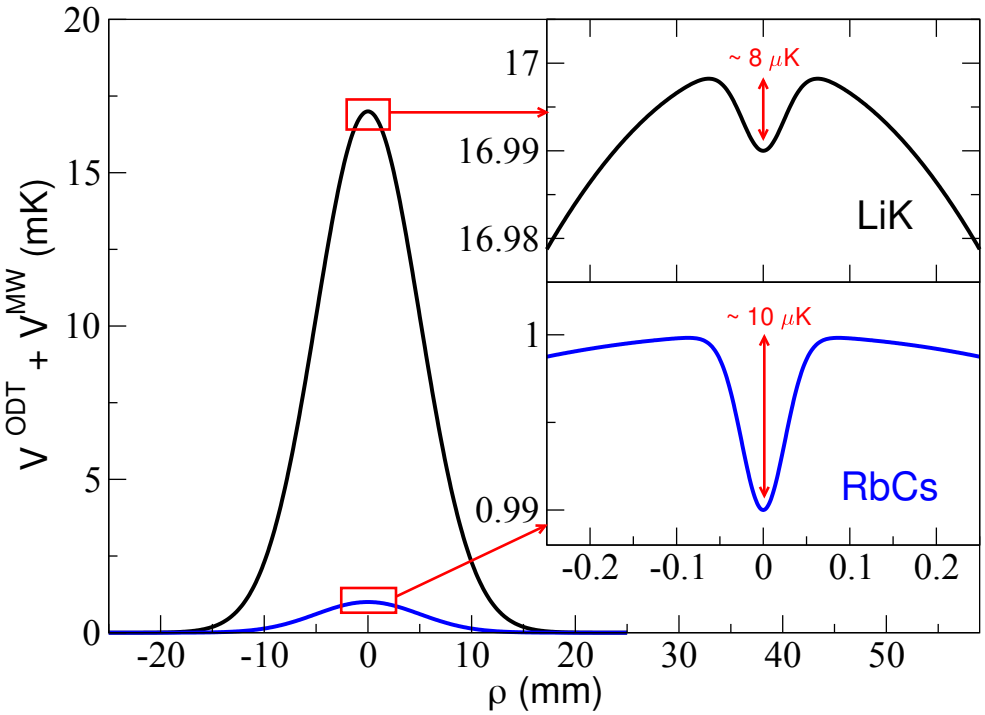

Figure A.1: Total effective potential due to the interaction of the molecules with the microwave and the optical radiation for the LiK and the RbCs system. The blue-detuned microwave radiation leads to a repulsive potential while the red-detuned optical radiation leads to an attractive potential. The insets show that the potentials remain deep enough to trap the molecules.

A.3 Electronic and nuclear spin structure. Effect of a magnetic field

The repulsive curve correlating to the $j = 0 + j = 1$ threshold in Fig. 4.1 is due to the electric dipole-dipole interaction between the two molecules. The electric dipole moment is carried along the molecular axis and the dipole-dipole interaction is mediated by the rotational quantum numbers j of the molecules, more specifically in the present case by the interaction between the $j = 0$ and $j = 1$ rotational states of the molecules. Then the repulsive curve and hence the shielding mechanism is mediated only by the rotational structure of the molecules. Neglecting the fine or hyperfine structure of the molecules is a good assumption as far as the electronic and the nuclear spins act as spectators, or in other words they are decoupled enough from the rotational structure.

For $^1\Sigma$ molecules, the total electronic spin is $s = 0$ and there is no fine structure. But $^1\Sigma$ molecules possess a hyperfine structure [271, 272]. One of the highest contribution is the electric quadrupole term [273]:

$$V_{eqQ_k} \propto \frac{(eqQ)_k}{4}$$

where $(eqQ)_k$ is the coupling constant between the electric quadrupole of the nucleus $k = A, B$ and the gradient of the surrounding electric field in the molecule AB. The coupling constants are on the order of MHz ($\sim 50\mu$K). The other hyperfine terms such as the nuclear spin-rotation and the nuclear spin-nuclear spin interactions are generally smaller, on the order of kHz ($\sim$ 50nK) or Hz [271, 272]. An appropriate basis set to describe the molecule-molecule quantum states is the uncoupled nuclear spin one $\{j_1\ m_{j_1}\ m_{i_{A_1}}\ m_{i_{B_1}} + j_2\ m_{j_2}\ m_{i_{A_2}}\ m_{i_{B_2}}\}$. i_k, m_{i_k} are the nuclear spin quantum numbers of the nucleus $k = A, B$. Due to the unavoidable hyperfine structure, the sketch in Fig. 4.1 is somewhat modified. The threshold $j = 0 + j = 1$ is not degenerate anymore at long range and splits following the three components $m_j = 0, \pm 1$ of the $j = 1$ state, due to the presence of the hyperfine term V_{eqQ_k}. However, the repulsive character of the curve in Fig. 4.1 still remains. When an applied magnetic field B is zero or small, the individual uncoupled hyperfine quantum numbers, characterized by $i_A\ m_{i_A}\ i_B\ m_{i_B}$, are not good quantum numbers due to the presence of the electric quadrupole term (or the nuclear spin-nuclear spin term). But by increasing the magnetic field, they become nearly good quantum numbers due to the Zeeman term:

$$V_{Z_k} \propto -g_k\, \mu_N\, B$$

where g_k is the nuclear g factor of the nucleus $k = A, B$ and μ_N is the nuclear magneton. Typically, when the Zeeman term is bigger than the electric quadrupole interaction term, one can consider that the hyperfine states start to act as spectators and represent good individual uncoupled quantum numbers. This yields an estimation of the magnetic field B^* (much) above which neglecting the hyperfine state is valid and the shielding will remain unaffected. Then, B^* is defined when $|V_{Z_A}| + |V_{Z_B}| \simeq |V_{eqQ_A}| + |V_{eqQ_B}|$ and implies a rough estimation of [103]:

$$B^* \simeq \frac{|(eqQ)_A| + |(eqQ)_B|}{4\,(|g_A| + |g_B|)\,\mu_N} \simeq \frac{|(eqQ)_A[\mathrm{MHz}]| + |(\mathrm{eqQ})_\mathrm{B}[\mathrm{MHz}]|}{|g_A| + |g_B|} \times 328\ \mathrm{G/MHz}. \quad \text{(A.3.1)}$$

The corresponding values of B^* are provided in table A.1. For example using Eq. A.3.1 for the RbCs system, we find a value of $B^* = 106$ G. A similar study [104] explored the effect of the hyperfine structure. The authors explicitely included the hyperfine structure in their quantum calculation. They showed that for sufficiently high magnetic fields, the hyperfine structure can be safely neglected as far as the rotational quantum number m_j becomes a nearly good quantum number. Our arguments about the decoupling between the rotation and the spin structure then follow directly the conclusions of their work. From their numerical calculations, they found that for $B > 100$ G the hyperfine structure can be neglected for the RbCs system. Our analytical value of $B^* = 106$ G presented above using Eq. A.3.1 seems then a good semi-quantitative estimation above which the hyperfine-free regime starts to occur.

For $^2\Sigma$ molecules, the electronic spin is $s = 1/2$ and the molecules also possess a fine structure besides the hyperfine structure [274]. One of the highest contribution is the electronic spin-rotation interaction term:

$$V_{s.j} \propto \gamma_{s.j}$$

where $\gamma_{s.j}$ is the coupling constant between the electronic spin and the rotation. The coupling constant is on the order of MHz. In the uncoupled spin basis set $\{j_1\ m_{j_1}\ m_{s_1}\ m_{i_1} + j_2\ m_{j_2}\ m_{s_2}\ m_{i_2}\}$, where s, m_s, i, m_i are now the electronic and nuclear spin quantum numbers of a molecule, similar arguments hold than for $^1\Sigma$ molecules. For the spin states to be spectators, the application of a magnetic field will decouple them from the rotational structure. The Zeeman term is given by:

$$V_Z \propto -g_e\,\mu_B\,B$$

where $g_e \simeq -2$ is the g factor of the electron and μ_B is the Bohr magneton. As above, the Zeeman term V_Z has to overcome the electronic spin-rotation interaction term $V_{s.j}$. A rough estimation of the magnetic field B^* for which $|V_Z| = |V_{s.j}|$ is:

$$B^* \simeq \frac{|\gamma_{s.j}|}{2\,\mu_B} \simeq |\gamma_{s.j}[\text{MHz}]| \times 0.357\ \text{G/MHz}. \tag{A.3.2}$$

In the case where the electronic spin-nuclear spin interaction term:

$$V_{s.i} \propto b_{s.i}$$

is higher than the electronic spin-rotation interaction term, the uncoupled spin basis set is not appropriate. It is then more convenient to use a coupled spin basis set $\{j_1\ m_{j_1}\ f_1\ m_{f_1} + j_2\ m_{j_2}\ f_2\ m_{f_2}\}$ where f is the total spin with $|s-i| \leq f \leq s+i$. This is just a change of the spin states labelling from s, m_s, i, m_i to s, i, f, m_f. In this case, the total spin quantum number f has to be decoupled from the rotational one j. As f is coupled to j via the $V_{s.j}$ interaction, the magnetic field is still estimated by Eq. A.3.2.

A.4 Table of relevant parameters for different molecules

We provide in table. A.1 a summary of relevant parameters for different $^1\Sigma$ and $^2\Sigma$ molecules. We use the values in [191, 275, 272] for the $^1\Sigma$ molecules and [276, 55, 277, 278, 279, 280, 281, 282, 283, 284, 285, 286, 287, 288, 289, 290, 274] for $^2\Sigma$ molecules. μ is the reduced mass, B_{rot} the rotational constant and d the permanent electric dipole moment. s_{r_3} and s_{E_3} are respectively the characteristic length and energy of the dipole-dipole interaction. $\tilde{B}_{rot}$ is the rescaled rotational constant. The systems are ordered in increasing values of $\tilde{B}_{rot}$. Ω and E are receptively the Rabi frequency and the ac electric field needed to be applied for reaching the maximum value of $\tilde{\Omega} = 0.18$ taken in our study. Δ is the detuning corresponding to the value of $\tilde{\Delta} = 0.025$ fixed in our study. Finally, B^* is an estimation of the magnetic field (much) above which the fine or hyperfine structure can be neglected. It is given by Eq. A.3.1 for $^1\Sigma$ molecules and Eq. A.3.2 for $^2\Sigma$ molecules, using the values $(eqQ), g, \gamma_{s.j}$ of [272, 274, 287, 289, 290].

	μ (a.u.)	B_{rot}(GHz)	d (D)	$s_{r_3}(a_0)$	s_{E_3}(K)	$\tilde{B}_{rot}$	$\Omega/2\pi$ (MHz) at $\tilde{\Omega}=0.18$	E(kV/cm) at $\tilde{\Omega}=0.18$	Δ (MHz) at $\tilde{\Delta}=0.025$	B^*(G)
$^1\Sigma$										
^{7}Li^{23}Na	27349	12.741	0.51	2188	1.2×10^{-6}	5.07×10^{5}	2293	9	318	65
^{41}K^{87}Rb	116547	1.109	0.64	14568	6.38×10^{-9}	8.34×10^{6}	200	0.62	28	296
^{87}Rb^{133}Cs	200349	0.510	1.25	96207	8.5×10^{-11}	2.87×10^{8}	92	0.15	13	106
^{23}Na^{41}K	58288	2.818	2.85	146234	1.3×10^{-10}	1.07×10^{9}	507	0.35	70	178
^{41}K^{133}Cs	158470	0.899	1.91	178279	3.1×10^{-11}	1.38×10^{9}	162	0.17	22	110
^{7}Li^{41}K	43729	8.784	3.53	168978	1.3×10^{-10}	3.33×10^{9}	1581	0.89	220	150
^{23}Na^{87}Rb	100167	2.098	3.43	365108	1.2×10^{-11}	8.52×10^{9}	378	0.22	52	309
^{7}Li^{87}Rb	85608	7.615	4.14	454902	8.9×10^{-12}	4.10×10^{10}	1371	0.66	190	309
^{23}Na^{133}Cs	142090	1.739	4.70	972605	1.2×10^{-12}	7.10×10^{10}	313	0.13	43	37
^{7}Li^{133}Cs	127531	6.535	5.46	1179020	8.9×10^{-13}	3.52×10^{11}	1176	0.42	163	22
$^2\Sigma$										
^{84}CaOH	51920	10.02	1.465	34572	2.5×10^{-9}	1.9×10^{8}	1804	2.4	251	12
^{87}Rb^{172}Yb	235922	0.37	1.218	108351	5.7×10^{-11}	3.1×10^{8}	66	0.11	9	19
^{87}Rb^{84}Sr	155695	0.540	1.54	114309	7.8×10^{-11}	3.34×10^{8}	97	0.13	13.5	12
^{133}Cs^{172}Yb	277845	0.25	1.478	187897	1.6×10^{-11}	7.52×10^{8}	45	0.06	6	-
^{84}SrOH	91979	7.47	1.9	102788	1.6×10^{-10}	2.2×10^{9}	1345	1.4	187	26
^{40}Ca^{19}F	53740	10.26	3.07	156797	1.2×10^{-10}	4.12×10^{9}	1848	1.2	257	13
^{40}CaH	37342	126.8	2.53	73996	7.7×10^{-10}	7.88×10^{9}	22824	18	3169	466
^{88}Sr^{19}F	97437	7.52	3.47	363094	1.2×10^{-11}	2.9×10^{10}	1354	0.77	188	27
^{138}Ba^{19}F	143009	6.471	3.17	444881	5.6×10^{-12}	5.57×10^{10}	1165	0.73	162	29
^{89}Y^{16}O	95611	11.63	4.524	605801	4.5×10^{-12}	1.24×10^{11}	2094	0.92	291	3

Table A.1: Relevant parameter for $X^1\Sigma$ and $X^2\Sigma$ molecules. We provide useful conversion factors: 1 u. $\simeq$ 1822.88 a.u.; 1 a.u. $\simeq$ 219475 cm^{-1}; 1 a.u. $\simeq$ 2.5417D; $1a_0 \simeq 0.529\times10^{-10}$ m; 1 a.u. $\simeq$ 315775 K; 1 a.u. $\simeq 2.80\times10^{-17}$ cm^2; 1 a.u. $\simeq 6.126\times10^{-9}$ cm^3/s; 1 a.u. $\simeq 5.1422\times10^6$kV/cm.

Appendix B

Simplified static electric field shielding

Let's consider bi-alkali molecules prepared in their $X^1\Sigma^+$ electronic ground states and in the same nuclear spin states. j_τ represents the rotationnal quantum number of the molecule τ = 1,2 and m_{j_τ} the quantum number associated to its projection onto the quantization axis $\hat{z}$. l represents the orbital angular momentum quantum number of the two molecules, and m_l the quantum number associated to l_z. The molecule-molecule bare states are given by:

$$|j_1, m_{j_1}, j_2, m_{j_2}, l, m_l\rangle \tag{B.0.1}$$

and the dipole-dipole interaction is defined as:

$$V_{DD} = \frac{\vec{\mu}_1 \cdot \vec{\mu}_2 - 3\,(\vec{\mu}_1 \cdot \hat{r})\,(\vec{\mu}_2 \cdot \hat{r})}{4\pi\epsilon_0 r^3} \tag{B.0.2}$$

where μ_τ the permanent electric dipole of the molecule τ. We can express the matrix elements in the bare basis as:

$$\begin{aligned}
&\left\langle j_1, m_{j_1}, j_2, m_{j_2}, l, m_l \left| V_{DD} \right| j_1', m_{j_1}', j_2', m_{j_2}', l', m_l' \right\rangle \\
&\quad = \frac{-\sqrt{30}\mu_1\mu_2}{4\pi\epsilon_0 r^3}(-1)^{m_l+m_{j_1}+m_{j_2}} \sqrt{(2l+1)\,(2l'+1)}\sqrt{(2j_1+1)\,(2j_1'+1)} \\
&\times \sqrt{(2j_2+1)\,(2j_2'+1)} \begin{pmatrix} 1 & 1 & 2 \\ p_1 & p_2 & -p \end{pmatrix} \begin{pmatrix} j_1 & 1 & j_1' \\ 0 & 0 & 0 \end{pmatrix} \begin{pmatrix} j_1 & 1 & j_1' \\ -m_{j_1} & p_1 & m_{j_1}' \end{pmatrix} \\
&\times \begin{pmatrix} j_2 & 1 & j_2' \\ 0 & 0 & 0 \end{pmatrix} \begin{pmatrix} j_2 & 1 & j_2' \\ -m_{j_2} & p_2 & m_{j_2}' \end{pmatrix} \begin{pmatrix} l & 2 & l' \\ 0 & 0 & 0 \end{pmatrix} \begin{pmatrix} l & 2 & l' \\ -m_l & -p & m_l' \end{pmatrix}
\end{aligned} \tag{B.0.3}$$

with:

$$\begin{cases} p = p_1 + p_2 \\ p_1 = m_{j_1} - m_{j_1}' \\ p_2 = m_{j_2} - m_{j_2}' \\ p = m_l' - m_l. \end{cases} \tag{B.0.4}$$

In our studies, we consider molecules prepared in $m_\tau = 0$. Therefore, $p_1 = 0$ and $p_2 = 0$, involving:

$$\begin{cases} p = p_1 + p_2 = 0 \\ p = m_l' - m_l = 0 \longrightarrow m_l' = m_l. \end{cases} \tag{B.0.5}$$

In the basis $|j_1, 0, j_2, 0, l, m_l\rangle \equiv |j_1, j_2, l, m_l\rangle$, the matrix elements of the dipole-dipole interaction are given by:

$$\begin{aligned}\langle j_1, j_2, 0, l, m_l \,|V_{DD}|\, j_1', j_2', 0, l', m_l\rangle &= \frac{-2\mu_1\mu_2}{4\pi\epsilon_0 r^3}(-1)^{m_l} \\ &\times \sqrt{(2l+1)\,(2l'+1)}\sqrt{(2j_1+1)\,(2j_1'+1)}\sqrt{(2j_2+1)\,(2j_2'+1)} \\ &\times \begin{pmatrix} j_1 & 1 & j_1' \\ 0 & 0 & 0 \end{pmatrix}^2 \begin{pmatrix} j_2 & 1 & j_2' \\ 0 & 0 & 0 \end{pmatrix}^2 \begin{pmatrix} l & 2 & l' \\ 0 & 0 & 0 \end{pmatrix} \begin{pmatrix} l & 2 & l' \\ -m_l & 0 & m_l \end{pmatrix}. \end{aligned} \tag{B.0.6}$$

The general formula for the integral of three spherical harmonics

$$\begin{aligned}\int_0^{2\pi}\int_0^{\pi} Y_{l_1}^{m_1}(\theta,\phi) Y_{l_2}^{m_2}(\theta,\phi) Y_{l_3}^{m_3}(\theta,\phi)\sin\theta d\theta d\phi \\ = \sqrt{\frac{(2l_1+1)\,(2l_2+1)\,(2l_3+1)}{4\pi}} \begin{pmatrix} l_1 & l_2 & l_3 \\ 0 & 0 & 0 \end{pmatrix} \begin{pmatrix} l_1 & l_2 & l_3 \\ m_1 & m_2 & m_3 \end{pmatrix}\end{aligned} \tag{B.0.7}$$

can be used and adapted for our study:

$$\begin{aligned}&\int_0^{2\pi}\int_0^{\pi} Y_l^{*m_l}(\theta,\phi) Y_2^0(\theta,\phi) Y_{l'}^{m_l}(\theta,\phi)\sin\theta d\theta d\phi \\ &= \int_0^{2\pi}\int_0^{\pi} Y_l^{*m_l}(\theta,\phi)\left[\frac{1}{4}\sqrt{\frac{5}{\pi}}\left(3\cos^2\theta - 1\right)\right] Y_{l'}^{m_l}(\theta,\phi)\sin\theta d\theta d\phi \\ &= (-1)^{m_l}\sqrt{\frac{5(2l+1)\,(2l'+1)}{4\pi}} \begin{pmatrix} l & 2 & l' \\ 0 & 0 & 0 \end{pmatrix} \begin{pmatrix} l & 2 & l' \\ -m_l & 0 & m_l \end{pmatrix}. \end{aligned} \tag{B.0.8}$$

Using Eq. B.0.8 into Eq. B.0.6, we obtain:

$$\begin{aligned}\langle j_1, j_2, l, m_l \,|V_{DD}|\, j_1', j_2', l', m_l\rangle &= \left\langle l, m_l \left| \frac{(1-3\cos^2\theta)}{4\pi\epsilon_0 r^3} \right| l', m_l \right\rangle \\ &\times \mu_1\mu_2\sqrt{(2j_1+1)\,(2j_1'+1)}\sqrt{(2j_2+1)\,(2j_2'+1)} \begin{pmatrix} j_1 & 1 & j_1' \\ 0 & 0 & 0 \end{pmatrix}^2 \begin{pmatrix} j_2 & 1 & j_2' \\ 0 & 0 & 0 \end{pmatrix}^2. \end{aligned} \tag{B.0.9}$$

We have separated the internal rotation of the molecules from the orbital moment l of the two molecules. However, this formalism is not adapted for molecules in a presence of an external static electric field. The stark effect mixes the different rotational states. So, we can define the dressed rotational states as $\left|\tilde{j}_\tau\right\rangle = \sum_n b_{j_\tau} |j_\tau\rangle$. Finally, the matrix elements of the dipole-dipole interaction in the dressed molecule-molecule basis are given by:

$$\begin{aligned}\langle \tilde{j}_1, \tilde{j}_2, l, m_l \,|V_{DD}|\, \tilde{j}_1', \tilde{j}_2', l', m_l\rangle &= \left\langle l, m_l \left| \frac{(1-3\cos^2\theta)}{4\pi\epsilon_0 r^3} \right| l', m_l \right\rangle \\ &\times \sum_{j_1}\sum_{j_2}\sum_{j_1'}\sum_{j_2'} b_{j_1} b_{j_2} b_{j_1'} b_{j_2'} \mu_1\mu_2\sqrt{(2j_1+1)\,(2j_1'+1)} \\ &\times \sqrt{(2j_2+1)\,(2j_2'+1)} \begin{pmatrix} j_1 & 1 & j_1' \\ 0 & 0 & 0 \end{pmatrix}^2 \begin{pmatrix} j_2 & 1 & j_2' \\ 0 & 0 & 0 \end{pmatrix}^2 \end{aligned} \tag{B.0.10}$$

and then:

$$\left\langle \tilde{j}_1, \tilde{j}_2, l, m_l \left| V_{DD} \right| \tilde{j}'_1, \tilde{j}'_2, l', m_l \right\rangle = \left\langle l, m_l \left| \frac{(1 - 3\cos^2\theta)}{4\pi\epsilon_0 r^3} \right| l', m_l \right\rangle \times \sum_{j_1} \sum_{j'_1} b_{j_1} b_{j'_1} \mu_1 \sqrt{(2j_1+1)(2j'_1+1)} \begin{pmatrix} j_1 & 1 & j'_1 \\ 0 & 0 & 0 \end{pmatrix}^2 \times \sum_{j_2} \sum_{j'_2} b_{j_2} b_{j'_2} \mu_2 \sqrt{(2j_2+1)(2j'_2+1)} \begin{pmatrix} j_2 & 1 & j'_2 \\ 0 & 0 & 0 \end{pmatrix}^2 . \quad \text{(B.0.11)}$$

One can define a generalized induced dipole moment [214] between a dressed rotation state $\tilde{j}$ and $\tilde{j}'$ as:

$$d^{\tilde{j} \to j'} = \mu \sum_{j} \sum_{j'} b_j^* b_{j'} \sqrt{(2j+1)(2j'+1)} \begin{pmatrix} j & 1 & j' \\ 0 & 0 & 0 \end{pmatrix}^2 \quad \text{(B.0.12)}$$

and express Eq. B.0.11 as:

$$\left\langle \tilde{j}_1, \tilde{j}_2, l, m_l \left| V_{DD} \right| \tilde{j}'_1, \tilde{j}'_2, l', m_l \right\rangle = \left\langle l, m_l \left| \frac{d^{\tilde{j}_1 \to \tilde{j}'_1} d^{\tilde{j}_2 \to \tilde{j}'_2}}{4\pi\epsilon_0 r^3} \left(1 - 3\cos^2\theta\right) \right| l', m_l \right\rangle . \quad \text{(B.0.13)}$$

This comes back to take an effective classical dipole-dipole interaction

$$\frac{d^{\tilde{j}_1 \to \tilde{j}'_1} d^{\tilde{j}_2 \to \tilde{j}'_2}}{4\pi\epsilon_0 r^3} \left(1 - 3\cos^2\theta\right) \quad \text{(B.0.14)}$$

but with generalized induced dipole moments, including transition dipole moments responsible for inelastic transitions between rotational states.

Appendix C

Loss rate equations

The evolution of the average number of molecules in a gas follows the rate equation [291]:

$$\frac{dn}{dt} = -\beta^{3B} n^3 - \beta^{2B} n^2 - \beta^{1B} n \tag{C.0.1}$$

where β^{3B}, β^{2B} and β^{1B} corresponds respectively to the three-body, two-body and one-body loss rate coefficients.

C.1 Two-body loss rates

In this section, we focus on the two-body collision rate equation:

$$\frac{dn}{dt} = -\beta^{2B} n^2 \tag{C.1.1}$$

whose solutions are given by:

$$n(t) = \frac{n_0}{1 + n_0\,\beta^{2B}\,t} = \frac{n_0}{1 + \frac{t}{\tau_{2B}}} \tag{C.1.2}$$

with n_0 the initial number of molecules. We can then extract the characteristic time between two events of two-body collisions:

$$\tau_{2B} = \frac{1}{n_0\,\beta^{2B}}. \tag{C.1.3}$$

C.2 Three-body loss rates

In this section, we focus on the three-body collision rate equation:

$$\frac{dn}{dt} = -\beta^{3B} n^3 \tag{C.2.1}$$

whose solutions are given by:

$$n(t) = \frac{n_0}{\sqrt{1 + 2\,n_0^2\,\beta^{3B}\,t}} = \frac{n_0}{\sqrt{1 + \frac{t}{\tau_{3B}}}} \tag{C.2.2}$$

We can then extract the characteristic time between two events of three-body collisions:

$$\tau_{3B} = \frac{1}{2n_0^2\,\beta^{3B}}. \tag{C.2.3}$$

Appendix D

Simple continuum states Li_2

j	v	Energy (K)
0	0	-434,194
2	0	-431,893
4	0	-426,532
6	0	-418,130
8	0	-406,718
10	0	-392,339
12	0	-375,046
14	0	-354,906
0	1	-349,821
2	1	-347,681
4	1	-342,698
6	1	-334,891
16	0	-331,998
8	1	-324,292
10	1	-310,947
18	0	-306,413
12	1	-294,911
20	0	-278,259
14	1	-276,255
0	2	-274,927
2	2	-272,951
4	2	-268,348
6	2	-261,139
16	1	-255,063
8	2	-251,360
22	0	-247,658
10	2	-239,057
18	1	-231,433
12	2	-224,290
24	0	-214,749

j	v	Energy (K)
0	3	-209,203
2	3	-207,391
14	2	-207,134
20	1	-205,480
4	3	-203,173
6	3	-196,572
16	2	-187,680
8	3	-187,624
26	0	-179,691
22	1	-177,338
10	3	-176,381
18	2	-166,035
12	3	-162,908
0	4	-152,496
2	4	-150,853
14	3	-147,288
24	1	-147,159
4	4	-147,032
28	0	-142,665
20	2	-142,324
6	4	-141,056
8	4	-132,968
16	3	-129,620
10	4	-122,823
22	2	-116,697
26	1	-115,120
12	4	-110,698
18	3	-110,026
0	5	-104,799
30	0	-103,877

j	v	Energy (K)
2	5	-103,335
4	5	-99,9298
14	4	-96,6858
6	5	-94,6144
24	2	-89,3275
20	3	-88,6510
8	5	-87,4357
28	1	-81,4268
16	4	-80,9037
10	5	-78,4608
12	5	-67,7785
0	6	-66,2020
22	3	-65,6705
2	6	-64,9295
32	0	-63,5680
18	4	-63,4966
4	6	-61,9750
26	2	-60,4241
6	6	-57,3743
14	5	-55,5040
8	6	-51,1859
30	1	-46,3223
20	4	-44,6449
10	6	-43,4933
16	5	-41,7845
24	3	-41,2997
0	7	-36,8163
2	7	-35,7559
12	6	-34,4109
4	7	-33,3003

j	v	Energy (K)
28	2	-30,2395
6	7	-29,4962
18	5	-26,8108
22	4	-24,5779
8	7	-24,4205
14	6	-24,0927
34	0	-22,0180
10	7	-18,1873
0	8	-16,6046
26	3	-15,8104
2	8	-15,7822
4	8	-13,8893
16	6	-12,7484
6	8	-10,9917
12	7	-10,9612
20	5	-10,8378
32	1	-10,0995
8	8	-7,20402
0	9	-5,06478
2	9	-4,51313
24	4	-3,60018
4	9	-3,26695
14	7	-2,98528
10	8	-2,71272
6	9	-1,43702
18	6	-0,67973
0	10	-0,59317
2	10	-0,33494

Table D.1: The 118 simple continuum states for the Li+Li_2 system.

Bibliography

[1] H. J. Metcalf and P. van der Straten, *«Laser Cooling and Trapping»*, Springer-Verlag, 1999.

[2] C. E. Wieman, D. E. Pritchard, and D. J. Wineland, *Atom cooling, trapping, and quantum manipulation*, Rev. Mod. Phys. **71**, S253 (1999).

[3] S. Chu, *Cold atoms and quantum control*, Nature **416**, 206 (2002).

[4] C. N. Cohen-Tannoudji, *Nobel Lecture: Manipulating atoms with photons*, Rev. Mod. Phys. **70**, 707 (1998).

[5] S. Chu, *Nobel Lecture: The manipulation of neutral particles*, Rev. Mod. Phys. **70**, 685 (1998).

[6] W. D. Phillips, *Nobel Lecture: Laser cooling and trapping of neutral atoms*, Rev. Mod. Phys. **70**, 721 (1998).

[7] W. Ketterle and N. Van Druten, *Evaporative cooling of trapped atoms*, Adv. At. Mol. Opt. **37**, 181 (1996).

[8] E. A. Cornell and C. E. Wieman, *Nobel Lecture: Bose-Einstein condensation in a dilute gas, the first 70 years and some recent experiments*, Rev. Mod. Phys. **74**, 875 (2002).

[9] W. Ketterle, *Nobel lecture: When atoms behave as waves: Bose-Einstein condensation and the atom laser*, Rev. Mod. Phys. **74**, 1131 (2002).

[10] B. DeMarco and D. S. Jin, *Onset of Fermi Degeneracy in a Trapped Atomic Gas*, Science **285**, 1703 (1999).

[11] R. Stebbings, F. Dunning, F. W. Dunning, *et al.*, *«Rydberg states of atoms and molecules»*, Cambridge University Press, 1983.

[12] T. F. Gallagher, *«Rydberg Atoms»*, Cambridge University Press, 1994.

[13] J.-P. Connerade, *«Highly Excited Atoms»*, Cambridge University Press, 1998.

[14] T. F. Gallagher and P. Pillet, *Dipole–Dipole interactions of Rydberg atoms*, Adv. At. Mol. **56**, 161 (2008).

[15] D. Comparat and P. Pillet, *Dipole blockade in a cold Rydberg atomic sample*, JOSA B **27**, A208 (2010).

[16] M. Saffman, T. G. Walker, and K. Mølmer, *Quantum information with Rydberg atoms*, Rev. Mod. Phys. **82**, 2313 (2010).

[17] R. Löw, H. Weimer, J. Nipper, J. B. Balewski, B. Butscher, H. P. Büchler, and T. Pfau, *An experimental and theoretical guide to strongly interacting Rydberg gases*, J. Phys. B **45**, 113001 (2012).

[18] A. Browaeys, D. Barredo, and T. Lahaye, *Experimental investigations of dipole–dipole interactions between a few Rydberg atoms*, J. Phys. B **49**, 152001 (2016).

[19] C. H. Greene, A. Dickinson, and H. Sadeghpour, *Creation of polar and nonpolar ultra-long-range Rydberg molecules*, Phys. Rev. Lett. **85**, 2458 (2000).

[20] V. Bendkowsky, B. Butscher, J. Nipper, J. P. Shaffer, R. Löw, and T. Pfau, *Observation of ultralong-range Rydberg molecules*, Nature **458**, 1005 (2009).

[21] W. Li, T. Pohl, J. Rost, S. T. Rittenhouse, H. Sadeghpour, J. Nipper, B. Butscher, J. Balewski, V. Bendkowsky, R. Löw, *et al.*, *A homonuclear molecule with a permanent electric dipole moment*, Science **334**, 1110 (2011).

[22] D. Booth, S. Rittenhouse, J. Yang, H. Sadeghpour, and J. Shaffer, *Production of trilobite Rydberg molecule dimers with kilo-Debye permanent electric dipole moments*, Science **348**, 99 (2015).

[23] T. Niederprüm, O. Thomas, T. Eichert, C. Lippe, J. Pérez-Ríos, C. H. Greene, and H. Ott, *Observation of pendular butterfly Rydberg molecules*, Nat. Commun. **7**, 1 (2016).

[24] C. Lippe, T. Eichert, O. Thomas, T. Niederprüm, and H. Ott, *Excitation of Rydberg Molecules in Ultracold Quantum Gases*, Phys. Status Solidi B **256**, 1800654 (2019).

[25] S. Willitsch, M. T. Bell, A. D. Gingell, and T. P. Softley, *Chemical applications of laser-and sympathetically-cooled ions in ion traps*, Phys. Chem. Chem. Phys. **10**, 7200 (2008).

[26] Z. Idziaszek, T. Calarco, P. S. Julienne, and A. Simoni, *Quantum theory of ultracold atom-ion collisions*, Phys. Rev. A **79**, 010702 (2009).

[27] S. Willitsch, *Very cool molecular ions*, Nat. Phys. **6**, 240 (2010).

[28] P. F. Staanum, K. Højbjerre, P. S. Skyt, A. K. Hansen, and M. Drewsen, *Rotational laser cooling of vibrationally and translationally cold molecular ions*, Nat. Phys. **6**, 271 (2010).

[29] T. Schneider, B. Roth, H. Duncker, I. Ernsting, and S. Schiller, *All-optical preparation of molecular ions in the rovibrational ground state*, Nat. Phys. **6**, 275 (2010).

[30] S. Willitsch, *Coulomb-crystallised molecular ions in traps: methods, applications, prospects*, Int. Rev. Phys. Chem. **31**, 175 (2012).

[31] A. Härter and J. Hecker Denschlag, *Cold atom–ion experiments in hybrid traps*, Contemp. Phys. **55**, 33 (2014).

[32] P. Eberle, A. D. Dörfler, C. Von Planta, K. Ravi, D. Haas, D. Zhang, S. Willitsch, and S. Y. T. Van de Meerakker, *Ion-Atom and Ion-Molecule Hybrid Systems: Ion-Neutral Chemistry at Ultralow Energies*, J. Phys. Conf. Ser. (Online) **635**, 7 (2015).

[33] R. Côté, *Ultracold Hybrid Atom–Ion Systems*, Adv. At. Mol. **65**, 67 (2016).

[34] M. Tomza, K. Jachymski, R. Gerritsma, A. Negretti, T. Calarco, Z. Idziaszek, and P. S. Julienne, *Cold hybrid ion-atom systems*, Rev. Mod. Phys. **91**, 035001 (2019).

[35] D. Zhang and S. Willitsch, *«Cold Ion Chemistry », Chapter 12 in «Cold Chemistry : Molecular Scattering and Reactivity Near Absolute Zero»*, Edited by O. Dulieu and A. Osterwalder, The Royal Society of Chemistry, 2018.

[36] K.-K. Ni, S. Ospelkaus, M. H. G. de Miranda, A. Peter, B. Neyenhuis, J. J. Zirbel, S. Kotochigova, P. S. Julienne, D. S. Jin, and J. Ye, *A High Phase-Space-Density Gas of Polar Molecules*, Science **322**, 231 (2008).

[37] G. Quéméner and P. S. Julienne, *Ultracold molecules under control!*, Chem. Rev. **112**, 4949 (2012).

[38] S. Ospelkaus, A. Pe'er, K.-K. Ni, J. Zirbel, B. Neyenhuis, S. Kotochigova, P. Julienne, J. Ye, and D. Jin, *Efficient state transfer in an ultracold dense gas of heteronuclear molecules*, Nat. Phys. **4**, 622 (2008).

[39] J. G. Danzl, E. Haller, M. Gustavsson, M. J. Mark, R. Hart, N. Bouloufa, O. Dulieu, H. Ritsch, and H.-C. Nägerl, *Quantum gas of deeply bound ground state molecules*, Science **321**, 1062 (2008).

[40] T. Takekoshi, L. Reichsöllner, A. Schindewolf, J. M. Hutson, C. R. Le Sueur, O. Dulieu, F. Ferlaino, R. Grimm, and H.-C. Nägerl, *Ultracold dense samples of dipolar RbCs molecules in the rovibrational and hyperfine ground state*, Phys. Rev. Lett. **113**, 205301 (2014).

[41] J. W. Park, S. A. Will, and M. W. Zwierlein, *Ultracold dipolar gas of fermionic* ^{23}Na^{39}K *molecules in their absolute ground state*, Phys. Rev. Lett. **114**, 205302 (2015).

[42] M. Guo, B. Zhu, B. Lu, X. Ye, F. Wang, R. Vexiau, N. Bouloufa-Maafa, G. Quéméner, O. Dulieu, and D. Wang, *Creation of an ultracold gas of ground-state dipolar* ^{23}Na^{87}Rb *molecules*, Phys. Rev. Lett. **116**, 205303 (2016).

[43] P. K. Molony, P. D. Gregory, Z. Ji, B. Lu, M. P. Köppinger, C. R. Le Sueur, C. L. Blackley, J. M. Hutson, and S. L. Cornish, *Creation of ultracold* ^{87}Rb^{133}Cs *molecules in the rovibrational ground state*, Phys. Rev. Lett. **113**, 255301 (2014).

[44] K. K. Voges, P. Gersema, M. Meyer zum Alten Borgloh, T. A. Schulze, T. Hartmann, A. Zenesini, and S. Ospelkaus, *Ultracold Gas of Bosonic* ^{23}Na^{39}K *Ground-State Molecules*, Phys. Rev. Lett. **125**, 083401 (2020).

[45] R. Bause, A. Schindewolf, R. Tao, M. Duda, X.-Y. Chen, G. Quéméner, T. Karman, A. Christianen, I. Bloch, and X.-Y. Luo, *Collisions of ultracold molecules in bright and dark optical dipole traps*, Phys. Rev. Research **3**, 033013 (2021).

[46] M. Viteau, A. Chotia, M. Allegrini, N. Bouloufa, O. Dulieu, D. Comparat, and P. Pillet, *Optical Pumping and Vibrational Cooling of Molecules*, Science **321**, 232 (2008).

[47] A. S. Coolidge, H. M. James, and R. D. Present, *A study of the Franck-Condon principle*, J. Chem. Phys. **4**, 193 (1936).

[48] N. R. Hutzler, H.-I. Lu, and J. M. Doyle, *The buffer gas beam: An intense, cold, and slow source for atoms and molecules*, Chem. Rev. **112**, 4803 (2012).

[49] H. L. Bethlem, M. R. Tarbutt, J. Küpper, D. Carty, K. Wohlfart, E. Hinds, and G. Meijer, *Alternating gradient focusing and deceleration of polar molecules*, J. Phys. B **39**, R263 (2006).

[50] S. Y. Van De Meerakker, H. L. Bethlem, and G. Meijer, *Taming molecular beams*, Nat. Phys. **4**, 595 (2008).

[51] S. Y. van de Meerakker, H. L. Bethlem, N. Vanhaecke, and G. Meijer, *Manipulation and control of molecular beams*, Chem. Rev. **112**, 4828 (2012).

[52] E. Narevicius and M. G. Raizen, *Toward cold chemistry with magnetically decelerated supersonic beams*, Chem. Rev. **112**, 4879 (2012).

[53] T. Köhler, K. Góral, and P. S. Julienne, *Production of cold molecules via magnetically tunable Feshbach resonances*, Rev. Mod. Phys. **78**, 1311 (2006).

[54] C. Chin, R. Grimm, P. Julienne, and E. Tiesinga, *Feshbach resonances in ultracold gases*, Rev. Mod. Phys. **82**, 1225 (2010).

[55] P. S. Żuchowski, J. Aldegunde, and J. M. Hutson, *Ultracold RbSr Molecules Can Be Formed by Magnetoassociation*, Phys. Rev. Lett. **105**, 153201 (2010).

[56] A. Fioretti, D. Comparat, A. Crubellier, O. Dulieu, F. Masnou-Seeuws, and P. Pillet, *Formation of Cold* Cs_2 *Molecules through Photoassociation*, Phys. Rev. Lett. **80**, 4402 (1998).

[57] H. R. Thorsheim, J. Weiner, and P. S. Julienne, *Laser-induced photoassociation of ultracold sodium atoms*, Phys. Rev. Lett. **58**, 2420 (1987).

[58] J. Weiner, V. S. Bagnato, S. Zilio, and P. S. Julienne, *Experiments and theory in cold and ultracold collisions*, Rev. Mod. Phys. **71**, 1 (1999).

[59] K. M. Jones, E. Tiesinga, P. D. Lett, and P. S. Julienne, *Ultracold photoassociation spectroscopy: Long-range molecules and atomic scattering*, Rev. Mod. Phys. **78**, 483 (2006).

[60] M. Zeppenfeld, B. G. Englert, R. Glöckner, A. Prehn, M. Mielenz, C. Sommer, L. D. van Buuren, M. Motsch, and G. Rempe, *Sisyphus cooling of electrically trapped polyatomic molecules*, Nature **491**, 570 (2012).

[61] D. Comparat, *Molecular cooling via Sisyphus processes*, Phys. Rev. A **89**, 043410 (2014).

[62] I. Kozyryev, L. Baum, K. Matsuda, B. L. Augenbraun, L. Anderegg, A. P. Sedlack, and J. M. Doyle, *Sisyphus laser cooling of a polyatomic molecule*, Phys. Rev. Lett. **118**, 173201 (2017).

[63] M. Zeppenfeld, M. Motsch, P. W. Pinkse, and G. Rempe, *Optoelectrical cooling of polar molecules*, Phys. Rev. A **80**, 041401 (2009).

[64] A. Prehn, M. Ibrügger, R. Glöckner, G. Rempe, and M. Zeppenfeld, *Optoelectrical cooling of polar molecules to submillikelvin temperatures*, Phys. Rev. Lett. **116**, 063005 (2016).

[65] E. S. Shuman, J. F. Barry, and D. DeMille, *Laser cooling of a diatomic molecule*, Nature **467**, 820 (2010).

[66] J. Barry, D. McCarron, E. Norrgard, M. Steinecker, and D. DeMille, *Magneto-optical trapping of a diatomic molecule*, Nature **512**, 286 (2014).

[67] L. Anderegg, B. L. Augenbraun, Y. Bao, S. Burchesky, L. W. Cheuk, W. Ketterle, and J. M. Doyle, *Laser cooling of optically trapped molecules*, Nat. Phys. **14**, 890 (2018).

[68] N. Schlosser, G. Reymond, I. Protsenko, and P. Grangier, *Sub-poissonian loading of single atoms in a microscopic dipole trap*, Nature **411**, 1024 (2001).

[69] A. Browaeys, D. Barredo, and T. Lahaye, *Experimental investigations of dipole–dipole interactions between a few Rydberg atoms*, J. Phys. B **49**, 152001 (2016).

[70] M. Olshanii, *Atomic scattering in the presence of an external confinement and a gas of impenetrable bosons*, Phys. Rev. Lett. **81**, 938 (1998).

[71] D. Petrov and G. Shlyapnikov, *Interatomic collisions in a tightly confined Bose gas*, Phys. Rev. A **64**, 012706 (2001).

[72] I. Bloch, J. Dalibard, and W. Zwerger, *Many-body physics with ultracold gases*, Rev. Mod. Phys. **80**, 885 (2008).

[73] J. D. Weinstein, R. DeCarvalho, T. Guillet, B. Friedrich, and J. M. Doyle, *Magnetic trapping of calcium monohydride molecules at millikelvin temperatures*, Nature **395**, 148 (1998).

[74] J. van Veldhoven, H. L. Bethlem, and G. Meijer, *AC electric trap for ground-state molecules*, Phys. Rev. Lett. **94**, 083001 (2005).

[75] L. Baum, N. B. Vilas, C. Hallas, B. L. Augenbraun, S. Raval, D. Mitra, and J. M. Doyle, *1D magneto-optical trap of polyatomic molecules*, Phys. Rev. Lett. **124**, 133201 (2020).

[76] B. G. Englert, M. Mielenz, C. Sommer, J. Bayerl, M. Motsch, P. W. Pinkse, G. Rempe, and M. Zeppenfeld, *Storage and adiabatic cooling of polar molecules in a microstructured trap*, Phys. Rev. Lett. **107**, 263003 (2011).

[77] B. C. Sawyer, B. L. Lev, E. R. Hudson, B. K. Stuhl, M. Lara, J. L. Bohn, and J. Ye, *Magnetoelectrostatic trapping of ground state OH molecules*, Phys. Rev. Lett. **98**, 253002 (2007).

[78] S. Ospelkaus, K.-K. Ni, D. Wang, M. H. G. de Miranda, B. Neyenhuis, G. Quéméner, P. S. Julienne, J. L. Bohn, D. S. Jin, and J. Ye, *Quantum-State Controlled Chemical Reactions of Ultracold Potassium-Rubidium Molecules*, Science **327**, 853 (2010).

[79] P. S. Żuchowski and J. M. Hutson, *Reactions of ultracold alkali-metal dimers*, Phys. Rev. A **81**, 060703 (2010).

[80] J. N. Byrd, J. A. Montgomery Jr, and R. Côté, *Structure and thermochemistry of K_2Rb, KRb_2, and K_2Rb_2*, Phys. Rev. A **82**, 010502 (2010).

[81] E. R. Meyer and J. L. Bohn, *Product-state control of bi-alkali-metal chemical reactions*, Phys. Rev. A **82**, 042707 (2010).

[82] A. Chotia, B. Neyenhuis, S. A. Moses, B. Yan, J. P. Covey, M. Foss-Feig, A. M. Rey, D. S. Jin, and J. Ye, *Long-lived dipolar molecules and Feshbach molecules in a 3D optical lattice*, Phys. Rev. Lett. **108**, 080405 (2012).

[83] J. W. Park, Z. Z. Yan, H. Loh, S. A. Will, and M. W. Zwierlein, *Second-scale nuclear spin coherence time of ultracold $^{23}Na^{40}K$ molecules*, Science **357**, 372 (2017).

[84] M. Guo, X. Ye, J. He, G. Quéméner, and D. Wang, *High-resolution internal state control of ultracold $^{23}Na^{87}Rb$ molecules*, Phys. Rev. A **97**, 020501 (2018).

[85] T. M. Rvachov, H. Son, A. T. Sommer, S. Ebadi, J. J. Park, M. W. Zwierlein, W. Ketterle, and A. O. Jamison, *Long-lived ultracold molecules with electric and magnetic dipole moments*, Phys. Rev. Lett. **119**, 143001 (2017).

[86] M. Mayle, B. P. Ruzic, and J. L. Bohn, *Statistical aspects of ultracold resonant scattering*, Phys. Rev. A **85**, 062712 (2012).

[87] M. Mayle, G. Quéméner, B. P. Ruzic, and J. L. Bohn, *Scattering of ultracold molecules in the highly resonant regime*, Phys. Rev. A **87**, 012709 (2013).

[88] Y. Liu, M.-G. Hu, M. A. Nichols, D. D. Grimes, T. Karman, H. Guo, and K.-K. Ni, *Photo-excitation of long-lived transient intermediates in ultracold reactions*, Nat. Phys. **16**, 1132 (2020).

[89] P. D. Gregory, J. A. Blackmore, S. L. Bromley, and S. L. Cornish, *Loss of Ultracold* ^{87}Rb^{133}Cs *Molecules via Optical Excitation of Long-Lived Two-Body Collision Complexes*, Phys. Rev. Lett. **124**, 163402 (2020).

[90] A. Christianen, M. W. Zwierlein, G. C. Groenenboom, and T. Karman, *Trapping laser excitation during collisions limits the lifetime of ultracold molecules*, Phys. Rev. Lett. **123**, 12 (2019).

[91] A. Christianen, T. Karman, and G. C. Groenenboom, *Quasiclassical method for calculating the density of states of ultracold collision complexes*, Phys. Rev. A **100**, 032708 (2019).

[92] G. Quéméner and J. L. Bohn, *Electric field suppression of ultracold confined chemical reactions*, Phys. Rev. A **81**, 060701 (2010).

[93] A. Micheli, Z. Idziaszek, G. Pupillo, M. A. Baranov, P. Zoller, and P. S. Julienne, *Universal Rates for Reactive Ultracold Polar Molecules in Reduced Dimensions*, Phys. Rev. Lett. **105**, 073202 (2010).

[94] M. H. G. de Miranda, A. Chotia, B. Neyenhuis, D. Wang, G. Quéméner, S. Ospelkaus, J. L. Bohn, J. Ye, and D. S. Jin, *Controlling the quantum stereodynamics of ultracold bimolecular reactions*, Nat. Phys. **7** (2011).

[95] G. Quéméner and J. L. Bohn, *Dynamics of ultracold molecules in confined geometry and electric field*, Phys. Rev. A **83**, 012705 (2011).

[96] A. V. Avdeenkov, M. Kajita, and J. L. Bohn, *Suppression of inelastic collisions of polar* $^1\Sigma$ *state molecules in an electrostatic field*, Phys. Rev. A **73**, 022707 (2006).

[97] G. Wang and G. Quéméner, *Tuning ultracold collisions of excited rotational dipolar molecules*, New J. Phys. **17**, 035015 (2015).

[98] M. L. González-Martínez, J. L. Bohn, and G. Quéméner, *Adimensional theory of shielding in ultracold collisions of dipolar rotors*, Phys. Rev. A **96**, 032718 (2017).

[99] K. Matsuda, L. De Marco, J.-R. Li, W. G. Tobias, G. Valtolina, G. Quéméner, and J. Ye, *Resonant collisional shielding of reactive molecules using electric fields*, Science **370**, 1324 (2020).

[100] J.-R. Li, W. G. Tobias, K. Matsuda, C. Miller, G. Valtolina, L. De Marco, R. R. Wang, L. Lassablière, G. Quéméner, J. L. Bohn, *et al.*, *Tuning of dipolar interactions and evaporative cooling in a three-dimensional molecular quantum gas*, Nature Physics **17**, 1144 (2021).

[101] A. Micheli, G. Pupillo, H. Büchler, and P. Zoller, *Cold polar molecules in two-dimensional traps: Tailoring interactions with external fields for novel quantum phases*, Phys. Rev. A **76**, 043604 (2007).

[102] A. V. Gorshkov, P. Rabl, G. Pupillo, A. Micheli, P. Zoller, M. D. Lukin, and H. P. Büchler, *Suppression of Inelastic Collisions Between Polar Molecules With a Repulsive Shield*, Phys. Rev. Lett. **101**, 073201 (2008).

[103] L. Lassablière and G. Quéméner, *Controlling the Scattering Length of Ultracold Dipolar Molecules*, Phys. Rev. Lett. **121**, 163402 (2018).

[104] T. Karman and J. M. Hutson, *Microwave Shielding of Ultracold Polar Molecules*, Phys. Rev. Lett. **121**, 163401 (2018).

[105] T. Karman and J. M. Hutson, *Microwave shielding of ultracold polar molecules with imperfectly circular polarization*, Phys. Rev. A **100**, 052704 (2019).

[106] T. Karman, *Microwave shielding with far-from-circular polarization*, Phys. Rev. A **101**, 042702 (2020).

[107] L. Anderegg, S. Burchesky, Y. Bao, S. S. Yu, T. Karman, E. Chae, K.-K. Ni, W. Ketterle, and J. M. Doyle, *Observation of microwave shielding of ultracold molecules*, Science **373** (2021).

[108] T. Xie, M. Lepers, R. Vexiau, A. Orbán, O. Dulieu, and N. Bouloufa-Maafa, *Optical Shielding of Destructive Chemical Reactions between Ultracold Ground-State NaRb Molecules*, Phys. Rev. Lett. **125**, 153202 (2020).

[109] L. De Marco, G. Valtolina, K. Matsuda, W. G. Tobias, J. P. Covey, and J. Ye, *A degenerate Fermi gas of polar molecules*, Science **363**, 853 (2019).

[110] A. Micheli, G. Brennen, and P. Zoller, *A toolbox for lattice-spin models with polar molecules*, Nat. Phys. **2**, 341 (2006).

[111] R. Barnett, D. Petrov, M. Lukin, and E. Demler, *Quantum magnetism with multicomponent dipolar molecules in an optical lattice*, Phys. Rev. Lett. **96**, 190401 (2006).

[112] H. P. Büchler, E. Demler, M. Lukin, A. Micheli, N. Prokof'ev, G. Pupillo, and P. Zoller, *Strongly correlated 2D quantum phases with cold polar molecules: Controlling the shape of the interaction potential*, Phys. Rev. Lett. **98**, 060404 (2007).

[113] H. Büchler, A. Micheli, and P. Zoller, *Three-body interactions with cold polar molecules*, Nat. Phys. **3**, 726 (2007).

[114] G. Pupillo, A. Micheli, H.-P. Büchler, and P. Zoller, *«Condensed matter physics with cold polar molecules», Chapter 10 in «Cold Molecules: Theory, Experiment, Applications»*, Edited by R. Krems, B. Friedrich, W. C. Stwalley, CRC Press, 2009.

[115] A. V. Gorshkov, S. R. Manmana, G. Chen, J. Ye, E. Demler, M. D. Lukin, and A. M. Rey, *Tunable superfluidity and quantum magnetism with ultracold polar molecules*, Phys. Rev. Lett. **107**, 115301 (2011).

[116] A. V. Gorshkov, S. R. Manmana, G. Chen, E. Demler, M. D. Lukin, and A. M. Rey, *Quantum magnetism with polar alkali-metal dimers*, Phys. Rev. A **84**, 033619 (2011).

[117] D. DeMille, *Quantum computation with trapped polar molecules*, Phys. Rev. Lett. **88**, 067901 (2002).

[118] S. Yelin, K. Kirby, and R. Côté, *Schemes for robust quantum computation with polar molecules*, Phys. Rev. A **74**, 050301 (2006).

[119] S. F. Yelin, D. DeMille, and R. Côté, *«Quantum information Process with ultracold polar molecules», Chapter 17 in «Cold Molecules: Theory, Experiment, Applications»*, Edited by R. Krems, B. Friedrich, W. C. Stwalley, CRC Press, 2009.

[120] P. Pellegrini and M. Desouter-Lecomte, *Quantum gates driven by microwave pulses in hyperfine levels of ultracold heteronuclear dimers*, Eur. Phys. J. D **64**, 163 (2011).

[121] M. Ortner, Y. Zhou, P. Rabl, and P. Zoller, *Quantum information Process in self-assembled crystals of cold polar molecules*, Quantum Inf. Process. **10**, 793 (2011).

[122] E. Kuznetsova, S. F. Yelin, and R. Côté, *An atom–molecule platform for quantum computing*, Quantum Inf. Process. **10**, 821 (2011).

[123] M.-G. Hu, Y. Liu, D. Grimes, Y.-W. Lin, A. Gheorghe, R. Vexiau, N. Bouloufa-Maafa, O. Dulieu, T. Rosenband, and K. Ni, *Direct observation of bimolecular reactions of ultracold KRb molecules*, Science **366**, 1111 (2019).

[124] M.-G. Hu, Y. Liu, M. A. Nichols, L. Zhu, G. Quéméner, O. Dulieu, and K.-K. Ni, *Nuclear spin conservation enables state-to-state control of ultracold molecular reactions*, Nat. Chem. **13**, 435 (2021).

[125] Y. Liu, M.-G. Hu, M. A. Nichols, D. Yang, D. Xie, H. Guo, and K.-K. Ni, *Precision test of statistical dynamics with state-to-state ultracold chemistry*, Nature **593**, 379 (2021).

[126] R. V. Krems, *Cold controlled chemistry*, Phys. Chem. Chem. Phys. **10**, 4079 (2008).

[127] L. D. Carr, D. DeMille, R. V. Krems, and J. Ye, *Cold and ultracold molecules: science, technology and applications*, New J. Phys. **11**, 055049 (2009).

[128] D. Jin and J. Ye, *Polar molecules in the quantum regime*, Phys. Today **64**, 27 (2011).

[129] M. Kirste, X. Wang, H. C. Schewe, G. Meijer, K. Liu, A. van der Avoird, L. M. Janssen, K. B. Gubbels, G. C. Groenenboom, and S. Y. van de Meerakker, *Quantum-state resolved bimolecular collisions of velocity-controlled OH with NO radicals*, Science **338**, 1060 (2012).

[130] M. L. González-Martínez, O. Dulieu, P. Larrégaray, and L. Bonnet, *Statistical product distributions for ultracold reactions in external fields*, Phys. Rev. A **90**, 052716 (2014).

[131] B. Kendrick, J. Hazra, and N. Balakrishnan, *The geometric phase controls ultracold chemistry*, Nat. Commun. **6**, 1 (2015).

[132] L. Liu, J. Hood, Y. Yu, J. Zhang, N. Hutzler, T. Rosenband, and K.-K. Ni, *Building one molecule from a reservoir of two atoms*, Science **360**, 900 (2018).

[133] V. Flambaum and M. Kozlov, *Enhanced Sensitivity to the Time Variation of the Fine-Structure Constant and m_p/m_e in Diatomic Molecules*, Phys. Rev. Lett. **99**, 150801 (2007).

[134] T. Wall, *Preparation of cold molecules for high-precision measurements*, J. Phys. B **49**, 243001 (2016).

[135] A. Ceulemans, L. Chibotaru, and P. Fowler, *Molecular anapole moments*, Phys. Rev. Lett. **80**, 1861 (1998).

[136] J. Baron, W. C. Campbell, D. DeMille, J. M. Doyle, G. Gabrielse, Y. V. Gurevich, P. W. Hess, N. R. Hutzler, E. Kirilov, I. Kozyryev, *et al.*, *Order of magnitude smaller limit on the electric dipole moment of the electron*, Science **343**, 269 (2014).

[137] P. Aggarwal, H. L. Bethlem, A. Borschevsky, M. Denis, K. Esajas, P. A. Haase, Y. Hao, S. Hoekstra, K. Jungmann, T. B. Meijknecht, *et al.*, *Measuring the electric dipole moment of the electron in BaF*, Eur. Phys. J. D **72**, 1 (2018).

[138] D. DeMille, J. Doyle, and A. Sushkov, *Probing the frontiers of particle physics with tabletop-scale experiments*, Science **357**, 990 (2017).

[139] M. S. Safronova, D. Budker, D. DeMille, D. F. J. Kimball, A. Derevianko, and C. W. Clark, *Search for new physics with atoms and molecules*, Rev. Mod. Phys. **90**, 025008 (2018).

[140] K.-A. Suominen, M. J. Holland, K. Burnett, and P. Julienne, *Optical shielding of cold collisions*, Phys. Rev. A **51**, 1446 (1995).

[141] K.-A. Suominen, *Theories for cold atomic collisions in light fields*, J. Phys. B **29**, 5981 (1996).

[142] R. Napolitano, J. Weiner, and P. S. Julienne, *Theory of optical suppression of ultracold-collision rates by polarized light*, Phys. Rev. A **55**, 1191 (1997).

[143] L. Delves, *Tertiary and general-order collisions*, Nucl. Phys. **9**, 391 (1958).

[144] L. Delves, *Tertiary and general-order collisions (II)*, Nucl. Phys. **20**, 275 (1960).

[145] F. T. Smith, *Generalized Angular Momentum in Many-Body Collisions*, Phys. Rev. **120**, 1058 (1960).

[146] F. T. Smith, *A Symmetric Representation for Three-Body Problems. I. Motion in a Plane*, J. Math. Phys. **3**, 735 (1962).

[147] R. C. Whitten and F. T. Smith, *Symmetric Representation for Three-Body Problems. II. Motion in Space*, J. Math. Phys. **9**, 1103 (1968).

[148] B. R. Johnson, *On hyperspherical coordinates and mapping the internal configurations of a three body system*, J. Chem. Phys. **73**, 5051 (1980).

[149] G. C. Schatz and A. Kuppermann, *Quantum mechanical reactive scattering for three-dimensional atom plus diatom systems. I. Theory*, J. Chem. Phys. **65**, 4642 (1976).

[150] R. T. Pack and G. A. Parker, *Quantum reactive scattering in three dimensions using hyperspherical (APH) coordinates. Theory*, J. Chem. Phys. **87**, 3888 (1987).

[151] G. Quéméner, *Étude quantique de collisions moléculaires à ultra-basse énergie: applications aux alcalins et alcalino-terreux*, PhD thesis, Université Rennes 1, 2006.

[152] B. K. Kendrick, R. T. Pack, R. B. Walker, and E. F. Hayes, *Hyperspherical surface functions for nonzero total angular momentum. I. Eckart singularities*, J. Chem. Phys. **110**, 6673 (1999).

[153] G. Quéméner, *«Ultracold collisions of molcules », Chapter 12 in «Cold Chemistry : Molecular Scattering and Reactivity Near Absolute Zero»*, Edited by O. Dulieu and A. Osterwalder, The Royal Society of Chemistry, 2018.

[154] G. Quéméner, J.-M. Launay, and P. Honvault, *Ultracold collisions between Li atoms and Li_2 diatoms in high vibrational states*, Phys. Rev. A **75**, 050701 (2007).

[155] S. Ospelkaus, K.-K. Ni, D. Wang, M. H. G. de Miranda, B. Neyenhuis, G. Quéméner, P. S. Julienne, J. L. Bohn, D. S. Jin, and J. Ye, *Quantum-State Controlled Chemical Reactions of Ultracold Potassium-Rubidium Molecules*, Science **327**, 853 (2010).

[156] K.-K. Ni, S. Ospelkaus, D. Wang, G. Quéméner, B. Neyenhuis, M. H. G. de Miranda, J. L. Bohn, J. Ye, and D. S. Jin, *Dipolar collisions of polar molecules in the quantum regime*, Nature **464**, 1324 (2010).

[157] X. Ye, M. Guo, M. L. González-Martínez, G. Quéméner, and D. Wang, *Collisions of ultracold ^{23}Na^{87}Rb molecules with controlled chemical reactivities*, Sci. Adv. **4**, eaaq0083 (2018).

[158] M. Guo, X. Ye, J. He, M. L. González-Martínez, R. Vexiau, G. Quéméner, and D. Wang, *Dipolar Collisions of Ultracold Ground-State Bosonic Molecules*, Phys. Rev. X **8**, 041044 (2018).

[159] J. F. E. Croft, J. L. Bohn, and G. Quéméner, *Unified model of ultracold molecular collisions*, Phys. Rev. A **102**, 033306 (2020).

[160] M. Born and R. Oppenheimer, *Zur quantentheorie der molekeln*, Ann. Phys. (Berlin) **389**, 457 (1927).

[161] N. R. Kestner, *The Theory of Intermolecular Forces*, J. Am. Chem. Soc. **119**, 8584 (1997).

[162] B. Johnson, *The multichannel log-derivative method for scattering calculations*, J. Comput. Phys. **13**, 445 (1973).

[163] R. de Vogelaere, *A method for the numerical integration of differential equations of second order without explicit first derivatives*, J. Res. Nat. Bur. Standards **54** (1955).

[164] W. A. Lester, *De Vogelaere's Method for the Numerical Integration of Second-Order Differential Equations without Explicit First Derivatives: Application to Coupled Equations Arising from the Schrödinger Equation*, J. Comput. Phys. **3**, 322–326 (1968).

[165] F. Mrugal/a and D. Secrest, *The generalized log-derivative method for inelastic and reactive collisions*, J. Chem. Phys. **78**, 5954 (1983).

[166] J. C. Light and R. B. Walker, *An R matrix approach to the solution of coupled equations for atom–molecule reactive scattering*, J. Chem. Phys. **65**, 4272 (1976).

[167] G. A. Parker, T. G. Schmalz, and J. C. Light, *A variable interval variable step method for the solution of linear second order coupled differential equations*, J. Chem. Phys. **73**, 1757 (1980).

[168] G. A. Parker, J. C. Light, and B. Johnson, *The logarithmic derivative-variable interval variable step hybrid method for the solution of coupled linear second-order differential equations*, Chem. Phys. Lett. **73**, 572 (1980).

[169] D. Yang, J. Zuo, J. Huang, X. Hu, R. Dawes, D. Xie, and H. Guo, *A Global Full-Dimensional Potential Energy Surface for the K_2Rb_2 Complex and Its Lifetime*, J. Phys. Chem. Lett. **11**, 2605 (2020).

[170] M. Abramowitz and I. A. Stegun, *«Handbook of Mathematical Functions with Formulas, Graphs, and Mathematical Tables»*, Dover, 1964.

[171] T. V. Tscherbul, Y. V. Suleimanov, V. Aquilanti, and R. V. Krems, *Magnetic field modification of ultracold molecule–molecule collisions*, New J. Phys. **11**, 055021 (2009).

[172] H. A. Bethe, *Theory of Disintegration of Nuclei by Neutrons*, Phys. Rev. **47**, 747 (1935).

[173] E. P. Wigner, *On the Behavior of Cross Sections Near Thresholds*, Phys. Rev. **73**, 1002 (1948).

[174] F. Dalfovo, S. Giorgini, L. P. Pitaevskii, and S. Stringari, *Theory of Bose-Einstein condensation in trapped gases*, Rev. Mod. Phys. **71**, 463 (1999).

[175] A. J. Leggett, *Bose-Einstein condensation in the alkali gases: Some fundamental concepts*, Rev. Mod. Phys. **73**, 307 (2001).

[176] D. DeMille, D. R. Glenn, and J. Petricka, *Microwave traps for cold polar molecules*, Eur. Phys. J. D **31**, 375 (2004).

[177] S. V. Alyabyshev and R. V. Krems, *Controlling collisional spin relaxation of cold molecules with microwave laser fields*, Phys. Rev. A **80**, 033419 (2009).

[178] J. H. Shirley, *Solution of the Schrödinger equation with a Hamiltonian periodic in time*, Phys. Rev. **138**, B979 (1965).

[179] G. Floquet, *Sur les équations différentielles linéaires à coefficients périodiques*, Ann. Sci. Éc. Norm. Supér. **12** (1883).

[180] O. Atabek, R. Lefebvre, and T. Nguyen-Dang, *Theory of intense laser-induced molecular dissociation: From simulation to control*, Handb. Numer. Anal. **10**, 745 (2003).

[181] M. Kuhlmann and M. Stöckler, *«Quantum Field Theory»*, Springer International Publishing, 2018.

[182] R. Zare and V. Kleiman, *«Angular Momentum: Understanding Spatial Aspects in Chemistry and Physics»*, Wiley, 1988.

[183] R. Vexiau, M. Lepers, M. Aymar, N. Bouloufa-Maafa, and O. Dulieu, *Long-range interactions between polar bialkali ground-state molecules in arbitrary vibrational levels*, J. Chem. Phys. **142**, 214303 (2015).

[184] M. Guo, B. Zhu, B. Lu, X. Ye, F. Wang, R. Vexiau, N. Bouloufa-Maafa, G. Quéméner, O. Dulieu, and D. Wang, *Creation of an Ultracold Gas of Ground-State Dipolar* ^{23}Na^{87}Rb *Molecules*, Phys. Rev. Lett. **116**, 205303 (2016).

[185] B. R. Johnson, *The renormalized Numerov method applied to calculating bound states of the coupled-channel Schroedinger equation*, J. Chem. Phys. **69**, 4678 (1978).

[186] A. V. Avdeenkov and J. L. Bohn, *Linking Ultracold Polar Molecules*, Phys. Rev. Lett. **90**, 043006 (2003).

[187] A. V. Avdeenkov, D. C. E. Bortolotti, and J. L. Bohn, *Field-linked states of ultracold polar molecules*, Phys. Rev. A **69**, 012710 (2004).

[188] B. Gao, *General form of the quantum-defect theory for $-1/r^\alpha$ type of potentials with $\alpha > 2$*, Phys. Rev. A **78**, 012702 (2008).

[189] S. Kotochigova, *Dispersion interactions and reactive collisions of ultracold polar molecules*, New J. Phys. **12**, 073041 (2010).

[190] M. Lepers, R. Vexiau, M. Aymar, N. Bouloufa-Maafa, and O. Dulieu, *Long-range interactions between polar alkali-metal diatoms in external electric fields*, Phys. Rev. A **88**, 032709 (2013).

[191] P. S. Żuchowski, M. Kosicki, M. Kodrycka, and P. Soldán, *van der Waals coefficients for systems with ultracold polar alkali-metal molecules*, Phys. Rev. A **87**, 022706 (2013).

[192] E. B. Norrgard, D. J. McCarron, M. H. Steinecker, M. R. Tarbutt, and D. DeMille, *Submillikelvin Dipolar Molecules in a Radio-Frequency Magneto-Optical Trap*, Phys. Rev. Lett. **116**, 063004 (2016).

[193] S. Truppe, H. J. Williams, M. Hambach, L. Caldwell, N. J. Fitch, E. A. Hinds, B. E. Sauer, and M. R. Tarbutt, *Molecules cooled below the Doppler limit*, Nat. Phys. **13**, 1173 (2017).

[194] L. Anderegg, B. L. Augenbraun, E. Chae, B. Hemmerling, N. R. Hutzler, A. Ravi, A. Collopy, J. Ye, W. Ketterle, and J. M. Doyle, *Radio Frequency Magneto-Optical Trapping of CaF with High Density*, Phys. Rev. Lett. **119**, 103201 (2017).

[195] L. Anderegg, B. L. Augenbraun, Y. Bao, S. Burchesky, L. W. Cheuk, W. Ketterle, and J. M. Doyle, *Laser cooling of optically trapped molecules*, Nat. Phys. **14**, 890 (2018).

[196] M. T. Hummon, M. Yeo, B. K. Stuhl, A. L. Collopy, Y. Xia, and J. Ye, *2D Magneto-Optical Trapping of Diatomic Molecules*, Phys. Rev. Lett. **110**, 143001 (2013).

[197] J. D. Weinstein, R. deCarvalho, T. Guillet, B. Friedrich, and J. M. Doyle, *Magnetic trapping of calcium monohydride molecules at milliKelvin temperatures*, Nature **395**, 148 (1998).

[198] B. Pasquiou, A. Bayerle, S. M. Tzanova, S. Stellmer, J. Szczepkowski, M. Parigger, R. Grimm, and F. Schreck, *Quantum degenerate mixtures of strontium and rubidium atoms*, Phys. Rev. A **88**, 023601 (2013).

[199] T. Chen, W. Bu, and B. Yan, *Structure, branching ratios, and a laser-cooling scheme for the ^{138}BaF molecule*, Phys. Rev. A **94**, 063415 (2016).

[200] A. Cournol, P. Pillet, H. Lignier, and D. Comparat, *Rovibrational optical pumping of a molecular beam*, Phys. Rev. A **97**, 031401 (2018).

[201] I. Kozyryev, L. Baum, K. Matsuda, B. L. Augenbraun, L. Anderegg, A. P. Sedlack, and J. M. Doyle, *Sisyphus Laser Cooling of a Polyatomic Molecule*, Phys. Rev. Lett. **118**, 173201 (2017).

[202] A. Guttridge, S. A. Hopkins, M. D. Frye, J. J. McFerran, J. M. Hutson, and S. L. Cornish, *Production of ultracold Cs^*Yb molecules by photoassociation*, Phys. Rev. A **97**, 063414 (2018).

[203] A. Guttridge, M. D. Frye, B. C. Yang, J. M. Hutson, and S. L. Cornish, *Two-photon photoassociation spectroscopy of CsYb: Ground-state interaction potential and interspecies scattering lengths*, Phys. Rev. A **98**, 022707 (2018).

[204] F. Münchow, C. Bruni, M. Madalinski, and A. Görlitz, *Two-photon photoassociation spectroscopy of heteronuclear YbRb*, Phys. Chem. Chem. Phys. **13**, 18734 (2011).

[205] M. Schmidt, L. Lassablière, G. Quéméner, and T. Langen, *Self-bound dipolar droplets and supersolids in molecular Bose-Einstein condensates*, **arXiv:2111.06187** (2021).

[206] K. Matsuda, L. De Marco, J.-R. Li, W. G. Tobias, G. Valtolina, G. Quéméner, and J. Ye, *Resonant collisional shielding of reactive molecules using electric fields*, Science **370**, 1324 (2020).

[207] H. Hellmann, *Zur Rolle der kinetischen Elektronenenergie für die zwischenatomaren Kräfte*, Z. Phys. **85**, 180 (1933).

[208] R. P. Feynman, *Forces in molecules*, Phys. Rev. **56**, 340 (1939).

[209] K.-K. Ni, *A quantum gas of polar molecules*, PhD thesis, University of California, 2009.

[210] G. Quéméner and J. L. Bohn, *Shielding $^2\Sigma$ ultracold dipolar molecular collisions with electric fields*, Phys. Rev. A **93**, 012704 (2016).

[211] G. Quéméner and J. L. Bohn, *Strong dependence of ultracold chemical rates on electric dipole moments*, Phys. Rev. A **81**, 022702 (2010).

[212] G. Quéméner, J. L. Bohn, A. Petrov, and S. Kotochigova, *Universalities in ultracold reactions of alkali-metal polar molecules*, Phys. Rev. A **84**, 062703 (2011).

[213] J. L. Bohn, M. Cavagnero, and C. Ticknor, *Quasi-universal dipolar scattering in cold and ultracold gases*, New J. Phys. **11**, 055039 (2009).

[214] A. V. Gorshkov, S. R. Manmana, G. Chen, E. Demler, M. D. Lukin, and A. M. Rey, *Quantum magnetism with polar alkali-metal dimers*, Phys. Rev. A **84**, 033619 (2011).

[215] W. E. Perreault, N. Mukherjee, and R. Zare, *Quantum control of molecular collisions at 1 Kelvin*, Science **358**, 356 (2017).

[216] W. E. Perreault, N. Mukherjee, and R. N. Zare, *Cold quantum-controlled rotationally inelastic scattering of HD with H_2 and D_2 reveals collisional partner reorientation*, Nat. Chem. **10** (2018).

[217] W. E. Perreault, N. Mukherjee, and R. N. Zare, *HD (v = 1, j = 2, m) orientation controls HD − He rotationally inelastic scattering near 1 K*, J. Chem. Phys. **150**, 174301 (2019).

[218] B. K. Kendrick, *Geometric phase effects in the $H + D_2 \rightarrow HD + D$ reaction*, J. Chem. Phys. **112**, 5679 (2000).

[219] P. Soldán, M. T. Cvitaš, J. M. Hutson, P. Honvault, and J.-M. Launay, *Quantum Dynamics of Ultracold* $\mathrm{Na} + \mathrm{Na}_2$ *Collisions*, Phys. Rev. Lett. **89**, 153201 (2002).

[220] G. Quéméner, P. Honvault, J.-M. Launay, P. Soldán, D. E. Potter, and J. M. Hutson, *Ultracold quantum dynamics: Spin-polarized* $\mathrm{K} + \mathrm{K}_2$ *collisions with three identical bosons or fermions*, Phys. Rev. A **71**, 032722 (2005).

[221] M. T. Cvitaš, P. Soldán, J. M. Hutson, P. Honvault, and J.-M. Launay, *Ultracold Li + Li_2 Collisions: Bosonic and Fermionic Cases*, Phys. Rev. Lett. **94**, 033201 (2005).

[222] M. T. Cvitaš, P. Soldán, J. M. Hutson, P. Honvault, and J.-M. Launay, *Ultracold collisions involving heteronuclear alkali metal dimers*, Phys. Rev. Lett. **94**, 200402 (2005).

[223] J. Croft, C. Makrides, M. Li, A. Petrov, B. Kendrick, N. Balakrishnan, and S. Kotochigova, *Universality and chaoticity in ultracold K + KRb chemical reactions*, Nat. Commun. **8**, 1 (2017).

[224] J. F. E. Croft, N. Balakrishnan, and B. K. Kendrick, *Long-lived complexes and signatures of chaos in ultracold K_2 + Rb collisions*, Phys. Rev. A **96**, 062707 (2017).

[225] B. K. Kendrick, *Quantum reactive scattering calculations for the cold and ultracold $Li + LiNa \rightarrow Li_2 + Na$ reaction*, J. Chem. Phys. **154**, 124303 (2021).

[226] B. R. Johnson, *The classical dynamics of three particles in hyperspherical coordinates*, J. Chem. Phys. **79**, 1906 (1983).

[227] B. R. Johnson, *The quantum dynamics of three particles in hyperspherical coordinates*, J. Chem. Phys. **79**, 1916 (1983).

[228] R. T. Pack and G. A. Parker, *Quantum reactive scattering in three dimensions using hyperspherical (APH) coordinates. III. Small θ behavior and corrigenda*, J. Chem. Phys. **90**, 3511 (1989).

[229] D. Wang and A. Kuppermann, *Hyperspherical Harmonics for Triatomic Systems*, J. Phys. Chem. A **107**, 7290 (2003).

[230] J.-M. Launay and M. Le Dourneuf, *Hyperspherical close-coupling calculation of integral cross sections for the reaction $H + H_2 \rightarrow H_2 + H$*, Chem. Phys. Lett. **163**, 178 (1989).

[231] G. A. Parker, R. B. Walker, B. K. Kendrick, and R. T Pack, *Accurate quantum calculations on three-body collisions in recombination and collision-induced dissociation. I. Converged probabilities for the $H + Ne_2$ system*, J. Chem. Phys. **117**, 6083 (2002).

[232] F. D. Colavecchia, F. Mrugała, G. A. Parker, and R. T Pack, *Accurate quantum calculations on three-body collisions in recombination and collision induced dissociation. II. The smooth variable discretization enhanced renormalized Numerov propagator*, J. Chem. Phys. **118**, 10387 (2003).

[233] D. A. Brue, *Quantum reactive scattering: Collision induced dissociation*, PhD thesis, The University of Oklahoma, 2010.

[234] H. Goldstein, *«Classical Mechanics»*, Addison-Wesley, 1980.

[235] C. Eckart, *The kinetic energy of polyatomic molecules*, Phys. Rev. **46**, 383 (1934).

[236] A. Kuppermann and Y.-S. M. Wu, *The geometric phase effect shows up in chemical reactions*, Chem. Phys. Lett. **205**, 577 (1993).

[237] Y.-S. M. Wu and A. Kuppermann, *The importance of the geometric phase effect for the $H + D_2 \rightarrow HD + D$ reaction*, Chem. Phys. Lett. **235**, 105 (1995).

[238] A. Kuppermann and Y.-S. M. Wu, *The quantitative prediction and lifetime of a pronounced reactive scattering resonance*, Chem. Phys. Lett. **241**, 229 (1995).

[239] C. Eckart, *Some studies concerning rotating axes and polyatomic molecules*, Phys. Rev. **47**, 552 (1935).

[240] J. D. Louck and H. W. Galbraith, *Eckart vectors, Eckart frames, and polyatomic molecules*, Rev. Mod. Phys. **48**, 69 (1976).

[241] L. Wolniewicz, *A new numerical procedure for the construction of orthonormal hyperspherical functions*, J. Chem. Phys. **90**, 371 (1989).

[242] J. C. Light, I. P. Hamilton, and J. V. Lill, *Generalized discrete variable approximation in quantum mechanics*, J. Chem. Phys. **82**, 1400 (1985).

[243] S. T. Rittenhouse, J. von Stecher, J. P. D'Incao, N. P. Mehta, and C. H. Greene, *The hyperspherical four-fermion problem*, J. Phys. B: At., Mol. Opt. Phys. **44**, 172001 (2011).

[244] H. Suno, B. D. Esry, C. H. Greene, and J. P. Burke, *Three-body recombination of cold helium atoms*, Phys. Rev. A **65**, 042725 (2002).

[245] J. Söding, D. Guéry-Odelin, P. Desbiolles, F. Chevy, H. Inamori, and J. Dalibard, *Three-body decay of a rubidium Bose-Einstein condensate*, Appl. Phys. B **69**, 257 (1999).

[246] R. J. Le Roy, *Long-Range Potential Coefficients From RKR Turning Points: C_6 and C_8*, Can. J. Phys. **52**, 246 (1974).

[247] M. Lepers and O. Dulieu, *Long-range interactions between ultracold atoms and molecules including atomic spin–orbit*, Phys. Chem. Chem. Phys. **13**, 19106 (2011).

[248] J. P. D'Incao, C. H. Greene, and B. D. Esry, *The short-range three-body phase and other issues impacting the observation of Efimov physics in ultracold quantum gases*, J. Phys. B: At. Mol. Opt. Phys. **42**, 044016 (2009).

[249] R. Wynar, R. Freeland, D. Han, C. Ryu, and D. Heinzen, *Molecules in a Bose-Einstein condensate*, Science **287**, 1016 (2000).

[250] N. Zahzam, T. Vogt, M. Mudrich, D. Comparat, and P. Pillet, *Atom-molecule collisions in an optically trapped gas*, Phys. Rev. Lett. **96**, 023202 (2006).

[251] P. Staanum, S. D. Kraft, J. Lange, R. Wester, and M. Weidemüller, *Experimental investigation of ultracold atom-molecule collisions*, Phys. Rev. Lett. **96**, 023201 (2006).

[252] E. R. Hudson, N. B. Gilfoy, S. Kotochigova, J. M. Sage, and D. DeMille, *Inelastic collisions of ultracold heteronuclear molecules in an optical trap*, Phys. Rev. Lett. **100**, 203201 (2008).

[253] J. Deiglmayr, M. Repp, R. Wester, O. Dulieu, and M. Weidemüller, *Inelastic collisions of ultracold polar LiCs molecules with caesium atoms in an optical dipole trap*, Phys. Chem. Chem. Phys. **13**, 19101 (2011).

[254] N. Balakrishnan, V. Kharchenko, R. Forrey, and A. Dalgarno, *Complex scattering lengths in multi-channel atom–molecule collisions*, Chem. Phys. Lett. **280**, 5 (1997).

[255] N. Balakrishnan, R. Forrey, and A. Dalgarno, *Quenching of H_2 vibrations in ultracold ^{3}He and ^{4}He collisions*, Phys. Rev. Lett. **80**, 3224 (1998).

[256] E. Bodo, F. A. Gianturco, and E. Yurtsever, *Vibrational quenching at ultralow energies: Calculations of the Li_2 + He superelastic scattering cross sections*, Phys. Rev. A **73**, 052715 (2006).

[257] G. Polovy, E. Frieling, D. Uhland, J. Schmidt, and K. W. Madison, *Quantum-state-dependent chemistry of ultracold $^6Li_2$ dimers*, Phys. Rev. A **102**, 013310 (2020).

[258] M. T. Cvitaš, P. Soldán, J. M. Hutson, P. Honvault, and J.-M. Launay, *Interactions and dynamics in Li + Li_2 ultracold collisions*, J. Chem. Phys. **127**, 074302 (2007).

[259] F. D. Colavecchia, J. P. Burke, W. J. Stevens, M. R. Salazar, G. A. Parker, and R. T Pack, *The potential energy surface for spin-aligned Li_3 and the potential energy curve for spin-aligned Li_2*, J. Chem. Phys. **118**, 5484 (2003).

[260] G. C. Schatz, *The analytical representation of electronic potential-energy surfaces*, Rev. Mod. Phys. **61**, 669 (1989).

[261] D. Yang, J. Zuo, J. Huang, X. Hu, R. Dawes, D. Xie, and H. Guo, *A global full-dimensional potential energy surface for the K_2Rb_2 complex and its lifetime*, J. Phys. Chem. Lett. **11**, 2605 (2020).

[262] A. Christianen, T. Karman, R. A. Vargas-Hernández, G. C. Groenenboom, and R. V. Krems, *Six-dimensional potential energy surface for $NaK - NaK$ collisions: Gaussian process representation with correct asymptotic form*, J. Chem. Phys. **150**, 064106 (2019).

[263] J. Kłos, Q. Guan, H. Li, M. Li, E. Tiesinga, and S. Kotochigova, *Roaming pathways and survival probability in real-time collisional dynamics of cold and controlled bialkali molecules*, Sci. Rep. **11**, 1 (2021).

[264] J. F. Croft, J. L. Bohn, and G. Quéméner, *Unified model of ultracold molecular collisions*, Phys. Rev. A **102**, 033306 (2020).

[265] G. Quéméner, J. F. E. Croft, and J. L. Bohn, *Electric field dependence of complex-dominated ultracold molecular collisions*, arXiv e-prints **2109**, 02602 (2021).

[266] C. Cohen-Tannoudji, G. Grynberg, and J. Dupont-Roc, *«Atom-Photon Interactions: Basic Processes and Applications»*, Wiley, 1992.

[267] F. Reif, *«Fundamentals of Statistical and Thermal Physics»*, McGraw Hill, 1965.

[268] Z. Idziaszek and P. S. Julienne, *Universal Rate Constants for Reactive Collisions of Ultracold Molecules*, Phys. Rev. Lett. **104**, 113202 (2010).

[269] N. Vanhaecke and O. Dulieu, *Precision measurements with polar molecules: the role of the black body radiation*, Mol. Phys. **105**, 1723 (2007).

[270] D. P. Dunseith, S. Truppe, R. J. Hendricks, B. E. Sauer, E. A. Hinds, and M. R. Tarbutt, *A high quality, efficiently coupled microwave cavity for trapping cold molecules*, J. Phys. B **48**, 045001 (2015).

[271] J. Aldegunde, B. A. Rivington, P. S. Żuchowski, and J. M. Hutson, *Hyperfine energy levels of alkali-metal dimers: Ground-state polar molecules in electric and magnetic fields*, Phys. Rev. A **78**, 033434 (2008).

[272] J. Aldegunde and J. M. Hutson, *Hyperfine structure of alkali-metal diatomic molecules*, Phys. Rev. A **96**, 042506 (2017).

[273] J. Aldegunde and J. M. Hutson, *Hyperfine energy levels of alkali-metal dimers: Ground-state homonuclear molecules in magnetic fields*, Phys. Rev. A **79**, 013401 (2009).

[274] J. Aldegunde and J. M. Hutson, *Hyperfine structure of $^2\Sigma$ molecules containing alkaline-earth-metal atoms*, Phys. Rev. A **97**, 042505 (2018).

[275] J. N. Byrd, J. A. Montgomery, and R. Côté, *Long-range forces between polar alkali-metal diatoms aligned by external electric fields*, Phys. Rev. A **86**, 032711 (2012).

[276] J. Chen and T. C. Steimle, *The permanent electric dipole moment of calcium monodeuteride*, J. Chem. Phys. **128**, 144312 (2008).

[277] R. Guérout, M. Aymar, and O. Dulieu, *Ground state of the polar alkali-metal-atom–strontium molecules: Potential energy curve and permanent dipole moment*, Phys. Rev. A **82**, 042508 (2010).

[278] T. C. Steimle, P. J. Domaille, and D. O. Harris, *Rotational analysis of SrF using a cw tunable dye laser*, J. Mol. Spectrosc. **68**, 134 (1977).

[279] W. Ernst, J. Kändler, S. Kindt, and T. Törring, *Electric dipole moment of SrF from high-precision stark effect measurements*, Chem. Phys. Lett. **113**, 351 (1985).

[280] C. Ryzlewicz and T. Törring, *Formation and microwave spectrum of the $^2\Sigma$-radical barium-monofluoride*, Chem. Phys. **51**, 329 (1980).

[281] W. E. Ernst, J. Kändler, and T. Törring, *Hyperfine structure and electric dipole moment of BaF*, J. Chem. Phys. **84**, 4769 (1986).

[282] A. Bernard and R. Gravina, *The emission spectrum of yttrium monoxide - New rotational and vibrational results*, Astrophys. J. Suppl. Ser. **52**, 443 (1983).

[283] R. D. Suenram, F. J. Lovas, G. T. Fraser, and K. Matsumura, *Pulsed-nozzle Fourier-transform microwave spectroscopy of laser-vaporized metal oxides: Rotational spectra and electric dipole moments of YO, LaO, ZrO, and HfO*, J. Chem. Phys. **92**, 4724 (1990).

[284] W. J. Childs, L. S. Goodman, U. Nielsen, and V. Pfeufer, *Electric-dipole moment of CaF by molecular beam, laser-rf, double-resonance study of Stark splittings*, J. Chem. Phys. **80**, 2283 (1984).

[285] L. A. Kaledin, J. C. Bloch, M. C. McCarthy, and R. W. Field, *Analysis and Deperturbation of the States of CaF*, J. Mol. Spectrosc. **197**, 289 (1999).

[286] T. C. Steimle, D. A. Fletcher, K. Y. Jung, and C. T. Scurlock, *A supersonic molecular beam optical Stark study of CaOH and SrOH*, J. Chem. Phys. **96**, 2556 (1992).

[287] D. A. Fletcher, M. A. Anderson, W. L. Barclay, and L. M. Ziurys, *Millimeter-wave spectroscopy of vibrationally excited ground state alkaline-earth hydroxide radicals*, J. Chem. Phys. **102**, 4334 (1995).

[288] Q. Shao, L. Deng, X. Xing, D. Gou, X. Kuang, and H. Li, *Ground State Properties of the Polar Alkali-MetalYtterbium Molecules: A Comparative Study*, J. Phys. Chem. A **121**, 2187 (2017).

[289] T. C. Steimle, J. Gengler, and J. Chen, *A study of band systems of calcium monohydride (CaH) using a supersonic molecular beam source and laser-induced fluorescence detection*, Can. J. Chem. **82**, 779 (2004).

[290] C. Ryzlewicz, H.-U. Schütze-Pahlmann, J. Hoeft, and T. Törring, *Rotational spectrum and hyperfine structure of the radicals BaF and BaCl*, Chem. Phys. **71**, 389 (1982).

[291] P. D. Gregory, M. D. Frye, J. A. Blackmore, E. M. Bridge, R. Sawant, J. M. Hutson, and S. L. Cornish, *Sticky collisions of ultracold RbCs molecules*, Nat. Commun. **10**, 3104 (2019).

université PARIS-SACLAY

ÉCOLE DOCTORALE
Ondes et matière (EDOM)

Titre : Collisions de molécules dipolaires ultra-froides contrôlées par champs électrique et électromagnétique
Mots clés : Collisions, Matière froide, Molécules dipolaires, Dynamique quantique

Résumé : Depuis plus de 20 ans, des avancées majeures ont été réalisées dans la formation, le refroidissement et le piégeage de molécules dipolaires. Il est maintenant possible de former des molécules dans un état quantique bien défini à des températures de l'ordre de quelques centaines de nanokelvins. Le prochain défi expérimental est d'atteindre des régimes de dégénérescence quantique pour créer des condensats de Bose-Einstein ou des gaz de Fermi dégénérés moléculaires, impliquant d'obtenir des densités plus élevées et d'atteindre des températures plus basses. Cependant, ces conditions sont difficiles à obtenir car de nombreuses molécules sont détruites ou perdues lors de collisions à deux corps ou trois corps. L'objectif de cette thèse est de développer des méthodes d'écrantage pour supprimer ces processus de pertes. Ces méthodes exploitent les propriétés à longue portée de l'interaction dipôle-dipôle, qui peuvent être contrôlées par l'application de champs externes. En utilisant un formalisme quantique indépendant du temps, basé sur les coordonnées de Jacobi ou sur les coordonnées hypersphériques, je montre que l'utilisation d'un champ électrique statique est efficace pour réduire les pertes à deux corps et à trois corps dans le cas de molécules préparées dans leur premier état rotationnel excité. Je démontre également que les pertes à deux corps peuvent être fortement réduites pour des molécules initialement préparées dans leur état rotationnel fondamental en utilisant un champ micro-onde. Cette dernière méthode offre des outils pour contrôler la partie réelle et imaginaire de la longueur de diffusion molécule - molécule, grandeur clé qui caractérise la stabilité et la contrôlabilité d'un condensat de Bose-Einstein. Enfin, j'applique le code numérique à trois corps que j'ai développé pour étudier des collisions réactives atome - diatome. Ce code permettra également d'explorer des phénomènes de recombinaison à trois corps et de dissociation induite par collisions. Toutes ces méthodes laissent entrevoir un large éventail d'applications pour les molécules ultra-froides dans le domaine de la physique à N-corps, à l'instar des atomes ultra-froids.

Title : Collisions of ultracold dipolar molecules controlled by electric and electromagnetic fields
Keywords : Collisions, Cold matter, Dipolar molecules, Quantum dynamics

Abstract : For more than 20 years, major advances have been made in the formation, cooling and trapping of dipolar molecules. It is now possible to form molecules in a well-defined quantum state at temperatures on the order of a few hundreds of nanokelvins. The upcoming experimental challenge is to reach for the quantum degeneracy regime to create molecular Bose-Einstein condensates or degenerate Fermi gases, which require higher densities and much lower temperatures. However, these conditions are hard to achieve because many molecules are destroyed or lost in two-body or three-body collisions. The goal of this thesis is to develop shielding methods that can suppress these loss processes. These methods exploit the long-range properties of the dipole-dipole interaction, which can be controlled by applied external fields. Using a time-independent quantum formalism, based on Jacobi or hyperspherical coordinates, I show that a static electric field can be used to reduce the two-body and three-body losses for molecules prepared in their first excited rotational state. I also demonstrate that the two-body losses can be strongly reduced for molecules initially prepared in their ground rotational state using a microwave field. This latter method also provides tools to control the real and imaginary part of the molecule - molecule scattering length, which is a key-parameter that characterizes the stability and the controllabiity of a Bose-Einstein condensate. Finally, I apply the numerical code I have developed to study reactive atom - diatom collisions. This code will also enable studies of three-body recombination and collision-induced dissociation phenomena. All these methods open the door for a rich many-body physics for ultracold molecules, similar to that for ultracold atoms.